Arborescent Core–Shell–Corona Copolymers by Self-Assembly as Templates for the Preparation of Metallic Nanoparticles

by

Aklilu F Worku

A thesis
presented to the University of Waterloo
in fulfillment of the
thesis requirement for the degree of
Doctor of Philosophy
in
Chemistry

Waterloo, Ontario, Canada, 2020

Examining Committee Membership

The following served on the Examining Committee for this thesis. The decision of the Examining Committee is by majority vote.

External Examiner	Jung Kwon (John) Oh Professor
Supervisor(s)	Mario Gauthier Professor
Internal Member	Jean Duhamel Professor
Internal-external Member	Yuning Li Professor
Other Member(s)	Juewen Liu Professor

AUTHOR'S DECLARATION

I hereby declare that I am the sole author of this thesis. This is a true copy of the thesis, including any required final revisions, as accepted by my examiners.

I understand that my thesis may be made electronically available to the public.

Abstract

The preparation of metallic nanoparticles has been a rapidly growing field of research in recent years, because of the unique physical properties and applications of these materials. The development of applications for nanomaterials and nanostructures generally requires control over their size, size distribution, morphology, and chemical composition. Different methods have been developed to that end.

Arborescent copolymers, a unique type of graft copolymers with a dendritic architecture, were previously investigated as templates for the preparation of metallic nanoparticles. Specifically, polystyrene-*graft*-[poly(2-vinylpyridine)-*block*-polystyrene] copolymers were obtained by successive functionalization and anionic grafting reactions leading to a covalently bonded, layered structure with a core of arborescent polystyrene, an inner shell of poly(2-vinyl pyridine) (P2VP), and a corona of polystyrene chains. While these materials were shown to be useful as template, due to their inherent stability, their synthesis was limited by very low grafting yields in most cases.

In this Thesis a new method is demonstrated for the preparation of arborescent core–shell–corona structures called arborescent copolymer complexes (ACC), namely polystyrene-*graft*-poly(2-vinylpyridine)-*graft*-poly(acrylic acid)-*block*-polystyrene, obtained by the self-assembly of arborescent polystyrene-*graft*-poly(2-vinylpyridine) copolymers with poly(acrylic acid)-*block*-polystyrene copolymers via weak acid–weak base interactions. It involves anionic grafting for the synthesis of the arborescent polystyrene-*graft*-poly(2-vinyl pyridine) substrates, atom transfer radical polymerization (ATRP) to synthesize the poly(acrylic acid)-*block*-polystyrene copolymers, and mixing the two components in solution in appropriate ratios to prepare the polymeric templates in high yield. This is a new, simpler approach to the synthesis of core–shell–corona (CSC) structures comparable to those obtained by tedious anionic grafting procedures using “living” block copolymers.

The complexation reaction was investigated using dynamic light scattering (DLS), transmission electron microscopy (TEM) and atomic force microscopy (AFM) analysis. In most cases, an increase in size was observed after a substrate was complexed with a block copolymer to yield self-assembled structures with a single, narrow size population. The DLS data, together with the non-aggregated particles of uniform size observed in the AFM and TEM images, provided strong evidence for the formation of the desired CSC complexes.

Different generations (G2–G4) of ACCs were successfully loaded with tetrachloroauric acid ($HAuCl_4$), and intramolecular phase separation was especially apparent for higher generation (G3 and G4) templates, producing a variety of morphologies including spherical, ring-like, raspberry, and core–shell metal distributions. Subsequent reduction with sodium borohydride ($NaBH_4$) yielded aggregation-free gold nanoparticles with a size ranging from 4 to 17 nm inside the polyion complexes.

Overall, the results obtained in the current investigation clearly show that ACCs, obtained in high yield by a simple self-assembly procedure using arborescent polystyrene-*graft*-poly(2-vinylpyridine) and poly(acrylic acid)-*block*-polystyrene copolymers, have great potential as templates for the preparation of metallic nanoparticles. The nanomorphologies obtained with the ACCs are comparable to those observed for arborescent polystyrene-*graft*-poly(2-vinylpyridine)-*block*-polystyrene systems in many cases. Not only the simplicity of the self-assembly approach, but also the versatility of the process enables the synthesis of a wide range of these interesting materials on a larger (multi-gram) scale, which will facilitate the investigation of their properties in relation to applications in different areas such as sensors and catalysts.

Acknowledgements

I would like to express my appreciation to many individuals who have been encouraging, supporting, and guiding me throughout my journey.

First and foremost I would like to express my deep gratitude to my supervisor, Prof. Mario Gauthier. It would not have been possible to accomplish this research without his unreserved thoughtfulness, support, guidance, and understanding.

I would like to thank my supervisory committee members Prof. Jean Duhamel, Prof. Juewen Liu, Prof. Pavle Radovanovic, and Prof. Yuning Li, and the external examiner, Prof. Jung Kwon (John) Oh, for their valued recommendations.

It is my desire to thank my ATRP mentors, Dr. Olivier Nguon and Dr. An Nguyen, for their guidance and time at the beginning of the project, but also for their friendship. I truly appreciate Dr. Mosa Alsehli for his help with preparatory SEC, kind friendship, thoughts and encouragements during difficult times.

I would also like to extend my regards to my colleagues at the University of Waterloo for being good friends, and for valuable discussions during the program: Ala Alturk, Dr. Daisuke Aoki, Dr. Deepak Vishnu, Dr. Firmin Moingeon, Dr. Hemali Lad, Dr. Ilias Mahmud, Joanne Fernandez, Liying Wang, Dr. Mehdi Neqal, Paul Dymond, Dr. Ryan Amos, Dr. Toufic Aridi, Victoria Hisko, Yahya Alzahrany and all other current and past associates from the Gauthier, Duhamel, and Wang laboratories. Without the good working environment which they provided, the completion of this project would not have been possible.

Furthermore, I would like to express my appreciation to my family and parents for their love, support, and encouragement. I also would like to thank the Ethiopian community, and particularly to the Debresina Kidanemhret Church congregation, who have been helping and encouraging me during difficult times.

Last but not least, I would like to thank the University of Waterloo and the Natural Sciences and Engineering Research Council of Canada (NSERC) for their financial support.

Dedication

I dedicate this work to my beloved son, Nuab Worku, who has been missing a fatherhood relationship for an extended period throughout this project. I also dedicate this work to my late sister, who passed away in the middle of this project, and has always been my inspiration and encouragement for achievement at the highest level possible, may God rest your soul in peace.

Table of Contents

List of Figures

List of Tables

List of Schemes

List of abbreviations

2VP	2-Vinylpyridine
AA	Acrylic acid
ACC	Arborescent copolymer complex
ACPS	Arborescent copolymer substrate
AFM	Atomic force microscopy
ATRP	Atom transfer radical polymerization
DTAB	Decyltrimethylammonium bromide
Au NPs	Gold nanoparticles
BCP	Block copolymer
CAC	Critical aggregation concentration
CMC	Critical micelle concentration
CMT	Critical micelle temperature
CS	Core–shell
CSC	Core–shell–corona
CTAB	Hexadecyltrimethylammonium bromide
DLS	Dynamic light scattering
DLVO	Derjaguin, Landau, Verwey and Overbeek
DMF	N,N-Dimethylformamide
DNA	Deoxyribonucleic acid
DRI	Differential refractive index
equiv	Equivalent
FRET	Fluorescence resonance energy transfer
FTIR	Fourier transform infrared
GPC	Gel permeation chromatography
N_2H_4	Hydrazine
HBP	Hyperbranched polyglycidol
HEA	2-Hydroxyethyl acrylate
HPG	Hyperbranched polyglycerol
HYPAM	Hyperbranched polyamidoamine
IL	Ionic liquid
IR	Infrared
LALS	Low angle light scattering
LCST	Lower critical solution temperature
LED	Light-emitting diode
LSPR	Localized surface plasmon resonance
MHS	Mark–Houwink–Sakurada
MAA	Methacrylic acid
mol%	Mole percent
MNP	Metallic nanoparticle

MWD	Molecular weight distribution
NEG	Nona(ethylene glycol)
NMP	Nitroxide-mediated polymerization
NMR	Nuclear magnetic resonance
NP	Nanoparticle
OEGMA	Oligo(ethylene glycol) methacrylate
P2VP	Poly(2-vinylpyridine)
P4VP	Poly(4-vinylpyridine)
PAA	Poly(acrylic acid)
PAA-*b*-PS	Poly(acrylic acid)-*block*-polystyrene
PAMAM	Poly(amidoamine)
PCL	Poly(Ɛ-caprolactone)
PDI	Polydispersity index
PEG	Poly(ethylene glycol)
PEI	Polyethyleneimine
PEO	Poly(ethylene oxide)
PFS	Poly(9,9-bis(4′-sulfnoatobutyl)fluorene-*co-alt*-1,4-phenylene)
PGA	Poly(glutamic acid)
PHEA	Poly(2-hydroxyethyl acrylate)
PIC	Polyion complex
PMAA	Poly(methacrylic acid)
PMDETA	N,N,N′,N″,N″-Pentamethyldiethylenetriamine
PMMA	Poly(methyl methacrylate)
PMPP	Polymethylphenylphosphazene
PPY	Polypyrrole
PPV	Polyphenylenevinylene
PS	Polystyrene
PS-*b*-P2VP	Polystyrene-*block*-poly(2-vinylpyridine)
PS-*b*-P4VP	Polystyrene-*block*-poly(4-vinyl pyridine)
P(MEO_2MA)	Poly(2-(2-methoxyethoxy)ethyl methacrylate
PtBA	Poly(*tert*-butyl acrylate)
PTFE	Polytetrafluoroethylene
PVP	Poly(N-vinyl-2-pyrrolidone)
PY	Pyrrole
RAFT	Reversible addition-fragmentation chain transfer
RALS	Right-angle light scattering
RI	Refractive index
RMS	Root-mean-square
rpm	Revolutions per minute
SEC	Size-exclusion chromatography
SF	Silk fibroin
SPR	Surface plasmon resonance

TEG	Triethylene glycol
TEM	Transmission electron microscopy
TFA	Trifluoroacetic acid
TGD	Transgeden
THF	Tetrahydrofuran
TMSPMA	(3-Trimethoxysilyl)propyl methacrylate
TTIP	Titanium tetraisopropoxide
UV-vis	Ultraviolet-visible

List of symbols

Đ	Dispersity
D_h	Hydrodynamic diameter
D_t	Translational diffusion coefficient
DP_n	Number-average degree of polymerization
f	Branching functionality
g	Graft
G_n	Generation number
K_B	Boltzmann constant
$\bar{M}n$	Number-average molar mass
$\bar{M}w$	Weight-average molar mass
$\bar{M}v$	Viscosity-average molar mass
r	Radius
R	Ideal gas constant
Rg	Radius of gyration
$< R_{g0} >^{1/2}$	Root-mean-square end-to-end distance
Rh	Hydrodynamic radius
s	Singlet (NMR)
T	Temperature
V	Volume
VA	Attractive van der Waals potential
Vh	Hydrodynamic volume
VR	Repulsive electrostatic potential
Vmax	Potential energy barrier to agglomeration
NA	Avogadro constant
K, α	Mark–Houwink–Sakurada parameters
dn/dc	Refractive index increment
e	Electron charge (Euler's number)
$g^{(2)}(t)$	Second-order autocorrelation function
n	Refractive index of solution
n_o	Refractive index of solvent
x	Mole fraction
$\bar{X}_n$	Number-average degree of polymerization
Γ	Autocorrelation function decay rate
δ	Chemical shift or Hansen solubility parameter
η	Viscosity
[η]	Intrinsic viscosity
θ	Scattering angle
λ	Wavelength
ρ	Density

σ	Standard deviation
μ^2	Variance of the decay rate

Chapter 1: Foreword

1.1 Opening remarks

Nanomaterials can serve in applications that would be rather difficult to implement with conventional materials,[1] and metallic nanoparticles (MNPs), in particular, have received much attention due to their unique physicochemical properties. As a result, these materials have found applications in different areas including separation,[2] imaging,[3] sensing,[4,5] biomedicine,[6] cancer therapy,[7-9] drug delivery,[3] and catalysis.[10-13] The atomic structure and size of metallic nanoparticles usually determine their properties, moreover the stability of nanoparticle can influence their applicability. Consequently, many studies over the last decades focused on the development of stable MNPs, with a controllable size and a uniform size distribution. Due to their unusual optical properties (e.g., surface plasmon resonance) and high chemical stability,[14] gold nanoparticles have been likely the most widely investigated metallic nanoparticles.[15]

Small molecules, surfactants and polymers have been commonly used as stabilizers in the synthesis of stable Au NPs. The ability of polymers to self-assemble or covalently bond to the Au surface makes them effective stabilizers. The effectiveness of polymeric stabilizers depends on several parameters such as their molecular architecture, the presence of functional groups, their molecular weight, and the solvent used. Different polymer architectures including linear, star-branched, and highly branched polymers have been studied for the preparation and the stabilization of gold nanoparticles,[16] but only a few investigations used dendritic polymers containing 2-vinylpyridine units, and mostly in aqueous environments.[17] To the best of our knowledge, this Thesis reports the first example of complex (core–shell–corona) arborescent copolymer structures prepared and used as templates for the preparation of metallic nanoparticles in organic solvents.

1.2 Research objectives and thesis outline

The research reported in this Thesis emphasizes the synthesis and the characterization of arborescent copolymer complex stabilizers serving in the preparation of metallic (primarily gold) nanoparticles. The main objective is to explore self-assembly as an alternate approach to the synthesis of arborescent core–shell–corona (CSC) structures in high yield, which has been a challenging task by the anionic covalent grafting techniques previously used for that purpose. The thesis objectives also include demonstrating the application of CSC structures as effective stabilizers for the preparation of Au NPs. The different nanomorphologies of gold nanoparticles stabilized by arborescent copolymer complexes that were obtained were investigated by different characterization techniques, to contribute to the understanding of these systems.

This Thesis is organized into seven chapters. Following this foreword, a detailed review of the different methods reported for the preparation of stable metallic nanoparticles (mainly gold) is provided in Chapter 2. In this literature review, the different stabilizer types used for the preparation of metallic nanoparticles such as surfactants, block copolymer micelles, star-block copolymers, dendrimers, hyperbranched and arborescent copolymers are discussed. It is demonstrated that the characteristics of the nanoparticles obtained depend on many factors including the types of stabilizer and reducing agent used, the metal loading level, and the preparation protocol employed. Details on the synthesis and the characterization of some of the polystyrene-*graft*-poly(2-vinylpyridine) arborescent copolymers and the poly(acrylic acid)-*block*-polystyrene (PAA-*b*-PS) copolymers that served in the formation of core–shell–corona arborescent copolymer complexes are provided in Chapter 3. In Chapter 4, the preparation of arborescent copolymer complexes (ACCs) by the self-assembly of arborescent copolymers and block copolymers in organic solvents is discussed. These complexes served in the preparation of gold nanoparticles. The ability of the ACCs to coordinate with $HAuCl_4$, and the different nanostructures observed upon coordination are discussed in Chapter 5. The reduction of the $HAuCl_4$ loaded in the

ACCs to Au^0 is discussed in Chapter 6. This includes an investigation of the loading level and of different solvent systems on the nanomorphologies obtained. The overall conclusions drawn from the work, including a summary of the results, original contributions to knowledge and suggestions for future work, are presented in Chapter 7.

In accordance with the University of Waterloo Thesis guidelines, each chapter is arranged as a manuscript for publication in a scientific journal. An introductory section, giving related background information on the topic, is followed by sections reporting the experimental methods used, the results obtained and their discussion, and the conclusions drawn from the work reported in each chapter. A general abstract for the whole study was provided at the beginning of the thesis. Moreover, a separate list of references for each chapter is provided at the end of the Thesis.

Chapter 2: Polymer-Stabilized Metallic Nanoparticles: Theory, Synthesis and Applications

2.1 Introduction

2.1.1 Nanoscience and nanotechnology

Nanotechnology is not new, but rather dates back to the fourth century A.D. It is indeed believed that the artefact in the British Museum called the "Lycurgus Cup" (**Figure 2-1**), made during the Roman Empire,[1-3] is an indication of its true age. This cup alters the color of light because it contains gold and silver nanoparticles with a size of about 70 nm. Not only the presence of these additives, but also the way in which they are structured within the glass is critical in determining its properties.[2] The Romans obviously were not aware that they were using nanotechnology, but the world has nonetheless been influenced by nanomaterials for centuries.[1] The "Lycurgus Cup" is not only a beautiful and ancient work of art, but also a strong reminder of the developments in nanotechnology.[2]

Figure 2-1. The "Lycurgus Cup" as seen in transmitted (left) and reflected (right) light. Reprinted with permission from reference 2.

In the modern era, self-reproducing, programmable architectures were identified by John von Neumann as early as the 1940s.[4] Richard Feynman, a Nobel Prize-winning physicist, published the best-known nanotechnology paper entitled "There's plenty of room at the bottom" based on a talk to the American Physical Society in 1959, to highlight the stimulating promises of nanotechnology if scientists were able to control substances as single atoms.[4,5] He also talked about the importance of developing high performance instruments such as electron microscopes.[5] Norio Taniguchi, from the

Tokyo University of Science, first used the term nanotechnology in 1974 to describe semiconductor processes such as thin film deposition and ion beam milling, providing control on the order of nanometers. Despite the contributions of Feynman and Taniguchi, nanotechnology remained dormant until the publication of K. Eric Drexler's 1986 book "Engines of Creation: The coming era of nanotechnology", highlighting new thoughts on the promises and risks of nanoscale technologies,[4] and the scientific community became acquainted with the term nanotechnology with the foundation of the Journal of Nanotechnology in 1989.[5]

In the Greek language nano means "dwarf", which in combination with technology refers to processes occurring on the 10^{-9} m scale.[4,6] Many definitions of nanotechnology indeed refer to dimensions: According to the national nanotechnology initiative in the United States, for example, "Nanotechnology is the understanding and control of matter at dimensions between approximately 1 and 100 nanometers, where unique phenomena enable novel applications".[7] Similarly, Cao[8] in his textbook defined nanotechnology as the "design, fabrication, application of nanostructures and the fundamental understanding of the relationships between physical properties or phenomena and material dimensions".[8] Many agree that if one physical dimension of matter falls within the nanometer scale (<100 nm), it may be called a nanostructured material.[6-8] According to the Control Engineering Magazine of Katzel,[1] nano does not just mean small; it is the setting of atoms and molecules into well-organized patterns to achieve something. Nanotechnology is the skill and the discipline of operating at the atomic or molecular scale of matter.[1]

Nanomaterials have desirable properties that cannot be achieved with common chemicals and materials, and which can become much more significant when they are combined to make a material. For instance, the addition of insignificant amounts of nanoparticles to bulk materials like polymers can suffice to bring new properties to these composites, but the way in which the nanoparticles were synthesized and their surface characteristics influence the results. Therefore for a specific application,

it is important to decide whether nanomaterials could be incorporated to obtain desirable properties.[9] There are two approaches to the synthesis of nanomaterials, top-down and bottom-up. Attrition or milling is a typical top-down method in manufacturing nanoparticles, while colloidal dispersions are a good example of a bottom-up approach.[8]

2.1.2 Metallic nanoparticles

Metallic nanoparticles (MNPs) are of interest due to their applications in different areas. Their atomic structure and size usually determine their properties; it has long been predicted that nanoparticles with a size comparable to small molecules would show electronic structures different from the bulk metal. The resulting physical properties are neither those of the atomic compounds nor of the bulk metal, but rather strongly depend on the particle size and shape, the inter-particle distance, and the nature of the stabilizing agent used.[10] Due to quantum size effects, their very high aspect ratio[6,11] and their high degree of dispersion (the proportion of surface atoms vs. total number of atoms in the particle),[12] MNPs exhibit physical and chemical properties distinct from the bulk state and isolated atoms.[11,13] Many nanoparticles also have dimensions much smaller than the wavelength of light, which renders them transparent and very useful for applications in cosmetics, coatings and packaging.[6]

The lack of stability of many nanoparticle preparations has, to some extent, hampered the development of real world applications for nanomaterials.[14] This highlights the fact that research in the development of stable nanoparticles requires particular attention to exploit their advantages.

2.1.3 Synthetic methods for metallic nanoparticles

Over the past decades, many synthetic methods have been developed to prepare MNPs of controllable size, size distribution and morphology. This is partly because noble MNPs (e.g. Au, Ag, Pd, Pt) have received much attention due to their unique physicochemical properties and their potential applications

in fields[14] such as separation,[15] imaging,[16-18] sensing, [17,19] medicine,[17] chemotherapy[1], cancer therapy,[20] photothermal therapy,[21] optical trapping,[22] drug delivery[23] and, in particular, catalysis.[24-29]

The techniques used to synthesize nanoparticles can be regrouped into chemical and physical methods. Physical methods include plasma reduction, metal vapor deposition, laser ablation and electron beam or γ–irradiation, whereas chemical methods include chemical reduction, microemulsions, thermal decomposition and electrochemical synthesis. The above division reflects the fact that the particles can be obtained either by dispersion and aggregation procedures, called top-down (mainly physical) methods, or be built from separate atoms by bottom-up (mostly chemical) methods.[30] In the top-down procedures, a bulk metal is systematically broken down to generate MNPs with desired dimensions (**Scheme 2.1**). However the top-down method is limited with respect to control over the size and shape of the particles, and their subsequent functionalization. In contrast, the bottom-up strategy is by far more common and effective,[31] because of its improved ability to attain nanostructures with fewer defects, a more homogeneous chemical composition, and better short- and long-range ordering. Since this method is driven mainly by a reduction in the Gibbs free energy, the nanostructures and nanomaterials produced are in a state closer to thermodynamic equilibrium. In contrast, the top-down methods typically produce much internal stress, along with surface defects and contamination.[8] In the bottom-up strategy, the formation of MNPs originates from individual molecules or atoms (**Scheme 2-1**) because it typically involves a chemical or biological reduction. Chemical reduction consists in two distinct steps: nucleation and growth.[13] Nucleation is the process whereby a discrete particle in a new phase forms in an initially single-phase system, whereas growth is defined as the deposition of additional material on the nuclei causing them to increase in size.

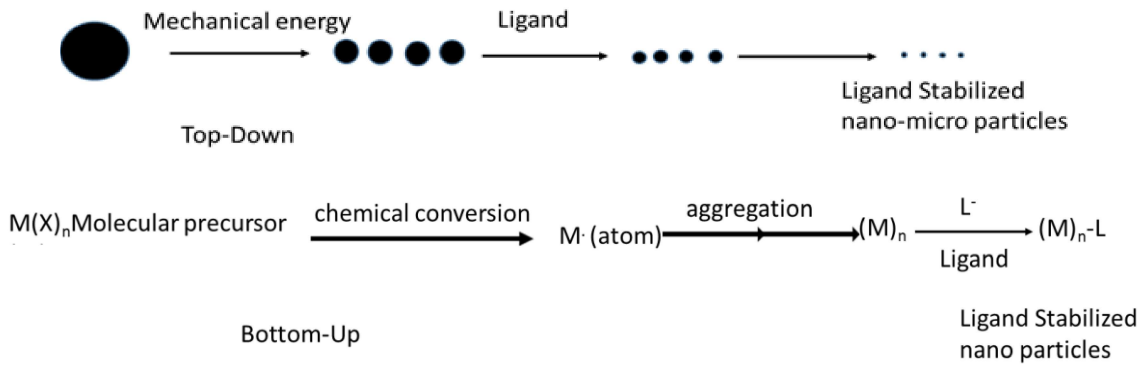

Scheme 2-1. Schematic representation of the synthesis of NPs by top-down (top) and bottom-up (bottom) approaches. Adapted with permission from reference 31. Copyright 2013 Elsevier.

The size distribution of MNPs depends largely on the relative rates of these two distinct processes.[32] When nucleation and growth are accomplished within the same process, it is called *in situ* synthesis; otherwise, it is called a *seed-growth* method.[13] In the *in situ* method, a reducing reagent is used to reduce metal ions that nucleate to form nanoparticles in the presence of protective ligands. Either the concentration of metal ions or the prevention of further growth by a protective ligand can determine the nanoparticle size.[31] In the *seed-growth* method small size MNP seeds are first prepared, and grown in a second step by introducing a solution containing a metal precursor, reducing and stabilizing agents. The first step is important in determining the size, shape and surface properties of the MNPs.[13] Bare nanoparticles can be stabilized either through the sorption of molecules from the surroundings, or by lowering the surface area through coagulation and agglomeration.[30] Stabilizing nanoparticles still remains a significant challenge.

2.1.4 Stabilization methods

Due to their enormous specific surface area (1 nm^3 particles have an area of ca. 2.8×10^7 cm^2/g, as compared to 28 cm^2/g for 0.1 cm^3 particles), bare metallic nanoparticles possess a huge surface energy (ca. 560 J/g for 1 nm^3 particles, vs. 2.6×10^{-4} J/g for 0.1 cm^3 particles) and are thus thermodynamically

unstable or metastable. One of the main challenges in the preparation of metallic nanoparticles is thus to overcome their high surface energy, to prevent them from growing in size by reducing their total surface energy. Diverse mechanisms may be involved in reducing the overall surface energy of particles: (I) Surface relaxation, whereby the atoms or ions at the surface shift inwards; (II) surface restructuring, or the formation of strained chemical bonds by combining surface dangling bonds; (III) surface adsorption, namely the adsorption of terminal chemical species onto the surface of the particles, by creating chemical bonds or through weak attractive forces such as electrostatic or van der Waals forces; and (IV) composition segregation, i.e. impurity deposition on the surface through solid-state diffusion. Protecting nanoparticles from aggregation requires stabilizing additives to shield the particles from each other, by building a protective layer. For example, ionic surfactants provide electrostatic stabilization to avoid agglomeration, whereas covering the surface with a layer of capping ligands or polymer provides steric stabilization.[33] Understanding the detailed mechanism of different stabilization methods is essential to synthesize stable, uniform and useable nanoparticles.

2.1.4.1 Electrostatic stabilization (kinetic stabilization method)

In the theoretical framework described by Derjaguin, Landau, Venvey and Overbeek, also known as the DLVO theory, the total interaction potential between two electrostatically stabilized particles is the sum of the van der Waals attractive and electrostatic repulsive potentials, the latter arising from the presence of a double layer of counterions surrounding the particles. This theory works well in describing the interactions between two electrically charged particles approaching each other, whereby the electric charges are homogeneously distributed over their surface (**Figure 2-2**). For spherical particles at far distances, both the van der Waals attraction and electrostatic repulsion potentials reduce to zero (**Figure 2-3**). The potential energy curve becomes negative (attractive) at short distances due to the dominant van der Waals attraction, but reaches a positive (repulsive) maximum as the electric repulsion potential dominates the van der Waals potential. The height of the maximum is called the

repulsion barrier; if it is greater than about 10 kT (where k is Boltzmann's constant and T is the absolute temperature), Brownian motions cannot overcome the repulsive barrier and agglomeration does not occur.

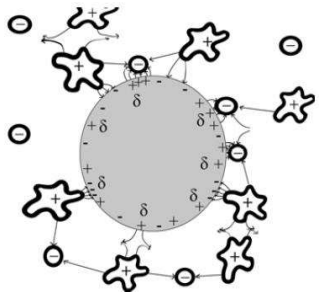

Figure 2-2. Representation of the electrostatic stabilization of a metal particle by interacting cations and anions establishing surface charges surrounding the metal. Reprinted with permission from reference 12. Copyright 2011 by the Authors.

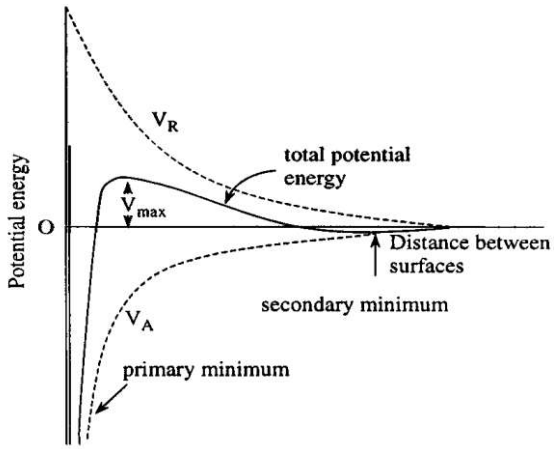

Figure 2-3. Schematic representation of DLVO potential: V_A = attractive van der Waals potential, V_R = repulsive electrostatic potential, and V_{max} = repulsion barrier due to the combined potentials. Reprinted with permission from reference 8. Copyright 2004 Imperial College Press.

However electrostatic stabilization, which is based on kinetics, has its weaknesses. It works best for dilute systems and is electrolyte-sensitive; once the particles agglomerate, they are very difficult or

impossible to redisperse, and the dispersions are difficult to spread on multi-phase surfaces since different solids develop different surface charges and electric potentials.[8]

2.1.4.2 Steric stabilization (polymeric stabilization)

Steric or polymeric stabilization is a thermodynamic stabilization method widely used for colloidal dispersions, as shown in **Figure 2-4**. It has a number of advantages over electrostatic stabilization in that since it is a thermodynamic method, agglomerated particles are usually redispersible; very high concentrations can be accommodated; they are less electrolyte-sensitive, and more amenable to spreading on multi-phase surfaces. Large or bulky additives are effective stabilizers because of the geometric restrictions they introduce around nanoparticles.[13] When the dimensions of the stabilizer are significantly larger than the size of the nanoparticles, a spherical topology typically results since the stabilizer encapsulates the nanoparticles (**Figure 2-4B**). High molecular weight polymers are often employed as stabilizers for MNPs.

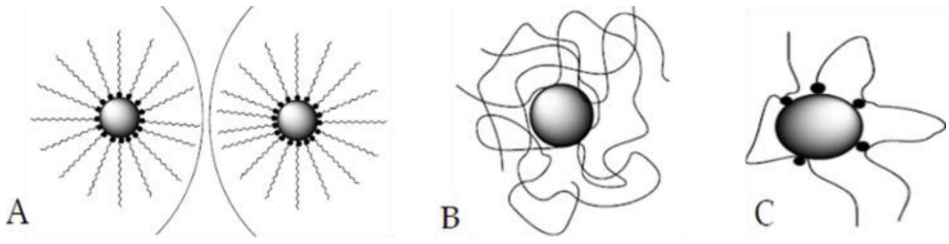

Figure 2-4. Schematic representation of steric stabilization: (a) Elongated or conical molecules adsorbed via anchoring centers (black dots) hinder close contact. (b) Long polymer threads encapsulating a nanoparticle. (c) Chelate effect, when the stabilizer is adsorbed via more than one anchoring center (black dots). Reprinted with permission from reference 12. Copyright 2011 by the Authors.

2.1.4.3 Electrosteric stabilization

This refers to a situation when nanoparticles are stabilized by both electrostatic and steric effects. Ionic liquids (IL), for example, can stabilize MNPs in the absence of surfactants, polymers or capping ligands. In addition to electrostatic stabilization via hydrophobic and steric interactions, ILs can stabilize metal nanoclusters with an "additional" DLVO contribution related to their networking behavior through hydrogen bonding. The insertion of metal nanoparticles in a supramolecular ionic liquid network thus provides electrostatic and steric (electrosteric) stabilization primarily through the formation of an ionic layer around the MNPs. It is shown in **Figure 2-5** that an ionic liquid based on the imidazolium cation can form a strong network with different anions, from the small tetrafluoroborate (BF_4^-), hexafluorophosphate (PF_6^-) and trifluoromethyl sulfonate ($CF_3SO_3^-$) ions, to the large bis(trifluoromethylsulfonyl)amide ($(CF_3SO_2)_2N^-$) anion via electrostatic and hydrogen bonding interactions, thus providing electrosteric stabilization to added MNPs.[34] As mentioned earlier, the successful synthesis of relatively monodisperse metallic nanoparticles relies on the separation of the nucleation and growth steps in the reaction, and on the prevention of aggregation with stabilizing agents. Polymers and surfactants are often used as electrostatic, steric or electrosteric stabilizers.[35] The synthesis of nanoparticles with specific characteristics in terms of composition, morphology, size and size uniformity is usually necessary to achieve desirable physical properties. Many synthetic strategies were investigated to prepare stable metallic nanoparticles satisfying these criteria. The different methods presented in the literature to achieve this include using small molecules such as surfactants,[36] self-assembled block copolymer micelles,[37,38] star-block copolymers,[24,39] and unimolecular micelle-like compounds.[40,41]

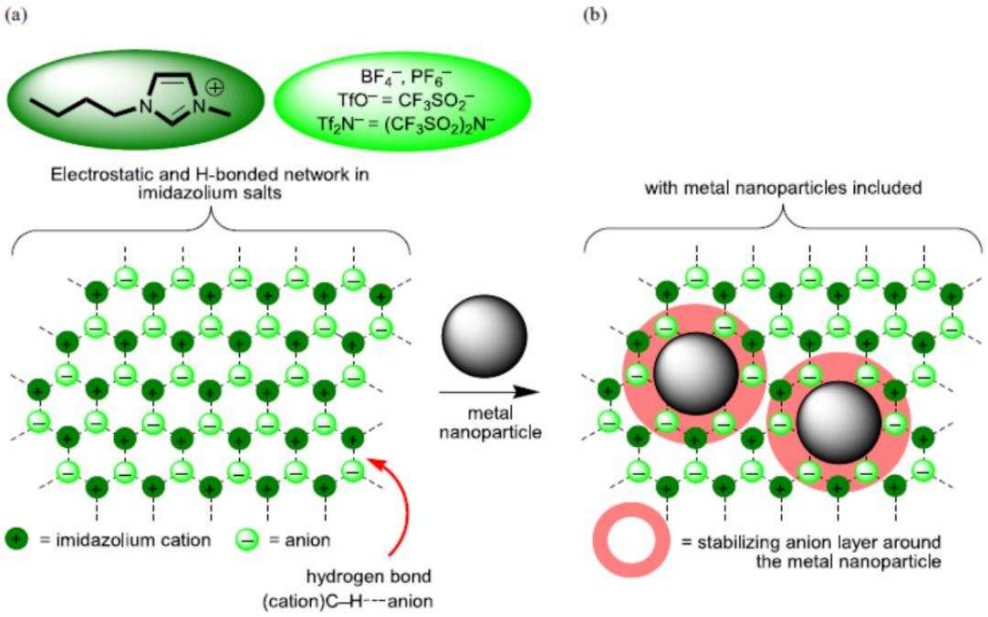

Figure 2-5. (a) Supramolecular network structure of a 1,3-dialkylimidazolium-based IL. (b) The insertion of MNPs in the network provides electrosteric stabilization through the formation of a primary anion layer around the MNPs. Reprinted with permission from reference 33. Copyright 2011 Elsevier B.V

This Thesis mainly focuses on the synthesis and the characterization of self-assembled complex structures based on arborescent substrates, and their use as templates for the preparation of stable MNPs, particularly gold nanoparticles (Au NPs). Consequently, the following sections provide an overview of the types of supports employed for that purpose and the characteristics of the MNPs obtained. Particular attention will be provided to polyion complex (PIC) micelles, their use as templates for Au NPs, and (briefly) the applications of Au NPs incorporating stabilizing agents.

2.2 Surfactants and small molecule stabilizers

Surfactants are amphiphilic molecules with a polar segment called the "head" and a nonpolar part called the "tail".[42] Surfactants exist as individual molecules at low concentrations, but above a concentration called the critical micelle concentration (CMC) they organize themselves (self-assemble) to form

aggregates called micelles[43] and reversed (inverted) micelles,[44] in aqueous solutions and in organic solvents, respectively. In aqueous solutions the apolar organic segments associate, leaving the polar (ionic or nonionic) head groups exposed to the solvent (**Figure 2-6**). For reverse micelles in organic solvents, the polar groups cluster to form the core of the micelles while the hydrocarbon fragments make up the outer layer.[42] Above the CMC, the monomers (isolated surfactant molecules) and micelles exist at dynamic equilibrium.[45]

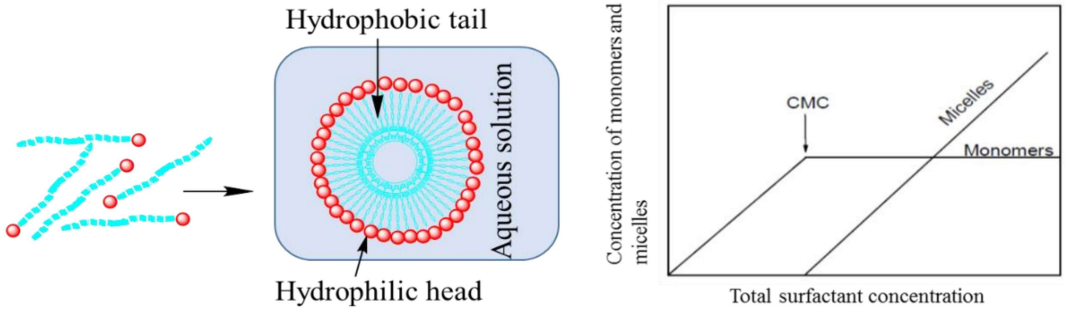

Figure 2-6. Micelle formation from surfactant molecules (left), and concentration of monomeric and micellar species as a function of the total surfactant concentration (right). Adapted with permission from references 46 and 47. Copyright 1992 Elsevier Science Ltd.

Below the CMC the surfactant only exists as monomeric species, while above the CMC the concentration of monomeric species remains more or less constant (**Figure 2-6**). However starting from the CMC, the micelle concentration increases linearly with the surfactant concentration.[46,47]

Many surfactants, such as the examples provided in **Figure 2-7**, have been utilized to prepare metallic nanoparticles. Among these, hexadecyltrimethylammonium bromide (CTAB), a cationic surfactant, has been used extensively as both stabilizer and template.[48] For example, Bal and coworkers reported that CTAB helped in the reductive preparation of Cu nanoclusters from Cu^{2+} ions without reducing reagents,[49] while Chakraborty and others used CTAB as stabilizer for the preparation of AgBr

nanoparticles from $AgNO_3$,[48] whereby CTAB served both as a stabilizing reagent and a source of bromide ions. Thiol- and amine-functionalized surfactants also served as stabilizers for the preparation of many types of metallic nanoparticles. For instance, Au nanoparticles were successfully stabilized with dodecanethiol ($C_{12}H_{25}SH$) by Brust et al.[50] Yang and coworkers also synthesized small Pt nanoparticles (**Figure 2-8**) with 1-dodecanethiol and dodecylamine stabilizers.[51] Thiol-functionalized imidazolium ionic liquids were used by Kim and coworkers to stabilize Pd nanoparticles.[52] Han et al., and Stevens et al. both used multidentate aromatic ligands known as resorcinarenes to stabilize Au nanoparticles.[53,54]

Synthetic strategies differ in their use of reducing agents, temperature, and their ability to produce water- versus organic-dispersible nanoparticles. The shape, size distribution and mean dimensions of MNPs also depend on the synthetic strategy employed.[55] *In situ* schemes and the Brust-Shiffrin method are most widely used to that end.

Among the *in situ* methods starting from simple molecules, the Turkevich technique for the preparation of Au NPs, where sodium citrate serves both as stabilizing and reducing agent, has been popular for a long time[13] for being able to yield spherical particles with good reproducibility.[32] For example, 20 nm Au nanoparticles (**Figure 2-9**) can be prepared in 5 minutes by simply heating a tetrachloroauric acid solution to its boiling point, and adding a trisodium citrate dihydrate solution quickly under vigorous stirring to obtain a wine-red colloidal dispersion.[32]

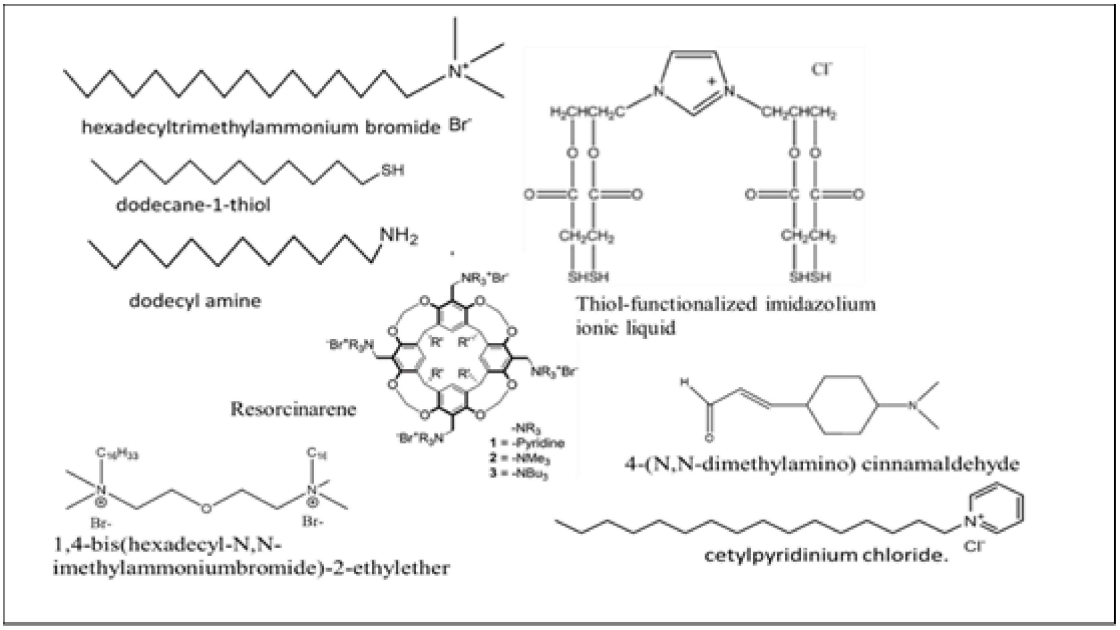

Figure 2-7. Some of the surfactants and small molecules used for the preparation of MNPs.[48-54,57,59]

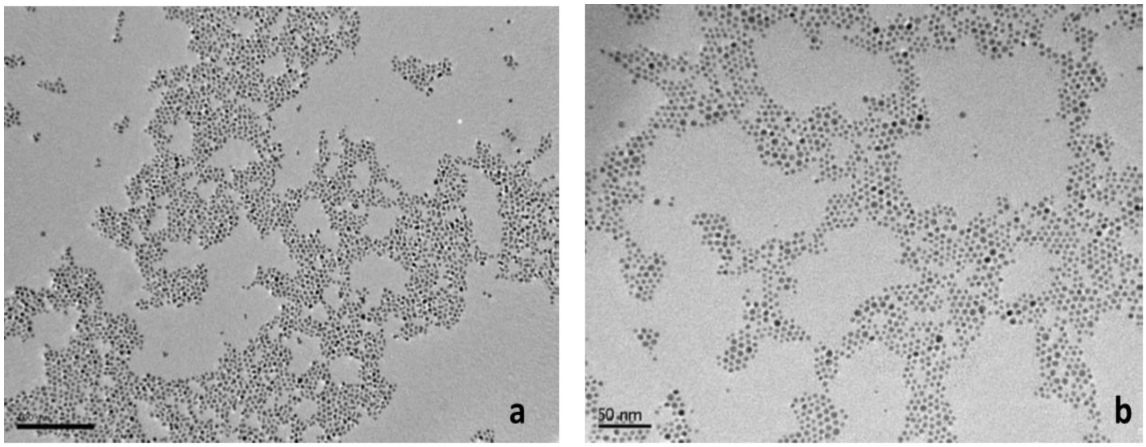

Figure 2-8. TEM image of 5.3 nm (a) 1-dodecanethiol-stabilized and (b) dodecylamine-stabilized Pt nanoparticles. Reprinted with permission from reference 51. Copyright 2006 Elsevier B.V.

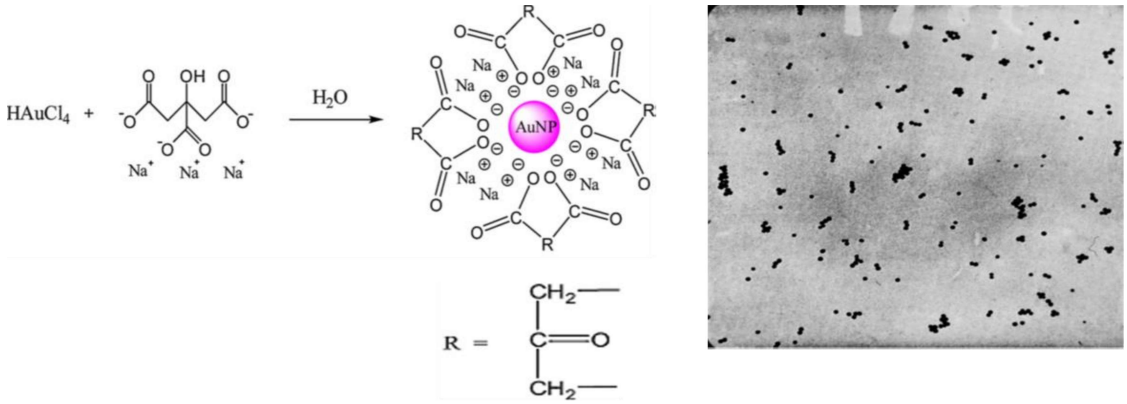

Figure 2-9. Au NP synthesis by the Turkevich method (left)[13] and electron micrograph of a gold sol (right) reduced with sodium citrate.[32] Reprinted with permission from references 13 and 32. Copyright 2013 Elsevier B.V. and 1951 Discussions of the Faraday Society.

The other approach applied extensively to the preparation of small molecule-stabilized nanoparticles is the Brust-Shiffrin technique, which is the earliest method reported for the preparation of thiol-stabilized metallic nanoparticles.[13,56] In this two-step technique, metal ions are extracted into an organic phase from an aqueous phase using a phase transfer catalyst, the aqueous phase is removed, and the metal ions are reduced in the organic phase in the presence of a stabilizing agent (**Figure 2-10**).

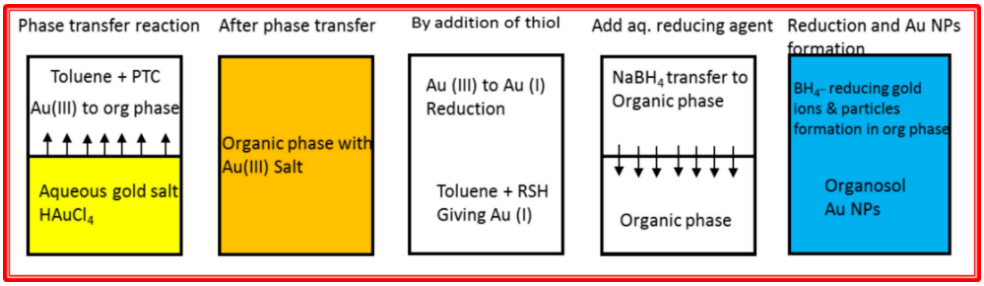

Figure 2-10. Step-by-step synthesis of thiol-capped gold nanoparticles by the Brust-Shiffrin method. Adapted with permission from reference 55. Copyright 2013 American Chemical Society.

Both Brust et al. and Uehara et al. prepared gold nanoparticles by extracting gold ions from an aqueous solution into a hydrocarbon phase (e.g. toluene) using tetraoctylammonium bromide (TOA^+Br^-) as phase transfer reagent. The transfer of the tetrachloroaurate ($AuCl_4^-$) ions proceeded by exchange with the more hydrophilic Br^- ion (**Equation 2-1**). Gold nanoparticles with a diameter of 1-3 nm were obtained after subsequent reduction in the organic phase with aqueous $NaBH_4$ in the presence of an alkanethiol as a capping agent (**Equation 2-2**).[50,56]

$$\mathbf{AuCl_4^-(aq) + N(C_8H_{17})_4^+ (toluene) \longrightarrow N(C_8H_{17})_4^+ AuCl_4^- (toluene)} \qquad \mathbf{(2\text{-}1)}$$

$$\mathbf{m\ AuCl_4^- (toluene) + n\ C_{12}H_{25}SH (toluene) + 3me^- \longrightarrow}$$
$$\mathbf{4\ mCl^- (aq) + (Au_m)(C_{12}H_{25}SH)_n (toluene)} \qquad \mathbf{(2\text{-}2)}$$

Macrocyclic and multidentate surfactants also gained attention as potential stabilizers with enhanced stability, permitting supramolecular interactions that can be valuable in catalytic applications.[55] Resorcinarenes were thus shown to act as encapsulating agents several times more efficient than dodecanethiol for the preparation of controllable size (both above and below 10 nm) stable Au nanoclusters in mesitylene. It was claimed that chemisorption, through multiple Au–O interactions, and steric hindrance both contributed to stabilizing the Au nanoclusters. This is notable since the affinity of oxygen for gold is relatively low, but the eight oxygen atoms along the edge of a resorcinarene head-group can favor adsorption on the Au surface in a cooperative manner.[54] Steric stabilization has also emerged as one of the key reasons for the use of resorcinarenes as stabilizers. Cationic resorcinarenes can electrostatically complex with negatively charged nanoparticle surfaces, and also stabilize them via steric hindrance. Resorcinarenes 1−3 (**Scheme 2-2a**) were indeed employed for the extraction of gold nanoparticles into toluene−acetonitrile solvent mixtures.[54] In comparison to aqueous citrate-stabilized gold nanoparticles, all three resorcinarenes led to a slightly red-shifted plasmon resonance peak. The

resorcinarene head-group influenced the stability of the nanoparticles, and resorcinarene 1 in particular yielded particles stable for several weeks. In the presence of thiourea, the resulting particles **(Scheme 2-2)** were so resistant to aggregation that they could be precipitated and redispersed in non-polar solvents.[57] This was attributed to two reasons: The interactions between the macrocyclic thiol headgroups and the nanoparticles are multidentate, and the well-separated, multiple long alkyl chains on the resorcinarenes ensure a high degree of freedom per chain in the surfactant layer for effective steric repulsion.

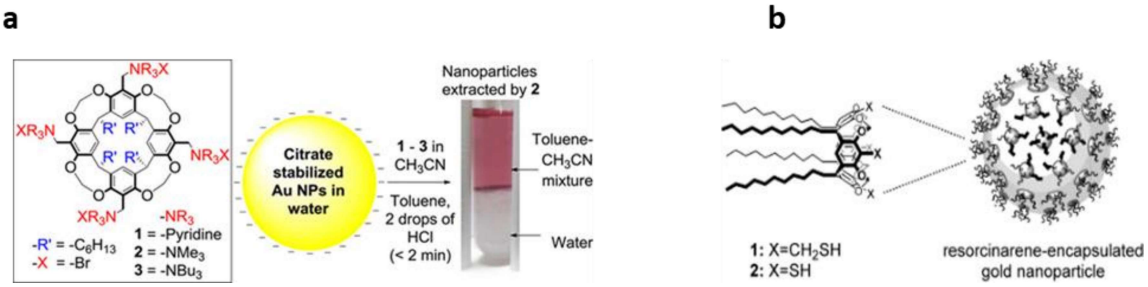

Scheme 2-2. (a) Phase transfer synthesis of gold nanoparticles with resorcinarenes and (b) Gold nanoparticle encapsulated by thiolated resorcinarene. Reprinted with permission from reference 53 and 54. Copyright 2014 & 1999 American Chemical Society.

Monodisperse Au nanoparticles ranging from 5-10 nm were also synthesized by the reduction of Au–decyltrimethylammonium bromide (Au–DTAB) precursors (**Scheme 2-3**) with super-hydride. The Au nanoparticles were synthesized by heating a mixture of Au–DTAB, ethylene glycol and tetrahydrofuran at 50 °C, followed by the addition of oleylamine as surfactant and reduction with super-hydride.[58] The size of the particles was controlled by varying the amount of oleylamine stabilizer used, smaller nanoparticles being obtained for higher stabilizer to gold ratios due to better passivation of the Au monomers in the reaction. The size distribution was better controlled at low temperature (50 °C). It was

also shown that the Au–DTAB complex was highly stable in air and moisture, and suitable for the large-scale synthesis of Au nanoparticles of uniform size. Moreover, the Au nanoparticles could be transferred to an aqueous phase after treatment with multidentate polymeric ligands containing imidazole groups (**Scheme 2-3**).

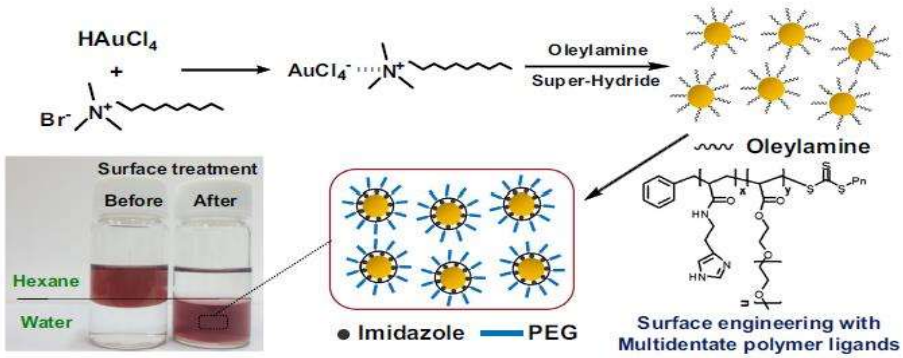

Scheme 2-3. Synthesis of oleylamine-stabilized gold nanoparticles. Adapted with permission from reference 58. Copyright 2016 S. Kim et al.

A seeded growth method was exploited by Tiwari et al. for the synthesis of Au, Ag, and Au–Ag alloy nanoparticles.[59] First Ag nanoseeds were synthesized from an aqueous solution of $AgNO_3$ with $NaBH_4$ as reducing agent, and used for the synthesis of Au, Ag and Au–Ag alloy NPs. Gemini surfactant molecules, in the form of Gemini-Z (1,4-bis(hexadecyl-N,N-dimethylammonium bromide)-2-ethyl ether), served as stabilizer for the NPs by covering the metal surface with a bilayer. This is because to maintain stability, the polar head group of gemini surfactants orient themselves in the direction of the two hydrophilic surfaces, namely the MNPs and the aqueous phase, thereby forming a bilayer. Different shapes of NPs could be obtained with high selectivity, depending on the ingredients used. For Ag mostly rod-shaped NPs were observed, whereas spheroidal particles were obtained for Au NPs, and the Au–Ag alloy NPs had a spherical shape.[59]

Multipurpose ionic surfactants were also employed in the electrochemical synthesis of metallic nanoparticles. Yu and coworkers thus reported the synthesis of Au nanorods in high yield using gold as an anode and platinum as a cathode in the presence of acetone.[60] Control of the growth of Au nanorods using "shape-inducing" reagents was demonstrated. The synthesis was conducted by electrolysis at a constant current of 3 A for 30 min at 38 ^{o}C with ultrasonication. The cationic hexadecyltrimethylammonium bromide (C16TAB) surfactant, serving both as supporting electrolyte and stabilizing reagent, was used in combination with another cationic surfactant, tetraoctylammonium bromide (TC8AB) to induce the rod shape, albeit the exact mechanism involved was not clear. The gold nanorods observed by TEM were assumed to form at the interface of the cathode and the electrolyte solution, where the bulk gold anode was converted to NPs.

2.3 Polymeric stabilizers

While amine- and thiol-functionalized surfactants, and other small molecules have been widely used for the synthesis of stable MNPs, polymeric stabilizers with thiol,[11] amine, benzaldehyde or other groups,[61,62] amphiphilic block copolymers,[63] branched and dendritic polymers[64] have likewise been reported to be effective stabilizers for Au NPs, because of their ability to either self-assemble or covalently bond with the Au surface.

The use of controlled polymerization techniques including anionic, cationic, atom transfer radical polymerization (ATRP), reversible addition-fragmentation chain transfer (RAFT) and nitroxide-mediated radical polymerization (NMP), in particular, has greatly contributed to the synthesis and the design of a wide variety of polymers useful as stabilizers for MNPs. These methodologies enabled the synthesis of new classes of polymers with specific properties, by combining different monomers or polymerization techniques, or by subsequently modifying the polymers with suitable functional groups.

In addition to improving long-term NP stability, polymeric stabilizers can also change the solubility characteristics of the NPs, improve their amphiphilic character, and tailor their properties.[13]

2.3.1 Homopolymer stabilizers

Over the past few decades control over particle size, stabilization, and organization promoted via polymers interacting with colloidal metal nanoparticles[62] has been achieved through functional groups such as 2-pyrrolidone, ethers, cyano, thiol, and pyridine.

2.3.1.1 Poly(ethylene glycol)-based thiols

Thiolated poly(ethylene glycol) (mPEG-SH) with molecular weights of 2100, 5400, 10 800, and 20 800 g/mol were used for the production of stable (5 to 60 nm) Au NPs through covalent thiol linkage in aqueous solutions.[11] Different reducing agents yielded NPs with various mean diameters. For example, using mPEG-SH with M_w = 10 800 g/mol, the stronger reducing agent $NaBH_4$ gave Au NPs with a diameter of 5 ± 1.5 nm at room temperature, while the milder reducing agent sodium citrate at 95 °C yielded ~15 ± 1.5 nm Au NPs, and the weakest ascorbic acid/sodium citrate reducing system at room temperature gave ~30 ± 4 nm nanoparticles. Increasing the amount of ascorbic acid used in the ascorbic acid/sodium citrate system resulted in ~60 ± 8 nm Au NPs. When $NaBH_4$ was used, mPEG-SH was directly mixed with $HAuCl_4$ before reduction, however in the other two cases, the NPs were capped with citrate before exchange with the mPEG-SH stabilizer. Since thiol groups have a strong affinity for Au, the covalent attachment of mPEG-SH to the Au surface was facile. The stability of the citrate-capped Au NPs and the PEG-stabilized Au NPs was compared in the presence of 0.157 mol/L NaCl. The citrate-capped Au NPs precipitated after 4 hours, while the mPEG-stabilized NPs were only slightly affected by the salt. The mPEG-stabilized NPs displayed size-dependent optical properties, with surface plasmon resonance (SPR) bands ranging from 514 to 534 nm in UV-visible spectroscopy analysis (**Figure 2-11**). The size of the Au NPs was also found to depend on the concentration and the

chain length of the mPEG used, the size increasing with both the concentration and the length of the mPEG chains. This was ascribed to the small number of mPEG molecules attached to the Au surface as the mPEG chain length increased. The concentration effect was less pronounced as the mPEG chain length was decreased. The nanoparticles thus obtained were stable for several months without precipitation. The NPs with a diameter < 30 nm displayed catalytic activity for the homocoupling of arylboronic acids, and were useful for the delivery of small interfering RNA (siRNA) to CT-26 cells without toxicity.[11]

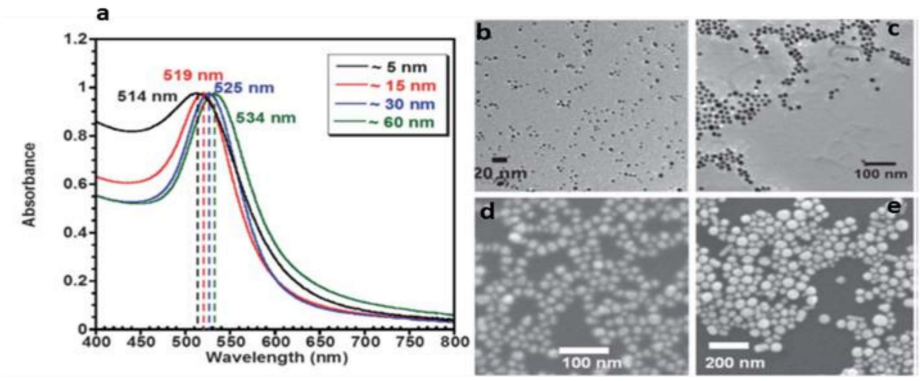

Figure 2-11. (a) UV-visible spectra and TEM/SEM micrographs for mPEG-SH coated Au NPs with a diameter of (b) 5 nm, (c) 15 nm, (d) 30 nm, and (e) 60 nm. Reprinted with permission from reference 11. Copyright 2013 the Royal Society of Chemistry.

2.3.1.2 Polymethylphenylphosphazene (PMPP)

When using tetraoctylammonium bromide to transfer $HAuCl_4$ from an aqueous solution to toluene, the addition of PMPP before reduction with $NaBH_4$ was useful to obtain Au nanoparticles within the PMPP domains (**Figure 2-12**), that were stable for at least six months.[62]

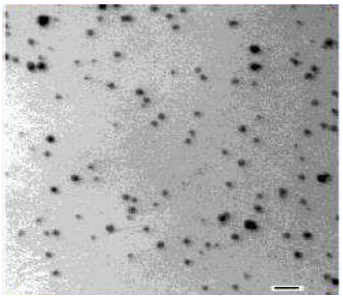

Figure 2-12. TEM image of 40:1 PMPP–nanoparticle composite. The scale bar is 20 nm. Reprinted with permission from reference 62. Copyright 2001 American Chemical Society.

The enhanced stability was attributed to the interaction of Au with the lone pair electrons of the nitrogen atoms in the backbone of the polymer. The size of the nanoparticles was controlled by varying the ratio of PMPP to $HAuCl_4$, a higher ratio yielding smaller nanoparticles, albeit the size distributions were rather broad. Average nanoparticle diameters of 7.4, 6.8 and 5.1 nm were obtained for PMPP to $HAuCl_4$ molar ratios of 4:1, 8:1 and 40:1, respectively.

2.3.1.3 Poly(N-vinyl-2-pyrrolidone) (PVP)

According to Tsunoyama et al.,[65] 1.5 nm Au particles (**Figure 2-13**) can be obtained using poly(N-vinyl-2-pyrrolidone) (PVP) as stabilizing agent, simply by rapidly injecting $NaBH_4$ into an aqueous solution of $HAuCl_4$ and PVP. The NPs grew further to 9.5 nm (**Figure 2-13b**) when using Na_2SO_3 for the reduction of $AuCl_4^-$. These NPs were investigated for their catalytic activity in the aerobic oxidation of benzylic alcohols (compounds 1a-1d in **Scheme 2-4**) to benzoic acids and benzaldehydes.[65] The effect of the size of the Au NPs was demonstrated, smaller (1.3 nm) NPs having a higher catalytic activity than larger (9.3 nm) NPs. This was ascribed to more effective O_2 activation by smaller NPs.[65]

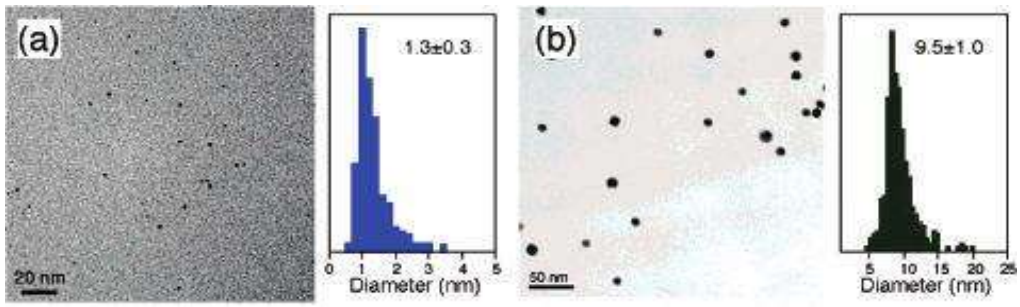

Figure 2-13. TEM micrographs and size distributions of Au:PVP NPs: (a) 1.5 nm, (b) 9.5 nm. Reprinted with permission from reference 65. Copyright 2005 American Chemical Society.

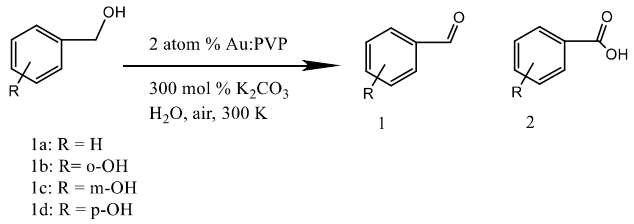

Scheme 2-4. Alcohol oxidation catalyzed by Au:PVP NPs. Adapted with permission from reference 65. Copyright 2005 American Chemical Society.

Polymer stabilization was also demonstrated by synthesizing homogeneous small (13 ± 2 nm) and large (56 ± 7 nm) diameter gold nanoparticles through reduction of $HAuCl_4$ in sodium citrate solutions at their boiling point as a first step.[66] Size control was achieved by varying the amount of sodium citrate used, larger amounts of sodium citrate yielding smaller NPs as expected. The resulting Au NPs were coated with PVP by vigorous stirring with the mixture overnight. The PVP-modified NPs were then further modified by mixing with silk fibroin (SF). The photothermal and optical properties of these nanocomposites were investigated, and it was found that they performed as nanoheaters when exposed to light because of their excellent light-to-heat conversion efficiency. The nanocomposites were also investigated as films cast onto fused silica plates or Si substrates by UV-visible spectroscopy. The

absorbance of a film with a low Au content showed a weak peak with a narrow spectral bandwidth, attributed to localized surface plasmon resonance (LSPR) extinction of the Au NPs. However, when the Au content was increased, the absorbance peak was enhanced significantly both in the LSPR and in the non-LSPR wavelength regions (**Figure 2-14**). To investigate their light-induced thermal behavior, composite films of Au NPs and silk fibroin (a highly water-soluble transparent material extracted from silkworm cocoons) were illuminated with white light from light-emitting diodes (LED) and halogen lamps. Interestingly, an increase in temperature on the order of 100 ºC was observed for both types of illuminations, and the magnitude of the temperature increase scaled with the Au content in the composites.

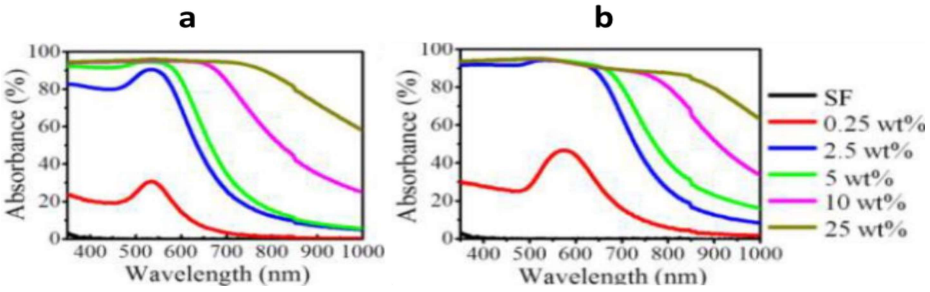

Figure 2-14. Absorbance spectra for (a) small Au NP/SF and (b) large Au NP/SF thin films with various Au contents. Reprinted with permission from reference 66. Copyright 2015 American Chemical Society.

2.3.1.4 Poly(9,9-bis(4'-sulfonatobutyl)fluorene-*co*-*alt*-1,4-phenylene) sodium salt (PFS)

The photoactive fluorophore poly(9,9-bis(4′-sulfonatobutyl)fluorene-*co*-*alt*-1,4-phenylene) sodium salt (PFS) was employed to synthesise 5.1 nm spherical monodisperse Au NPs by the Brust-Shiffrin method, i.e. mixing an aqueous PFS solution with $HAuCl_4$ under vigorous stirring and reduction with $NaBH_4$.[67] The resulting PFS–Au NPs were stable for months, as the fluorescent polyelectrolyte (PFS) is not only photoactive but also can act as electrosteric stabilizer. These PFS–Au NPs were applied as

sensors for the detection of cysteine. Since the strong emission of PFS is quenched strongly in the PFS-Au NP composites, so the fluorescence is very weak within the PFS–Au NP composites due to highly efficient fluorescence resonance energy transfer (FRET) between PFS and the Au NPs. Upon addition of cysteine to the PFS–Au NP composites, however, the PFS is displaced away from the Au NP surface (**Scheme 2-5.**) due to the strong interactions between the thiol group of cysteine and the Au NPs. As a result, the fluorescence of PFS is recovered, and the extent of recovery depends on the quantity of the cysteine added (**Figure 2-15**), which is the basis for its use as a sensor.

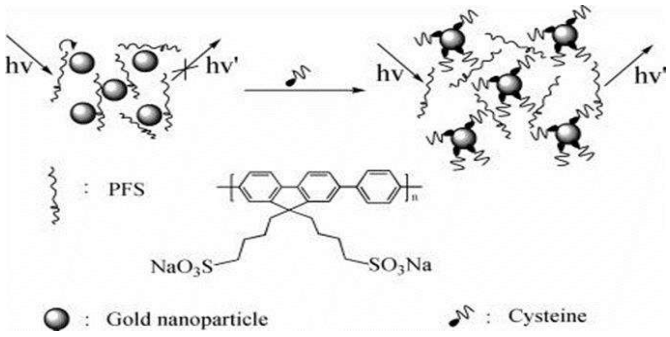

Scheme 2-5. Fluorescent sensors for cysteine detection. Adapted with permission from reference 67. Copyright 2007 American Chemical Society.

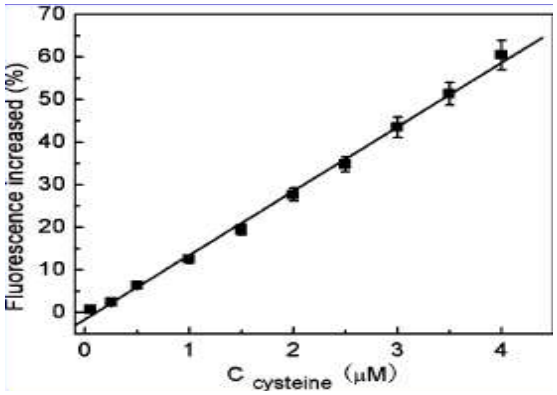

Figure 2-15. Increase in fluorescence intensity of PFS–Au NPs at 420 nm as a function of cysteine concentration. Reprinted with permission from reference 67. Copyright 2007 American Chemical Society.

2.3.2 Block copolymer stabilizers

Over the past few decades, amphiphilic block copolymers (BCPs) have received tremendous attention due to their applications in different fields of study, and to the development of facile routes for their synthesis by methods including ATRP, RAFT, cationic, and anionic polymerization. Major applications investigated for BCPs include drug delivery,[68] organic memory,[69] the encapsulation of hydrophobic compounds,[70] and the synthesis of metallic nanoparticles.[71] Block copolymer micelles generally offer benefits as compared to traditional surfactants used for this purpose. For instance, BCPs can have a much lower CMC than small molecule surfactants, and the size and morphology of BCP micelles can be tailored by varying the chain length and the composition of each block.[39,72] The stability of the NPs depends on the characteristics of the micelles, the solvent, concentration, pH, temperature, and ionic strength of the solutions. They can also form numerous phase-separated nanostructures and microstructures that can be tailored depending on their intended application.[73]

2.3.2.1 Block copolymer micelle formation

Depending on the number, the types of polymer segments present and the way in which they are attached, block copolymers can be described as linear diblock (AB),[74-81] Y-shaped diblock,[82] triblock (ABA, ABC),[83-86] and star-block copolymers $(AB)_n$[39] (**Figure 2-16)**, among other possibilities.

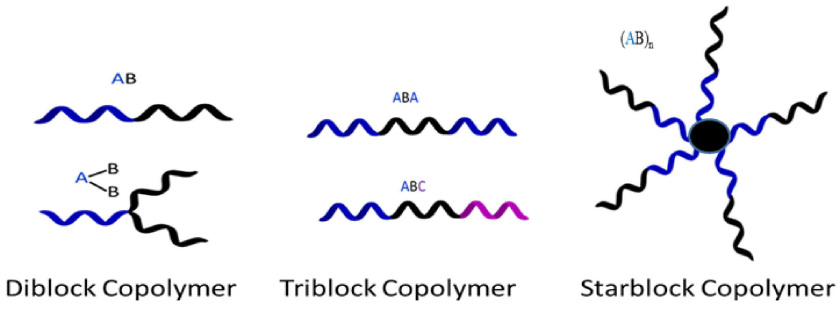

Figure 2-16. Schematic representation of block copolymer structures.

It is well-documented that when block copolymers are dissolved in a solvent selective for one of the blocks, they aggregate into micellar structures above their CMC. The concentration of free chains above the CMC is almost constant but depends strongly on the molecular weight and the polydispersity index of the copolymers.[63] Regular micelles in water have their core formed by the hydrophobic block(s) surrounded by a corona of soluble hydrophilic blocks, while reverse micelles may also form in organic solvents, mostly in the absence of water.[85]

Depending on the nature of the intermolecular driving forces promoting their formation, block copolymer micelles can be classified as amphiphilic, polyion complex (PIC), and hybrid polyion complex (HPIC) micelles.[87] Amphiphilic block copolymers self-assemble in water because their hydrophobic blocks are insoluble in water, due to their strongly negative second virial coefficient.[88] This process is concurrently stimulated by an increase in entropy of the solvent molecules, as the hydrophobic component is removed from the aqueous medium.[89]

Mixtures of a BCP containing an anionic polyelectrolyte block and another BCP with a cationic polyelectrolyte block can also self-assemble into micelles called polyion complex (PIC) micelles. If both BCPs contain a hydrophobic block reverse micelles should form in organic solvents, but in water this mixture will likely gel as a result of both hydrophobic and electrostatic interactions.[89] If both copolymers contain a hydrophilic but neutral block, they should form micelles in water that are stabilized by the neutral polymer in the corona. If the polyelectrolyte segments within the core of the PIC micelles interact with metals, hybrid polyion complex micelles can be formed.[87]

BCP micelles may form with different morphologies depending on the copolymer composition, the solvent composition, and the presence of salts or surfactants. The formation of complex morphologies such as vesicles and nanocapsule-like micelles require a high degree of control over the characteristics of the BCPs and the conditions used in the self-assembly process. By altering the properties of binary

solvent systems spherical, worm-like micelles, vesicles, networks of worm-like aggregates, as well as stacked and cylindrical micelles can be prepared.[90] It is also possible to use BCPs for the preparation of stable MNPs, by incorporating metal ions into one block of the BCP micellar structures through functional groups interacting with the metal, followed by reduction to yield the MNPs (**Scheme 2-6**). The following sections cover BCP micelles used in particular for the synthesis of Au NPs by different micellization strategies, factors affecting micellization, the synthetic approaches implemented for the fabrication of Au NPs, and the parameters (block length, concentration, temperature, pH, reducing agent, etc.) varied to control the resulting NPs.

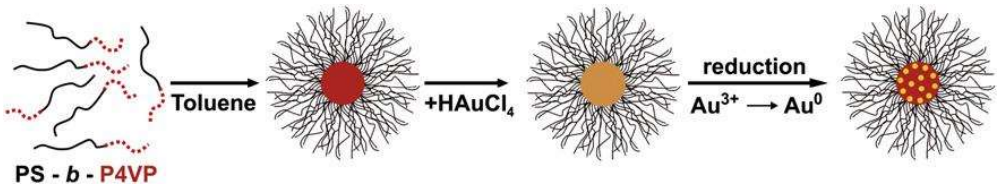

Scheme 2-6. Self-assembly of block copolymers into spherical micelles and preparation of PS-b-P[4VP(Au)] hybrid micelles in toluene. Reprinted with permission from reference 90. Copyright 2008 Elsevier Ltd.

2.3.2.2 Polystyrene-*block*-poly(2-vinylpyridine) (PS-*b*-P2VP)

Particularly relevant to this thesis work is the preparation of gold nanoparticles templated by polystyrene-*block*-poly(2-vinylpyridine) copolymers, forming inverse micelles with a polar P2VP core and a corona of PS chains when dissolved in a solvent selective for the PS units such as toluene.[63] Specifically, Au-containing BCP micelles were prepared by simply dissolving a BCP in toluene and adding 0.5 equiv of $HAuCl_4$ per 2VP unit. After allowing the micelles to solubilize the $HAuCl_4$ completely, a 10-fold amount of hydrazine (N_2H_4) with respect to $HAuCl_4$ was added. The excess hydrazine was converted to hydrazinium chloride (N_2H_5Cl) by adding HCl, and removed as a precipitate through centrifugation. In the first step the $HAuCl_4$ was thus selectively complexed by

protonating the 2VP units, which develop polyelectrolyte characteristics.[91] A higher core polarity favored the the solubilization of N_2H_4 in the second step, which facilitated the reduction of Au^{3+} to Au^0. Increased incompatibility between the core and solvent/shell phases, resulting from addition of the metallic salt, enhances phase separation between the core and the shell in these systems due to a dramatic increase in the Flory interaction parameter (χ). This process is also responsible for the enhancement of both the thermodynamic and kinetic stability of the micelles.[37] This strategy allowed the preparation of a range of nanostructures including spheres, vesicles, rods, and lamellae.

Analysis of the salt-loaded micelles by TEM (**Figure 2-17**) led to the formation of ultrasmall gold nanoparticles, since the salt was reduced inside the core of the micelles by the electron beam of the microscope according to **Equation 2-3**. This phenomenon was further confirmed in another investigation by Selvan and coworkers.[37] The addition of a 10-fold excess of hydrazine as reducing reagent (reacting according to **Equation 2-4**) resulted in the formation of isolated 9 nm gold particles of uniform size in each BCP micelle (**Figure 2-17c**). A lower amount of reducing reagent resulted in non-uniform Au NPs, however, indicating that the formation of nanoparticles was not concurrent in all the micelles. **Figure 2-17d** reveals the agglomeration of 2-4 Au NPs to form non-spherical nanoparticles by coagulation of individual micelles. This process was observed 30 min after the initial formation of uniform spherical nanoparticles in each micelle, as depicted in **Figure 2-17c**. It was postulated that the coagulation may have occurred due to swelling of the micelle core by excess N_2H_4, if the BCP chains did not sufficiently stabilize the core. To confirm this hypothesis, the hydrodynamic radius (R_h) of the micelles was compared before reduction, after scavenging the excess hydrazine with HCl immediately after reduction, and 30 minutes after reduction without the addition of HCl. The R_h obtained were 28, 30 and 38 nm under these conditions, respectively. The 2 nm increment from 28 to 30 nm could be due to the presence of by-products (HCl and N_2H_4) in the micelles, but the 10 nm increment clearly confirms the coalescence of non-stabilized micelles, which explains the TEM

analysis results in **Figure 2-17d**.[63] The PS shell of the micelles was not visible in the TEM pictures because of its low electron density, but it is evident from the hexagonal arrangement that it controlled the center-to-center spacing of the micelles.

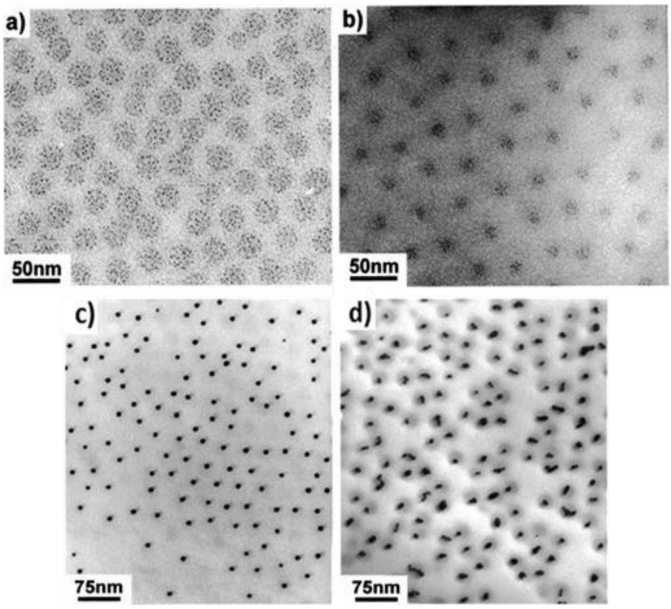

Figure 2-17. TEM micrographs for (a) a monolayer film of PS300-b-P2VP300 and (b) of PS325-b-P2VP75 block copolymer micelles loaded with of 0.5 equiv $HAuCl_4$ per 2VP unit, (c) 9 nm isolated gold particles cast from a solution of PS300-b-P2VP300 directly after reduction, and (d) micelles containing 2-4 gold particles, cast from a solution of PS300-b-P2VP300 30 min after reduction. Reprinted with permission from reference 63. Copyright 2000 American Chemical Society.

$$2\ HAuCl_4 + 6\ e^- \longrightarrow 2\ Au + 2\ HCl + 3\ Cl_2 \qquad (2\text{-}3)$$

$$4\ HAuCl_4 + 3\ N_2H_4 \longrightarrow 4\ Au + 3\ N_2 + 16\ HCl \qquad (2\text{-}4)$$

In another investigation of Selvan and coworkers, a PS300-*b*-P2VP300 diblock copolymer synthesized by anionic polymerization was dissolved in toluene at 5 mg/mL and loaded with 0.5 equiv of $HAuCl_4$, followed by the addition of different amounts of pyrrole (PY, at PY:$HAuCl_4$ ratios of 0.02, 0.2, 1.0, 2.0, 3.0, 4.0 and 10.0).[37] As mentioned earlier, the chloroaurate $AuCl_4^-$ ions binding with the

micelle core (**Scheme 2-7**) enhance the stability of the micelles. The polar PY molecules can likewise diffuse into the core of the micelles where $AuCl_4^-$ is present, which results in the oxidation of pyrrole and the formation of polypyrrole (PPY), as confirmed by FTIR analysis through the presence of characteristic bipolaron bands. UV analysis (**Figure 2-18**) also revealed that the absorbance band at 325 nm, corresponding to the diblock copolymer/$HAuCl_4$ complex, disappeared. However for PY:$HAuCl_4$ ratios greater than 0.2 a new broad band appeared around 450 nm, corresponding to the π-π* transition of the PPY chains. The formation of PPY was accompanied by the formation of ultra-small Au particles with a broad absorbance maximum between 400 and 500 nm, as confirmed by UV analysis **(Figure 2-18**).

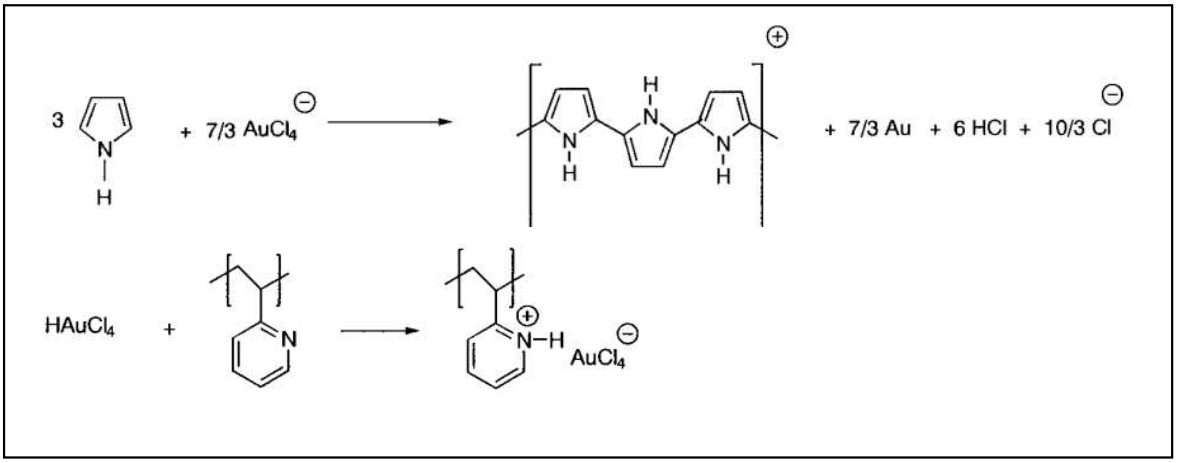

Scheme 2-7. Protonation of the pyridine unit by $HAuCl_4$ (bottom), and oxidation of pyrrole to yield polypyrrole with simultaneous formation of elementary Au (top). Adapted with permission from reference 37. Copyright 1998 WILEY-VCH Verlag GmbH, D-69469 Weinheim.

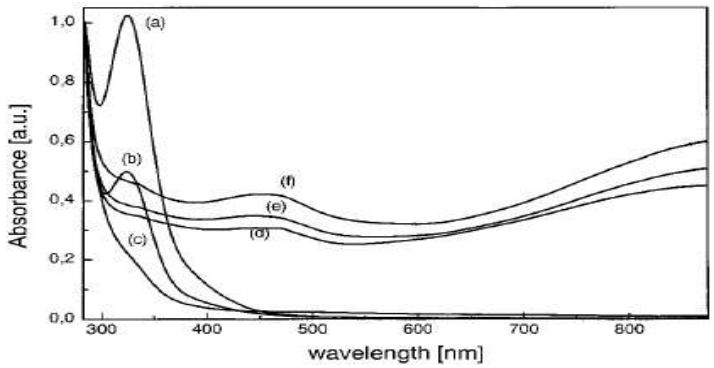

Figure 2-18. UV-vis spectra for colloidal polymer solutions obtained with different PY:$HAuCl_4$ ratios: (a) 0, (b) 0.02, (c) 0.2, (d) 1.0, (e) 4.0, (f) 10.0. Reprinted with permission from reference 37. Copyright 1998 WILEY-VCH Verlag GmbH.

TEM images of thin films cast from PS-*b*-P2VP copolymer solutions containing 0.5 equiv of $HAuCl_4$ without PY are provided in **Figure 2-19a**. Clusters of ultra-small spherical gold nanoparticles (dark spots) inside the spherical micelles were apparent before the addition of PY. However upon addition of PY, the small clusters disappeared and a rather diffuse dark spherical micellar core morphology was observed (**Figure 2-19b-d**), without change in appearance and diameter, regardless of the amount of PY added. Since the formation of Au^0 was concomitant with the growth of PPY, the Au was spread as ultra-small Au nanoparticles within the micelles. This was evidenced by UV analysis in **Figure 2-18**, with the absence of the characteristic SPR peak at around 520 nm, typical for small Au NPs, replaced by a broad absorbance band below 500 nm, typical for ultra-small (≤1 nm) aggregates of elementary gold. Upon annealing the PY-containing films at 130 °C, above the glass transition temperature (T_g) of both blocks, the ultra-small Au NPs merged to yield uniform 7 nm diameter Au NPs (**Figure 2-19e**) without destroying the micellar structures. In contrast, films without PY gave larger Au NPs and the micellar structures were destroyed upon annealing.

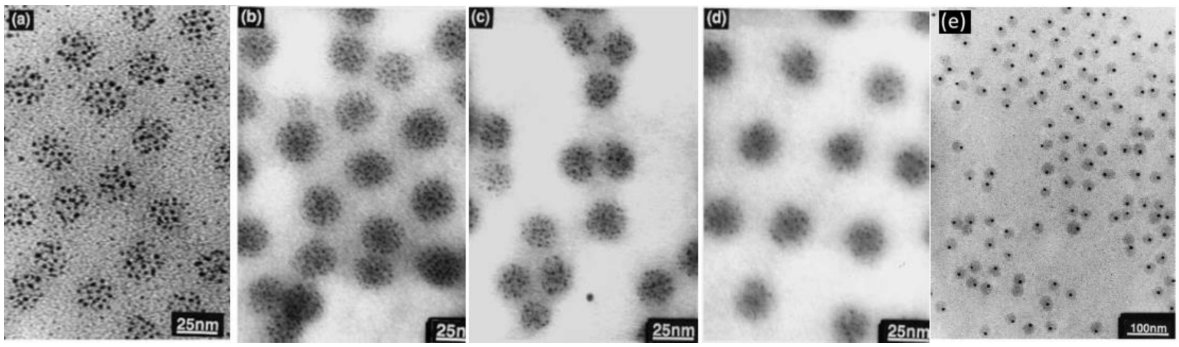

Figure 2-19. TEM micrographs for colloidal polymer films obtained with different PY:$HAuCl_4$ ratios: (a) 0, (b) 0.2, (c) 1.0, (d) 4.0. The core of the micelles is stained by Au and PPY. e) Colloidal polymer film (PY:$HAuCl_4$ = 3.0) after annealing at 130 ^oC for 140 min, exhibiting 7 nm-wide Au clusters encapsulated by PPY in each micelle. Reprinted with permission from reference 37. Copyright 1998 WILEY-VCH Verlag GmbH.

2.3.2.3 Polystyrene-*block*-poly(4-vinylpyridine) (PS-*b*-P4VP)

Pietsch and coworkers obtained 2-3 nm Au NPs of controllable size by a simple ‘‘one-pot’’ procedure for the micellization of polystyrene-*block*-poly(4-vinyl pyridine) (PS-*b*-P4VP), metal incorporation ($HAuCl_4$), and reduction with borane dimethylamine in a mixture of water and toluene.[90] Similarly to the P2VP systems described above, strong interactions exist between the protonated pyridine units of the PS-*b*-P4VP block copolymer and $AuCl_4^-$, while PS has no affinity for the metallic ion. Hence the NPs remained incorporated into the micelle cores after reduction. When using toluene, a solvent good for PS and poor for P4VP, spherical micelles (**Figure 2-20**) were formed with a solid core of P4VP surrounded by a PS corona. However for water/toluene mixtures, rod-like aggregates and ring-like morphologies were obtained (**Figure 2-20**). Since toluene is a good solvent for PS while water is a solvent for the ionic block, water can induce morphological changes by swelling of the P4VP component in the micelle core. According to Yu et al., BCP aggregate architectures are thermodynamically regulated by a combination of core-forming block chain entropy and chain

stretching forces, the repulsive interactions between the corona blocks, and the interfacial tension between the micelle core, the corona, and the solvent.[92]

Swelling of the P4VP blocks by water should increase stretching of the core chains. As the core grows larger, the PS shell may not be able to stabilize it effectively from the surrounding medium, which causes an increase in interfacial tension between the core and solvent, leading to additional destabilization and finally morphological transitions. Thus according to Pietsch and coworkers,[90] at H_2O/4VP ratios greater than unity, the micellar structures transformed into rod- and ring-like morphologies (**Figure 2-21**). Interestingly, these morphologies were not observed in the absence of the metal precursor but rather spherical structures, which could be due to weak hydrogen bonding between water and the 4VP units. Upon addition of $HAuCl_4$ however, the enhanced polarity of the P4VP segment and hydrogen bonding between water and the 4VP units induced morphology changes.

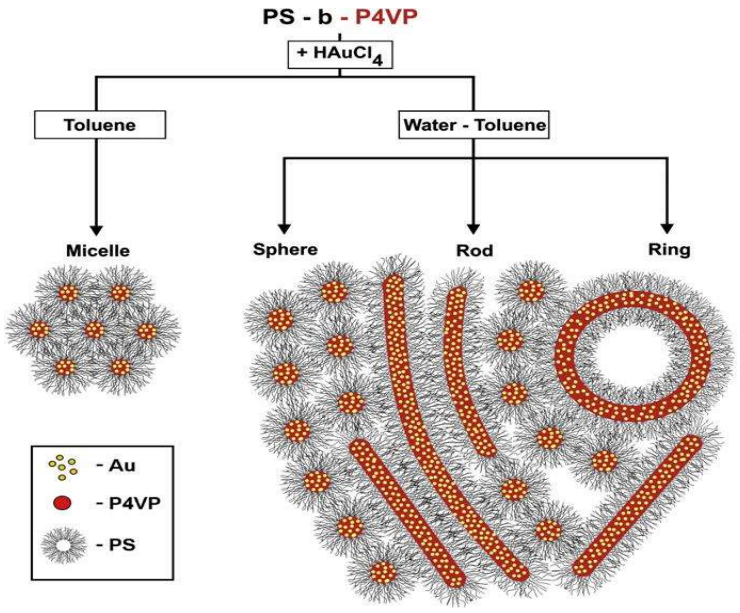

Figure 2-20. Spherical, rod, and ring-like micellar morphologies obtained by loading of $HAuCl_4$ into PS-b-P4VP block copolymer micelles in water/toluene mixtures. Reprinted with permission from reference 90. Copyright 2008 Elsevier Ltd.

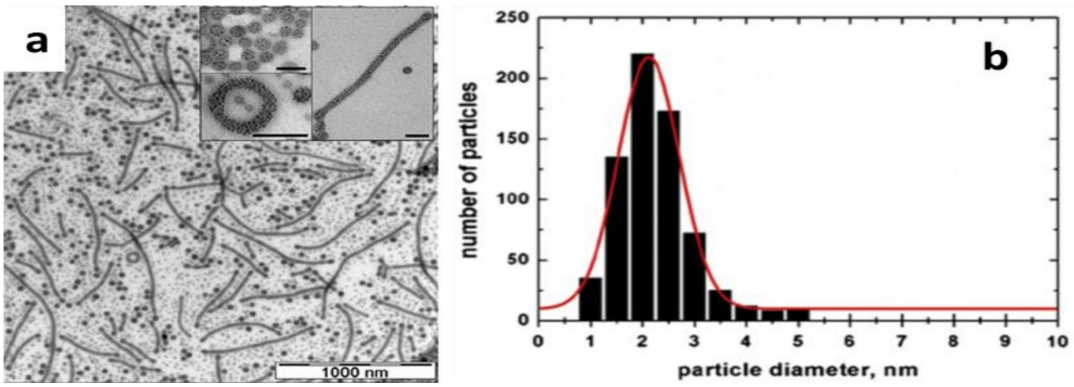

Figure 2-21. (a) TEM micrograph of metallic nano-objects (gold nanoparticles appear as black spots). The insets show distinct morphologies including spheres, rods and rings; the scale bars in the insets are 150 nm. (b) Plot of the particle size distribution as determined from the TEM measurements. A Gaussian fit yielded a mean particle diameter of 2.3 ± 0.6 nm. Reprinted with permission from reference 90. Copyright 2008 Elsevier Ltd.

2.3.2.4 Poly(2-(2-methoxyethoxy)ethyl methacrylate-*co*-oligo(ethylene glycol) methacrylate-*co*-(3-trimethoxysilyl)propyl methacrylate)

The preparation of temperature-responsive microgels based on poly(2-(2-methoxyethoxy)ethyl methacrylate-*co*-oligo(ethylene glycol) methacrylate-*co*-(3-trimethoxysilyl)propyl methacrylate), P(MEO_2MA-*co*-OEGMA-co-TMSPMA), and Au NPs was reported by Chen and coworkers.[93] The NPs obtained by this method displayed catalytic activity in the reduction of 4-nitrophenol upon heating to 70 °C (**Scheme 2-8**). RAFT polymerization was used for the synthesis of the copolymers with an average M_n between ~1500-2000 g/mol. Aqueous solutions of these copolymers were found to respond to temperature changes by forming microgels upon heating above 36 °C (i.e. the lower critical solution temperature, LCST). This was attributed to gradual cross-linking of the aggregates by hydrolysis and condensation of the methoxysilyl groups. An aqueous medium is favorable for the hydrolysis of the methoxysilyl groups, while the temperature above the LCST induces aggregation and therefore favors intra-particle condensation of the methoxysilyl groups. Mixing previously prepared Au NPs and P(MEO_2MA-*co*-OEGMA-*co*-TMSPMA) resulted in the attachment of some polymer chains to the Au

surface. Upon heating this mixture to 70 °C, the unbound polymer chains and the surface-modified Au NPs became hydrophobic and aggregated into hybrid particles **(Scheme 2-8).** Based on TEM analysis (**Figure 2-22**), a large number of Au NPs were apparent inside each microgel particle. The driving force for the formation of the Au-polymer hybrid microgels was supposed to be the temperature-induced co-aggregation and self-cross-linking process. The reduction of 4-nitrophenol to 4-aminophenol catalyzed by Au NPs incorporated in P(MEO_2MA-*co*-OEGMA-*co*-TMSPMA) microgels was demonstrated.

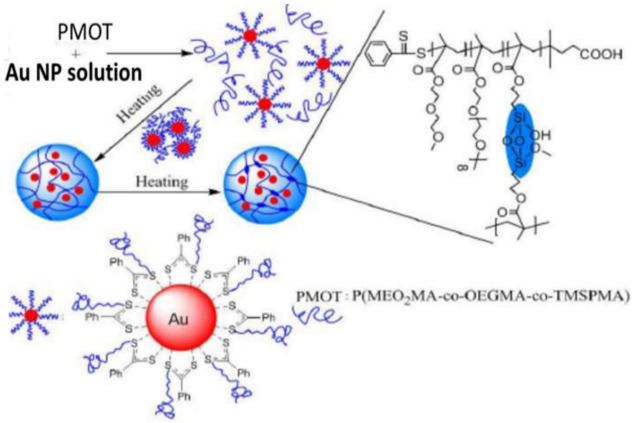

Scheme 2-8. Temperature-induced aggregation and cross-linking of P(MEO_2MA-co-OEGMA-co-TMSPMA) and Au NPs. Reprinted with permission from reference 93. Copyright the Royal Society of Chemistry.

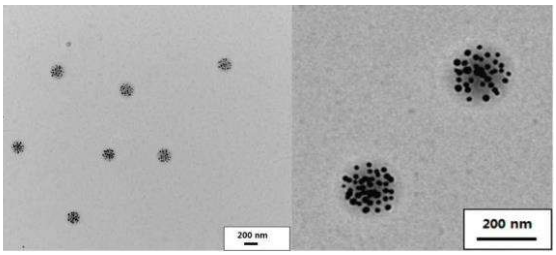

Figure 2-22. TEM images for the hybrid microgels, assembled from a 0.75 mg/mL solution of P(MEO_2MA-co-OEGMA-co-TMSPMA) in a Au NP dispersion. Reprinted with permission from reference 93. Copyright 2011 The Royal Society of Chemistry

2.3.2.5 Poly(ε-caprolactone) and poly(ethylene oxide) tri- and pentablock copolymers

Leiva and coworkers developed two procedures for the synthesis of Au NPs stabilized by poly(ε-caprolactone)-*block*-poly(ethylene oxide)-*block*-poly(ε-caprolactone) (PCL-*b*-PEO-*b*-PCL) triblock copolymers.[94] In the first approach, aqueous dispersions of aggregates were obtained by dialyzing a DMF-water solution of PCL-*b*-PEO-*b*-PCL block copolymer (**Figure 2-23**) against water. Since water is a solvent selective for the PEO block, it induced the aggregation of the PCL blocks to form a hydrophobic core. The resulting solution was mixed with $KAuCl_4$ under vigorous stirring to promote the reaction between PCL-*b*-PEO-*b*-PCL and $KAuCl_4$, yielding stable Au NPs. No external reducing agent was needed, since reduction of the gold ions was achieved through oxidation of the hydroxyl end groups[94,95] of the copolymer chains, and the hydrophilic PEO block formed a crown surrounding the hydrophobic core to provide steric stability.[94] Not only were large (194 ± 19 nm) Au NPs obtained by this method, but most of the NPs were also outside of the micelles (**Figure 2-24a**). This is because the micelles were not stable enough to limit the growth of the NPs, due to the low hydrophobicity of the core associated with the short hydrophobic PCL blocks. This was in agreement with UV analysis, which yielded a broad and asymmetric surface plasmon resonance (SPR) band, with a maximum shifting from 570 to 600 nm over 192 h. Much smaller Au NPs (14.4 nm) inside the micelles were synthesized by a second approach, whereby DMF solutions of $KAuCl_4$ and PCL-*b*-PEO-*b*-PCL were mixed to generate Au NPs and copolymer aggregates at the same time. The mixture was then diluted with and dialyzed against water to obtain aqueous solutions of stable Au NPs. According to Leiva et al., this approach was successful because the formation of Au clusters occurred in the vicinity of the hydrophobic copolymer segments, simultaneously with the formation of the hydrophobic micelle core.

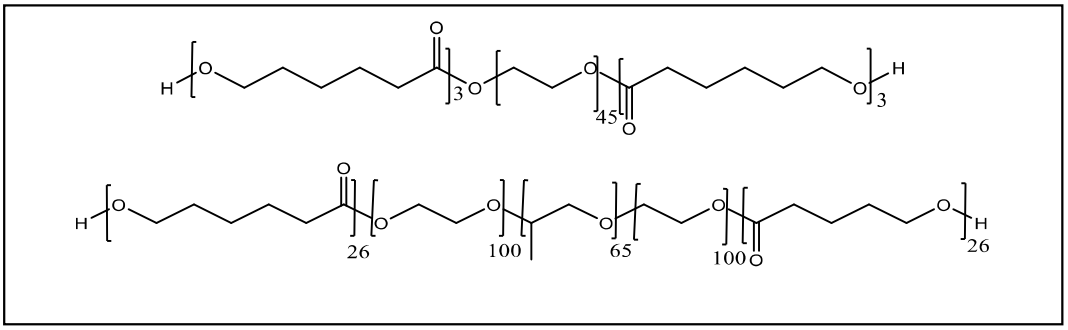

Figure 2-23. Chemical structure of PCL-b-PEO-b-PCL triblock and PCL-b-PEO-b-PPO-b-PEO-b-PCL pentablock copolymers. Adapted with permission from reference 94. Copyright 2014 Wiley Periodicals, Inc.

The two procedures discussed above were also applied to the preparation of Au NPs using a pentablock copolymer of PCL-*b*-PEO-*b*-PPO-*b*-PEO-*b*-PCL (**Scheme 2-9**).[94] The synthesis of Au NPs by direct reaction between the pentablock copolymer aggregates and gold resulted in relatively smaller (89 ± 55 nm) Au NPs as compared to the large (194 ± 19 nm) Au NPs obtained with the triblock copolymer under the same conditions. This was confirmed by TEM analysis, as seen in **Figure 2-24b**, where more copolymer aggregates seem to be attached to the NPs than in the case of the triblock copolymer aggregates (**Figure 2-24a**). Moreover, when the pentablock copolymer was used, the Au NP SPR band was also narrower (536 to 556 nm) and symmetrical in comparison to the bands obtained for the triblock copolymer.

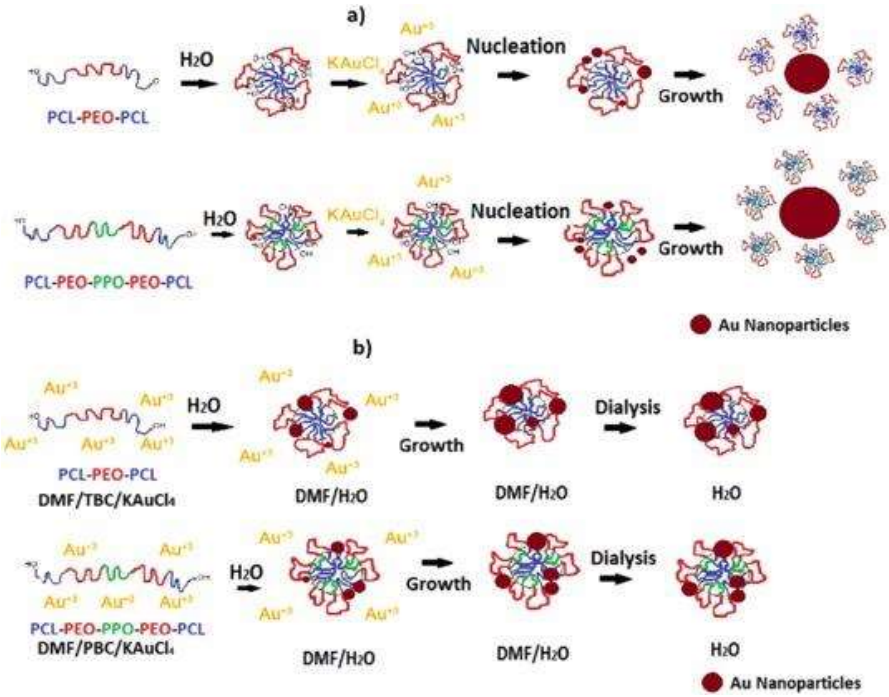

Scheme 2-9. Synthesis of gold nanoparticles (a) using copolymer aggregates; (b) simultaneously with aggregation of the copolymers. Reprinted with permission from reference 94. Copyright 2014 Wiley Periodicals, Inc.

When the protocol for the concurrent formation of copolymer aggregates and Au NPs was followed, smaller 19 nm Au NPs were also obtained. This is again presumably because the formation of Au clusters occurred in the vicinity of the hydrophobic core of the copolymer, simultaneously with the formation of the hydrophobic core of the micelle. However the size of the NPs prepared using pentablock copolymers (19 nm) was larger than for the triblock copolymer (14 nm); no explanations were provided for this observation.

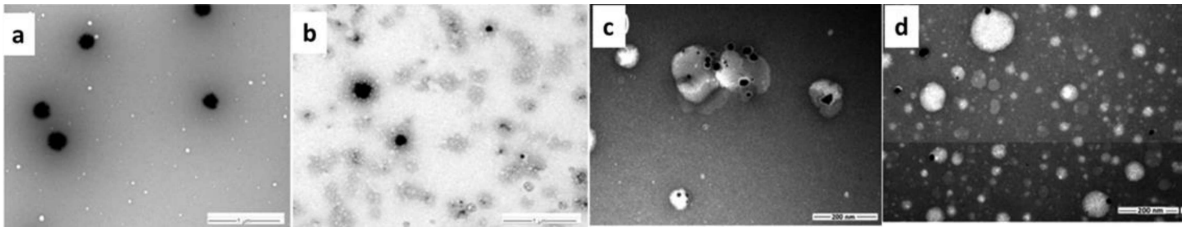

Figure 2-24. TEM images for Au NPs synthesized by the direct reaction between copolymer aggregates and gold: (a) PCL-b-PEO-b-PCL, (b) PCL-b-PEO-b-PPO-b-PEO-b-PCL copolymer, and Au NPs synthesized simultaneously with the aggregation of copolymers: (c) PCL-b-PEO-b-PCL and (d) PCL-b-PEO-b-PPO-b-PEO-b-PCL copolymer. Reprinted with permission from reference 94. Copyright 2014 Wiley Periodicals, Inc.

2.3.3 Star-block copolymer stabilizers

Star-shaped polymers are branched macromolecules with well-defined arms chemically bonded to a single core.[96] Characteristics like the number of arms, the degree of polymerization, the composition, and the chain architecture can be controlled in these systems. Controlling and knowing the properties of these polymers opens the door to different applications.

The synthesis of metallic nanoparticles for different applications depends upon several parameters, but particle stability over time is crucial. In this regard block copolymers have advantages in comparison to small molecule surfactants, as they provide enhanced kinetic stability and a lower CMC. Other benefits of block copolymer micelles include control over the micelle size by adjusting the molecular weight of the blocks, the composition, chemistry, and the solvent used.[25] One limitation of block copolymer micelles is that if polymer chains become detached, they may induce aggregation. Star-block copolymers behaving like unimolecular core–shell micelles may be able to minimize this issue. In star-block copolymers, micelle instability with decreasing concentration is less problematic because the core segments of the star-block copolymer are covalently bonded. In unimolecular micelles there is no equilibrium (exchange) between free chains and the micelles, since all the polymer chains

are secured to one single core. Therefore there is no CMC for star-block copolymers.[39] However they may still form supermicelles at higher concentrations, but this happens typically about three orders of magnitude above the CMC of the corresponding linear BCPs.[96] The synthesis of star-block copolymers can be achieved with very narrow molecular weight distributions (MWD), and with a variety of macromolecular architectures and compositions. NP synthesis can be restricted to the core of star-block copolymers, by controlling the inner core composition and the block length of the stars. For example, the amphiphilic star-block terpolymers PS28(P2VP-PtBA)28, containing equal number (28) of arms of PS (Mw = 3K) and P2VP-*b*-PtBA copolymer (Mw_{P2VP} = 16K, Mw_{PtBA} = 11K) linked to a polydivinylbenzene cross-linker core yielded mainly unimolecular micelles in toluene, with an average aggregation number of only 1.5.[96]

2.3.3.1 Polystyrene-*b*-poly(2-vinylpyridine) (PS-*b*-P2VP) star-block copolymers

Youk et al.[25] described the synthesis of PS-*b*-P2VP copolymers by living anionic polymerization, that were cross-linked into star-block copolymers (containing 65.1 % of PS and 34.9% of P2VP), by adding ethylene glycol dimethacrylate (**Scheme 2-10**). Although the report did not mention the number of arms obtained, it was stated that due to the nature of the coupling reaction the number of arms could vary. However based on the M_w of the star-block copolymers and the block copolymer quoted in the study, the average branching functionality was ~ 4 arms per molecule. The resulting star-block copolymers were dissolved in toluene at 5 mg/mL and the P2VP core was loaded with 0.1, 0.3, and 0.5 equiv of $HAuCl_4 \cdot 3H_2O$ per 2VP unit in toluene by stirring for 24 h. A characteristic yellow color was observed, showing that $HAuCl_4 \cdot 3H_2O$ was successfully complexed by the 2VP units. Reduction was performed by adding the metal-loaded polymer solution to a solution of 0.768 equiv hydrazine (N_2H_4) per $HAuCl_4$. Both the size and size distribution of the resulting Au NPs depended on the loading level, a lower loading resulting in a smaller size and a narrower size distribution. It was determined from **Figure 2-25** that 4 ± 0.06, 5.6 ± 0.1, and 6.8 ± 0.3 nm diameter single Au NPs were obtained per star-block

copolymer molecule at 0.1, 0.3 and 0.5 equiv loading levels, respectively, and the dispersions were stable for up to one month.

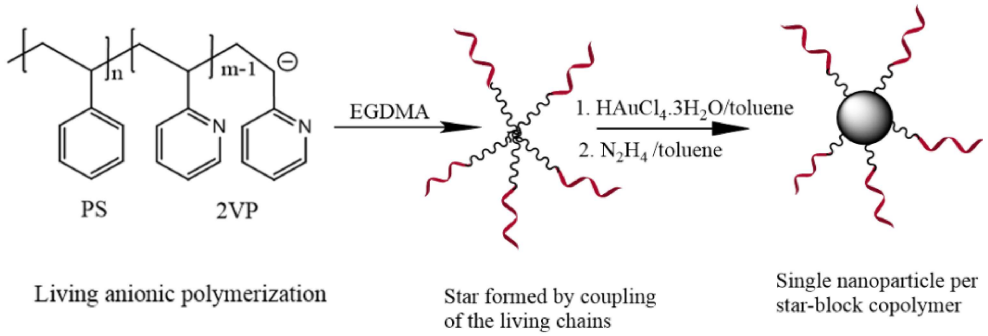

Scheme 2-10. Synthesis of PS-b-P2VP star-block copolymer from PS-b-P2VP diblock copolymer. Adapted with permission from reference 25. Copyright 2002 American Chemical Society.

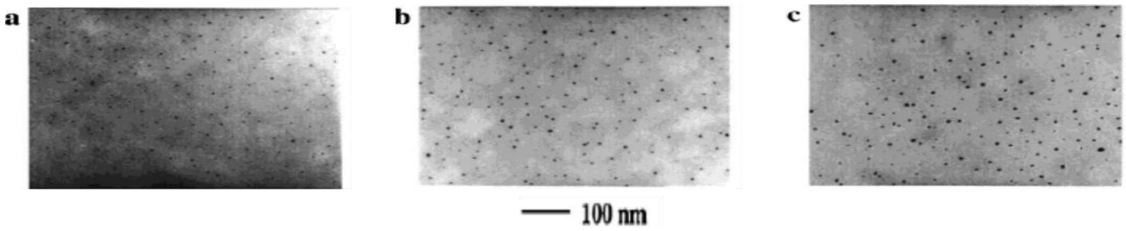

Figure 2-25. TEM micrographs for gold nanoparticles at different loading levels of $HAuCl_4$ one month after reduction: (a) 0.1 equiv (4 ± 0.06 nm), (b) 0.3 equiv (5.6 ± 0.1 nm), and (c) 0.5 equiv (6.8 ± 0.25 nm). Reprinted with permission from reference 25. Copyright 2002 American Chemical Society.

2.3.3.2 Polystyrene-*block*-poly(glutamic acid) (PS-*b*-PGA) star-block copolymers

Abraham et al. synthesized triarm star-shaped polystyrene-*block*-poly(glutamic acid) (PS-*b*-PGA)$_3$ copolymers with three different compositions (**Table 2-1**) by a combination of ATRP and ring-opening polymerization (ROP) techniques. Triarm star polystyrene was first synthesized using a cyanurate-based trifunctional initiator by ATRP, followed by ROP of γ-benzyl glutamate N-carboxyanhydride

and hydrolysis of the benzyl groups to yield the desired triarm star (PS-*b*-PGA)$_3$ copolymer.[97] Stable micelles were prepared either by dialysis of a DMF-water mixture of star-block copolymer solution against water in the presence of an ion-exchange resin (since poly(glutamic acid) is not very soluble in water at neutral pH), or by diluting a very small amount of a concentrated star-block copolymer solution in DMF with a large amount of water, followed by heating to 110 °C. While the polymer molecules existed in a unimolecular form at higher temperatures, they self-assembled into stable multimolecular micelles when the temperature was decreased, as confirmed by DLS measurements (**Figure 2-26**). Based on the DLS experiments, the critical micelle temperature (CMT) of these solutions was ~ 63 °C. An increase in scattering intensity was also apparent below the CMT and was attributed to micelle aggregation, due to the interactions of the hydrophilic PGA segments below the CMT. This was further confirmed by TEM analysis (**Figure 2-27**), which showed that the spherical micelles self-assembled into necklace-like linear aggregates.

Table 2-1. Characteristics of PS-b-PGA triarm block-star copolymers used for micellization studies. Reprinted with permission from reference 97. Copyright 2007 Wiley Periodicals, Inc.

Polymer	M_n[a]	M_n[b]	M_w/M_n[b]
(~PS50-*b*-PGA100)$_3$	18,600	15,300	1.23
(~PS100-*b*-PGA100)$_3$	23,200	16,800	1.27
(~PS100-*b*-PGA50)$_3$	17,300	14,700	1.15

a) Calculated from ^{1}H NMR analysis. b) Calculated from SEC analysis.

For the preparation of Au-polymer conjugates, commercially purchased 20 nm Au colloids were first dispersed in DMF before the addition of a phosphothiolipid (1,2-dipalmitoyl-*sn*-glycero-3-phosphothioethanol) and block copolymer solution in DMF, heating to 110 °C, and cooling slowly. The thiol groups capped the surface of the gold nanoparticles, while the phosphate and carbonyl groups

promoted hydrogen bonding with the carboxylic acid functionalities of the star-block copolymer **(Scheme 2-11)** to yield stable gold-polymer conjugates (**Figure 2-28)**.

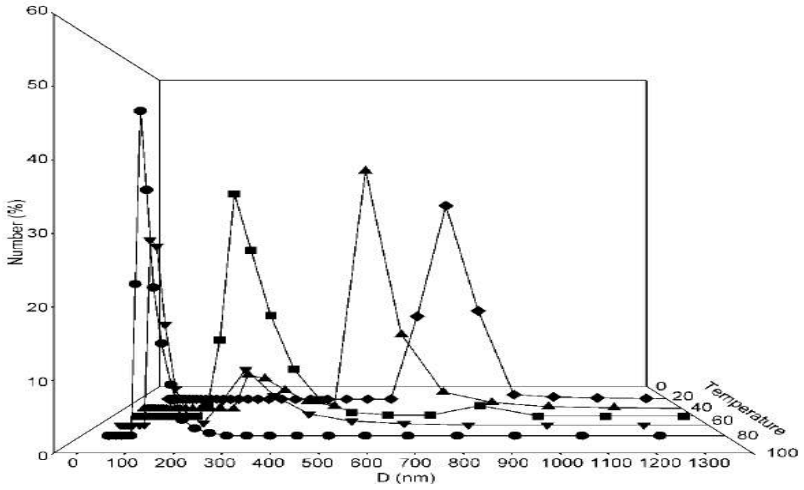

Figure 2-26. Influence of temperature on the diameter and distribution of PS-b-PGA micelles/micellar aggregates in solution. Reprinted with permission from reference 97. Copyright 2007 Wiley Periodicals, Inc.

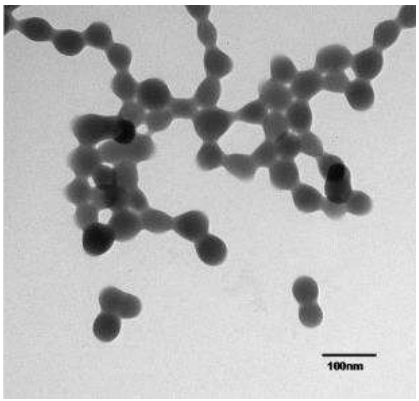

Figure 2-27. TEM images for spherical (PS-b-PGA)3 triarm copolymer micelles self-organized into necklace-like linear arrays (scale bar = 100 nm). Reprinted with permission from reference 97. Copyright 2007 Wiley Periodicals, Inc.

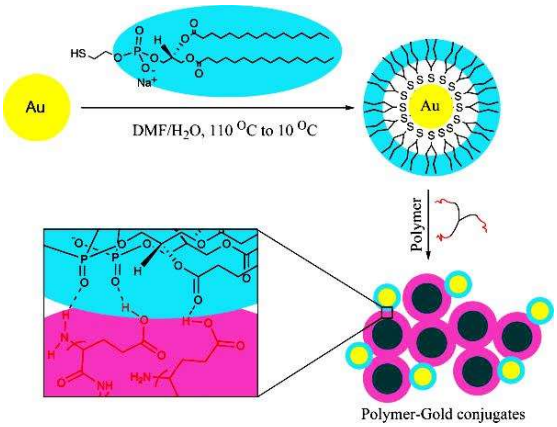

Scheme 2-11. Preparation of gold nanoparticle–(PS-b-PGA)$_3$ micelle conjugates. The hydrogen bonding interactions between the lipid layer and the micelle shell are shown in the inset. The structure of the phosphothio surface-capping ligand is also depicted. Reprinted with permission from reference 97. Copyright 2007 Wiley Periodicals, Inc.

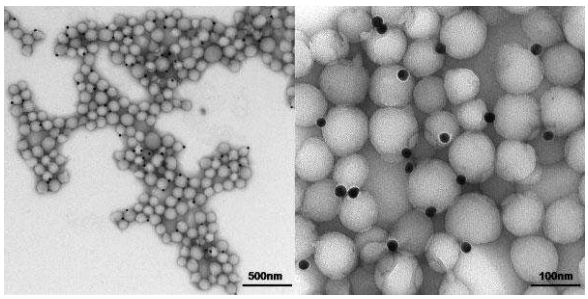

Figure 2-28. TEM images for micelle–gold nanoparticle conjugates. Surface-modified gold nanoparticles are attached to the hydrophilic surface of the (PS100-b-PGA100)$_3$ tri-arm copolymer micelles. Reprinted with permission from reference 97. Copyright 2007 Wiley Periodicals, Inc.

2.3.3.3 Poly(ethylene oxide)-*block*-poly(ε-caprolactone) (PEO-*b*-PCL) star-block copolymers

Five-arm star-shaped poly(ethylene oxide)-*block*-poly(ϵ-caprolactone) (PEO-*b*-PCL)$_5$ copolymers were also utilized for the preparation of Au NPs. A low molecular weight five-arm star PEO macroinitiator core (M_n = 2150 g/mol overall) was used for the ring-opening polymerization of ϵ-

caprolactone to produce PCL coronal blocks of variable length (**Table 2-2**) but with identical PEO core characteristics. The resulting five-arm star-shaped block copolymers were dissolved in DMF and loaded with $KAuCl_4$ before reduction with $NaBH_4$ (2 equiv per $AuCl_4^-$, as opposed to 10 equiv used in most investigations). Since the gold salt preferentially interacted with the PEO core of the star-block copolymer, the $KAuCl_4$/EO molar ratio was used as the controlling parameter.[39] Loading with 0.25 equiv of $KAuCl_4$/EO yielded better results than higher molar ratios, which led to $KAuCl_4$ molecules outside the PEO core and nucleation outside the micelles.

Table 2-2. Characteristics of PEG-b-PCL star-block copolymers before loading, and after loading and reduction. Adapted with permission from reference 39. Copyright 2005 American Chemical Society.

Sample	1	2	3	4	5	6
M_n[a] (g/mol)	4200	6400	8200	9600	11200	13100
DP_{PCL}	3	6	9	12	15	18
D_h[b] (nm)	3.2±0.5	3.4±0.8	4.5±1.0	5.1±0.7	6.4±0.9	7.4±0.8
D_{TEM}[c] (nm)	5.9±0.5	6.8±0.6	3.4±0.2	3.2±0.8	4.0±0.2	3.6±0.2
D_{TEM}[d] (nm)	5.2±0.5	3.6±0.1	3.7±0.1	3.5±0.1	3.5±0.1	2.9±0.1

a) Calculated by ^1H NMR; b) D_h measured by DLS in DMF from data extrapolated to zero concentration; c) before reduction with $NaBH_4$; d) after reduction with $NaBH_4$.

The hydrodynamic diameter (D_h) of the star-block copolymers measured by DLS increased with the length of the PCL blocks as expected. The length of the PCL blocks also affected the size and size distribution of the nanoparticles obtained, with larger (5.2 ± 0.5 nm) and broader size distributions observed for NPs prepared with the shorter PCL block samples (e.g. sample 1), as seen in **Figure 2-29**. This may be due to the coalescence of particles being favored when the PCL block is too short (DP = 3), so as to minimize NP interactions. Three observations further confirmed this: Very large Au NPs were obtained by the same method, but without any polymer. Highly polydisperse Au NPs also resulted

when using PCL star polymers without the PEO blocks. Moreover, large Au NP clusters were observed for samples 1 and 2 (with shorter PCL blocks, **Figure 2-29**) after one month, while samples 3-6 (with relatively longer PCL blocks, **Figure 2-29**) were stable for up to 6 months.

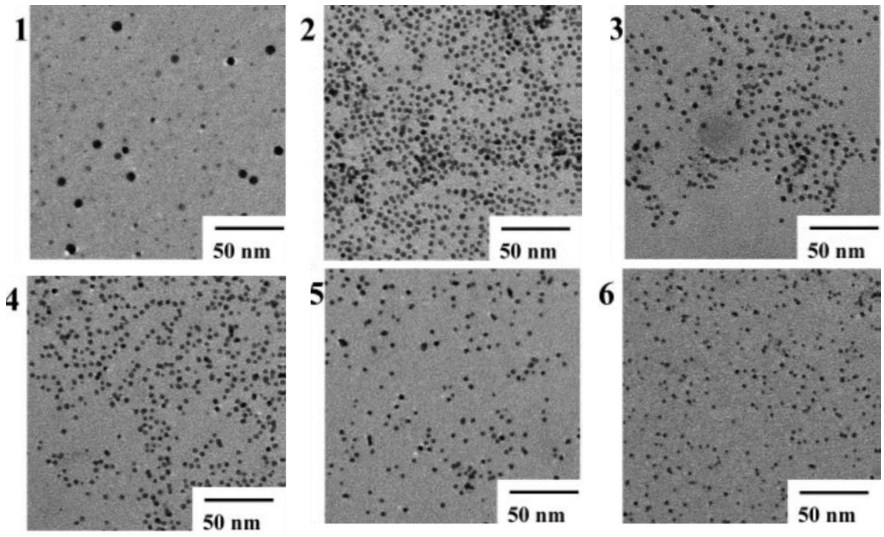

Figure 2-29. TEM micrographs for gold nanoparticles prepared with star-block copolymers 1-6 (Table 2-2) with a $KAuCl_4$/EO molar ratio of 1/4 and after reduction with $NaBH_4$ ($KAuCl_4$/$NaBH_4$ molar ratio of 1/2). Reprinted with permission from reference 39. Copyrights 2005 American Chemical Society.

2.3.4 Dendritic polymers

The molecular architecture of dendritic polymers is characterized by the presence of multiple branching levels, with a controllable number of branches, terminal groups and molecular weight. The main dendritic polymer families reported include dendrimers, hyperbranched and dendrigraft polymers (**Figure 2-30**). Since their introduction as controlled structure polymers in the late 1970's, several groups have made major contributions in the synthesis of this type of polymers (**Table 2-3**). The characteristic multi-level branched architecture of dendritic polymers is a consequence of sequential coupling reactions occurring in the synthesis of these materials. These coupling reactions can involve

the addition of small molecule building blocks, as in the case of dendrimers and hyperbranched polymers, while macromolecular building blocks are used in the synthesis of dendrigraft polymers.[98]

Dendrimer structures, with precisely controlled repeating patterns, well-defined size, shape and topology, are typically condensation polymers derived from polyfunctional AB_n monomers, through cycles of monomer protection, condensation, product purification and deprotection leading to successive generations. They can be prepared with very narrow molecular weight distributions (MWD) and polydispersity indices (PDI = M_w/M_n) as low as 1.01.

The synthesis of hyperbranched polymers, in contrast, typically involves one-pot condensation reactions of unprotected AB_n monomers to give a randomly branched and imperfect structure. Due to this, hyperbranched polymers have higher polydispersities (PDI > 2) in most cases.

Dendrigraft (also known as arborescent or tree-like) polymers combine characteristics of the two aforementioned dendritic polymers. The synthetic strategy used is based on successive grafting reactions of macromolecular building blocks rather than small molecules, to produce highly branched polymers in a few reaction steps. Successive cycles of substrate functionalization, grafting and purification are most commonly used to produce different generations of dendrigraft polymers. The main advantage of this approach is that a high molecular weight is attained in a few reaction steps, while the molecular weight distribution is relatively narrow, with PDI ≤ 1.1 in most cases.

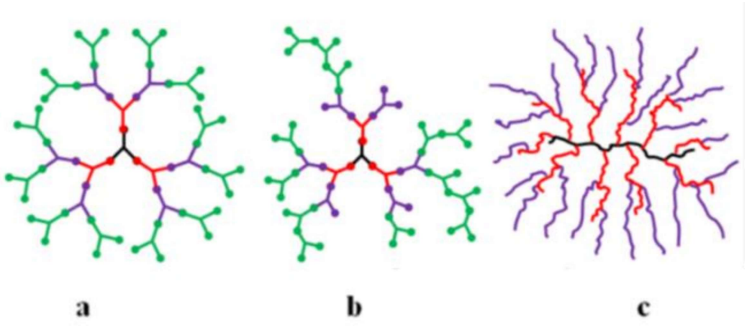

Figure 2-30. Structure of dendritic polymers: (a) dendrimer, (b) hyperbranched polymer, (c) dendrigraft polymer. Reprinted with permission from reference 99. Copyright 2004 Elsevier Ltd.

Table 2-3. Early peer-reviewed publications on dendritic molecules (1978–1991). Adapted with permission from reference 100. Copyright John Wiley & Sons Limited

Lead Authors	Year
From Cascade Growth to Dendrimers	
Vögtle	1978
Maciejewski	1982
De Gennes	1983
Tomalia/Turro/Goddard	1985-1990
Newkome/Baker	1985-1990
Fréchet/Hawker	1990-1991
Miller/Neeman	1990
Random Hyperbranched Polymers	
Odian/Tomalia	1988
Kim/Webster	1990
Fréchet/Hawker	1991
Dendrigraft Arborescent Polymers	
Gauthier/Möller	1991
Tomalia	1991

2.3.4.1 Dendrimers for the preparation of MNP

Dendrimers, also known as cascade, cauliflower or starburst molecules, have attracted much attention since their introduction in 1978 by Buhleier and others. Sometime later, Tomalia developed a technique for the synthesis for what is considered to be "true dendrimers",[100] namely highly branched polymers with a high concentration of surface functional groups having a similar microenvironment.[101] Their structure consists of repeating patterns, typically arising from small molecule building blocks of the AB_2-type, with cycles of protection, condensation and deprotection reactions to achieve complete conversion of the peripheral B groups in each reaction cycle (generation).[102] Addition of the first layer results in a generation 1 (G1) dendrimer, and further cycles or layers yield successive generations (G2, G3, etc.) dendrimers. Though synthetically challenging, control over the structure, physical and chemical properties of dendrimers can be achieved by varying the core type, the monomer branching functionality, and the type of terminal functional groups used in the reactions. Under optimal conditions dendrimers can be prepared with very narrow molecular weight distributions, predetermined molecular weights, and tailored interior/surface topographies. Dendrimers of lower generations tend to exist in relatively open conformations, whereas higher generations adopt a spherical three-dimensional shape.[103] Even though the number of terminal functional groups increases exponentially for successive generations in dendrimers, the rate of increase in molecular weight per generation is relatively low (2- to 3-fold).[104] Consequently, their diameter only increases linearly with the generation number (**Table 2-4**). This characteristic of dendrimers leads to a denser structure as the generation number increases, but also favors the development of structural imperfections due to incomplete reactions. In other words, the average distance between the terminal groups decreases for the higher generations as compared to the lower generations, which gives a close-packed spherical exterior surrounding internal cavities. This characteristic is very interesting, for example, to control the access of small molecules to catalysts encapsulated in dendrimers. The properties of dendrimers strongly depend on the type of monomer

used to build their interior, and on the functional groups present on their exterior. Polar reactive groups like amines[64] or carboxylic acids[103] in the inner structure, in combination with the ability to tune the peripheral groups, provide a means to control the dielectric properties of dendrimers,[105] and is particularly useful to selectively encapsulate metal ions or polar small molecules in dendrimers.

The encapsulation of metal ions in dendrimers can involve covalent attachment, electrostatic interactions, complexation reactions, or a combination thereof. Metal ions can be complexed within the interior and/or at the periphery of dendrimers. Functionalizing the exterior selectively with metal-complexing functional groups such as carboxylic acid,[103] amine,[26,105] hydroxyl,[106] amide,[107] imine[28] or thiol [108] groups allows the selective complexation of metals at the periphery. Molecules derived from natural components like DNA-based dendrimers[109] can also encapsulate MNPs within their cavities. The complexation of metal ions entirely within dendrimers can be achieved by functionalizing the exterior with non-complexing entities such as hydroxyl groups. For example, substituting ethanolamine for ethylenediamine in the last step of the PAMAM dendrimer synthesis yielded hydroxyl-terminated PAMAM dendrimers as shown in **Scheme 2-12**. It is also possible to protonate selectively peripheral acid or amine groups, by adjusting the solution pH, to make the functionalities at the periphery non-complexing. Once metals ions are loaded in dendrimers, they can be reduced to produce dendrimer-encapsulated nanoparticles. One problem associated with using steric or electrostatic stabilizers for the preparation of MNPs is passivation of the NPs by the stabilizer, which may limit the usefulness of active sites on the nanoparticles for applications like catalysis. The use of dendrimer templates is nevertheless useful as it provides kinetic stabilization to the nanoparticles, thus avoiding aggregation of the NPs, hopefully without excessive passivation of the active sites.[105]

The use of dendrimers as stabilizers has other advantages: For instance, since the reduction takes place inside the dendrimer containing a specific number of complexed metal ions within each molecule, stoichiometric control over nanoparticle size may be possible. Another advantage is that dendrimer-

encapsulated nanoparticles may be relatively sterically unhindered, which can minimize surface passivation. Furthermore, nanoparticle dispersibility can be improved by modifying the terminal groups on the dendrimer surface, depending on the application.[31] Numerous metals have been incorporated within dendrimers such as Pt,[26, 28,106,107,110] Pd,[28] Rh,[107] Ag[28] and Au,[103,111] but our main focus will be on Au nanoparticles.

Table 2-4. Physical Characteristics of PAMAM Dendrimers. Reprinted with permission from reference 105. Copyright 2005 American Chemical Society.

Generation	Number of surface group	Number of tertiary amines	Molecular weight [a]	Diameter (nm)[b]
0	4	2	517	1.5
2	16	14	3,256	2.9
4	24	62	14,215	4.5
6	256	254	58,048	6.7
8	1024	1022	233,383	9.7
10	4096	4094	934,720	13.5

a) Molecular weight based on defect-free, ideal structure, and amine-terminated dendrimers. b) Molecular dimensions determined by size exclusion chromatography (SEC) analysis.

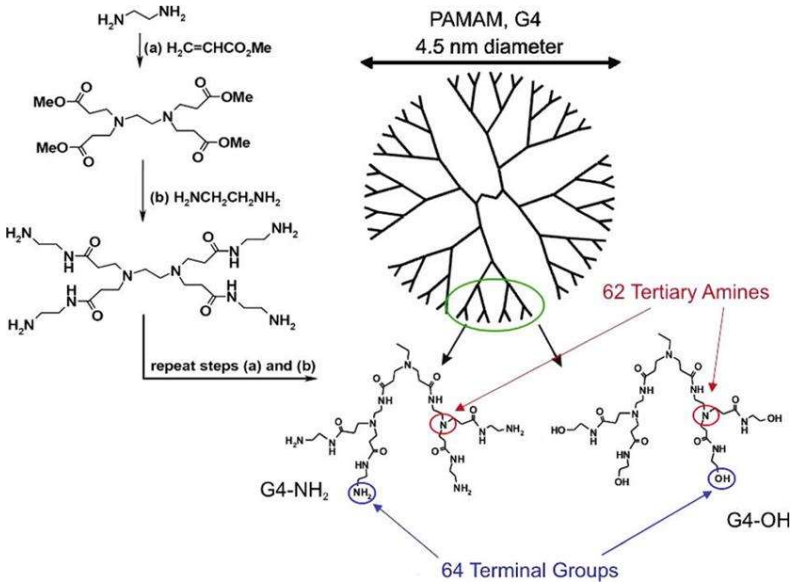

Scheme 2-12. Synthesis and structure of fourth-generation, amine-terminated (G4-NH_2) and hydroxyl-terminated (G4-OH) PAMAM dendrimers. Reprinted with permission from reference 105. Copyright 2005 American Chemical Society.

2.3.4.2 Polyamidoamine (PAMAM) dendrimers

The group of Crooks[111,112] used G2, G4 and G6 PAMAM dendrimers for the preparation of stable Au colloids, while Esumi et al.[103] used G3-G5 PAMAM dendrimers to obtain stable Au, Pt and Ag NPs. The findings for Au NPs display very similar trends for both groups in most cases, regardless of the experimental conditions used. The generation number appears to influence the nanoparticle size but in a rather unexpected fashion, as smaller NPs were obtained for higher generations. As compared with linear polymers, the useful dendrimer concentration to obtain stable gold nanoparticles can be tremendously low. For example, Garcia et al. prepared dendrimer-stabilized 2-3 nm Au colloids (dendrimer/Au nanocomposites) simply by mixing an aqueous solution of $HAuCl_4 \cdot 3H_2O$ with a methanol solution of G2 or G4 amine-terminated PAMAM dendrimers, followed by reduction with $NaBH_4$. The molar ratio of Au to primary amine groups in the dendrimers was maintained constant at

1:11 in these experiments.[111] The dendrimers can interact with the Au colloids not only through the terminal primary amine groups, but also with the inner secondary and tertiary amine functionalities. Although the 2° and 3° amines can also be protonated, it was rationalized by Esumi et al.[103] that the primary amino groups of PAMAM which are at the periphery (with an estimated $pK_{NH2} \sim 9.7$) must be protonated before reduction upon addition of the aqueous solution of the acidic $HAuCl_4$ salt. This leads to electrostatic attractions between the NH_3^+ of the dendrimer and $AuCl_4^-$. However upon addition of $NaBH_4$ in the reduction process the solution becomes basic, so the primary amine lone pairs should interact with the Au surface.[103] Despite weak Au/amine interactions, the attachment of an alkylamine monolayer on the Au surface should result in kinetically stabilized Au colloids.[113] Chelation also plays a role in improving the stability of Au NPs, as there is a large number of amine groups per dendrimer. However aggregation through dendrimer-induced bridging may also occur if the degree of amine functionalization is high.

Both G2 and G4 PAMAM dendrimers provided stable Au colloids, but the dendrimer generation was found to influence the size of the particles. The TEM pictures in **Figure 2-31** show that the colloids formed with the G2 dendrimers were insignificantly larger (3.0 ± 1.0 nm) than those formed with the G4 dendrimers (2.7 ± 0.6 nm). This is in agreement with the findings of Esumi et al., wherein the average particle size of Au NPs for the PAMAM dendrimers of generation G5 (2.2 nm ± 0.7) was significantly smaller than for G3 dendrimers (5.5 nm ± 1.3). It was rationalized that larger dendrimers have the capacity to envelop the growing particles and serve as templates for particle growth.

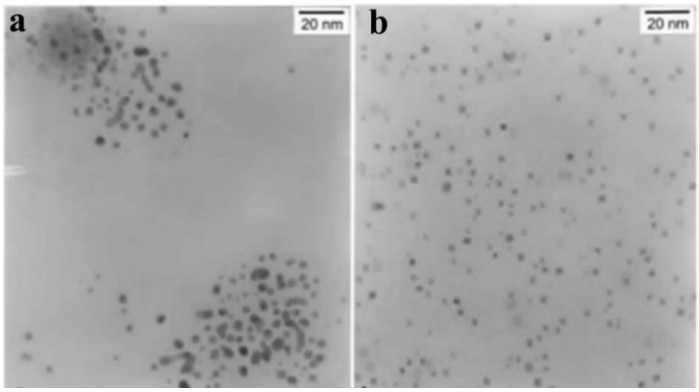

Figure 2-31. TEM micrographs for nanocomposites formed using (a) G2 and (b) G4 dendrimers. Average particle diameter: (a) 3.0 ± 1.0 and (b) 2.7 ± 0.6 nm. Reprinted with permission from reference 111. Copyright 1998 American Chemical Society.

The Au NPs formed with the lower generation dendrimers were also found to be less uniform and more aggregated than those synthesized with the higher generation dendrimers, although the preparation was carried out with a constant ratio of primary amine groups to $AuCl_4^-$ for both generations. The authors[111] attributed this to the different number of terminal amine groups for the two generations, namely 16 for G2 and 64 for G4, as well as to their topology. Since the G4 molecules are much larger than the G2 molecules, they can envelop the growing NPs better. The G4 molecules are also spheroids, while the G2 molecules are expected to be more oblong, so the G4 molecules may be better suited as templates for particle growth. The size observed by TEM was consistent with UV-vis characterization results, showing that the SPR band for Au was red-shifted by 12 nm for the Au NPs stabilized by the G2 dendrimers, even though λ_{max} was the same in both cases. This was likewise attributed to the larger size of the G2-derived NPs.

PAMAM dendrimers of generations G3-G5 were also employed for the preparation of Au and Pt NPs by Esumi et al. As mentioned above, the findings of these researchers for Au NPs displayed trends very similar to the results reported by Crooks et al. in most cases. In this case, the metallic salts and

dendrimers were separately dissolved in water and mixed with the desired metal ion to surface functional group ratio. Reduction was achieved with an ice-chilled aqueous $NaBH_4$ solution (10-fold relatively to the metal ions).[103] As in the previous cases, the size of the Au nanoparticles obtained depended on the generation number for G3-G5 PAMAM dendrimers: At a constant ratio of [dendrimer]/[Au^{3+}], the average particle size for the G5 PAMAM was smaller (2.2 nm ± 0.7) than for the G3 PAMAM (5.5 nm ± 1.3). The size also decreased rapidly, and then more gradually upon increasing the [dendrimer]/[Au^{3+}] ratio (**Figure 2-32**). These results confirm that PAMAM dendrimers are effective stabilizers for the preparation of Au NPs.

Both Crooks and Esumi attempted to confirm the presence of interactions between the Au NPs and the PAMAM dendrimers using FT-IR spectroscopy. Unfortunately only amide bands characteristic for the dendrimer branches were observed, with and without Au NPs, in both cases. This could be due to adsorption of the Au NPs at the periphery of the dendrimers.

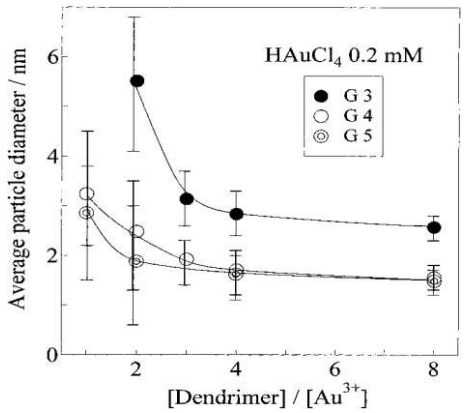

Figure 2-32. Average Au NP diameter as a function of the [PAMAM dendrimer]/[Au^{3+}] ratio. Reprinted with permission from reference 103. Copyright 2000 American Chemical Society.

2.3.4.3 Polyphenylenevinylene−polyamidoamine (PPV−PAMAM) hybrid dendrimers

Hybrid PAMAM dendrimers having a polyphenylenevinylene (PPV) core, PPV−PAMAM, of generations G1-G3 were synthesized and used in the preparation of Au NPs by Guerra and coworkers.[114] The synthesis of this hybrid dendrimer, called transgeden (TGD Gn), was accomplished starting from a poly(phenylenevinylene) (PPV) trialdehyde core as a π-conjugated building block. Following Michael addition and amidation reactions, G1-G3 PAMAM hybrid dendrimers were synthesized **(Scheme 2-13).** The TGD dendrimer molecules of generations Gn (n = 1−3) had a critical aggregation concentration (CAC), as determined using Nile Red, a fluorescein heterocyclic dye that fluoresces at 635 nm in organic media but is quenched by water. The fluorescence intensity of Nile Red is thus enhanced when it is encapsulated within a self-assembled hydrophobic structure, but decreases below the CAC. The inflection point in a plot of the fluorescence intensity vs. log concentration of the dendrimer corresponds to the CAC. Based on this technique, the CAC at pH 7.4 for the G1 TGD was found to be 144 ± 21 μM, while for G2 it was 17 ± 12 μM. It was not possible to determine a CAC for the G3 TGD, even though aggregation was evident from DLS measurements. It was therefore believed that aggregation was induced by hydrogen bonding for G3 TGD, due to its thicker PAMAM shell, and by π−π interactions for the smaller G1 and G2 molecules.

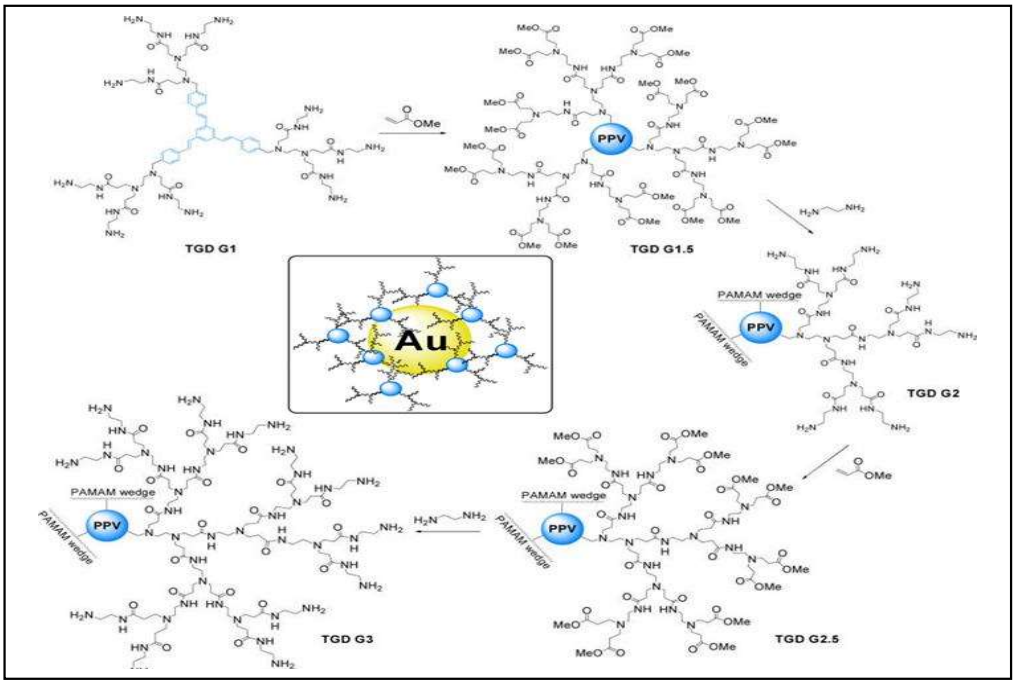

Scheme 2-13. Preparation of PPV−PAMAM Hybrid Dendrimers, and stabilization of Au NPs by multiple molecules (center). Adapted with permission from reference 114. Copyright 2013 American Chemical Society.

The preparation of Au NPs with the TGD dendrimers was similar to the PAMAM systems, except for the requirement of maintaining the concentration of the molecules well above their CAC (0.5 mM in water), and involving electrostatic complexation of the gold salt ($HAuCl_4$) by the exterior amino groups of TGD, followed by chemical reduction with $NaBH_4$. The NH_3^+:Au^{3+} molar ratio was an important factor controlling the stability and the average size of the NPs. At the minimum useful ratio (10:1) the NPs were stable for several months, while below that ratio the NPs precipitated quickly after reduction. For the G1 TGD, monodisperse spherical nanoparticles were obtained with a size depending on the NH_3^+:Au^{3+} ratio (**Table 2-5**). While pure G1 PAMAM dendrimers usually yield larger nanoparticles (> 5 nm), in this case only smaller NPs were found, which is indicative of the role of the PPV core of the hybrid dendrimer. Another reason that may account for the smaller size Au NPs is that

several dendrimer molecules can surround every NP (**Scheme 2-13**), as they were prepared at a concentration above the CAC. The gold nanoparticles are indeed stabilized within the interior of the supramolecular TGD G1 aggregates.

Table 2-5. DLS analysis of gold nanoparticles prepared with TGD dendrimers.[114]

Compound	**TGD G1**	**TGD G2**	**TGD G3**	**TGD G1d**	**TGD-$(Au)^0$ 10:1[c]**	**TGD-$(Au)^0$ 25:1[c]**	**TGD-$(Au)^0$ 50:1[c]**	**TGD-$(Au)^0$ 75:1[c]**
DLS (nm)	54±6[a]	48±10[a]	83±24[a]	57±12	8±2	11±2	86±15	79±21
Size (nm)[b]					3.7±0.9	3.2±0.9	3.5± 0.8	2.3±0.4

a) In 138 mM NaCl, 2.7 mM KCl and 10 mM PBS solutions. b) Size of Au NPs from TEM. c) NH_3^+:Au^{3+} ratio with 0.5 mM in water.

2.3.4.4 Polypropyleneimine (PPI) dendrimers

Murugan and Rangasamy investigated the two-step synthesis of G2 polypropyleneimine (PPI) dendrimer-supported Au NPs, bound to a cross-linked polystyrene-poly(4-vinylpyridine) matrix, and their catalytic activity in the reduction of 4-nitrophenol.[115] The insoluble PS-P4VP beads were swollen in THF and functionalized with carboxylic acid groups using chloroacetic acid in the presence of K_2CO_3. The carboxylic acid-functionalized PS-P4VP beads were then swollen in DMF and grafted with PPI dendrimers in the presence of dimethylaminopyridine to obtain PS-P4VP-PPI. That material was suspended in water followed by addition of aqueous $HAuCl_4$, and subsequent reduction with aqueous $NaBH_4$ yielded PS-P4VP-PPI-AuNPs (**Scheme 2-14**). The complexation of Au^{3+} by PPI was confirmed by the change in color of the polymer phase to yellow, while the color of the supernatant solution gradually faded. The rigid PPI-grafted polymer beads not only were useful for the stabilization of Au NPs, but also could be packed easily in a column for heterogeneous catalysis reactions. By this method, Au NPs with an average size of 15 nm in the PS-P4VP-PPI matrix were obtained based on high

resolution TEM and SEM analysis, that were useful for at least 10 cycles of catalytic reduction of 4-nitrophenol.

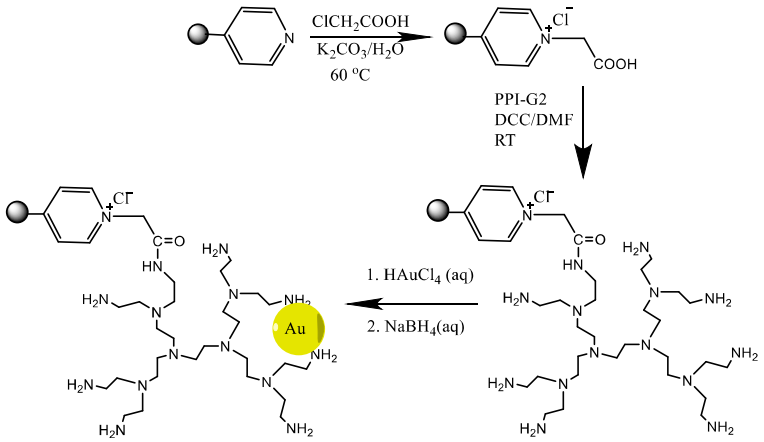

Scheme 2-14. Preparation of cross-linked insoluble poly(4-vinylpyridine) beads grafted with PPI-G2 dendrimer and preparation of heterogeneous NP catalysts viz., PS-P4VP-PPI-Au NPs. Adapted with permission from reference 115. Copyright 2010 Wiley Periodicals, Inc.

Prior to Murugan and Rangasamy, Pietsch and coworkers also used PPI dendrimers (G2-G5), after modification with a maltose shell, for the preparation of < 3 nm Au NPs in aqueous solutions, either in the presence or the absence of a reducing reagent ($NaBH_4$).[116] An $HAuCl_4$/dendrimer mixture in a 3:1 molar ratio, by reduction with $NaBH_4$, yielded 1.4 ± 0.7 nm and 1.1 ± 0.5 nm Au NPs in the G2 and G4 maltose-modified PPI dendrimers, respectively. The higher generation dendrimers again gave smaller particles with a narrower size distribution. No significant size and size distribution differences were observed among the higher generation (G3-G5) dendrimers, however. The NPs were also prepared without reducing agent, by simply mixing three equiv of $HAuCl_4$ with one equiv of glycodendrimers (G2-G5), to take advantage of the maltose shell as both reducing agent and stabilizer for the nanoparticles. It was suggested that the reduction of gold ions took place by oxidation of the hydroxyl groups of maltose, presumably converted to carbonyl groups.[117] This is in agreement with the more

recent work of Leiva et al.,[94] who reported the reduction of gold ions by the hydroxyl end groups of PCL-*b*-PEO-*b*-PCL copolymers. The results obtained with maltose-promoted reduction depended on the generation number of the dendrimers, as seen by the color and UV-vis response shown in **Figure 2-33** (right). The inset in the figure shows the range of colors obtained (blue for G2, violet for G3-G4 and red for G5). The absorption at longer wavelengths for the G2–G4 dendrimers was related to the formation of aggregates

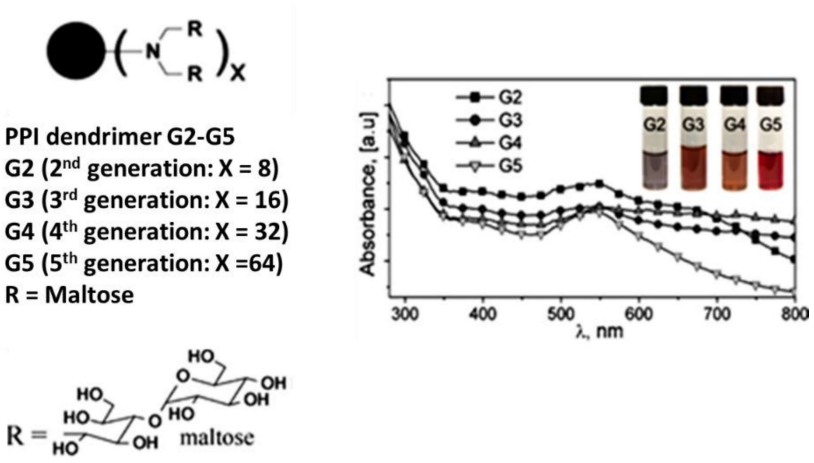

Figure 2-33. Schematic representation of maltose-modified G2–G5 PPI dendrimers (left), and UV–vis spectra for maltose modified PPI G2–G5-stabilized Au-nanoparticles after 28 h (right); the inset shows solutions containing the nanoparticles. Reprinted with permission from reference 116. Copyright 2009 Elsevier B.V.

In the case of the G2 dendrimer, the larger particles (9.2 ± 4.5 nm) obtained are indicative of inadequate protection of the NPs. For the G3 dendrimer, the Au NPs were slightly smaller and more uniform (7.4 ± 2.1 nm). Only the higher generation (G4 and G5) PPI dendrimers gave small NPs (< 3 nm), albeit with bimodal size distributions (**Figure 2-34**) at 1.2 ± 0.3 nm and 7.8 ± 2.4 nm for the G4 system, and at 1.3 ± 0.4 nm and a few large particles at 8.2 ± 6.4 nm for the G5 molecules. This is nevertheless indicative of more effective stabilization by the higher generation dendrimers. It was also

pointed out that unmodified PPI (without maltose) did not display auto-reductive properties. As compared to the NPs obtained with a reducing agent ($NaBH_4$), the auto-reduction nanoparticles were larger and less uniform in size.

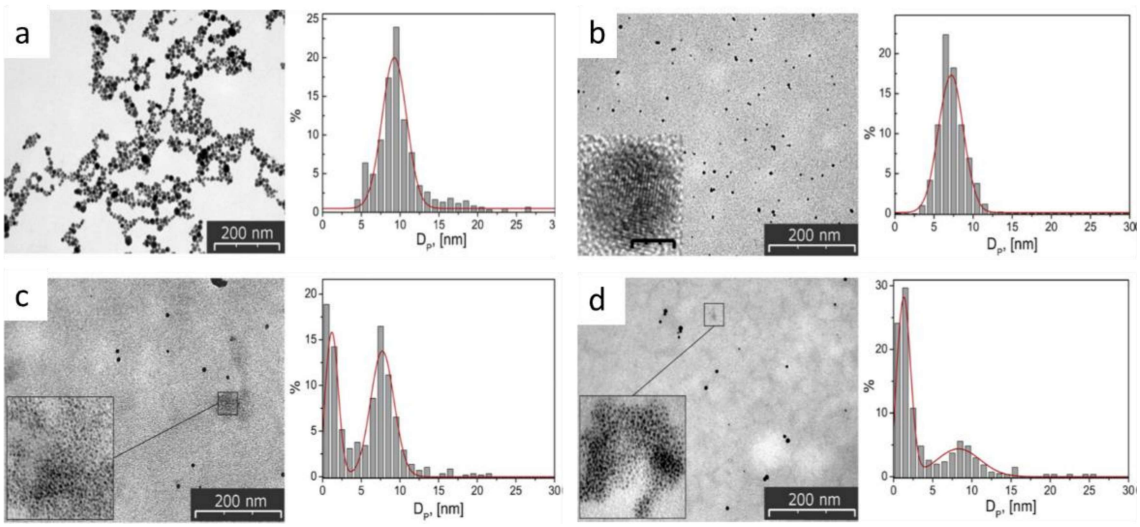

Figure 2-34. TEM images and particle size distribution histograms for Au NPs formed by reduction of $HAuCl_4$ with (a) G2, (b) G3, (c) G4 and (d) G5 maltose-modified PPI dendrimers. The inset in (b) shows the HR-TEM micrograph of an individual Au NP (scale bar 5 nm); the insets in (c) and (d) are magnifications of the indicated regions. Reprinted with permission from reference 116. Copyright 2009 Elsevier B.V.

2.3.4.5 Ethylene glycol-containing dendrimers

Dendrimers of generations G0-G2 derived from arene-type cores, and terminated with either 27, 81 or 243 triethylene glycol (TEG) tethers, were synthesized by click chemistry and employed for the preparation of Au NPs.[118] These dendrimers were complexed with a stoichiometric amount of $HAuCl_4$ with respect to the triazole groups, and reduced with $NaBH_4$ in methanol. The resulting Au NPs for a 1:1 $AuCl_4^+$:triazole ratio were characterized by UV-vis spectroscopy and TEM. The UV-vis spectrum had a band around 540 nm for the Au NPs prepared with the G0 dendrimers, whereas no SPR band was

observed for the G1 and G2 products. It was further confirmed by TEM (**Figure 2-35**) that the Au NPs prepared with the G0 template were larger (4.1 ± 0.5 nm), while the G1 and G2 dendrimers only gave 1.9 ± 0.4 nm and 1.8 ± 0.4 nm Au NPs, respectively, which explains the absence of SPR band in the G1 and G2 systems. Upon increasing the G1 dendrimer loading to 20 equiv of $HAuCl_4$ per triazole group, the size of the NPs increased from 1.9 ± 0.4 nm (for a 1:1 Au^{3+}:triazole ratio) to 11.3 ± 1 nm.

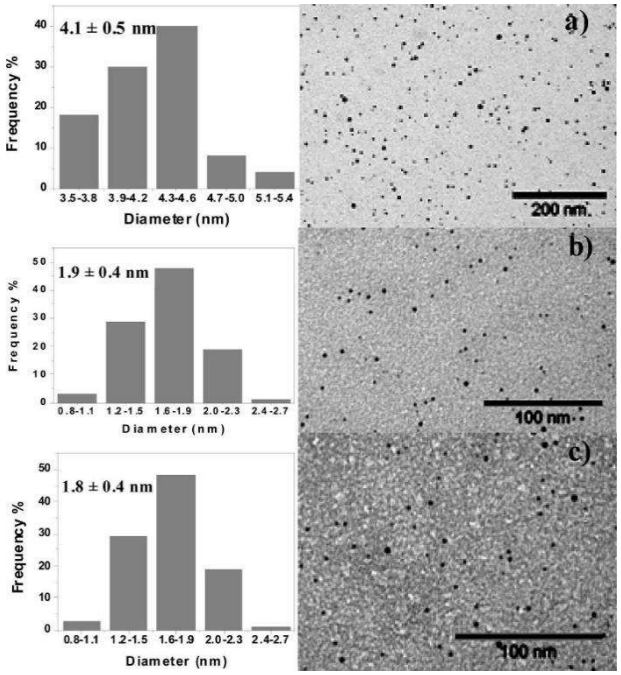

Figure 2-35. TEM images and size distributions for triethylene glycol dendrimer–Au NPs (a) G0-Au, (b) G1-Au and (c) G2-Au NPs. Reprinted with permission from reference 118. Copyrights 2010 American Chemical Society.

The authors claimed that for the stabilization of Au NPs in methanol, both the PEG and triazole groups in the dendrimers were crucial. This is because the Au^{3+} ions are coordinated by the intradendritic triazole ligands of the "click" dendrimers, and Au NP stabilization is provided by the adjacent TEGylated dendrons. Indeed, NPs prepared by a similar procedure but without PEG or triazole groups, or both, simply precipitated out of solution after the addition of $NaBH_4$ **(Table 2-6)** and were

larger than when using $NaBH_4$ with the triazole-TEG dendrimers and a stoichiometric ratio of $HAuCl_4$. This could be related to slow reduction leading to overlap of the nucleation and growth steps, since a significant time interval (3.5 h to 1 day) was required for complete reduction under these conditions. The suggested reduction mechanism by PEG was oxidative cleavage of the C-O bonds by the strong oxidizer Au^{3+}.[118]

Table 2-6. Growth of Au NPs stabilized by G0, G1 and G2 arene core TEG-terminated dendrimers in water without external reducing agent. Adapted with permission from reference 118. Copyright 2010 American Chemical Society

Dendrimer	Equiv Au per dendron	Au NP D_h (nm)
G0	1	23±0.5
G0	2	26±1.0
G0	5	32±1.0
G1	1	34±1.0
G1	2	36±0.5
G1	5	38±1.0
G2	1	36±0.5
G2	2	38±1.0
G2	5	42±1.0

Nona(ethylene glycol) or NEG dendrimers, containing 9 intradendritic triazole groups, with either 550 or 2000 PEG branches (abbreviated as DEND550 and DEND2000), were also synthesized by click chemistry (**Scheme 2-15**) and used for the synthesis of stable Au NPs in aqueous solutions.[119] The preparation of the NPs was achieved by the same method described for the TEG systems above. Varying the Au^{3+}/triazole (1:1, 5:1, 10:1, and 20:1) ratio influenced the size of the NPs, lower ratios giving smaller NPs (**Table 2-7**). This can be attributed to the fact that the $AuCl_4^-$ metal ion is coordinated with the triazole group when the ratio is low, so the Au NPs would be restricted inside the dendrimer (**Figure 2-36** left), leading to a smaller size and probably a narrower size distribution as well. For molar ratios

greater than one, Au NPs also formed outside the dendrimer since not all the $AuCl_4^-$ could be coordinated by the triazole, leading to larger NPs. Stabilization of the larger NPs in this case should involve several dendrimer molecules (**Figure 2-36** right).

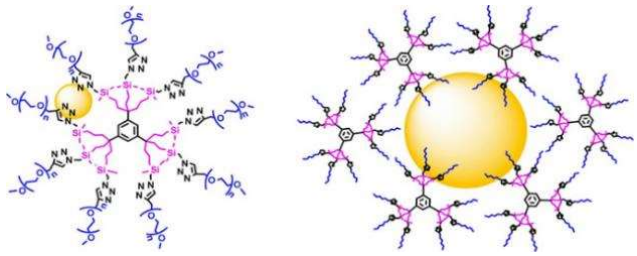

Figure 2-36. Dendrimer-stabilized small Au NPs by encapsulation (left), and large Au NP stabilization by several dendrimers (right). Reprinted with permission from reference 119. Copyright 2014 American Chemical Society.

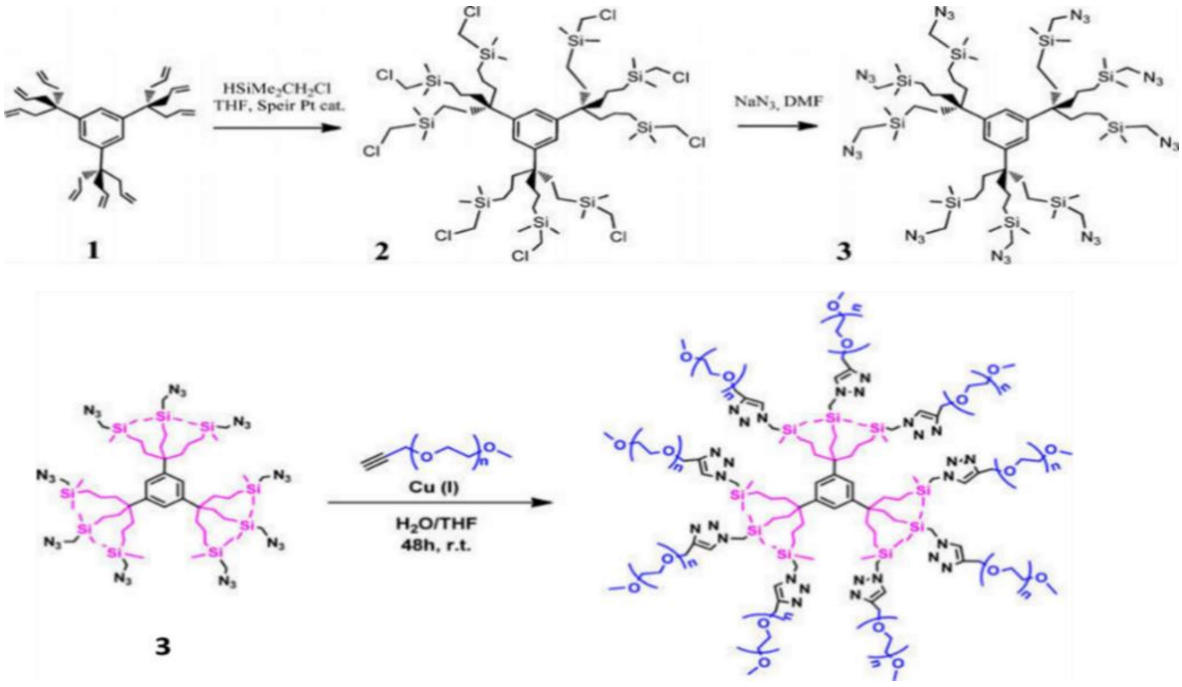

Scheme 2-15. Synthesis of PEGylated dendrimers by "Click" chemistry. Adapted with permission from reference 119. Copyright 2014 American Chemical Society.

The PEG tether length clearly influenced the size of the NPs: The Au NPs prepared with the PEG-2000 tethers were smaller (1.8 nm for Au-DEND2000-1) than when using the corresponding PEG-500 tethers (3.2 nm for Au-DEND550-1). This may be related to the mobility of Au atoms and very small Au NPs, whereby mobility should be more restricted by the longer PEG-2000 tethers. These NEG triazole dendrimer-stabilized Au NPs were successfully employed as catalysts for the reduction of *p*-nitrophenol to *p*-aminophenol.

Table 2-7. TEM and SPR data for NEG dendrimer-stabilized Au NPs. Reprinted with permission from reference 119. Copyright 2014 American Chemical Society.

Au NP	SPR (nm)	TEM (d, nm)	Au atoms/NP
Au-DEND550-1a	516	3.2	1000
Au-DEND550-5a	535	7.3	12 000
Au-DEND550-10 a	537	9	22 000
Au-DEND550-20 a	538	12	53 000
Au-DEND2000-1 a	-	1.8	180
Au-DEND2000-5 a	526	5.7	5700
Au-DEND2000-10 a	529	8.7	20 200
Au-DEND2000-20 a	538	11.4	45 000

a) *The last digit represents the $AuCl_4^-$/triazole ratio.*

2.3.4.6 Oligothia dendrimers

The oligothia dendrimers (S_6G0, S_6G1, and S_9G1) shown in **Figure 2-37** were utilized by D'Aléo and coworkers to prepare stable Au NPs by the Brust-Shiffrin method. The results obtained were compared with other sulfur-containing ligands ($Dend_3S$, SH_6 and MS_6, in **Figure 2-37**) in terms of performance for the formation and the stabilization of Au NPs under similar conditions.[120] One equiv of $HAuCl_4$ per sulfur atom was used. The NPs obtained with the lower generation dendrimer Au/S_6G0 (2.8 ± 1.1 nm) had a high size dispersity and were unstable, while those obtained with S_6G1 had two populations with

diameters of 1.8 ± 0.6 and 3.1 ± 0.2 nm. The S_9G1 dendrimers also yielded NPs with a high polydispersity, but these were stable for several months and smaller (1.9 ± 0.9 nm) than those derived from both S_6G0 and S_6G1. This suggests that the size of the NPs not only depended on the dendrimer generation, but also on the branching type for these systems.

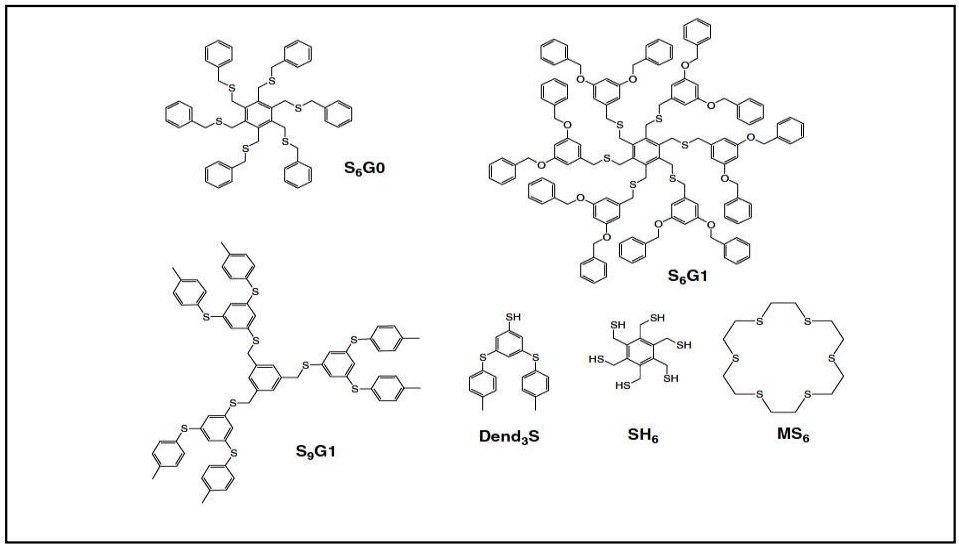

Figure 2-37. Oligothia dendrimers and ligand structures with acronyms. Reprinted with permission from reference 120. Copyright 2004 WILEY-VCH Verlag GmbH &Co.

The use of the small molecule ligands S_6H and MS_6 for the preparation of Au NPs was investigated for comparison with S_6G1, due to the similar number of sulfur atoms in their structure. Interestingly, S_6H produced very few 3.0 ± 1.2 nm Au NPs and many large Au clusters, which illustrates that even though S_6H (serving as core for S_6G1) has the same number of sulfur atoms as S_6G1, it behaves differently because of the lack of branching. When MS_6 was used no particles were formed, which suggests insufficient stabilization by the weakly binding cyclic aliphatic thioether.

2.3.4.7 Tetrahedron DNA-based dendrimers

A step-by-step approach was employed to synthesize tetrahedron DNA dendrimers, using their sticky end-segment to hybridize with other tetrahedron DNA units. Generation zero (TG_0), first generation (TG_1) and second generation (TG_2) tetrahedron DNA dendrimers (**Figure 2-38**), with diameters of 11.4, 34.8 and 59.6 nm, respectively, were prepared by this step-by-step process. With systematically designed DNA building blocks, hybridization was only allowed between the sticky ends of the TG_n substrate and the building blocks to obtain the next generation, TG_{n+1}. The tetrahedron DNA dendrimers were investigated to encapsulate gold nanoparticles, because the tetrahedron DNA building blocks used to construct the dendrimers have a cavity able to accommodate approximately 2.6 nm diameter spheres.[109]

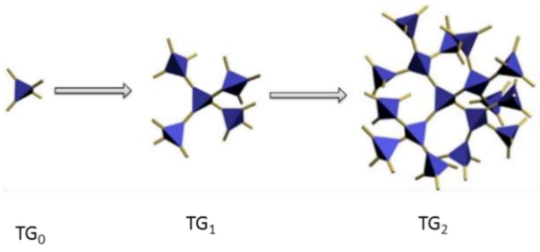

Figure 2-38. Step-by-step assembly of tetrahedron DNA dendrimers. Reprinted with permission from reference 109. Copyrights 2014 Elsevier Ltd.

Au NPs with a diameter of 3 nm were prepared separately and then encapsulated inside the tetrahedron DNA building blocks, prior to the assembly into dendritic structures. Since the Au NPs were encapsulated within the tetrahedron DNA used for the step-by-step synthesis of tetrahedron DNA dendrimers, the TG_n dendrimers already contained encapsulated Au NPs, as shown in the TEM images of **Figure 2-39**.

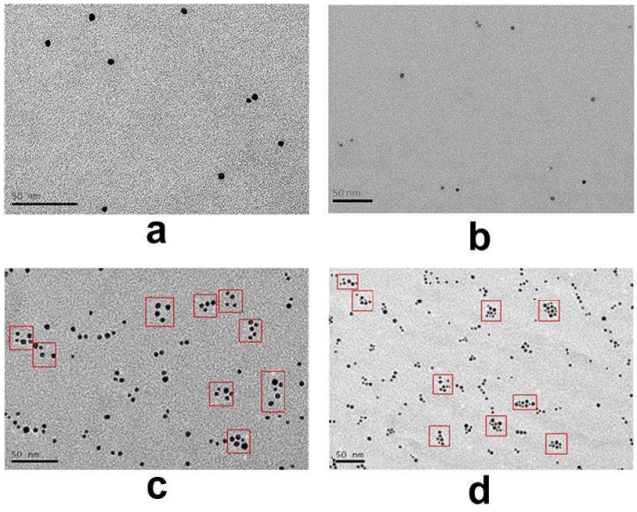

Figure 2-39. TEM images for gold nanoparticles (a) without stabilizer and (b)-(d) encapsulated in TG_0, TG_1 and TG_2 DNA-based dendrimers, respectively (scale bars are 50 nm). Reprinted with permission from reference 109. Copyright 2014 Elsevier Ltd.

2.3.5 Hyperbranched polymer stabilizers for MNPs

The examples reviewed so far demonstrated how dendrimers can be used as nanoreactors to stabilize and control the growth of MNPs, by complexation of the metal ions within or along the periphery of the dendrimers, or through multimolecular dendrimer assemblies. One limitation of dendrimers is their complicated synthesis, involving multi-step protection, condensation and deprotection reaction cycles.[114] In contrast, the synthesis of hyperbranched polymers typically involves one-pot condensation reactions of unprotected AB_n-type ($n \geq 2$) monomers, or alternately the addition polymerization of AB* inimers (containing both a B* initiator fragment and a vinyl group A within the molecule, serving as monomer). These synthetic features usually result in random branching and broader molecular weight distributions than for dendrimers.[121] As compared with perfectly branched monodisperse, but costly and time-consuming dendrimer syntheses,[121-124] hyperbranched polymers are more readily available but

also have a molecular structure and properties comparable to dendrimers in many cases, and are thus able to stabilize metallic nanoparticles.

2.3.5.1 Polyamidoamine (HYPAM) hyperbranched polymers

Hyperbranched HYPAM, chemically analogous to the PAMAM dendrimers, was synthesized by Pérignon and others in a single-step reaction of a hexaester (MA6-TREN) with a triamine (**Scheme 2-16**). The generation number attained, analogous to the PAMAM dendrimers, depended on the molar ratio of triamine to hexaester (MA6-TREN) used. For example, a 10:1 ratio gave HYPAM4, similar to G4 PAMAM, while a 8:1 ratio yielded a product (HYPAM5), close to G5 PAMAM.

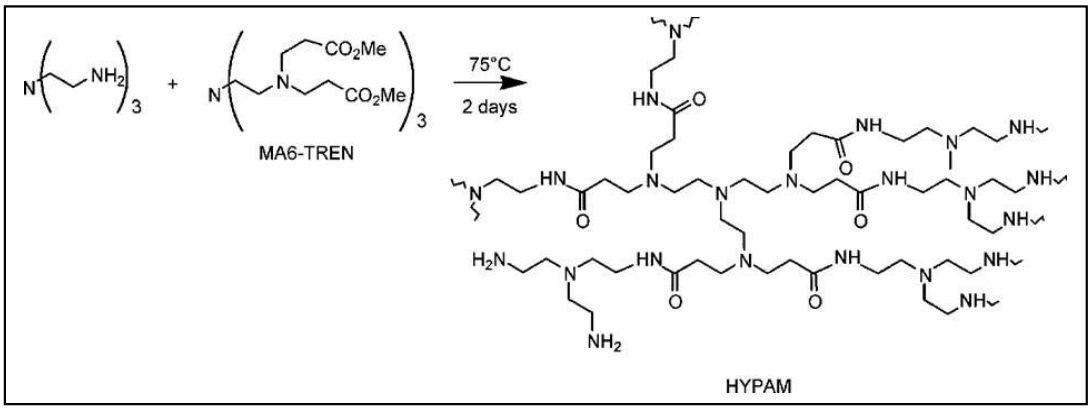

Scheme 2-16. Synthesis and structure of HYPAM hyperbranched polymers. Reprinted with permission from references 122 and 123. Copyright 2007 American Chemical Society.

HYPAM4 and HYPAM5 were employed for the synthesis of Au NPs by reduction with $NaBH_4$.[122] The maximum loading capacity of HYPAM4 for Au^{3+} was found to be 150 ions per molecule, which is much higher than for the analogous PAMAM4 dendrimers (50 ions). This was attributed to the open structure of the hyperbranched polymers as compared to their dendrimer analogues. This allowed the complexation of a larger number of $HAuCl_4$ molecules by the internal functional groups of the

hyperbranched structures, and thus a higher loading level, even though the molar mass was quite comparable for both systems.

The influence of the amount of $NaBH_4$ vs. gold ions in the reduction step used was also investigated. A large excess of reducing agent only led to an insignificant decrease in NP size: For a $NaBH_4/HAuCl_4$ ratio increasing from 1 to 5, the average size of the nanoparticles decreased from 5.6 ± 1.6 nm to 4.0 ± 1.0 nm. Larger amounts of reducing reagent made the reaction more difficult to control due to changes in pH, and consequently changes in the protonation level of the stabilizer. An increase in the $HAuCl_4$/HYPAM4 ratio to ≥ 150 also caused an increase in the size of the nanoparticles (**Figure 2-40**) for the same amount of $NaBH_4$ used. This was attributed to the rapid formation of gold nanoparticles outside the hyperbranched structures, which induced aggregation**.**

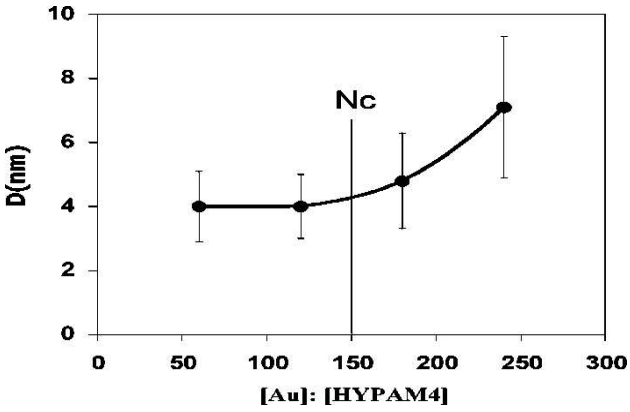

Figure 2-40. Mean diameter of Au NPs formed by reduction with $NaBH_4$ (5 equiv) as a function of the $HAuCl_4$/polymer ratio for $HYPAM_4$. Reprinted with permission from reference 122. Copyright 2007 American Chemical Society.

When the amino functionalities were transformed into gluconic amide groups (HYPAM*x*G structure), Au NPs formed without external reducing reagents due to the presence of reducing hydroxyl groups. This is again in agreement with the report by Leiva et al.,[94] where the reduction of gold ions was observed by oxidation of hydroxyl end groups of PCL3-*b*-PEO45-*b*-PCL3 copolymers, and by

Pietsch and coworkers[116] for maltose-containing dendrimers. The nanoparticles obtained in this case were again larger (15 nm) and were reported to have broader size distributions.

2.3.5.2 Polyester-polyethyleneimine-poly(ethylene glycol) (Hx-PEI-PEG) hyperbranched polymers

Unique amphiphilic hyperbranched polymer structures (Hx-PEI-PEG) were synthesized by conjugating poly(ethylene glycol) (PEG) chains with aliphatic hyperbranched polyesters (Hx), after converting their terminal hydroxyl groups to carboxyl with succinic anhydride, and then grafting low-molecular-weight polyethyleneimine (PEI) segments by click chemistry (**Scheme 2-17**). This hyperbranched polymer was successfully used to support Au NPs,[125] at loading levels (ratio of nitrogen groups to $AuCl_4^-$) of 0.25, 1, 5, and 10. The gold ions can interact with the PEI chains, forming an inner layer between the hyperbranched polyester core and the PEG shell components. According to Dai et al.,[125] the higher concentration of amino groups in Hx-PEI-PEG enabled the reduction of the gold ions. This was evident from the red color of the solutions observed after standing for one hour, as well as from the characteristic SPR peak observed above 500 nm. The reducing ability of H40-PEI-PEG was pH-dependent however, with better reduction at lower pH (4). At lower pH, the amino groups are protonated and have higher electron donating ability for Au ion reduction than the non-protonated amino groups at high pH (10). However since the rate of self-reduction was low at room temperature, the reduction was facilitated by the addition of $NaBH_4$. The mean particle diameter for H40-PEI-PEG-stabilized Au NPs obtained with $NaBH_4$ was found to be 8.1 ± 1.4 nm, 7.6 ± 0.9 nm and 6.9 ± 0.8 nm at pH 4.0, 7.0 and 10.0, respectively. The NP size therefore decreased as the pH was increased, albeit the decreases observed are rather insignificant if the uncertainty limits are considered, and the NP size also became more uniform. The more uniform size distribution was explained as follows: At the lower pH (4.0), autoreduction by H40-PEI-PEG may have slowly produced Au seeds, which grew from the residual Au ions after the addition of $NaBH_4$ to yield the Au NPs. At pH 10.0, however, Au seed

production would be much slower, such that the Au ions would only be reduced to Au NPs upon addition of $NaBH_4$. The smaller Au NPs had superior catalytic activity in the reduction of 4-nitrophenol. Lower generations of Hx-PEI-PEG, such as H20-PEI-PEG and H30-PEI-PEG, were nevertheless unable to stabilize Au NPs and only yielded black precipitates. This could be due to their relatively open structure, as these only had 16 or 32 hydroxyl groups within their polyester core, as compared with 64 hydroxyl groups for H40-PEI-PEG. This would favor leakage of the Au NPs out of the hyperbranched scaffold, and subsequent aggregation.

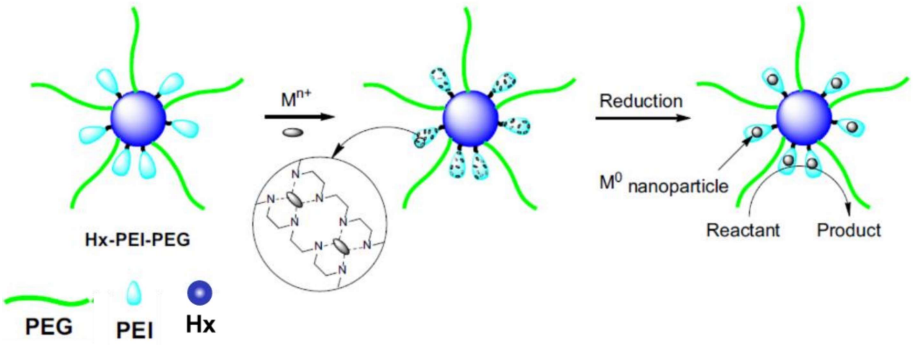

Scheme 2-17. Formation and catalytic reaction of hyperbranched Hx-PEI-PEG-stabilized Au NPs. Reprinted with permission from reference 125. Copyright 2016 Elsevier Inc.

2.3.5.3 Titania/polyglycidol hyperbranched nanohybrids

Hyperbranched polyglycidol (HBP) (**Figure 2-41**), containing many hydroxyl groups and polyether segments, was synthesized via anionic ring-opening polymerization. A high branching functionality was achieved by slow addition of glycidol to trimethylolpropane, partially (10%) deprotonated with potassium methoxide, over 12 h at 95 °C. This polymer was then reacted with titanium tetraisopropoxide (TTIP) to produce tunable titania/HBP hybrid nanostructures. These were employed by Li and coworkers[126] to encapsulate Au NPs (< 5 nm). This HBP served as capping agent for TTIP through the oxygen atoms from adjacent hydroxyl groups, while the ether segments were able to

coordinate with titanium. The resulting titania/HBP particles exhibited tunable morphologies including solid spheres, capsules and tubes, depending on the TTIP feeding method and the amount of water used. Solid and spherical titania/HBP particles were obtained by one-shot injection of 97 % TTIP (0.25, 0.20, and 0.15 mL) into 5 mL of an absolute ethanol solution of HBP (0.05 g/mL). Slow addition of the TTIP yielded hollow spherical titania/HBP particles. The addition of small amount of water (2.5-5 μL) into the above TTIP/HBP mixture also provided well-defined donut-like structures, while increasing the water content (10 μL) yielded tube-shaped hollow structures (**Figure 2-42**).

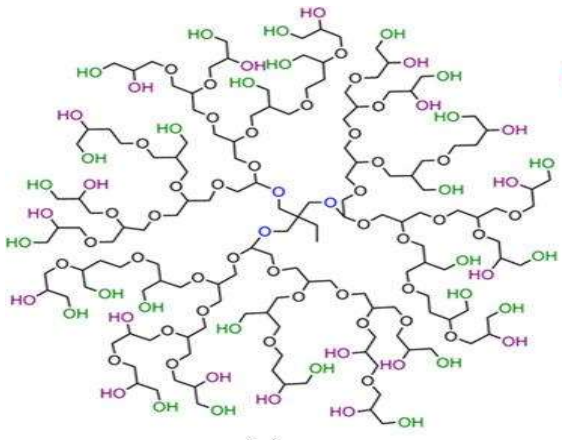

Figure 2-41. Hyperbranched polyglycidol architecture. Reprinted with permission from reference 126. Copyright 2010 Springer Science+Business Media B.V.

It was demonstrated that the size of the spherical titania/HBP particles could be decreased by decreasing the amount of TIPP in the reaction. The injection of 0.25, 0.20, and 0.15 mL TTIP (97 %) solution resulted in 420, 220, and 55 nm particles, respectively. These titania/HBP spherical particles were centrifuged and redispersed in water before mixing with an aqueous solution of $HAuCl_4$. The reduction of $AuCl_4^-$ was accomplished with the hydroxyl groups in the titania/HBP particles. The *in situ* formation of Au NPs with an average diameter < 5 nm was evident from TEM images. These Au

NPs, stabilized by the titania/HBP hybrid polymer structures, displayed catalytic activity in the reduction of 4-nitrophenol.

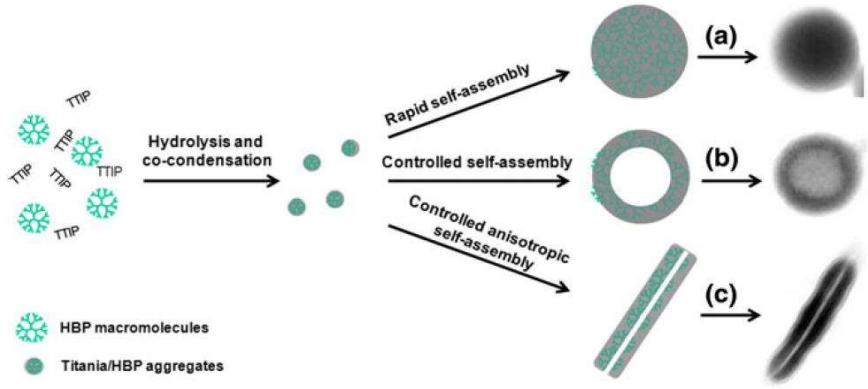

Figure 2-42. Formation of titania/HBP nanohybrids with controllable morphologies in a sol–gel process: (a) solid spheres, (b) hollow spheres and (c) nanotubes. Reprinted with permission from reference 126. Copyright 2010 Springer Science+Business Media B.V.

2.3.5.4 Hyperbranched polyglycerol with an alkyne core (HPG)

An emulsion polymerization technique was developed to synthesize both low (< 10 000 g/mol) and high (> 50 000 g/mol) molecular weight alkyne-core HPG polymers. Two methods were designed to produce these alkyne-functionalized HPGs: One method was by treating a diglyme solution of the triol initiator **1** (**Scheme 2-18**) with 10 mol% of sodium hydride, followed by slow addition of glycidol to produce HPG **2a**. The second method was using propargyl alcohol as an alkyne source to synthesize HPG **2b** in one step.

These HPGs were linked with different compounds (azide **7**, biotin azide **3**, and fluorescein azide **5**) through click chemistry (**Scheme 2-19**) via the alkyne focal point. The amine-functionalized HPG **8** was used to coat 13.5 ± 1.1 nm citrate-capped gold NPs through ligand exchange, which enhanced the stability of the NPs via steric protection.[127]

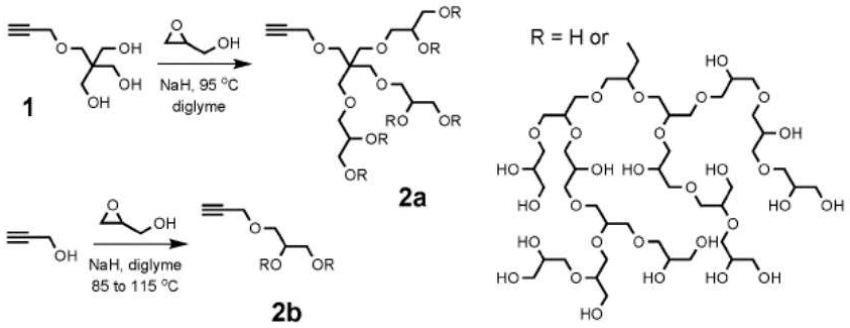

Scheme 2-18. Synthesis of alkyne-functionalized hyperbranched polymers HPG 2a and 2b. The structure of HPG is only representative. Reprinted with permission from reference 127. Copyright 2011 the Royal Society of Chemistry.

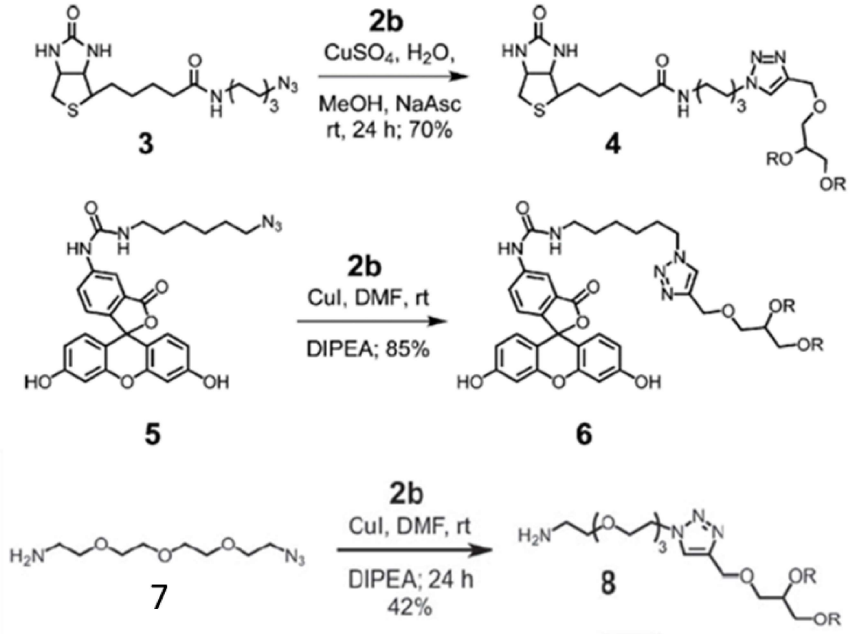

Scheme 2-19. Click chemistry with HPG. Adapted with permission from reference 127. Copyright 2011 the Royal Society of Chemistry.

2.3.6 Dendrigraft (arborescent) polymer stabilizers for MNP

As discussed so far, a number of dendrimers and hyperbranched polymers have been used for the preparation of MNPs. The limitations associated with dendrimers include their difficult synthesis and the slow rate of molecular weight increase per generation.[104] While high molecular weight hyperbranched polymers can be obtained in simple one-pot reactions,[128] the lack of control over their molecular weight and molecular weight distribution limits their applications as advanced soft nanomaterials.[102]

Dendrigraft (arborescent) polymers represent an interesting compromise to avoid the challenges presented by both dendrimers and hyperbranched polymers. The concept of dendrigraft branching was introduced for the first time independently in 1991 by two groups. Gauthier and Möller synthesized dendritic graft polystyrene, which they called arborescent (tree-like) structures,[104] while Tomalia et al. synthesized dendritic graft polyethyleneimine (PEI) identified as comb-burst polymers.[129] Both synthetic strategies are based on successive grafting reactions starting from a linear polymer substrate and macromolecular building blocks to produce branched polymers. Cycles of substrate functionalization and grafting reactions lead to successive generations of dendrigraft polymers. Grafting a suitably functionalized linear polymer with linear chains thus gives a comb-branched or generation zero (G0) structure. The next functionalization and grafting reactions yield a G1 polymer, and so on. The main advantages of dendrigraft polymer syntheses are that high molecular weights are attained in few reaction steps, and the molecules have relatively well-defined structures ($M_w/M_n < 1.10$ typically). The architecture of dendrigraft polymers can be controlled by varying either the branching density or the molecular weight of the branches.[104] While comb-branched graft copolymers of polystyrene-*graft*-poly(2-vinylpyridine) (PS-*g*-P2VP)[130] and polystyrene-*graft*-poly(4-vinylpyridine) (PS-*g*-P4VP)[131] were synthesized a long time ago, their branching functionality and molecular weight

was very limited as compared with arborescent polystyrene-*graft*-poly(2-vinylpyridine) copolymer systems.[132,133]

Arborescent polystyrene-*graft*-[poly(2-vinylpyridine)-*block*-polystyrene] copolymers with a core–shell–corona (CSC) structure (**Scheme 2-20**), in particular, were used as templates for the preparation of gold nanoparticles.[41] Functionalization of a branched PS substrate with acetyl functional groups, followed by grafting with "living" polystyrene-*block*-poly(2-vinylpyridine) anions, provided the CSC structures. The inner poly(2-vinylpyridine) (P2VP) shell of these tree-like macromolecules was used to complex $HAuCl_4$ as discussed for the other dendritic systems. These unimolecular micelles are interesting as templates in comparison to micelles formed by surfactants and linear block copolymers because they have no CMC, and also a very rigid structure. Variations in the molecular weight of the side chain building blocks and the number of grafting cycles provides control over the characteristics of the arborescent templates such as the core size, chain flexibility, layer thickness, etc. over a wider range than achievable through the self-assembly of block copolymers or with hyperbranched polymers.

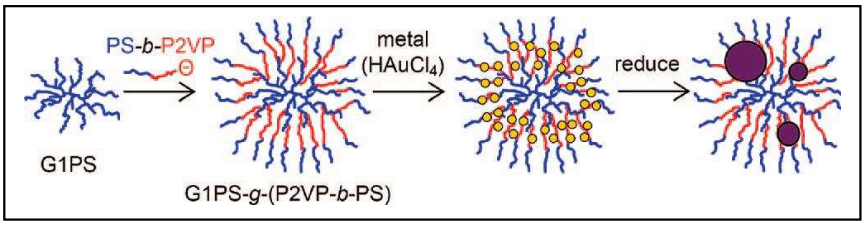

Scheme 2-20. G2 arborescent copolymer template synthesis, $HAuCl_4^-$ loading and reduction. Reprinted with permission from reference 41. Copyright 2008 American Chemical Society.

Arborescent copolymer templates PS-*g*-P2VP-*b*-PS (G0) and G1PS-*g*-P2VP-*b*-PS (G2), with 108 and 192 styrene units in the block copolymer chain segments forming their corona, respectively, were used for the synthesis of stable Au NPs by Dockendorff et al.[41] While $HAuCl_4$ was successfully loaded in both copolymers, the metal distribution within the templates appeared to be different: The metal

distribution in the G2 copolymer was denser on the edges than the center in TEM pictures, suggesting a hollow core morphology, while it was uniform for the G0 template (**Figure 2-43**).

Neither the loading level nor the generation number appeared to influence the diameter of the Au NPs obtained after hydrazine reduction, however. This is obviously different from the observations for other dendritic systems, where both the loading level and the generation number influenced the size of the Au NPs, but more generally for Au NPs stabilized by surfactants,[58] linear polymers,[62] block copolymer micelles,[40] star-block copolymer dendrimers[114] and hyperbranched polymers,[122] for which smaller Au NPs were observed when the ratio of $HAuCl_4$ to stabilizer was lowered. The generation number of PAMAM dendrimers[103] and Hx-PEI-PEG hyperbranched[124] polymers also influenced the characteristics of Au NPs, with smaller size particles obtained for higher generation templates. In the case of arborescent copolymers, only the hydrazine to $HAuCl_4$ ratio influenced the size and size distribution of the NPs, with smaller and more stable NPs obtained at higher hydrazine to $HAuCl_4$ ratios.

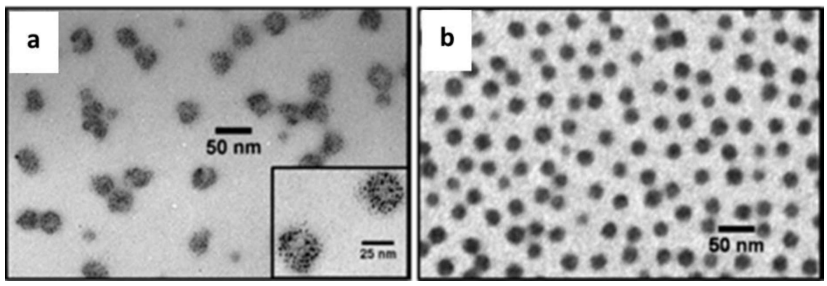

Figure 2-43. TEM micrographs for G2 (a) and G0 (b) templates loaded with 0.25 and 0.50 equiv $HAuCl_4$ per 2VP unit, respectively. Reprinted with permission from reference 41. Copyright 2008 American Chemical Society.

More recently, Nguyen et al. also reported the formation of arborescent polyion complex (PIC) micelles by self-assembly of an arborescent polystyrene-*graft*-poly(2-vinylpyridine) (G0PS-*g*-P2VP) copolymer with a poly(acrylic acid)-*block*-poly(2-hydroxyethyl acrylate) (PAA-*b*-PHEA) double-

hydrophilic block copolymer in aqueous media.[134] The arborescent PIC micelles were employed for the preparation of different metallic nanoparticles including Pd[135] and Fe_3O_4.[134] Details on the synthesis and the characterization of these PIC structures are provided in Chapter 3.

2.4 Conclusions

Among metallic nanoparticles gold is likely the most widely investigated system,[58] and different applications have been developed for these materials due to their unusual optical properties, size-dependent electrochemistry, and high chemical stability.[31] Many methods yielded stable gold nanoparticles with a controllable size and a uniform size distribution. The stabilizers reviewed for the preparation of gold nanoparticles in this Chapter included small molecule surfactants, homopolymers, self-assembled block copolymer reverse micelles, star-block copolymers, dendrimers, hyperbranched and arborescent copolymers. The stabilizing ability of these systems depends on numerous factors such as the molecular architecture, the availability of metal-binding functional groups, the molecular weight and the solvency conditions used. The characteristics of the nanoparticles obtained likewise depend on the specific stabilizer type and concentration used, but also on the presence of additives, reducing agents, the metal loading level, and the experimental conditions employed. Different synthetic strategies allowed the generation of nanostructures with characteristics desirable for specific applications.

Chapter 3: Synthesis and Characterization of Arborescent Polystyrene-*graft*-poly(2-vinylpyridine) and Poly(acrylic acid)-*block*-polystyrene Copolymers

3.1 Overview

One of the main goals of this Ph.D. project was the development of a convenient procedure for the preparation of arborescent core–shell–corona structures, through the self-assembly of arborescent polystyrene-*graft*-poly(2-vinylpyridine) (PS-*g*-P2VP) copolymers with block copolymers of poly(acrylic acid) and polystyrene (PAA-*b*-PS). While arborescent PS-*g*-P2VP copolymers derived from G0 and G1 arborescent polystyrene substrates (G0PS-*g*-P2VP30K and G1PS-*g*-P2VP30K, respectively) were already available, copolymers incorporating G2 (G2PS-*g*-P2VP13K) and G3 (G3PS-*g*-P2VP15K) polystyrene cores were also synthetized by established procedures based upon anionic polymerization and grafting. The synthesis of a series of PAA-*b*-PS copolymers was achieved by atom transfer radical polymerization (ATRP), starting with the preparation of short poly(*tert*-butyl acrylate) (P*t*BA) macroinitiators having number-average degrees of polymerization X_n = 10-17 and narrow molecular weight distributions ($M_w/M_n \leq 1.13$). The macroinitiator chains were then extended with longer (X_n = 85-395) polystyrene segments to obtain block copolymers with relatively narrow molecular weight distributions ($M_w/M_n \leq 1.26$). Hydrolysis of the *tert*-butyl ester group yielded the desired PAA-*b*-PS copolymers. All the materials synthesized for the self-assembly work were characterized by size exclusion chromatography (SEC) and proton nuclear magnetic resonance (^{1}H NMR) spectroscopy analysis, to confirm the success of the methods used at each step of the synthesis.

3.2 Introduction

Synthetic polymers can be classified, on the basis of their chain architecture, as linear, cross-linked, branched, and dendritic structures. Over the past three decades, dendritic polymers have attracted much attention as nanomaterials.[1] The dendritic polymers can be further subdivided, depending on the synthetic strategy used and the resulting architecture, into dendrimers, hyperbranched and dendrigraft polymers.

Dendrimers are characterized by a very high concentration of surface functional groups having a similar microenvironment.[2] Their structure consists in strictly controlled repeating patterns leading to macromolecules with a well-defined size, shape and topology. The synthesis of dendrimers typically involves AB_2-type monomers as building blocks with cycles of protection, condensation, and deprotection reaction steps.[3] Though synthetically more challenging, control over the structure, the physical and chemical properties of dendrimers can be achieved by changing the core type, the monomer branching functionality, and the terminal functional groups used in the molecules. Dendrimers can be prepared with very narrow molecular weight distributions (MWDs), with polydispersity values $PDI = M_w/M_n \leq 1.01$, but synthesizing high molecular weight dendrimers requires many reaction steps and purification cycles.[1-3]

Hyperbranched polymers, the second class of dendritic architectures, can be synthesized in much simpler one-pot reactions. Either condensation reactions of unprotected AB_n-type ($n \geq 2$) monomers, or addition reactions of AB* inimers and vinyl monomers can serve in the preparation of these materials. These synthetic approaches both lead to random branching and broader molecular weight distributions in comparison to dendrimers.[4]

The third class of dendritic architectures is dendrigraft (or arborescent) polymers. Dendrigraft branching was introduced for the first time in 1991, simultaneously in the form of arborescent (tree-like) polystyrene (PS)[5] and comb-burst polyethyleneimine (PEI).[6,7] In both cases, the synthetic strategy was based upon successive cycles of substrate functionalization and grafting reactions using polymer chains, starting from a linear polymer substrate. This synthetic strategy combines features from both dendrimers and hyperbranched polymers. Like dendrimers, it relies upon generation-based growth, but the building blocks are polymer chains rather than small molecules, and the grafting process is random, similarly to hyperbranched polymers. Consequently, the architecture is not as well-defined as for dendrimers, but the MWD remains narrow ($M_w/M_n \approx 1.1$). One significant advantage of arborescent

polymer syntheses is that a high molecular weight can be attained in a few reaction steps, so fewer reaction and purification steps are required to obtain high molecular weight polymers. The structure of arborescent polymers can be controlled by varying either the branching density or the molecular weight of the side chains.[5]

The strategy most commonly used for the preparation of arborescent polymers involved successive cycles of polymeric substrate functionalization and grafting with "living" linear polymer chains obtained by anionic polymerization. The anionic methodology was used to synthesize arborescent homopolymers and copolymers using either chloromethyl, bromomethyl, epoxide or acetyl coupling sites. Arborescent styrene homopolymers were thus obtained using chloromethylated[5] or acetylated[8,9] polystyrene and epoxydized poly(styrene-*co*-*p*-(3-butenyl)styrene)[10] substrates. Copolymers were obtained by grafting suitably functionalized arborescent polystyrene substrates with poly(*tert*-butyl methacrylate),[11] polyisoprene[12,13] or poly(2-vinylpyridine)[14,15] side chains. More recently, through a comparable living anionic *grafting onto* strategy but involving many steps, PS grafted with PMMA, and poly((2-methoxyethoxy)ethyl methacrylate) graft polymers were synthesized.[16]

As early as 1979, comb-branched graft copolymers of PS-*g*-P2VP[17] and PS-*g*-P4VP[18] were synthesized from partly chloromethylated polystyrene, but with limited branching functionalities and molecular weights. The anionic *grafting onto* method was later improved by Gauthier and others to synthesize high molecular weight, high branching functionality, and low polydispersity ($M_w/M_n \leq 1.1$) arborescent PS-*g*-P2VP copolymers from either chloromethylated[15] or acetylated[14] PS substrates. Moreover, arborescent polystyrene-*g*-[poly(2-vinylpyridine)-*b*-polystyrene] (PS-*g*-P2VP-*b*-PS) core–shell–corona copolymers were also synthesized from acetylated PS substrates.[19] This latter technique was applied to the synthesis of the additional arborescent copolymer samples needed for the current self-assembly investigation.

3.3 Experimental procedures

3.3.1 Arborescent copolymers

The arborescent copolymer samples used in this investigation were G0PS-*g*-P2VP30K (generation G1 overall), G1PS-*g*-P2VP30K (G2 overall), G2PS-*g*-P2VP13K (G3 overall), and G3PS-*g*-P2VP15K (G4 overall). These all contained polystyrene cores derived from 5000 g/mol linear polystyrene segments, functionalized and grafted sequentially starting from a 5000 g/mol linear PS substrate in 1-4 reaction cycles for the G0PS-G3PS substrates, respectively. This was followed by functionalization and grafting with 30000 g/mol P2VP side chains for the G1 and G2 copolymers, 13000 g/mol and 15000 g/mol for the G3 and G4 copolymers, respectively. In this context, a sample identified as G2PS-*g*-P2VP13K, for example, refers to a polymer with a G2PS core and 13000 g/mol P2VP side chains, and is also referred to as a G3 arborescent copolymer substrate (ACPS) in the self-assembly process.

Munam and Gauthier synthesized the G1 and G2 arborescent copolymers used in this study.[20,21] The G3 and G4 arborescent copolymers were newly synthesized as described briefly in the following sections. All the ACPSs were used for the preparation of arborescent copolymer complexes by self-assembly, metal loading and reduction, as discussed in the subsequent Chapters.

3.3.2 Reagent purification

***For anionic grafting reaction*:** Styrene (Sigma-Aldrich, for synthesis ≥ 99%, stabilized with ≤ 15 ppm 4-*tert*-butylcatechol) was first washed in a separatory funnel with 5% sodium hydroxide, and three times with distilled water to remove the inhibitor. It was then stirred overnight with calcium hydride powder (CaH_2, Sigma-Aldrich, reagent grade, 95%) before fractional distillation under reduced pressure and storage under nitrogen at -5°C. The monomer was further purified over phenylmagnesium chloride on a high vacuum line and transferred to an ampule before use.[8] Since phenylmagnesium chloride (Sigma-Aldrich, 2 M) was received as a solution in THF, the solvent was removed before it

was used to purify styrene. 2-Vinylpyridine (Sigma-Aldrich, reagent grade 97%) was stirred overnight with CaH_2 powder and distilled under reduced pressure. It was further purified with at least three freeze-pump-thaw cycles over CaH_2 powder on a high vacuum line and transferred to an ampule immediately before use. Tetrahydrofuran (Sigma-Aldrich, anhydrous ≥ 99.9%) was purified over sodium-benzophenone ketyl before it was distilled and transferred directly to the polymerization reactor through a PTFE line. Toluene (Sigma-Aldrich, ≥ 99.9%) was treated with *n*-butyllithium and styrene before it was distilled and transferred directly to the reactor through a PTFE line.

For the synthesis of PAA-b-PS by ATRP: *tert*-Butyl acrylate (*t*BA, Sigma-Aldrich, puriss grade ≥ 98.0 %) stabilized with ~ 0.01% hydroquinone monomethyl ether was first passed through a basic alumina column to remove the inhibitor. It was then stirred overnight with CaH_2 powder, subjected to fractional distillation under reduced pressure and stored under nitrogen at 4°C until needed. The styrene monomer used in the ATRP reaction was not subjected to the additional purification cycle with phenylmagnesium bromide as for anionic polymerization. N,N,N′,N″,N″-Pentamethyldiethylene-triamine (PMDETA, Sigma-Aldrich, 99%) was distilled under reduced pressure and stored under nitrogen at 4°C. Copper (I) bromide (CuBr, Sigma-Aldrich, 98%) was purified first by washing twice (for 4 and 24 h) with glacial acetic acid (Sigma-Aldrich, 99.75%), three times with ethanol (Sigma-Aldrich, ≥ 99.8%), and once with diethyl ether (Sigma-Aldrich, anhydrous, ≥ 99.0%). It was then dried overnight under vacuum and stored under nitrogen until needed. Methyl 2-bromopropionate (analytical standard 98%), acetone (> 99.7%), chloroform (> 99.5%), tetrahydrofuran (THF, anhydrous ≥ 99.9%), and trifluoroacetic acid (TFA, > 99.0%) were used as received from Sigma-Aldrich.

3.3.3 Synthesis of arborescent polystyrene homopolymers

The synthesis of the arborescent polystyrene substrates and the acetylation procedure were reported previously, [9,14,21] but will be described briefly for convenience. Anionic polymerization was used to synthesize 5000 g/mol linear polystyrene using *sec*-BuLi as initiator. The linear PS was randomly

functionalized with acetyl chloride and $AlCl_3$ to a 30 mol% acetylation level. To synthesize a G0PS arborescent polymer, a living linear PS with 5000 g/mol was capped with 2-3 units of 2-vinylpyridine and was titrated with a solution of the 30 mol% acetyl-functionalized linear polystyrene. The G1-G3PS samples were prepared by the same procedure, using the G(n-1) acetylated PS to titrate a living PS (5000 g/mol) solution and obtain the GnPS polymer. Detailed information on the synthesis can be obtained in the references listed above.

3.3.4 Synthesis of arborescent polystyrene-*graft*-poly(2-vinylpyridine) copolymers

Previously described experimental procedures[14,20] were used for the synthesis of the arborescent copolymers. As an example, the synthesis of the G2PS-*g*-P2VP13K arborescent copolymer is described briefly. Ampoules containing purified 26 mol% acetylated G2 polystyrene (0.60 g, 1.5 mequiv acetyl functionalities), 2-vinylpyridine (10.5 g, 0.100 mol in 10 mL of THF) monomer, and the dry THF line from the still were mounted on a five-neck reactor containing a magnetic stirring bar and LiCl (0.16 g, 3.8 mmol) and connected to a high-vacuum line. One neck was sealed with a rubber septum to introduce the initiator and remove samples. After evacuation under high vacuum, the reactor was flamed three times, filled with nitrogen, and dry THF (~ 100 mL) was added from the still. The LiCl was allowed to dissolve in the THF before the reactor was cooled to -78°C; 2-3 drops of the monomer were added, followed by *sec*-butyllithium solution (2-3 drops) to scavenge residual impurities, as confirmed by a faint red color persisting after stirring for about 5 min. A predetermined amount of *sec*-butyllithium solution (0.6 mL, 0.84 mmol, for a calculated side chain M_n = 14000 g/mol) was then added, followed by 2-vinylpyridine solution in THF drop-wise, resulting in an instantaneous color change to dark red. A side chain sample was removed after 45 min and terminated with degassed methanol. The remaining polymer solution was warmed to 0°C and titrated with the acetylated G2PS solution over 30 min, until the color changed to faint red. It was then allowed to warm to room temperature, which caused further fading of the color, and the reaction was terminated with degassed methanol. The crude product was

purified by fractionation to remove the non-grafted side chains, using THF/methanol (4/1 v/v) as solvent and *n*-hexane as non-solvent. The purified copolymer was recovered by precipitation in *n*-hexane and dried under vacuum. The G4 copolymer was further purified by preparatory SEC in DMF before analysis, however.

3.3.5 Synthesis of poly(*tert*-butyl acrylate) macroinitiators

Atom transfer radical polymerization (ATRP) was used to synthesize bromine-terminated poly(*tert*-butyl acrylate) (P*t*BA-Br) macroinitiators having number-average degrees of polymerization X_n = 10, 13, and 17, by a method adapted from Davis and Matyjaszewski.[22] Methyl 2-bromopropionate, copper (I) bromide, and PMDETA served as initiator, catalyst, and ligand, respectively, in degassed acetone as solvent at 60°C. Copper (I) bromide (CuBr; 150 mg, 1.04 mmol) was added to a Schlenk flask which was then sealed with a rubber septum and purged with nitrogen for 20 min. Previously distilled tBA (12 mL, 84 mmol) was added, followed by 5 mL of degassed acetone and PMDETA (0.22 mL, 1.98 mmol) with a syringe. The solution turned light green upon adding the PMDETA. The mixture was cooled to 0°C before adding the methyl 2-bromopropionate (0.22 mL, 1.96 mmol) initiator. After three freeze-pump-thaw cycles the flask was placed in a thermostatic oil bath at 60°C. The reaction was terminated after 2, 3, or 4.5 h for degrees of polymerization X_n = 10, 13, or 17, respectively, by exposing the reaction to the atmosphere and quenching with non-degassed acetone (10 mL).

3.3.6 Synthesis of poly(*tert*-butyl acrylate)-*block*-polystyrene (P*t*BA-*b*-PS) copolymers

All the PtBA-*b*-PS copolymers used in this work were prepared via ATRP.[22-25] In a typical experiment, 0.50 g of P*t*BA-Br (0.40 mmol, X_n = 10, M_n = 1200 g/mol, PDI = 1.08) and 150 mg of CuBr (1.04 mmol) were added to an oven-dried Schlenk flask with a magnetic stirring bar. The flask was sealed with a rubber septum, degassed and filled with nitrogen before 0.22 mL of PMDETA (1.98 mmol) and 22 mL of styrene (192 mmol) were introduced *via* syringe. The mixture was allowed to stir for at least

15 min, degassed with three freeze-pump-thaw cycles, and placed in a thermostatic oil bath at 100°C. The reaction was done in the bulk (without solvent), the monomer conversion being limited to ca. 50%. Samples were removed at certain time intervals using a nitrogen-filled gas-tight syringe to determine the monomer conversion and the molecular weight. The polymerization was stopped by allowing air into the reaction mixture and dilution with chloroform (~ 40 mL) before three extractions with water (~ 200 mL each).

***Macroinitiator (PtBA) Purification*:** Two different macroinitiator purification methods were investigated. The first one involved diluting the content of the Schlenk flask with acetone (50 mL), treating it with ~ 2 g of DOWEX MSC macroporous ion-exchange resin[25] for 1 h, and then passing the solution through a 10 cm height × 1 cm diameter column filled with activated neutral alumina (Sigma-Aldrich, Brockmann I grade, 150-mesh). The second step was repeated at least three times with new alumina to remove the copper catalyst from the polymer.[25]

In the second purification method, the content of the Schlenk flask was diluted with chloroform (40 mL) and transferred to a separatory funnel containing 200 mL of distilled water. The mixture was thoroughly shaken for at least 5 min to extract the copper and allowed to phase-separate for at least 10 min. The polymer solution (bottom layer) was collected while the water phase (top layer), with a bright blue color, was discarded as waste. This step was repeated 5 times, until no blue coloration was observed.

In both methods the solvent was removed on a rotary evaporator, the macroinitiator was dissolved in tetrahydrofuran (ca. 5 mL) and recovered by precipitation in 200 mL of 50/50 v/v mixture of water and methanol. The purified samples, recovered as clear to light yellow viscous oils, were dried under vacuum for at least 24 h before analysis by SEC and ^{1}H NMR spectroscopy.

***Block Copolymer (PtBA-b-PS) Purification*:** The second purification procedure described above for the macroinitiator was used for the block copolymer. Followed by dissolving in tetrahydrofuran (ca. 5 mL), recovered by precipitation in 200 mL methanol, and dried under vacuum before analysis by SEC and ^{1}H NMR spectroscopy.

3.3.7 Hydrolysis of the poly(*tert*-butyl acrylate) block

The hydrolysis of the *t*-butyl group using TFA was reported previously.[23-26] As an example of a typical hydrolysis reaction, a round bottom flask was loaded with P*t*BA17-*b*-PS195 (0.50 g; 0.37 mequiv *t*BA units) and dissolved in dichloromethane (20 mL). TFA (0.14 mL, 1.9 mmol, 5 equiv relatively to the *t*BA units) was added and the solution was stirred at room temperature for 24 h. The solvent was then removed, the residue was dissolved in THF (3 mL) and precipitated in methanol, filtered and dried under vacuum for 24 h (0.45 g, 90% recovery) before it was characterized by ^{1}H NMR spectroscopy.

3.3.8 ^{1}H Nuclear magnetic resonance (^{1}H NMR) spectroscopy

^{1}H NMR spectroscopy was used to determine the M_n of the *t*BA macroinitiators and P*t*BA-*b*-PS copolymers, and the composition of the PAA-*b*-PS arborescent PS-*g*-P2VP copolymers. The Bruker Avance-300 (300 MHz) nuclear magnetic spectrometer used was equipped with a z-gradient QNP 5 mm sample probe. $CDCl_3$ served as solvent, with the chemical shift of $CHCl_3$ serving as reference frequency. Each spectrum was acquired with 16 scans at a concentration of 25 mg/mL.

3.3.9 Size exclusion chromatography (SEC) analysis

An analytical SEC instrument was used for the characterization of the PtBA macroinitiators, the PtBA-*b*-PS copolymers, the arborescent PS, as well as the crude and fractionated PS-*g*-P2VP copolymers. The SEC system consisted a Viscotek GPCmax instrument (VE2001) equipped with a TDA 305 triple detector array with viscometer, refractive index (RI) and light scattering detectors (both low-angle (7^o) and right-angle (RALS)), as well as a UV detector (Viscotek 2600). Three PolyAnalytik SupeRes™

Series 300 mm × 8 mm linear mixed bed columns were used in the analysis. The elution was done with THF at a flow rate of 1.0 mL/min and a temperature of 35ºC, and the OmniSEC 4.6.1 software was used for data analysis. For the purification of the G4 ACPS preparative SEC was carried out in a Jordi Gel DVB 1000 Å, 250 mm × 22 mm preparative SEC column equipped with a Waters R401 differential refractometer detector. DMF with 0.2 g/L LiCl was used as a mobile phase at a flow rate of 3 mL/min. The sample was injected at a concentration of 6 mg/mL.

3.3.10 Static light scattering measurements

Static light scattering (SLS) measurements were performed at 25°C in THF on a Brookhaven laser light scattering system consisting in a BI-200 SM goniometer and a vertically polarized diode laser light source operating at a wavelength of 636 nm. Measurements were taken at 15° angle intervals between 30° and 120°. The samples were filtered through 0.45 μm pore size PTFE membrane filters and transferred directly to cylindrical cuvettes before the measurements. The results were analyzed using the Brookhaven software.

3.3.11 Dynamic light scattering measurements

The hydrodynamic radius (R_h) of the arborescent copolymer substrates (ACPSs) was measured by DLS in THF (0.8 mg/mL) at 25 °C on a Zetasizer NanoS90 Malvern Instruments system at a fixed angle of 90º, using glass cuvettes and a square aperture. The arborescent substrates were dissolved at least 24 h before analysis.

3.4 Result and discussion

3.4.1 Synthesis of PS substrates and functionalization

Gauthier and coworkers investigated in depth the synthesis of arborescent polystyrene by an anionic grafting onto strategy using acetylated substrates.[8,9] These PS cores served in the synthesis of the ACPS. To this end, a linear PS substrate with $M_n \approx 5000$ g/mol was synthesized by anionic polymerization

using *sec*-butyllithium as initiator in toluene at 0°C, functionalized with acetyl chloride, and grafted with linear PS ($M_n \approx 5000$ g/mol) side chains to obtain a comb-branched or generation zero polystyrene, G0PS. The subsequent arborescent polystyrene generations (G1PS – G3PS) were derived from additional cycles of acetylation and grafting reactions; an example of the synthetic scheme is given in **Appendix A-1**. The exact characteristics of the substrates and the side chains used in the synthesis of the polystyrene substrates are summarized in **Table 3-1**. Since the PS substrates were acetylated prior to grafting, the branching functionality (f_n) of the molecules was controlled through their acetylation level (F), given in **Table 3-1** (the equations used to calculate f_n are given in **Appendix A-3**, and the determination of the acetylation level by ^{1}H NMR analysis is discussed in **Appendix A-2**).

Table 3-1. Characteristics of polystyrene substrates.[20,21]

Polymer	Side chains		Arborescent polymer				
	M_n[d] (g/mol)	M_w/M_n[d]	F[e] (mol%)	M_n[f] (g/mol)	M_w/M_n[f]	G_y(%)[g]	f_n[h]
PS (linear)	-	-	30	5.2×10^3	1.06	-	-
G0PS b	5500	1.06	24	9.7×10^4	1.03	90	17
G1PS b	4900	1.07	21	1.1×10^6	1.03	70	205
PS (linear)	-	-	30	4.5×10^3	1.08	-	-
G0PS c	5300	1.10	25	6.5×10^4	1.10	49	12
G1PS c	4000	1.08	18	3.7×10^5	1.07	45	76
G2PS c	4800	1.08	22	1.6×10^6	1.10	39	256
G3PS c	5500	1.09	26	7.4×10^6	1.08	28	1054

a) *Substrates obtained by cycles of acetylation, grafting, and fractionation using $M_n \approx 5000$ g/mol polystyrene core and side chains. b) Polystyrene side chains capped with DPE and 3 equiv of 2VP used for the synthesis of G0PS-g-P2VP30K and G1PS-g-P2VP30K copolymer by Munam. c) Newly synthesized polystyrene side chains capped with 2-3 equiv of 2VP. d) Absolute values determined by SEC analysis with a linear polystyrene standards calibration curve. e) Acetylation level from ^{1}H NMR analysis. f) Absolute values determined by SEC-MALLS analysis. g) Grafting yield: fraction of side*

chains generated in the reaction becoming attached to the substrate. h) Number of branches added in the last grafting reaction.

The grafting yield provided in **Table 3-1** was calculated by SEC analysis, from the relative areas of the peaks obtained for the graft polymer and the side chains using the RI detector (the equations used for these calculations are described in **Appendix A-3**). The synthesis and the purification of the PS samples were monitored by size exclusion chromatography (SEC) analysis. A comparison of SEC traces obtained with the RI detector for the side chains, the G0PS substrate, the crude and the purified G1PS product are shown in **Figure 3-1** as an example.

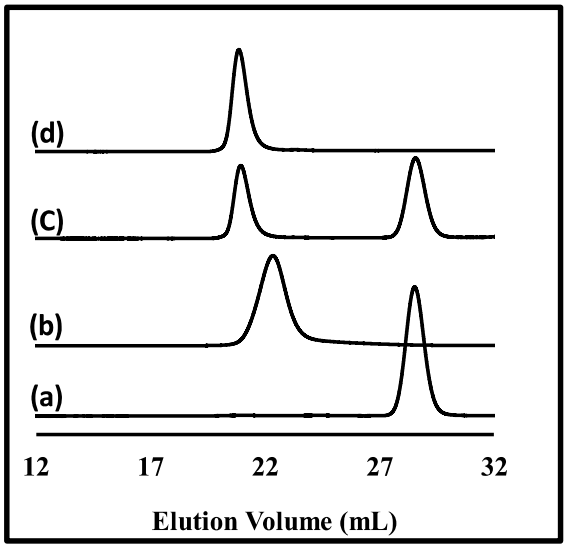

Figure 3-1. SEC traces for (a) PS side chains, (b) G0PS substrate, (c) G1PS crude product, and (d) fractionated G1PS.

3.4.2 Synthesis of arborescent copolymer substrates (ACPSs)

The ACPSs examined in this study had a PS core with a branched architecture, grafted with P2VP side chains of different lengths, namely G0PS-*g*-P2VP30K, G1PS-*g*-P2VP30K, G2PS-*g*-P2VP13K, and G3PS-*g*-P2VP15K. As explained earlier, in the notation system used to identify the ACPSs throughout

this thesis, the first number denotes the generation number of the PS core and the second number denotes the molecular weight of the P2VP side chains in kg/mol. Thus G0PS-*g*-P2VP30K refers to generation zero PS core grafted with 30000 g/mol P2VP side chains.

The synthesis of arborescent polystyrene-*graft*-poly(2-vinylpyridine) (PS-*g*-P2VP) copolymers was previously investigated in detail,[14,20] and the G0PS-*g*-P2VP30K and G1PS-*g*-P2VP30K copolymers were synthesized by Gauthier and Munam[20] from acetylated PS substrates. A similar anionic grafting strategy was used to obtain the G2PS-*g*-P2VP13K and G3PS-*g*-P2VP15K copolymers used in the current investigation. G2PS and G3PS substrates were newly synthesized starting from a linear PS unit and used for the synthesis of G2PS-*g*-P2VP13K and G3PS-*g*-P2VP15K copolymers. The acetylated arborescent G2PS and G3PS substrates were grafted with 13000 g/mol and 15000 g/mol P2VP side chains to yield the G2PS-*g*-P2VP13K and G3Ps-*g*-P2VP15K copolymers, respectively. The crude products were purified through at least three cycles of fractionation in mixtures of THF/methanol as solvent, and *n*-hexane as non-solvent. The G4 copolymer was further purified by preparatory SEC in DMF, since three cycles of fractionation did not suffice to remove all traces of side chain contaminants. The % 2VP content of the ACPSs (**Table 3-2**) was determined by ^{1}H NMR analysis as explained in **Appendix A-2**.

The purified arborescent copolymers (ACPSs) were characterized with SLS measurements in THF to obtain their weight-average molecular weight (M_w), radius of gyration (R_g), and second virial coefficient (A_2), which are reported in **Table 3-3**. The M_w was found to increase with the generation number as expected. The R_g (in nm) obtained for the G2, G3, and the G4 copolymers were 39.7 ± 2.4, 38.5 ± 2.4, and 67.7 ± 2.7 nm, respectively. The R_g of the G2 copolymer was comparable to the G3 sample, even though the M_w of the latter was greater, which implies that the G3 molecules were denser.

The R_g/R_h value, called either the ρ-parameter or prefactor δ, is useful to estimate the shape and structure of particles and macromolecules.[11] The magnitude of the ρ-parameter can be as low as 0.775 for rigid spheres of homogenous density, or as high as 5.5 for rods, while the theoretical value for star-branched polymers with a high branching functionality (f >>1) in a theta solvent is 1.079.[27] The ρ-parameter (R_g/R_h) values obtained for the G2, G3 and G4 copolymers were 1.09, 0.83, and 0.90, respectively. These findings suggest that the G2 copolymer, with longer (M_n = 30000 g/mol) P2VP side chains forming a thick corona, has a structure closer to a star-branched polymer, while the higher generation (G3 and G4) copolymers have a structure closer to homogeneous rigid spheres. These conclusions appear reasonable, as they are in agreement with the density increase inferred from the comparable R_g values obtained in spite of the M_n increase from the G2 to the G3 copolymer, but are also supported by the AFM and TEM analysis results provided in Chapter 4.

Table 3-2. Characteristics of the arborescent substrates used for the complexation reaction. Partly adapted from references 20 and 21.

Sample	Side chains		Graft copolymer				
	M_n (g/mol)	**M_w/M_n**	**M_n (g/mol)**	**M_w (g/mol)**	**M_w/M_n**	***f_n***	**Mol % 2VP[d]**
G0PS-g-P2VP30K	27700	1.08	2.3×10^{5}[a]	2.5×10^{5}[a]	1.1	83	96
G1PS-g-P2VP30K	32700	1.07	1.1×10^{6}[b]	1.2×10^{7}[c]	-	303	90
G2PS-g-P2VP13K	12900	1.10	1.5×10^{7}[b]	4.2×10^{7}[c]	-	1038	89
G3PS-g-P2VP15K	14900	1.03	3.5×10^{7}[b]	7.9×10^{7}[c]	-	1852	80

a) Absolute value from SEC-MALLS. b) Values estimated by combining the copolymer composition based on ^{1}H NMR analysis and the absolute M_n of the substrate. c) M_w obtained from static light scattering measurements, as the G2-G4 copolymers did not elute from the SEC column. d) Obtained from ^{1}H NMR spectroscopy analysis; f_n is the number of side chains added in the last grafting cycle.

Table 3-3. Characterization of the ACPSs by light scattering.

Sample	M_w (g mol^{-1})	R_g (nm)	R_h (nm)	A_2 (cm^3 mol g^{-2})
G1-*g*-P2VP30K	1.2×10^7	39.7±2.4	36.5±0.3	1.38×10^{-4}
G2-*g*-P2VP13K	4.2×10^7	38.5±1.5	46±0.3	2.12×10^{-4}
G3-*g*-P2VP15K	7.9×10^7	67.7±2.7	75±0.5	2.00×10^{-5}

3.4.3 Synthesis of Poly(acrylic acid)-*block*-polystyrene (PAA-*b*-PS) copolymers

Since its introduction by Matyjaszewski, Sawamoto and others, atom transfer radical polymerization (ATRP) has developed into one of the best established controlled radical polymerization (CRP) methods to synthesize polymers with a narrow molecular weight distribution, applicable to a broad range of monomers.

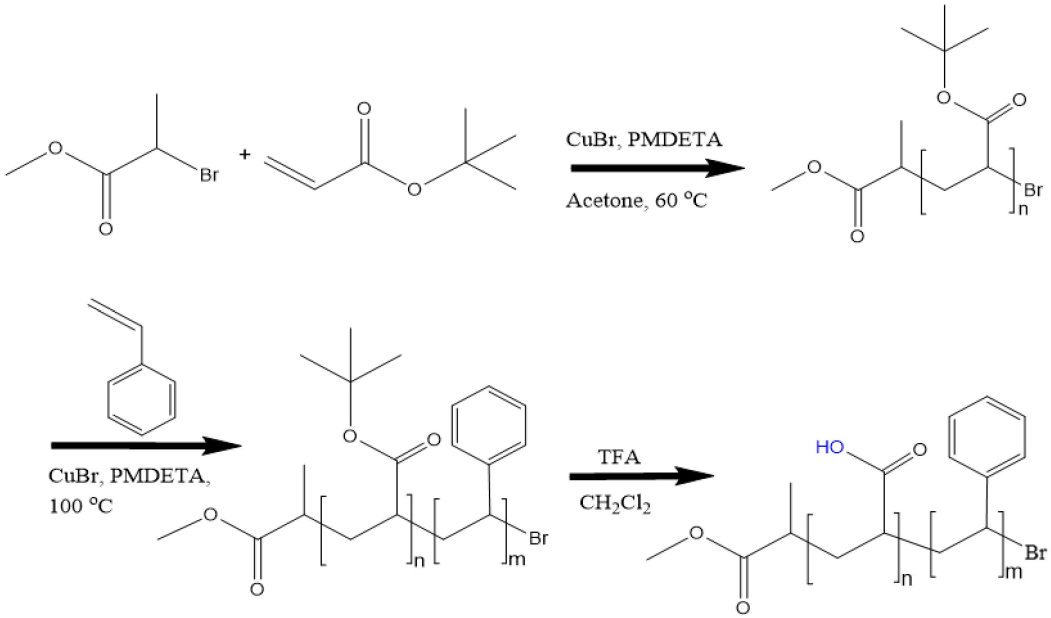

Scheme 3-1. Synthesis of poly(acrylic acid)-block-polystyrene (PAA-b-PS) copolymer via ATRP.

In the current investigation, ATRP was utilized for the synthesis of well-defined poly(*tert*-butyl acrylate) (P*t*BA) macroinitiators and poly(*tert*-butyl acrylate)-*block*-polystyrene (P*t*BA-*b*-PS) copolymers with narrow molecular weight distributions (Đ ≤ 1.13). P*t*BA samples with a low molecular weight (~ 1300-2200 g/mol) were first prepared by initiation with methyl 2-bromopropionate, using a combination of copper (I) bromide and PMDETA as catalyst and ligand, respectively, in degassed acetone at 60°C, as shown in **Scheme 3-1**. Since the goal was to use the corresponding PAA-*b*-PS copolymers to form stable complexes with the arborescent PS-*g*-P2VP copolymers, while leaving most 2VP units free for metal loading, PtBA macroinitiators were prepared containing 10-17 PAA units, corresponding to less than ~ 10 mol% PAA content in the final PAA-*b*-PS copolymers. Based on ^{1}H NMR spectroscopy analysis, the three P*t*BA macroinitiators synthesized had M_n = 1280, 1660, and 2180 g/mol, corresponding to 10, 13 and 17 repeating units, respectively (**Table 3-4**). The number-average degree of polymerization ($\bar{X}_n$) was calculated from the peak areas for the terminal methine proton (geminal to the bromine atom), with a chemical shift of 4.0-4.2 ppm (*a*), and the methine protons in the repeating units, at 2.1-2.4 ppm (*c*). Alternately, the peak areas for the methoxy protons (3.6-3.7 ppm, (*b*)) and the methine protons in the repeating units (*c*) could be used for the same purpose. Both analyses gave the same result, which confirms that every macroinitiator chain was terminated with a Br atom. In addition, signals for the methylene protons on the terminal monomer unit at δ 1.8 ppm (*d*), the backbone methylene protons at 1.5 ppm (*e*), a sharp peak of the *tert*-butyl protons at δ 1.4 ppm (*f*), and the terminal CH_3-protons from the initiator at 1.2 ppm (*g*) could be identified in the spectrum.

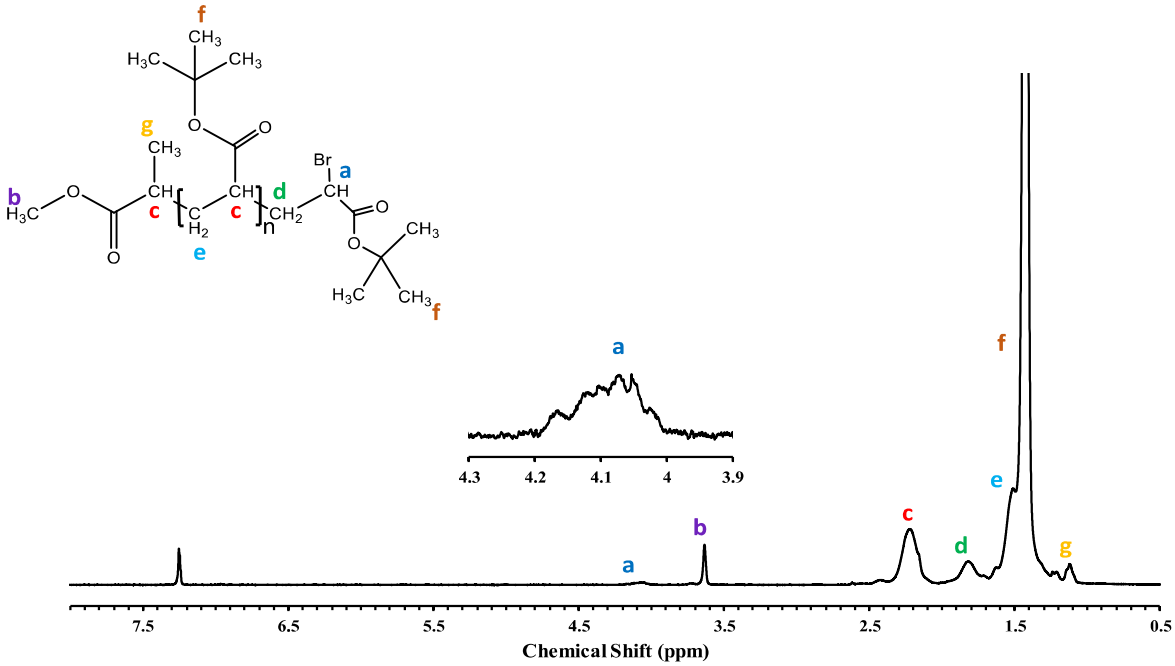

Figure 3-2. ^{1}H NMR spectrum for PtBA with X_n = 13 in $CDCl_3$.

The molecular weight of the P*t*BA samples was also determined by SEC analysis with polystyrene standards in THF. Unfortunately, the signal from the light scattering detector was much too noisy to allow absolute molecular weight determinations. The fact that the apparent (polystyrene-equivalent) values obtained by that method are in good agreement with the absolute values from NMR analysis (**Table 3-4**) is likely coincidental. **Figure 3-4** provides the DRI detector signals for all three P*t*BA samples (10, 13 and 17 units), with relatively narrow apparent molecular weight distributions ($Đ \leq$ 1.13).

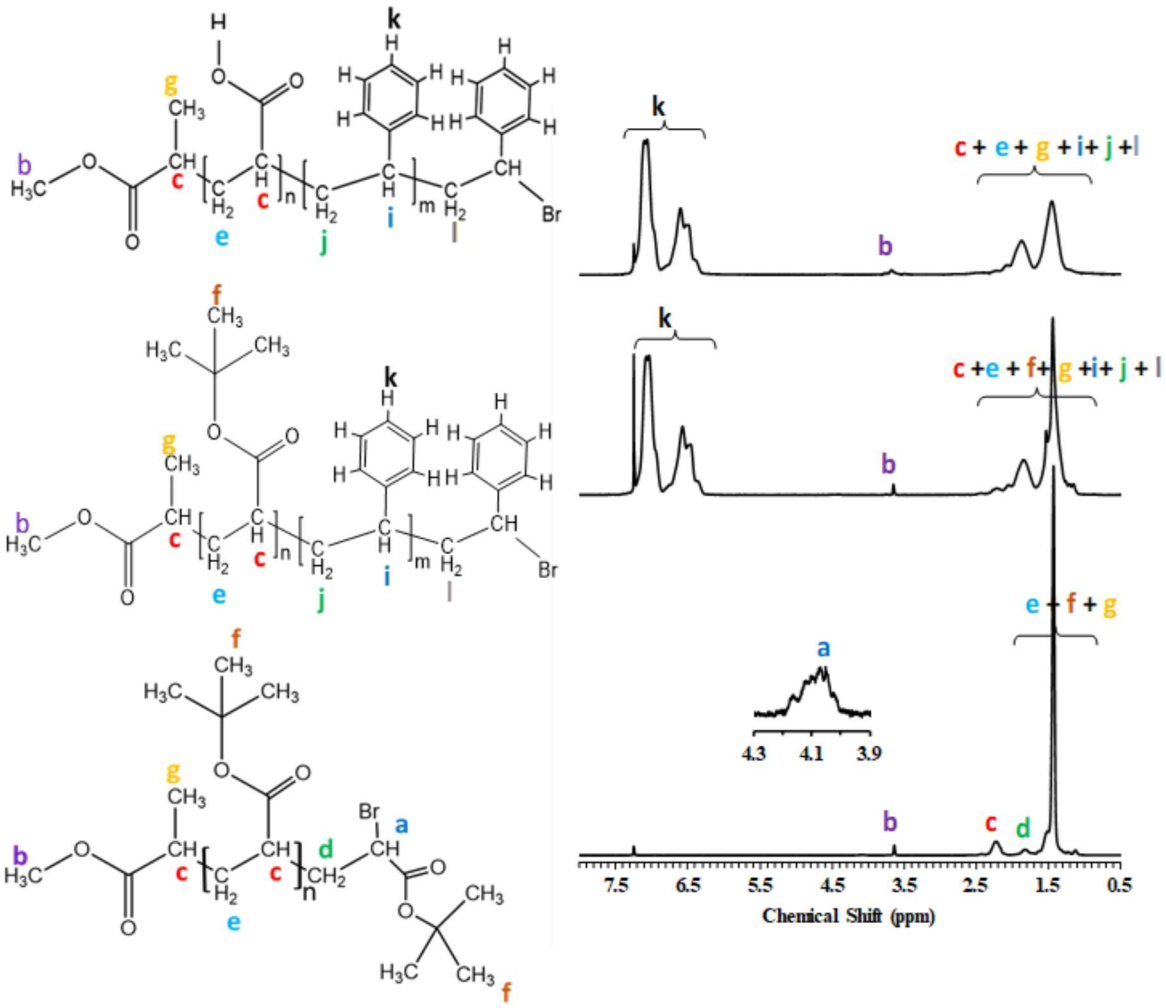

Figure 3-3. ^{1}H NMR spectra for PtBA (bottom), PtBA-b-PS (middle), and PAA-b-PS (top).

The P*t*BA macroinitiators were used to synthesize different P*t*BA-*b*-PS copolymer samples by ATRP (**Table 3-5**), in the presence of Cu(I)Br/PMEDTA as catalyst/ligand at 100ºC, without added solvent beyond the excess styrene present in the reaction. Typical ^{1}H NMR spectra obtained for the P*t*BA macroinitiator, and for the P*t*BA-*b*-PS copolymer before and after hydrolysis (PAA-*b*-PS) are compared in (**Figure 3-3**). These are consistent with the successful chain extension with PS, as the signals around 6.3–7.3 ppm (*k*) correspond to the aromatic protons of styrene. The presence of a methoxy proton signal

at 3.6-3.7 ppm (*b*) from the ATRP initiator fragment in the P*t*BA macroinitiator, and of a sharp *tert*-butyl peak at δ 1.4 ppm is also noted in the copolymers.[23] The degree of polymerization of the polystyrene block could be calculated either from the peak areas for the aromatic protons of styrene and the methoxy protons in the initiator fragment, or from the total peak area for the CH and CH_2 protons in the repeating units of the copolymer backbone. Successful chain extension of the macroinitiator with polystyrene was further confirmed very clearly by SEC analysis (**Figure 3-5**). The dn/dc values for the copolymers, used in the light scattering analysis, were calculated based on the weight fraction of each block determined from the NMR spectra. The dn/dc for PtBA in THF was taken as 0.059 mL/g,[28] and 0.185 mL/g for PS. The SEC DRI response revealed significant increases in molecular weight and narrow molecular weight distributions upon chain extension of the PtBA macroinitiators with PS. This result, in combination with the absence of P*t*BA in the DRI elution curve for the copolymers, most clearly confirms clean chain extension. The results obtained by SEC analysis were in good agreement with the ^{1}H NMR analysis results (**Figure 3-5**), which is not surprising since PS was the main component in the block copolymers.

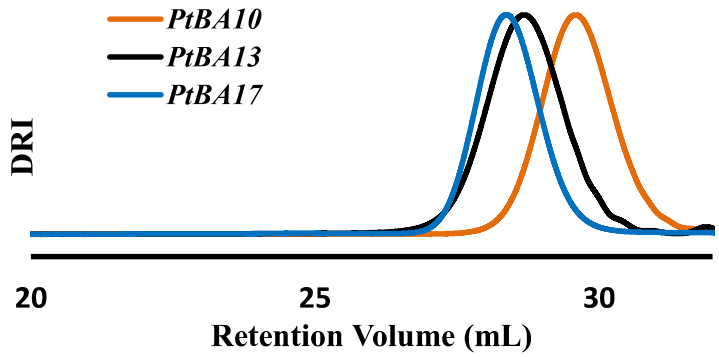

Figure 3-4. SEC DRI response for PtBA macroinitiators with (orange) 10, (black) 13 and (blue) 17 units.

Table 3-4. Characterization results for PtBA macroinitiators.

Sample	^{1}H NMR	SEC			Conversion (%)
	DP_n	M_n (g/mol)	M_n (g/mol)	PDI	
P*t*BA	10	1280	1400	1.13	83
P*t*BA	13	1660	1600	1.10	85
P*t*BA	17	2180	2200	1.09	78

The PAA-*b*-PS diblock copolymers were obtained by hydrolysis of P*t*BA-*b*-PS using 5 molar equiv of TFA with respect to the *t*BA units. ^{1}H NMR analysis of the product in chloroform-*d* (**Figure 3-3**) confirmed the complete removal of the *t*BA groups through the disappearance of the sharp peak at δ 1.4 ppm (*f*). Moreover, to confirm complete removal of the *t*BA group, the peak areas for the backbone CH and CH_2 protons of the repeating units at δ 1.1-2.0 ppm were compared with the peak area for the aromatic protons of polystyrene at δ 6.3-7.3 ppm. Complete removal of the *t*BA groups was also confirmed by ^{13}C NMR analysis (**Appendix A-4**).

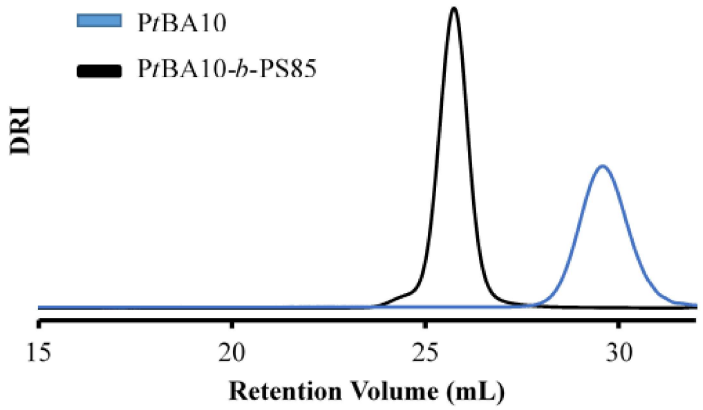

Figure 3-5. SEC traces for PtBA10 (blue) and PtBA10-b-PS85 (black).

Table 3-5. Characterization of PtBA-b-PS by ^{1}H NMR and SEC analysis.

Sample	^{1}H NMR		SEC	
	DP (PS)	M_n (g/mol)	M_n(abs) (g/mol)	PDI
PtBA10-*b*-PS85	85	1.0×10^4	1.9×10^4	1.05
PtBA10-*b*-PS205	205	2.3×10^4	2.9×10^4	1.13
PtBA10-*b*-PS260	260	2.8×10^4	3.0×10^4	1.20
PtBA10-*b*-PS305	305	3.3×10^4	3.5×10^4	1.14
PtBA13-*b*-PS156	156	1.8×10^4	2.0×10^4	1.13
PtBA13-*b*-PS330	330	2.3×10^4	2.8×10^4	1.26
PtBA13-*b*-PS390	390	4.2×10^4	4.0×10^4	1.17
PtBA17-*b*-PS195	195	2.3×10^4	2.7×10^4	1.24
PtBA17-*b*-PS250	250	2.8×10^4	3.3×10^4	1.13
PtBA17-*b*-PS395	395	4.3×10^4	5.8×10^4	1.08

3.5 Conclusions

While some arborescent polystyrene-*graft*-poly(2-vinylpyridine) copolymers were already available, additional copolymers of the higher generations (G2PS-*g*-P2VP13K and G3PS-*g*-P2VP15K) also needed to be synthesized and characterized for the current investigation according to reported procedures. Since SEC analysis of the arborescent copolymers was impossible, SLS measurements were used to determine their weight-average molecular weight.

PAA-*b*-PS block copolymers with different PAA and PS chain lengths were also synthesized by ATRP, starting from PtBA macroinitiators. Relatively narrow molecular weight distributions were obtained for the PtBA macroinitiator ($M_w/M_n \leq 1.13$) and the PAA-*b*-PS copolymers ($M_w/M_n \leq 1.26$).

Chapter 4: Arborescent Core–Shell–Corona Copolymers by Self-Assembly

4.1 Overview

Arborescent copolymer complexes (ACCs) with a core–shell–corona morphology were obtained by the self-assembly of different generations of arborescent copolymer substrates, polystyrene-*graft*-poly(2-vinylpyridine) (GnPS-*g*-P2VP, n = 0–3), with poly(acrylic acid)-*block*-polystyrene (PAA-*b*-PS) copolymers. The arborescent copolymers were obtained by anionic grafting of P2VP chain segments onto arborescent PS cores derived from successive grafting reactions of 5000 g/mol PS side chains. Atom transfer radical polymerization (ATRP) was employed for the synthesis of PAA-*b*-PS copolymers with 10–17 units of acrylic acid (AA) and long PS blocks (85–395 styrene units). The self-assembly protocol was optimized in terms of solvency conditions and concentration to obtain stable complexes. The influence of variations in the PAA and PS block lengths in the copolymers was investigated systematically. Dynamic light scattering (DLS) analysis was used to obtain the hydrodynamic diameter (D_h) and the size dispersity under different conditions. In many cases a significant D_h increase was observed from the arborescent substrate to the ACC, with single size populations in number, volume and intensity distributions, and a relatively low size dispersity ($Đ \leq 0.15$). Larger diameter increases were seen for longer PS blocks. Atomic force microscopy (AFM) and transmission electron microscopy (TEM) were also used to obtain size and morphology information for the samples. AFM analysis confirmed that a spherical shape was obtained for complexes derived from G1 and G2 substrates, while raspberry-like and toroidal morphologies resulted for G3 and G4 substrates, respectively.

4.2 Introduction

Polyelectrolytes, derived from ionizable monomers, have a strong tendency to adsorb on surfaces carrying a charge of the opposite type, or to form complexes when mixed with oppositely charged polyelectrolytes. Different terms have been suggested to refer to polyelectrolyte complexes.[1] This includes polyion complexes (PIC) by Harada et al.,[2] block ionomer complexes (BIC) by Kabanov et

al.,[3] complex coacervate core micelles (C3M) by Stuart et al.,[4] and interpolyelectrolyte complexes (IPEC) by Gohy et al.[5] and Pergushov et al.[6]

Simple block copolymers containing one ionizable block such as polystyrene-*block*-poly(acrylic acid) (PS-*b*-PAA) can also form aggregates when dissolved in a solvent selective for one of the segments.[7] Aggregates of block copolymers containing PAA or poly(methacrylic acid) (PMAA) segments have been studied extensively in aqueous media.[8] For example, Mai and Eisenberg determined that PS-*b*-PAA copolymers can self-assemble into different morphologies including spheres, rods, lamellae, vesicles, inverse rods and bicontinuous structures.[9] A number of studies also focused on inter-polyelectrolyte complexes. For example, Zhou et al. investigated complexes of PAA or PMAA with P4VP or P2VP in water/ethanol mixtures.[7] Complexes of PS-*b*-PAA with tetramethylammonium counterions in water were reported by Groenewegen et al.,[10] and Zhang et al.[11] examined complexes of PS-*b*-PAA and P4VP in ethanol. Most of the reports on this type of complex were based upon aqueous solutions[4,6,12,13] and focused on linear systems, albeit a few studies also involved branched polyelectrolytes. This includes a complex formed between sulfonated polystyrene/poly(ethylene oxide) brushes and quaternized poly(4-vinylpyridine) in water.[14] The self-assembly into fibers of anionic six-arm PMAA stars with cationic poly(2-(dimethylethylammonium iodide)ethyl methacrylate)$_6$ six-arm stars was also reported.[15] The formation of polyion complexes between arborescent core–shell G0PS-*g*-P2VP graft copolymers and PAA-*b*-PHEA block copolymers in aqueous media, also reported more recently,[16] is most directly related to the current investigation.

Interactions leading to the formation of polyelectrolyte complexes are generally assumed to include hydrogen bonding,[7,17] acid/base (ionic) interactions,[18,19] or a combination of both.[7] The strength of the interactions should depend on the type of polyelectrolyte and the interaction mode involved. For instance, P4VP and P2VP were reported to interact more strongly with PAA than with PMAA in water/ethanol mixtures.[7] This was attributed to protonation of the nitrogen of P4VP and P2VP by PAA

leading to ionic interactions, while this effect was not observed for PMAA under the same conditions due to its lower acidity. In addition to acid/base interactions, it was suggested that hydrogen bonding could also exist between PAA and the pyridine moieties, while PMAA likely only involved hydrogen bonding.

The size and morphology of polyelectrolyte complexes are influenced by parameters such as the molar ratio of the complementary polyelectrolytes, the block lengths and the solvent type. For example, the addition of a small amount of water to complexes of PS-*b*-PAA and PS-*b*-P4VP in DMF transformed the morphology of the complexes from spheres to rods and vesicles, and their size increased.[20] The complexes formed by PS-*b*-P4VP micelles and PAA in two different organic solvents (THF and DMF) displayed a significant increase in diameter for increasing P4VP block lengths, while a decrease in diameter was observed for complexes of PS-*b*-PAA core–shell (CS) micelles and PEG-*b*-P4VP copolymers upon complexation in DMF/ethanol mixtures.[11,21,22] Complexes with a raspberry-like morphology were reported for core–shell PS-*co*-PMAA random copolymer colloids, and for micelles of PS-*b*-P4VP in water.[23]

One efficient method to ensure the colloidal stability of polyelectrolyte aggregates is steric stabilization by a polymer bonded to the surface of the particles.[24,25] In organic solvents, a long neutral block bound to at least one of the polyelectrolytes is necessary to encapsulate the complex formed and enhance its stability.[26]

4.3 Methodology and scope of the present work

Most studies on the complexation of polyvinylpyridine and PAA segments discussed above were done in aqueous environments. This also includes the arborescent PIC micelles derived from G0PS-*g*-P2VP and PAA-*b*-PHEA, stabilized by the hydrophilic PHEA segments anchored on their surface. We now report the preparation of ACCs from different generations (G1–G4) of arborescent PS-*g*-P2VP

copolymers and PAA-*b*-PS with different block lengths in organic solvents, strerically stabilized by anchoring the PS segments on their surface. The ACCs were characterized in solution by DLS, and in their dry state by AFM and TEM.

The arborescent graft copolymers used in the investigation, obtained by anionic grafting, had a branched hydrophobic PS core and a shell of P2VP chains with a molecular weight of either 15 or 30 kg/mol. Hereafter the following nomenclature will be used for the arborescent copolymer substrates: The **G0PS-*g*-P2VP30K** and **G1PS-*g*-P2VP30K** samples, with 30 kg/mol P2VP side chains, are simply denoted as **G1** and **G2**, respectively, while **G2PS-*g*-P2VP13K** and **G3PS-*g*-P2VP15K**, with ~15 kg/mol P2VP side chains, are denoted as **G3** and **G4**, respectively. Note that in all cases, the **G1–G4** labels refer to the **overall generation number** of the arborescent substrates. The PAA-*b*-PS copolymers, synthesized by ATRP, had a PAA block with DP_n = 10, 13, or 17, and a long hydrophobic PS segment with DP_n = 85–395. Naming of the BCP samples is based on the DP_n of each segment, such that PAA10-*b*-PS260 refers to a BCP containing 10 acrylic acid (AA) units and 260 styrene units. Similarly to previous investigations,[20] the complexation of arborescent GnPS-*g*-P2VP with the PAA-*b*-PS copolymers is expected to proceed via acid/base (electrostatic) and/or hydrogen bonding, even though only electrostatic interactions are shown in **Figure 4-1** for simplicity. Since the arborescent copolymer substrates are relatively rigid, complexation may not lead to major morphology changes. An ACC obtained from an arborescent substrate of generation Gn (n = 1–4) and a PAAx-*b*-PSy copolymer (where x and y are the DP_n of PAA and PS, respectively) will be identified as Gn@PAAx-*b*-PSy.

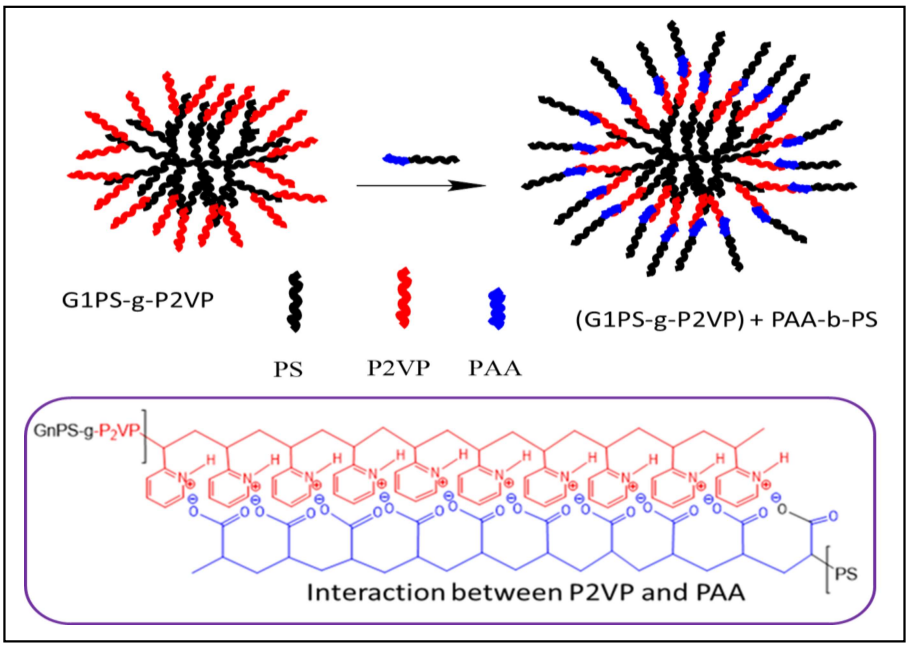

Figure 4-1. Arborescent copolymer complex formation by self-assembly.

4.4 Materials and methods

4.4.1 Synthesis of arborescent copolymers

The arborescent copolymers used in this study were synthesized either by Gauthier and Munam,[27] or else according to procedures described in Chapter 3.[28] The characteristics of the arborescent copolymers used in the investigation are summarized in **Table 4-1**.

Table 4-1.Characteristics of the arborescent copolymers used.

Sample	Side chains		Graft copolymer			
	M_n	M_w/M_n	M_n[a]	M_w	f_n[c]	Mol% 2VP[d]
G0PS-P2VP30K	27700	1.08	2.4×10^6	-	83	96
G1PS-P2VP30K	32700	1.07	1.1×10^7	1.2×10^7[b]	303	90
G2PS-P2VP13K	12900	1.10	1.5×10^7	4.2×10^7[b]	1038	89
G3PS-P2VP15K	14900	1.03	3.5×10^7	7.9×10^7[b]	1852	80

a) Values estimated by combining the copolymer composition based on ^{1}H NMR analysis and the absolute M_n of the substrate. b) M_w from static light scattering measurements. c) Number of P2VP branches added in the last grafting cycle. d) From ^{1}H NMR spectroscopy analysis.

4.4.2 Synthesis of poly(acrylic acid)-*block*-polystyrene (PAA-*b*-PS) copolymers

Atom transfer radical polymerization (ATRP) was employed to synthesize P*t*BA-*b*-PS copolymers by a method adapted from Davis and Matyjaszewski.[29] *tert*-Butyl acrylate (*t*BA) macroinitiators with DP_n = 10, 13 and 17 were first synthesized, and then used to grow long polystyrene blocks (DP_n = 85–395). The hydrolysis of the *tert*-butyl ester group of P*t*BA-*b*-PS was carried out with 5 equiv of trifluoroacetic acid per *t*BA unit in dichloromethane at room temperature for 24 h, as described elsewhere.[30] Detailed information on the synthesis and the hydrolysis of the block copolymers was provided in Chapter 3, and their characterization data are provided in **Table A4-1**.

4.4.3 Preparation of the arborescent copolymer complexes

In most cases, the arborescent copolymer substrate was dissolved in either pure THF, THF/ethanol, or toluene/ethanol mixtures, and the PAA-*b*-PS copolymer was added in a 1 : 1 w/w ratio relatively to the substrate in solution, dissolved in the same solvent and at the same concentration as the substrate. In a few cases, the block copolymer was mixed with the arborescent substrate in the solid state before dissolution in a solvent. Both mixing protocols yielded similar results, but for consistency solution mixing was preferred unless otherwise specified. In a typical procedure, a Gn arborescent copolymer

was dissolved overnight at a concentration of 0.8 mg/mL in a 20-mL vial. In a separate vial, PAA-*b*-PS was dissolved at 0.8 mg/mL in the same solvent. A 5-mL aliquot of PAA-*b*-PS solution was then added drop-wise to an equal volume of Gn substrate solution with stirring, which was continued for at least two days longer. Since the arborescent P2VP copolymer substrates were insoluble in pure toluene below 41 °C, different mixed solvent compositions were also examined. The G1 complexes were thus investigated only in THF/ethanol mixtures, while the G2 systems were studied in THF/ethanol and toluene/ethanol. The G3 and G4 complex systems were investigated in THF. In most cases, after the complexation step, the solvent was removed under vacuum or on a rotary evaporator. The sample was then redissolved in toluene (10 mL) and stirred for at least one day before characterization by DLS, TEM and AFM.

4.4.4 Dynamic light scattering (DLS)

DLS measurements were performed at 25 °C on a Zetasizer NanoS90 system from Malvern Instruments with a He-Ne laser light source (636 nm) at a fixed angle of 90°, using glass cuvettes with a square aperture. The arborescent substrates were dissolved at least 24 h before the analysis. The concentration was set to 0.8 mg/mL for most measurements, and the solutions were filtered using 0.45 μm PTFE filters.

4.4.5 Atomic force microscopy (AFM)

Tapping-mode AFM measurements were performed on a Nanoscope IIIa Multimode Digital Instruments Model MMAFM-2 device mounted on a vibration isolation table. The cantilever probes used were T300 Vista Probes with a silicon tip having a radius of 8 nm, 125 μm length, 40 μm width and 14 μm height, a spring constant of 40 $N \cdot m^{-1}$ and a resonant frequency of 300 kHz. The scan rate was typically set between 0.7 and 1 Hz, at a scan angle of 0°, acquiring 512 samples/line. To adjust the force applied on the surface the drive amplitude was varied between 25 and 50 mV, and the amplitude

set-point between 0.50 and 0.85 V. The sensitivity was controlled by adjusting the integral gain from 0.2 to 0.5, and the proportional gain from 2 to 6. The samples were prepared by casting 2–3 drops of a 0.8 mg/mL solution onto a freshly cleaved mica substrate and spinning at 3000 rpm. The images were analyzed with the Nanoscope Analysis software v1.40r1.

4.4.6 Transmission electron microscopy (TEM)

TEM imaging was performed on a Philips CM10 instrument operated at 60 kV. Thin films were prepared by casting one drop of a sample solution with a micro syringe onto 300-mesh copper TEM grids coated with carbon and Formvar® (Electron Microscopy Sciences, FCF300-CU). The films were then placed on a piece of 1 × 2 cm^2 Whatman filter paper. The pieces of paper with the grids were transferred to a 20 mL vial containing a crystal of iodine and left overnight to stain the P2VP phase. The TEM images were analyzed with the ImageJ (version 1.50i) processing software.

4.5 Results and discussion

4.5.1 Characterization by DLS: General considerations

The hydrodynamic diameter of the arborescent substrates and the resulting ACCs was determined in solution by DLS analysis. The velocity of Brownian motions for particles in solution depends on their size, and their diameter can be determined by measuring the rate at which the intensity of scattered light fluctuates in a DLS experiment. The correlator of the DLS instrument compares (correlates) the intensity of the signal at a time (τ) with the intensity after a very short time period ($\tau + \delta\tau$). Small particles move very rapidly in solution and their correlation function decays fast, while larger particles have a longer decay time,[31-33] as shown in **Figure 4-2**: The correlation curve for a block copolymer decays faster than for an arborescent polymer, and the slowest decay is observed for the resulting ACC, as expected. The time-resolved correlation function, $g^{(1)}(\tau)$ (**Equation 4-1**) describes the time

dependence of the correlation function, which can be analyzed by the cumulants method with **Equation 4-1**.[34,35]

$$g^{(1)}(\tau) = \int_0^\infty G(\Gamma)\, e^{[-\Gamma\tau]} d\Gamma \qquad \textbf{(4-1)}$$

where G(Γ) is the distribution function of decay rates Γ (the inverse of the correlation time). The translational diffusion coefficient (D_t) can be obtained from the decay rate $\Gamma = D_t q^2$, where q is the magnitude of the scattering vector[36-38] expressed as $\mathbf{q} = (4\pi\, n_o/\lambda)\, (\sin\frac{\theta}{2})$, where n_o is the refractive index of the dispersion medium (solvent), λ is the wavelength of the incident light, and θ is the scattering angle. The hydrodynamic diameter (D_h) of the particles can be estimated from the Stokes-Einstein equation $\mathbf{D_h} = (\mathbf{k_B T})/3\pi\eta D_t$, where k_B is Boltzmann's constant, T is the absolute temperature, and η is the viscosity of the solvent. The size dispersity (Đ) is expressed as $Đ = \mu_2/\langle\Gamma\rangle^2$, where μ_2 is the variance of the decay rate and $\langle\Gamma\rangle$ is the average decay constant.[37,39] Based on Rayleigh scattering, the intensity of light scattered by a particle is proportional to the sixth power of the particle radius (the volume squared). This is why the average radius determined by DLS, which is reported most commonly and also known as the Z-average radius, is weighted by the volume squared.[34] The Z-average hydrodynamic diameter (D_h^Z) arises directly from cumulants analysis of the DLS data[34,35,40] and was used primarily in this work, as the cumulants method is described in ISO standards (ISO 13321 : 1996E and ISO 22412 : 2008E) and was validated for particles in a size range of 60-400 nm,[41] comparable to the complexes generated in this work. However Intensity, volume- and number-weighted particle size distributions can also be calculated from the intensity data using the Mie theory,[42] and are also reported herein for comparison.

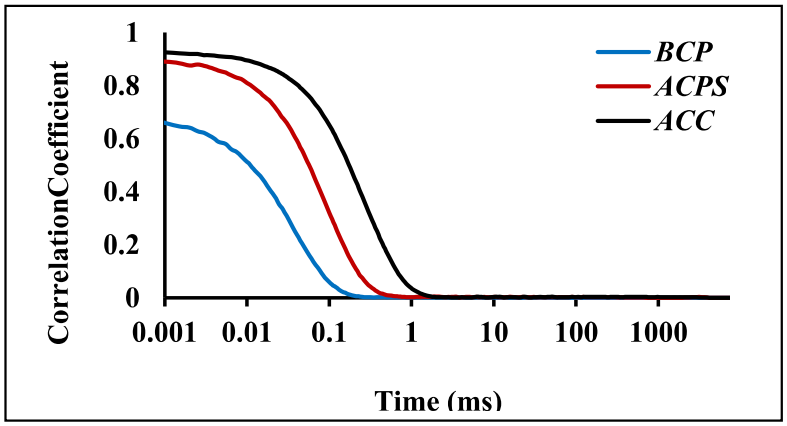

Figure 4-2. Correlation curves for PAA10-b-PS260 BCP (blue), G2 arborescent copolymer (red), and G2@PAA10-b-PS260 ACC (black).

4.5.2 Solution properties of arborescent copolymer substrates

The solution properties of the arborescent copolymer substrates (ACPSs) were investigated by DLS in THF, as these compounds are insoluble in toluene below 41 °C.[43] The intensity-weighted size distribution curves obtained for the G1–G4 ACPSs are provided in **Figure 4-3**. Narrow size distributions ($Đ \leq 0.08$) with one single population in the number-, volume- and intensity-weighted distributions were observed in all cases. The D_h^Z of the ACPS varied with the generation number as expected, with values of 38 ± 1, 73 ± 1, 92 ± 1, and 150 ± 1 nm for G1, G2, G3, and G4, respectively. The fact that the size of the substrates did not vary with their concentration (c = 0.1–1 mg/mL), as well as the low size dispersity obtained, demonstrate that the ACPSs exist as unimolecular species in THF. The solution properties of the PAA-*b*-PS copolymers are discussed in **Appendix B-1**. In that case, due to irreproducible results obtained in the DLS measurements, the D_h of the block copolymers was rather estimated from literature values of the intrinsic viscosity for PS.

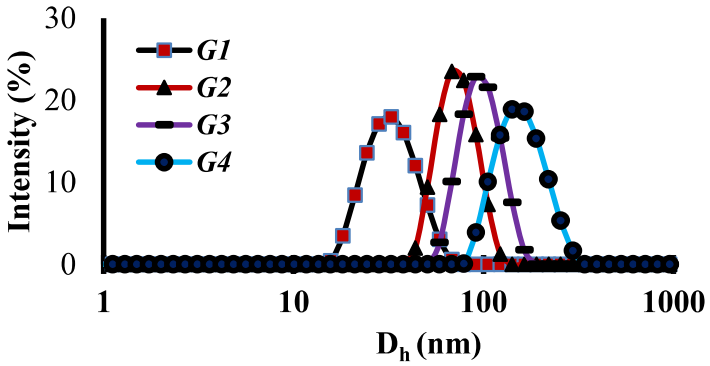

Figure 4-3. Size distribution curves for the arborescent copolymers at 0.8 mg/mL in THF.

4.5.3 The G1 ACC system

The complexation of PAA-*b*-PS with the 2-vinylpyridine copolymers was first investigated for the G1 substrate. The resulting complex was expected to have a core–shell–corona structure with a PS core, a P2VP/PAA inner shell, and a stabilizing PS layer forming a corona. Arborescent core–shell–corona templates obtained by ***anionic grafting***, with a structure similar to the ACC systems obtained by self-assembly, displayed interesting phase separation behavior in toluene after loading with metallic salts.[28] Since the ultimate objective of this work was to demonstrate the use of arborescent core–shell–corona templates obtained by ***complexation*** for the preparation of metallic nanoparticles, it would have been preferable to investigate the complexation reaction under exactly the same conditions, but this was obviously impossible due to the insolubility of the arborescent P2VP copolymers in pure toluene. Therefore the investigation was initiated in THF/ethanol mixtures (95/5, 90/10, or 80/20 by volume), starting with the G1 substrate in combination with the PAA10-*b*-PS85 or PAA13-*b*-PS390 copolymer, dissolved separately at 10 mg/mL. Selected results obtained for these initial attempts are presented herein.

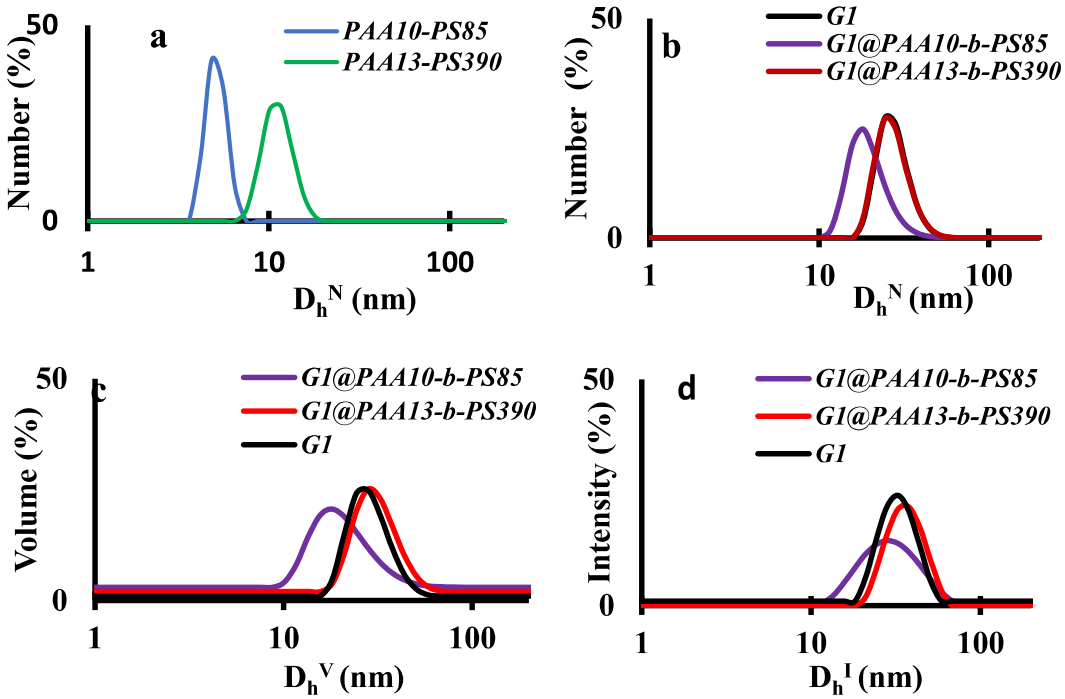

Figure 4-4. (a) DLS number-weighted size distributions for PAA10-b-PS85 and PAA13-b-PS390 in THF/ethanol mixture (90/10 V/V) at 5 mg/mL, and (b) number-weighted, (c) volume-weighted, and (d) intensity-weighted DLS size distributions for G1@PAA10-b-PS with different PS chain lengths in THF/ethanol mixture (90/10 V/V) at 0.8 mg/mL.

The block copolymer solution was added drop-wise to the G1 substrate solution, and allowed to stir for at least two days before it was diluted to 0.8 mg/mL with the same solvent for DLS analysis. The G1@PAA10-*b*-PS85 and G1@PAA13-*b*-PS390 complexes had monomodal size populations in intensity, volume and number distributions (**Figure 4-4**). This suggests the formation of well-defined complexes between the G1 arborescent substrate and the block copolymers, as no large-scale aggregation was detected. A low size dispersity ($Đ \leq 0.08$) was maintained, but the Z-average hydrodynamic diameter (D_h^Z) obtained for the G1@PAA10-*b*-PS85 complex was lower than the D_h^Z obtained for the parent G1 arborescent substrate. The D_h^Z values for G1@PAA10-*b*-PS85 were indeed 31 ± 1, 31 ± 1 and 29 ± 1 nm in 95/5, 90/10 and 80/20 THF/ethanol (v/v) mixtures by volume, respectively, as compared to 36 ± 1, 34 ± 1 and 32 ± 1 nm for the parent G1 substrate under the same

conditions. The modest decrease in D_h^Z for the complexes could be due to partial collapse of the P2VP chains in the shell upon complexation, as suggested by Zhang et al.[21,22] who observed a similar effect when core–shell micelles of PS200-*b*-PAA78 were complexed with a PEG45-*b*-P4VP56 double-hydrophilic block copolymer in ethanol. The decrease was attributed to the fact that even though a PEG corona was formed, it did not suffice to compensate for the collapse of the PAA component upon complexation with P4VP in the inner shell of the complex. In addition to structural collapse, another factor that may have contributed to the decrease in the current investigation is the relatively "open" or flexible structure of the G1 arborescent copolymer, with only 17 PS core branches and 83 P2VP shell chains (**Table 4-1**). As a result, the PAA10-*b*-PS85 component may be able to penetrate into the G1 copolymer substrate quite easily, resulting in a dense complex structure. An analogous explanation was provided to explain a size decrease observed in Langmuir-Blodgett films for poly(2-vinylpyridine)-*block*-poly(*tert*-butyl acrylate) heteroarm star terpolymer micelles derived from poly(styrene-*co*-divinylbenzene) microgel cores. In that case a size decrease from 55 ± 5 to 38 ± 5 nm, observed as the number of arms in the copolymers was varied from 18 to 56, was attributed to increased aggregation of the hydrophobic PS and P*t*BA blocks, leading to a more condensed structure.[44] Another study referred to a partial corona collapse when polybutadiene-*block*-poly(sodium methacrylate)-*block*-poly{2-[(methacryl-oyloxy)ethyl]trimethylammonium methyl sulfate} terpolymer micelles (D_h^Z = 214 nm) in aqueous media were complexed with poly(sodium 4-styrenesulfonate), leading to a D_h^Z decrease to 202 nm.[45]

To examine the influence of sample concentration, the 10 mg/mL G1@PAA10-*b*-PS85 complex solution was diluted to 0.2, 0.4, 0.8, 1.6 and 5 mg/mL for further characterization by DLS. All the samples exhibited single size populations in number, volume and intensity distributions at all concentrations, with only minor (almost insignificant) variations in the average diameters. The average values provided in **Figure 4-5a** were calculated for a series of at least 3 measurements, with the

uncertainties (error bars) corresponding to the standard deviation. It can be seen that the D_h^Z values measured for the G1@PAA10-*b*-PS85 complex over that concentration range in THF/ethanol mixtures in different ratios (95/5, 90/10 and 80/20 v/v) under all conditions ranged between 26–33 nm. When the solvent composition is considered, the size of the complexes was slightly larger in the 95/5 than in the 80/20 v/v THF/ethanol mixture. While no clear trend is observed in terms of the sample concentration within error limits, the D_h^Z values appear somewhat more consistent and nearly constant (~30 nm) from 0.8–10 mg/mL in the 90/10 v/v THF/ethanol mixture. The size dispersity was below 0.08 in all cases (**Figure 4-5b**), with slightly lower values obtained in the 80/20 v/v THF/ethanol mixture, but it is unclear whether the variations in dispersity observed among the different samples are significant, when considering the scattering observed among the data points in **Figure 4-5b**.

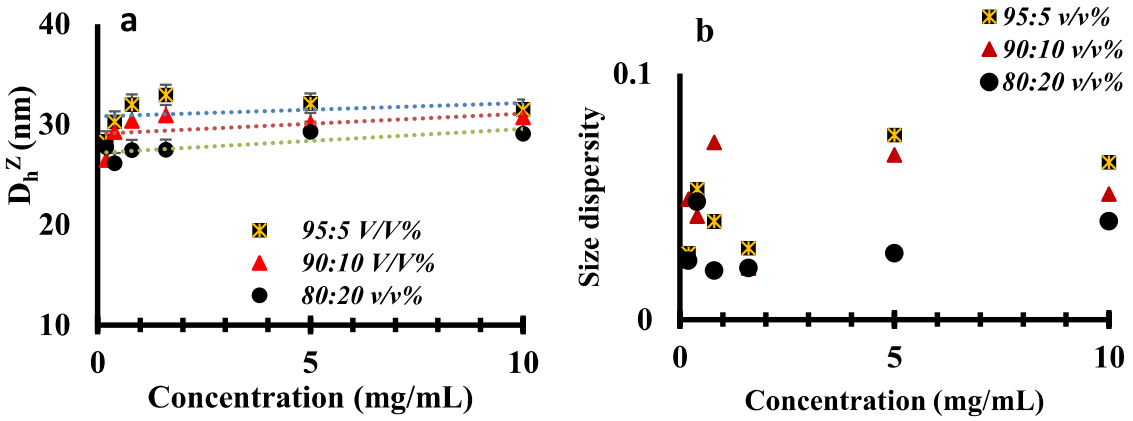

Figure 4-5. (a) Z-average hydrodynamic diameter (D_h^Z) and (b) size dispersity for G1@PAA10-PS85 ACC at different concentrations in THF/ethanol (95/5, 90/10, 80/20 v/v) mixtures. The D_h^Z of the substrate in THF/ethanol (95/5, 90/10, 80/20 v/v) was 36, 34 and 32 nm, respectively.

While the trends observed for the G1@PAA10-*b*-PS85 complex in the different THF/ethanol solvent compositions were somewhat unexpected, the complexation of the G1 substrate with block copolymers having longer PAA and PS blocks, namely PAA17-*b*-PS195 and PAA13-*b*-PS390, was also

investigated in the 90/10 v/v THF/ethanol mixture at a concentration of 0.8 mg/mL. The G1@PAA17-*b*-PS195 and G1@PAA13-*b*-PS390 complexes likewise exhibited monomodal size populations in number, volume and intensity distributions. The D_h^Z obtained for G1@PAA17-*b*-PS195 and G1@PAA13-*b*-PS390 complexes were 33 ± 1 and 35 ± 1 nm, respectively, larger than for G1@PAA10-*b*-PS85 (30 nm) and closer to the D_h^Z of the parent G1 substrate under the same conditions (34 nm). However these diameters are still lower than estimated by adding the D_h^Z of the substrate and twice the D_h of the block copolymers (**Appendix B-2, Table A4-2**), namely ~ 44 and 46 nm for G1@PAA17-*b*-PS195 and G1@PAA13-*b*-PS390, respectively, which is again consistent with collapse of the arborescent substrate upon complexation.

4.5.4 The G2 ACC system

The G2 copolymer complex was first investigated in 90/10 v/v THF/ethanol at 0.8 mg/mL, in combination with the PAA10-*b*-PS85 and PAA13-*b*-PS390 copolymers. The resulting complexes, G2@PAA10-*b*-PS85 and G2@PAA13-*b*-PS390, displayed single size populations in number, volume and intensity distributions, and a very low size dispersity (Đ = 0.02 in both cases). The hydrodynamic diameters (D_h^Z) obtained for G2@PAA10-*b*-PS85 and G2@PAA13-*b*-PS390 were 72 and 67 nm, respectively, as compared to 67 nm for the parent G2 substrate under the same conditions. Surprisingly, the longer BCP (PAA13-*b*-PS390) did not yield an increase in size while the shorter block copolymer (PAA10-*b*-PS85) produced a complex larger than the G1 substrate. In view of these apparently inconsistent results, a different solvent system was investigated for the formation of the complex, namely toluene/ethanol mixtures.

In toluene/ethanol (90/10 v/v) the D_h^Z of the G2 ACC increased relatively to the arborescent substrate in a more reasonable manner, the increase being larger for longer PS side chains: The G2 substrate had D_h^Z = 60 ± 1 nm in toluene/ethanol (90/10 v/v), while G2@PAA10-*b*-PS85 and G2@PAA13-*b*-PS390 were at 77 and 84 nm, respectively. This is also comparable with the values estimated from the size of

the isolated substrate and the block copolymers (< 5% difference), at 74 and 88 nm, respectively. The polydispersity of the complexes increased slightly relatively to the substrate but was still fairly low, with Đ = 0.07 and 0.11 for G2@PAA10-*b*-PS85 and G2@PAA13-*b*-PS390, respectively. The P2VP30K side chains in the ACPS would be expected to be mostly collapsed, as the substrate is not soluble in toluene below 41 °C.[43] Since the G2 ACPS is relatively dense (222 PS and 303 P2VP chains) as compared to the G1 substrate (17 PS and 83 P2VP side chains), we suggest that while the block copolymer could penetrate within the G1 ACPS, the formation of a complex with the G2 substrate more likely involved anchoring of the PAA block near the periphery of the P2VP shell.

Because the size variations with the PS block length were more consistent in the 90/10 v/v toluene/ethanol mixture, the influence of the BCP chain length was examined in more detail by DLS analysis at 0.8 mg/mL, for complexes obtained from PAA-*b*-PS copolymers with an equal number of AA units but different PS block lengths. Intensity- and number-weighted size distributions for a sample series containing 10 AA units, namely G2@PAA10-*b*-PS85, G2@PAA10-*b*-PS205, G2@PAA10-*b*-PS260 and G2@PAA10-*b*-PS305, are compared in **Figure 4-6**.

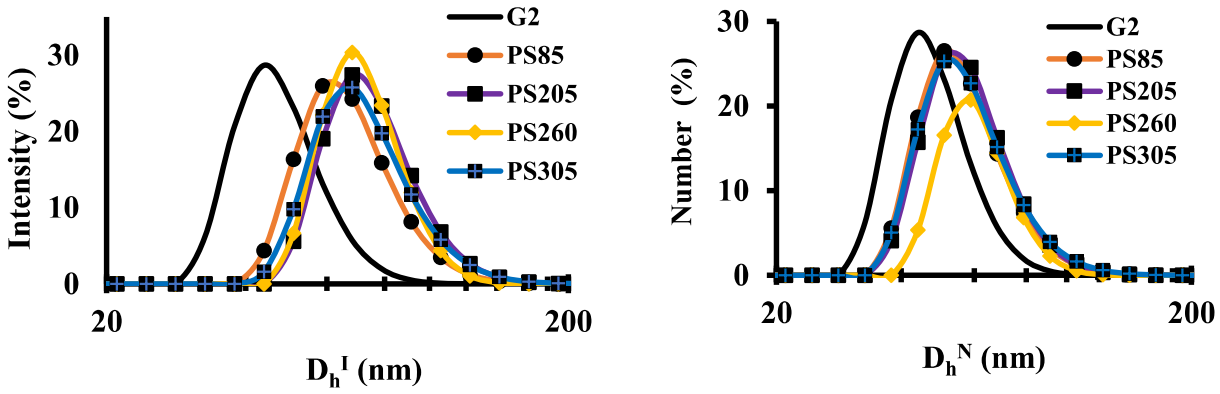

Figure 4-6. DLS intensity- (left) and number-weighted (right) size distributions for the G2 substrate and the G2@PAA10-b-PSx ACC with different PS chain lengths x in toluene/ethanol (90: 10 v/v) at 0.8 mg/mL.

It should be mentioned that after complexation, neither extensive aggregation nor side chain contaminants were detected in intensity, volume and number distributions, although the limitations of the DLS technique were discussed earlier. This observation, in particular when combined with the uniform spherical shape of the particles observed by AFM and TEM analysis (discussed in the subsequent sections), provides strong evidence for the formation of the complexes.[16] The D_h^Z of the complexes (74–81 nm), summarized in **Table 4-2**, was larger than for the parent G2 substrate (60 nm) under the same conditions, and larger increases were observed for BCPs with longer PS blocks. Very similar trends were observed when using copolymers with different PAA anchoring block lengths (**Figure 4-7a**). The influence of the PAA block size on the dimensions of the ACCs thus appears to be negligible in comparison with the PS block length (for a PS block DP_n = 85–395). The DLS data is provided in **Appendix B-2**, **Table A4-3**. The general trend for the G2-based systems shows that the D_h^Z of the complexes increased with the BCP block length, with a significant increase observed from the substrate (D_h^Z = 60 ± 1 nm) to the complexes (D_h^Z = 73 ± 1 nm to 90 ± 1 nm; **Figure 4-7a**). Since the D_h^Z values obtained by DLS for the block copolymers was deemed to be unreliable due to aggregation, their D_h was estimated using Mark–Houwink–Sakurada (MHS) parameters reported for polystyrene samples having a molecular weight identical with the block copolymers, as provided in **Appendix B-1** (**Table A4-2**). Unfortunately, these parameters are only available for pure solvents, and not for the solvent mixtures used in the current investigation, so these values should be viewed as approximate. In pure toluene, D_h for the block copolymers ranges from 7.2 nm (PAA10-*b*-PS85) to 13.7 nm (PAA17-*b*-PS395). Since D_h^Z for the G2 substrate was 60 nm, the theoretical diameter of the complex, estimated as $D_{h\ complex} = D_{h\ substrate} + 2D_{h\ copolymer}$, should therefore range from 74.4 to 87.4 nm. This calculation is obviously very approximate since, beyond the potential influence of ethanol on the dimensions of the block copolymer chains, it also assumes that the complexation process has no

influence on the conformation of the chains in the arborescent and the block copolymer components, and that complexation yields unimolecular ACC micelles. When comparing the experimentally determined D_h^Z with the corresponding theoretical values for the different ACCs in **Table 4-2** the agreement is generally very good, and follows the expected trend as a function of the PS segment length. One notable discrepancy is for G2@PAA10-*b*-PS85, with a D_h^Z (77 ± 1 nm) slightly larger than for G2@PAA10-*b*-PS205 (74 ± 1 nm). This may be related to the number of block copolymers attached to the substrate, which is larger for the ACC with the shorter PS block, and may favor a more extended chain conformation for G2@PAA10-*b*-PS85.

The experimentally determined aggregation number N^Z_{agg}, representing the average number of block copolymer molecules bound per arborescent copolymer, was estimated from the increase in z-average hydrodynamic volume[46,47] in the formation of the ACC and is reported in **Table 4-2**. Since equal masses of ACPS and BCP were used in the experiments, a theoretical aggregation number can also be calculated using the molecular weight of the ACPS and BCPs, if it is assumed that all the BCP chains are complexed, as $N_{agg(th)} = M_n(ACPS)/M_n(BCP)$; these are reported in **Table 4-2** for comparison. The calculated theoretical aggregation number $N_{agg(th)}$ is larger than the N^Z_{agg} values estimated from the hydrodynamic diameters in all cases, which may hint at the coexistence of free copolymer chains in the mixtures. It should be nevertheless considered that these calculations are very approximate since, beyond the potential influence of a small amount of aggregation on the diameters obtained, the calculations combine z-average diameters for the ACPS with diameters for the block copolymers estimated from viscometry. Partial collapse of the P2VP segments upon complexation, of the type hypothesized for the G1@PAAx-*b*-PSy substrates, would also explain the discrepancies observed.

Table 4-2. Hydrodynamic diameter, size dispersity and calculated block copolymer aggregation number (N_{agg}) for G2@PAA10-b-PS ACC with different PS block lengths in toluene/ethanol (90/10 v/v) mixtures.

Samples	D_h^Z (nm)	D_h^N (nm)	Đ	$D_h^Z{}_{(th)}$ (nm)	$N^Z{}_{agg}$	$N_{agg(th)}$
G2	60±1	48±1	0.02±0.01	-	-	-
G2@PS85	77±1	57±1	0.07±0.01	74±2	645	1100
G2@PS205	74±1	56±2	0.10±0.01	79±2	214	480
G2@PS260	79±1	55±1	0.13±0.01	80±2	277	390
G2@PS305	81±1	58±1	0.11±0.01	81±2	257	333

Aggregation number, $N^Z_{agg} = [D_h^Z(ACC)^3 - D_h^Z(ACPS)^3] / D_h(BCP)^3$; $N^N_{agg} = [D_h^N(ACC)^3 - D_h^N(ACPS)^3] / D_h^N(BCP)^3$. $N_{agg(th)}$ was calculated based on the molecular weights, $N_{agg(th)} = M_n(ACPS) / M_n(BCP)$.

In addition to potential variability in the calculations discussed above, some of the trends observed among the samples may hint at a low level of aggregation of the ACCs (i.e. the formation of a small amount of *multimolecular* ACCs, involving two or more ACPS molecules), which can have a large effect on the DLS results. Indeed, while the size dispersity of the G2 complexes (**Table 4-2**) remained relatively low (Đ ≤ 0.13), it was still clearly higher than for the substrate (Đ = 0.02), which suggests the formation of a small amount of multimolecular ACCs in the complexation process. The increase in Đ was also larger for block copolymers with longer polystyrene blocks ($DP_n \geq 300$; **Figure 4-7b**). This could be due to the formation of slightly elongated complexes and/or ACCs involving two ACPS molecules,[48] or else to small amounts of free block copolymer chains that could not be resolved as a second population in the DLS measurements. Imaging of the ACC samples by AFM, discussed in more detail later, appears to support this hypothesis (e.g. **Appendix B-3**, **Figure A4-3**). Furthermore, it has been reported that in complex formation, variations in the rate of addition of the two components can lead to size and size dispersity variations.[12] This may likewise have contributed to the differences observed, since an autotitrator was not used for the BCP addition in the current investigation.

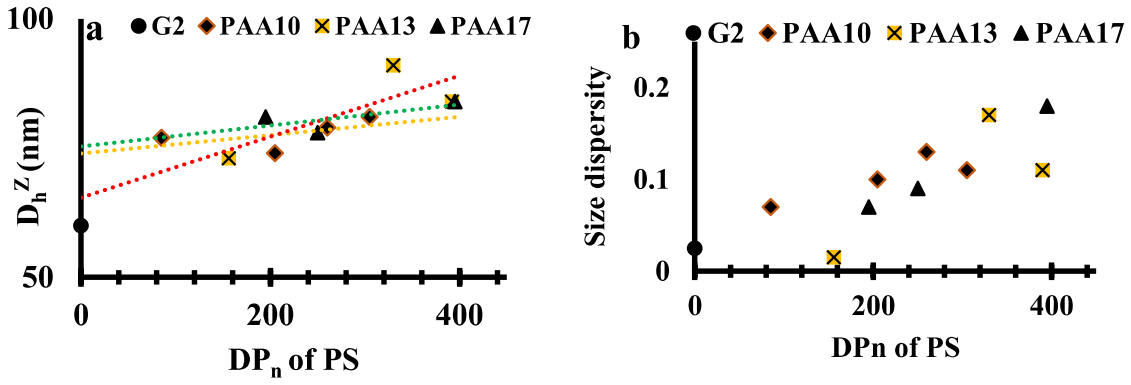

Figure 4-7. (a) Z-average hydrodynamic diameter and (b) size dispersity for G2@PAA-b-PS ACC with different PS block lengths in toluene/ethanol (90: 10 v/v) at 0.8 mg/mL.

The series of G2 complexes prepared in the toluene/ethanol mixture at 0.8 mg/mL from the BCP samples with 10 AA units, namely G2@PAA10-*b*-PS85, G2@PAA10-*b*-PS205, G2@PAA10-*b*-PS260 and G2@PAA10-*b*-PS305, were evaporated to dryness under vacuum and redissolved in pure toluene to obtain 0.8 mg/mL solutions. The hydrodynamic diameter of these complexes increased significantly after the solvent exchange to toluene (**Table 4-3)**: D_h^Z increased from 74–81 (± 1) nm in toluene/ethanol to 90–97 (± 1) nm in toluene. It seems unlikely that expansion of the polystyrene core in the ACPS would suffice to explain this increase, since their PS content was only about 10% by weight (**Table 4-1**). It is more likely due to expansion of the PS block in the block copolymers, or else to a small increase in the extent of ACC aggregation, although this was not clearly reflected in the PDI data (**Table 4-3**), the DLS distribution curves (**Appendix B-2**, **Figure** A4-2), nor TEM and AFM analysis (Section 4.5.8). To determine whether a low aggregation level might have influenced the DLS results, due to the poor solubility of the P2VP component in toluene, the D_h^Z for G2@PAA10-*b*-PS305 was measured at different temperatures between 25 and 70 °C. Only small and non-systematic variations in D_h^Z were observed, from 97 ± 1 nm at 25 °C to 105 ± 1 nm between 30-55 °C, 103 ± 1 nm at 55 °C and 102 ± 1

nm at 70 °C. Considering the good reproducibility of the results (standard deviations of 1–2 nm for the individual samples), aggregation due to unfavorable interactions between toluene and the P2VP phase of the ACCs seems unlikely to be at the origin of the size variations observed between the toluene/ethanol mixture and pure toluene.

Table 4-3. Comparison of the hydrodynamic diameter and size dispersity for G2@PAA10-b-PS ACCs in toluene/ethanol (90/10 v/v) mixtures and after solvent exchange to toluene.

Sample	Toluene/Ethanol (90/10 v/v)			Toluene		
	D_h^Z (nm)	D_h^N (nm)	Đ	D_h^Z (nm)	D_h^N (nm)	Đ
G2	60±1	48±1	0.02±0.01	-	-	-
G2@PS85	77±1	57±1	0.07±0.01	90±1	69±1	0.15±0.01
G2@PS205	74±1	56±2	0.10±0.01	94±1	76±2	0.06±0.05
G2@PS260	79±1	55±1	0.13±0.01	95±1	73±1	0.22±0.06
G2@PS305	81±1	58±1	0.11±0.01	97±1	71±2	0.10±0.02

The influence of concentration on the size of the complex was investigated systematically for sample G2@PAA13-*b*-PS390 by DLS. The complex was first prepared in triplicate at a concentration of 10 mg/mL from each component in a toluene/ethanol mixture (90/10 v/v), and then diluted to obtain samples at concentrations of 0.62, 1.25, 2.5 and 5 mg/mL. Three DLS measurements were completed for each sample (i.e. nine measurements for each concentration) to obtain size and size dispersity information. The results obtained (**Figure 4-8**) indicate that D_h^Z increased significantly with the sample concentration. It has been suggested that an increase in concentration can lead to changes in the size[49] determined by DLS due to multiple scattering, particle-particle interactions, and restricted diffusion.[41] To avoid these issues, DLS data can be extrapolated to infinite dilution. In the current case, however,

if the formation of ACCs is an equilibrium process, the trends observed in D^{Z}_{h} could also be due to a decrease in the number of BCPs becoming attached to the substrate with dilution.

The results in **Figure 4-8** show that as the concentration of G2@PAA13-*b*-PS390 was increased from 0.62 to 10 mg/mL, the D^{Z}_{h} increased from 69 to 94 nm, as compared to 60 nm for the bare G2 substrate. The diameter obtained at 5 mg/mL (84 nm) was comparable with the D^{Z}_{h}(th) value (86 nm). In comparison, the D^{N}_{h} values were comparable to the substrate (48 ± 1 nm) at lower concentrations, but larger at 5 and 10 mg/mL. Both intensity and number size distribution curves (**Figure 4-9**) are symmetrical, but the number-weighted size distribution curves do not show significant differences at the different concentrations, similarly to the average values.

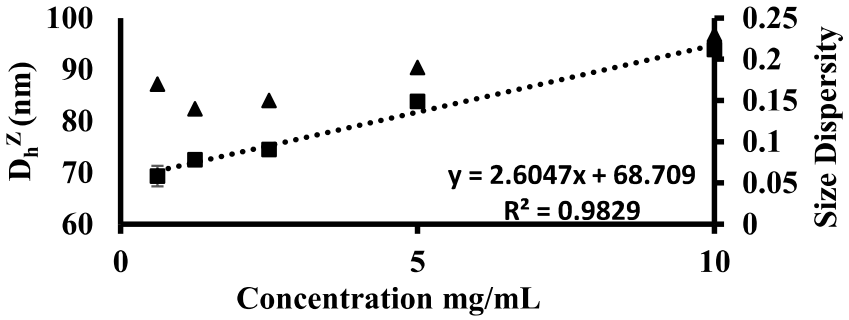

Figure 4-8. Hydrodynamic diameter (■) and size dispersity (▲) for G2@PAA13-b-PS390 in toluene/ethanol (90/10 v/v) at 0.62, 1.25, 2.5, 5 and 10 mg/mL overall concentrations. Since the errors are very small (~ ± 1 nm) except for the first data point (± 2 nm), the error bars are not visible because they are smaller than the data symbols.

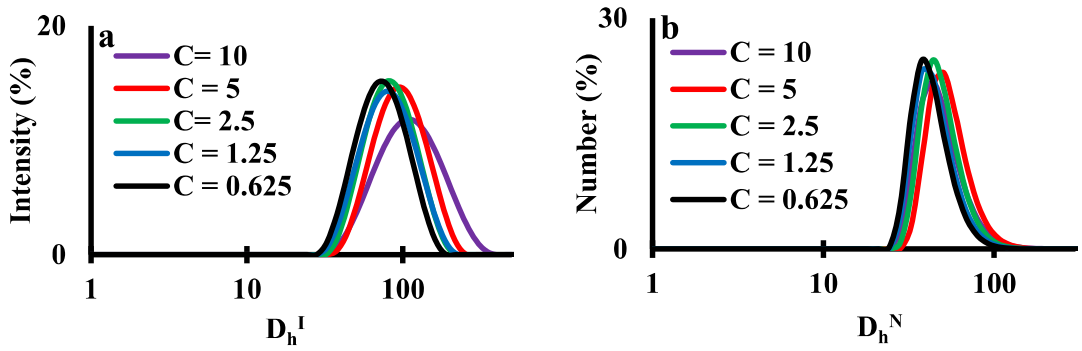

Figure 4-9. DLS intensity- (left) and number-weighted (right) size distributions for the G2@PAA13-b-PS390 ACC at different concentrations (mg/mL) in toluene/ethanol (90:10 v/v).

To determine whether free (non-complexed) side chains could be resolved by DLS, the G2 substrate was mixed with the protected (non-interacting) PtBA13-*b*-PS390 copolymer in a 1:1 ratio in the 90:10 v/v toluene/ethanol mixture and characterized. The intensity, volume and number distributions obtained for the mixture are depicted in **Figure 4-10.** Two populations are clearly visible in the intensity and volume distributions, with sizes corresponding to the substrate and the BCP. While the intensity distribution highlighted mostly (85%) the larger ACPS molecules, the volume and number distributions yielded a dominant BCP component (81% and 99%, respectively). In the number distribution, in particular, the dominant smaller population (12 nm) has a size essentially identical with the value measured for the protected pure block copolymer (13 nm) in **Figure 4-10a** and consistent with reported values for PS of comparable molecular weight in a good solvent.[50,51] Unfortunately, attempts to detect the block copolymer at lower BCP:ACPS ratios and for shorter block copolymers were not as successful, presumably due to the larger differences in relative scattering intensities for the two components.

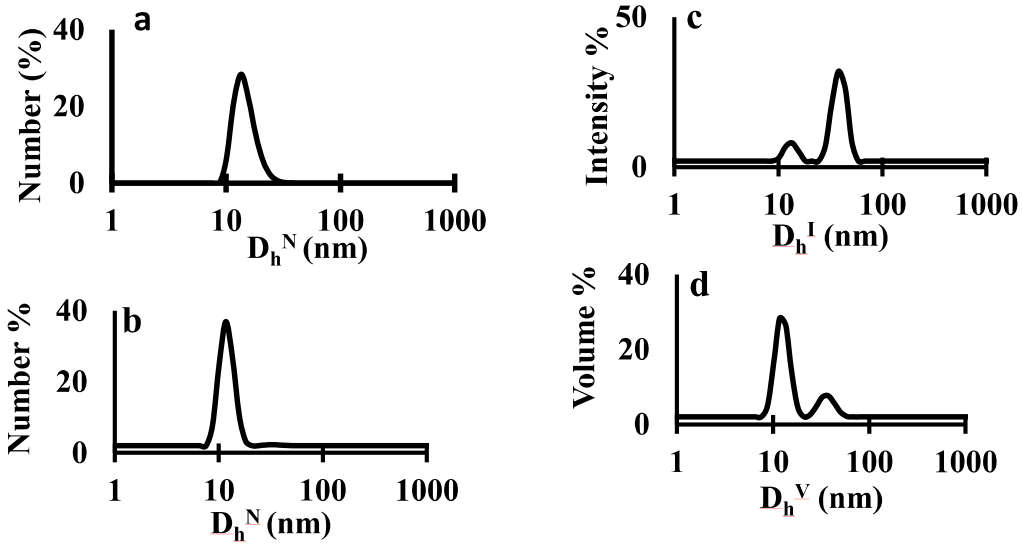

Figure 4-10. DLS size distribution results: (a) number-weighted distribution for PtBA13-b-PS390, and (b) number -, (c) intensity - and (d) volume -weighted distributions for a 1:1 w/w G2 and PtBA13-b-PS390 mixture in toluene/ethanol (90/10 v/v).

To investigate the influence of the BCP:ACPS mass ratio on the size of the ACCs, a series of G2@PAA13-*b*-PS390 samples in toluene/ethanol (90/10 v/v) at 0.8 mg/mL overall concentration were prepared at BCP:G2 ACPS mass ratios of 1–8. The hydrodynamic diameter (D_h^Z) obtained in each case, provided in **Figure 4-11**, increased as the mass ratio was varied from 1 to 8. This could be attributed to many factors. Beyond the concentration dependence issues discussed above for DLS measurements, these results could be interpreted in different ways. The weight fraction of PS in the ACCs increases with the BCP:ACPS mass ratio, which may cause the complex to swell increasingly due to favorable interactions with toluene. Increased PS-PS chain interactions can also cause the chains to partly stretch as more BCP chains are added.[52] Yet another possible explanation for this observation would be bridging between adjacent ACC micelles, but this seems unlikely since as the BCP:ACPS mass ratio is increased, the probability for the BCP substrates to interact with other ACPSs should decrease.[53]

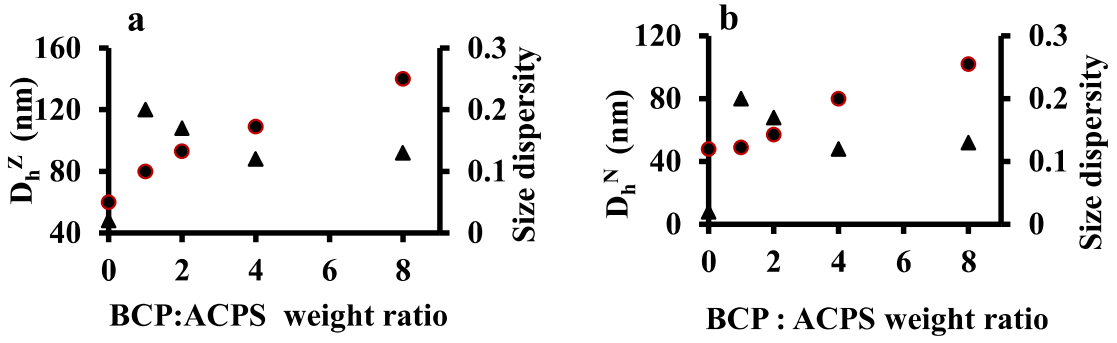

Figure 4-11. (a) Z-average and (b) number-weighted hydrodynamic diameter (●) and size dispersity (▲) for G2@PAA13-b-PS390 with different mass ratios of G2:PAA13-b-PS390 in toluene/ethanol (90:10 v/v) mixture at 0.8 mg/mL.

4.5.5 The G3 ACC system

The G3 arborescent copolymer was found to be poorly soluble in the 90:10 (v/v) toluene/ethanol mixtures, as the solution clogged 0.45 μm PTFE filters, and the D_h^Z obtained without filtration was unrealistic (700 ± 54 nm). Consequently, THF was selected as solvent for complex formation. The substrate (D_h^Z = 92 nm) was thus assembled in THF with the PAA-*b*-PS copolymers (0.8 mg/mL) having different PS block lengths. The THF was then removed under vacuum and replaced with an equal volume of toluene. The size and size distribution of the complexes were determined by DLS analysis in both THF and toluene.

The intensity- and number-weighted size distributions obtained are presented in **Figure 4-12** for the G3@PAA10-*b*-PS85, G3@PAA10-*b*-PS205, G3@PAA10-*b*-PS260 and G3@PAA10-*b*-PS305 complexes. The average D_h^Z of all the complexes in this series was 94 ± 1 nm in THF, only ~2 nm larger than the parent G3 substrate (92 nm). However after the THF was removed and replaced with toluene, D_h^Z increased significantly to 110-119 nm, larger than for the G3 substrate and the complexes prepared in THF. Detailed information on the D_h^Z and the size dispersity, along with D_h^N (for

comparison) for the G3 ACCs in THF and in toluene, is provided in **Table A4-4**. The D_h^Z values obtained in toluene for G3@PAA10-*b*-PS85, G3@PAA10-*b*-PS205, G3@PAA10-*b*-PS260 and G3@PAA10-*b*-PS305 ACCs were 118, 110, 114, and 119 nm, respectively. In spite of the fact that the bare G3 substrate was poorly soluble in toluene, the increased D_h^Z of the complexes in toluene relatively to the substrate (in THF) is still consistent with the attachment of the PS segments on the substrate. The increase in D_h^Z scales with the PS block length, with the exception of G3@PAA10-*b*-PS85 (D_h^Z = 118 nm). The higher average D_h^Z of G3@PAA10-*b*-PS85 is likely to be due to a low level of aggregation of that sample, as was confirmed by AFM imaging (*vide infra*). The D_h^N values obtained in THF for all the samples were lower than for the parent substrate, but in toluene they were larger (G3@PAA10-*b*-PS205), and somewhat less consistent than the D_h^Z values. The size dispersity of the complexes also increased from the substrate (Đ = 0.07) and was higher in toluene than in THF, reaching a maximum value (Đ ≤ 0.21) for G3@PAA10-*b*-PS85, again hinting at aggregation of that sample.

For complexes G3@PAA13-*b*-PS156, G3@PAA13-*b*-PS330 and G3@PAA13-*b*-PS390, prepared from the G3 substrate (D_h^Z = 92 nm) and the BCP samples with 13 AA units, the D_h^Z obtained in THF was 99, 95 and 93 nm, while in toluene it was 117, 119 and 89 nm, respectively. Therefore D_h^Z increased significantly in toluene for G3@PAA13-*b*-PS156 and G3@PAA13-*b*-PS330 relatively to the substrate (measured in THF), while there was no significant change (89 nm) for the complex with the longest PS block (G3@PAA13-*b*-PS390), albeit a low D_h^Z value (93 nm) was obtained for the complex in THF. It should also be noted that G3@PAA13-*b*-PS390 had a higher size dispersity (Đ = 0.36) than G3@PAA13-*b*-PS156 (Đ = 0.13) and G3@PAA13-*b*-PS330 (Đ = 0.25). It remains unclear why D_h^Z was lower for the G3@PAA13-*b*-PS390 complex than for the G3 substrate and the other ACCs. If an insufficient amount of BCP were adsorbed on the ACPS, it would indeed be expected to aggregate and give a higher D_h^Z. This could also be related to the presence of free BCP chains, even though the size

distribution curves (**Figure 4-13**) only displayed a single size population in both number and intensity distributions.

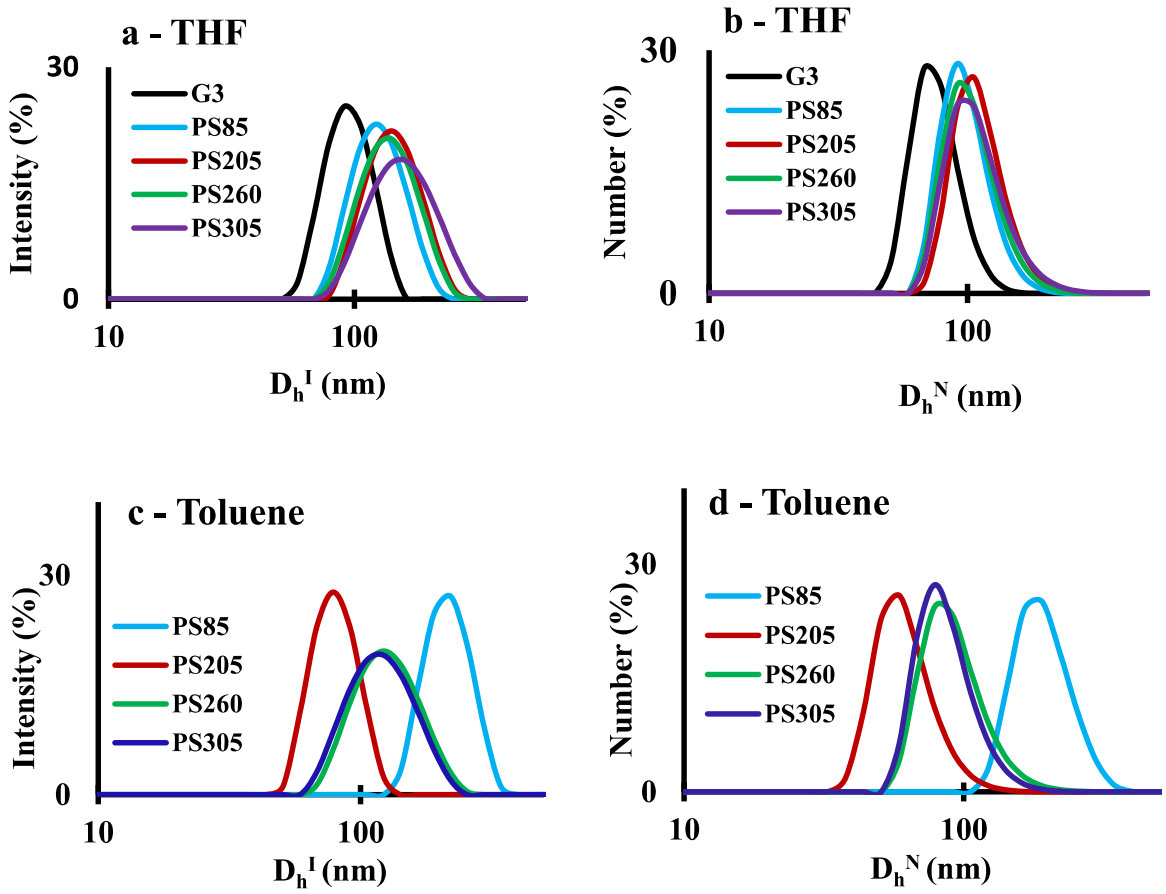

Figure 4-12. Intensity-weighted (a, c) and number-weighted (b, d) size distributions for G3 substrate and for 1:1 w/w ratio complexes with PAA10-b-PS having different PS block lengths at 0.8 mg/mL, in THF (a, b) and toluene (c, d).

The size distributions expressed as D_h^Z for the G3@PAA-*b*-PS complexes as a function of the PS block length, provided in **Figure 4-13**, show that in toluene the size was generally larger than in THF, regardless of the PS segment length, while in THF there was no appreciable difference between the ACCs and the substrate. It would make sense that the P2VP shell be collapsed in toluene, while the

stabilizing PS corona chains remain flexible. Since the PS core for the G3 substrate is larger than for the G1 and G2 substrates, while the P2VP segments are shorter, toluene swelling the PS core may lead to a larger size increase than for the G1 and G2 substrates. This may have contributed to the observed size increases, in addition to the PS corona. A small amount of aggregation may also have biased the results. The size dispersity remained relatively low (Đ ≤ 0.1) in THF but increased in toluene (Đ ≤ 0.36), except for G2@PAA10-*b*-PS260 (Đ = 0.08; **Figure 4-14**).

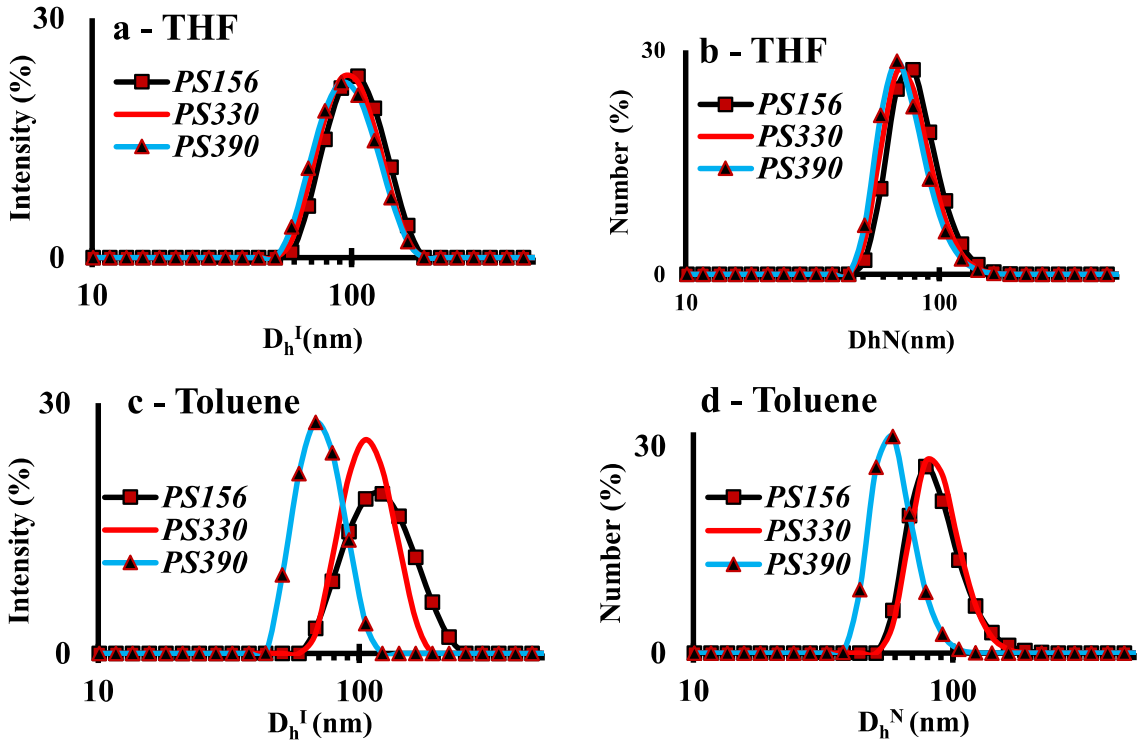

Figure 4-13. Intensity-weighted (a, c) and number-weighted (b, d) size distributions for a 1:1 w/w % complex of G3 and PAA13-b-PS with different PS chain lengths in THF(a, b) and in toluene (c, d) at 0.8 mg/mL.

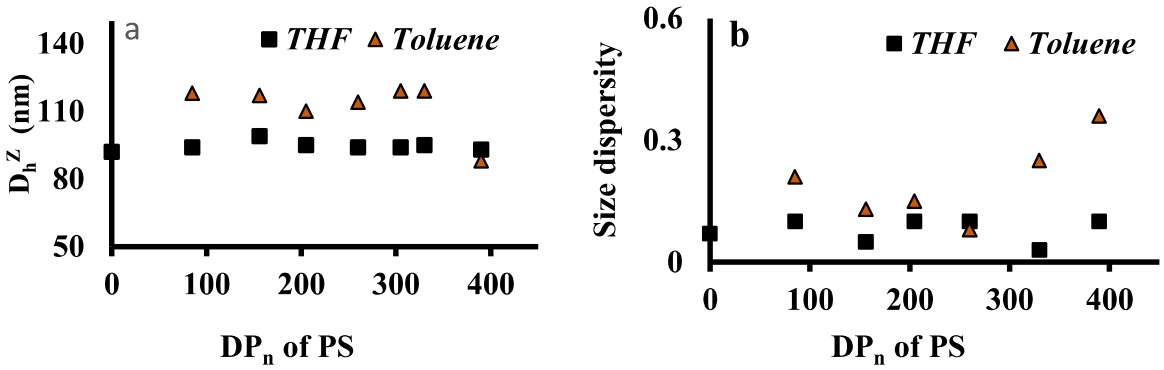

Figure 4-14. Z-average hydrodynamic diameter (a), and size dispersity (b) as a function of the PS DP_n for the BCP in G3@ PAA-b-PS complexes in THF (■) and toluene (▲) at 0.8 mg/ml.

4.5.6 The G4 ACC system

Similarly to the G3 substrate, the G4 ACPS was poorly soluble in the toluene/ethanol (90:10 v/v) mixtures: The solutions could not pass through a 0.45 µm PTFE filter, and D_h^Z without filtration was 1400 ± 300 nm. Therefore complex formation was likewise investigated in THF at 0.8 mg/mL; the THF was then removed and replaced with an equal volume of toluene. The G4 ACPS, with D_h^Z = 150 nm in THF, was mixed with PAA-*b*-PS having different segment lengths, and the size and size dispersity of the complexes were measured by DLS in both THF and toluene.

The DLS size distribution curves for the G4 substrate and for G4@PAA10-*b*-PS85, G4@PAA10-*b*-PS205, and G4@PAA10-*b*-PS260 complexes in THF are compared in **Figure 4-15**; a single population was observed in intensity, volume, and number distributions. The D_h^Z obtained for the G4@PAA10-*b*-PS85, G4@PAA10-*b*-PS205, and G4@PAA10-*b*-PS260 ACCs in THF was 183, 156 and 167 nm, respectively. The size therefore increased significantly (6–23 nm) in all cases for the complexes relatively to the substrate in THF, in contrast to the lower generations which only yielded 2–7 nm increases. The larger increase observed when the shorter block copolymer (PAA10-*b*-PS85) was used may be related to a low aggregation level. The D_h^Z and the size dispersity values obtained for the G4 complexes in THF and in toluene are provided in **Appendix B** (**Table A4-5**), with D_h^N included for

comparison. The D_h^Z in toluene for G4@PAA10-*b*-PS85, G4@PAA10-*b*-PS205, and G4@PAA10-*b*-PS260 complexes were 206, 154 and 160 nm, respectively, namely up to 56 nm larger (for G4@PAA10-*b*-PS85) than in THF. This larger increase could be due to aggregation, as the shorter PS85 blocks may not suffice to shield interparticle interactions. The size dispersity indeed remained below 0.05 in THF, but increased to 0.15 in toluene. Since the DLS size distribution curves (**Figure 4-16**) for the G4@PAA13-*b*-PS ACCs with different PS block lengths in THF and in toluene both show single size populations in intensity, volume, and number distributions, it does not appear that the aggregate population can be resolved from the main ACC population, but this nevertheless led to an increase in size dispersity.

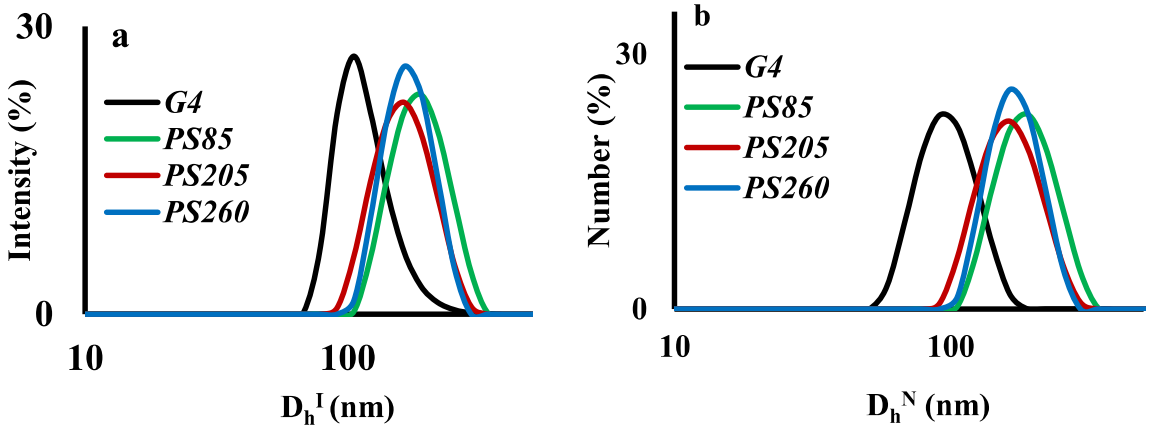

Figure 4-15. (a) Intensity-weighted and (b) number-weighted DLS size distributions for the G4 substrate and the G4@PAA10-b-PS ACC with different PS chain lengths in THF at 0.8 mg/mL.

The D_h^Z of the G4@PAA10-*b*-PS complexes for different PS block lengths in THF and in toluene are compared in **Figure 4-17a**, while the corresponding size dispersity values are provided in **Figure 4-17b**. The size dispersity for the ACC is lower in THF than in toluene, or else comparable in both solvents (for G4@PAA10-*b*-PS205, Đ = 0.05 in THF and 0.03 in toluene).

The D_h^Z values for the G4@PAA13-*b*-PS156, G4@PAA13-*b*-PS330, and G4@PAA13-*b*-PS390 ACCs in THF and in toluene are compared in **Figure 4-17c**. In THF the size increased significantly relatively to the substrate (150 nm) to 165, 171, and 169 nm for G4@PAA13-*b*-PS156, G4@PAA13-*b*-PS330, and G4@PAA13-*b*-PS390, respectively. The size increase in toluene was much more noticeable for the G4@PAA13-*b*-PS330 and G4@PAA13-*b*-PS390 ACCs, however, to 415 and 273 nm, respectively. In contrast, the size of G4@PAA13-*b*-PS156 (148 nm) in toluene was comparable to the substrate in THF. The size dispersity of the G4@PAA13-*b*-PS ACCs was likewise lower in THF ($Đ \leq 0.07$) than in toluene, reaching $Đ = 0.6$ for G4@PAA13-*b*-PS330 (**Figure 4-17d**). While this is very large as compared with other dispersity values reported in this thesis, the analysis was still considered reliable since the DLS instrument provider (Malvern Instruments) suggests that samples with $Đ \geq 0.7$ are considered to have very broad size distributions. Values in that range were not observed for any of the samples reported in this thesis.

The D_h^Z and the corresponding size dispersity values for the G4@PAA10-*b*-PS and G4@PAA13-*b*-PS ACCs are compared in **Figure 4-17e** and **Figure 4-17f**, respectively. D_h^Z increased for the ACCs relatively to the substrate, in both THF and toluene, in all cases except for G4@PAA13-*b*-PS156 in toluene, which yielded a size comparable with the substrate. The D_h^Z of the ACC was slightly lower in toluene than in THF for BCPs with shorter PS blocks (≤ PS260), namely G4@PAA10-*b*-PS85, G4@PAA13-*b*-PS156, G4@PAA10-*b*-PS205, and G4@PAA10-*b*-PS260, but for longer PS blocks (G4@PAA13-*b*-PS330 and G4@PAA13-*b*-PS390), the D_h^Z increase was over twice that in THF. As in the previous cases, the size dispersity for the ACCs was lower in THF than in toluene (**Figure 4-17f**): In THF, $Đ \leq 0.08$ for all the samples, while in toluene it reached up to 0.6 for G4@PAA13-*b*-PS330. This large Đ value is consistent with aggregation of the ACC, as well as possibly the presence of free (non-complexed) BCP molecules. As discussed in the following section, free BCP contaminant was

visible in the AFM images for the G4 ACC samples, as a second population of smaller particles presumably corresponding to aggregated BCP molecules.

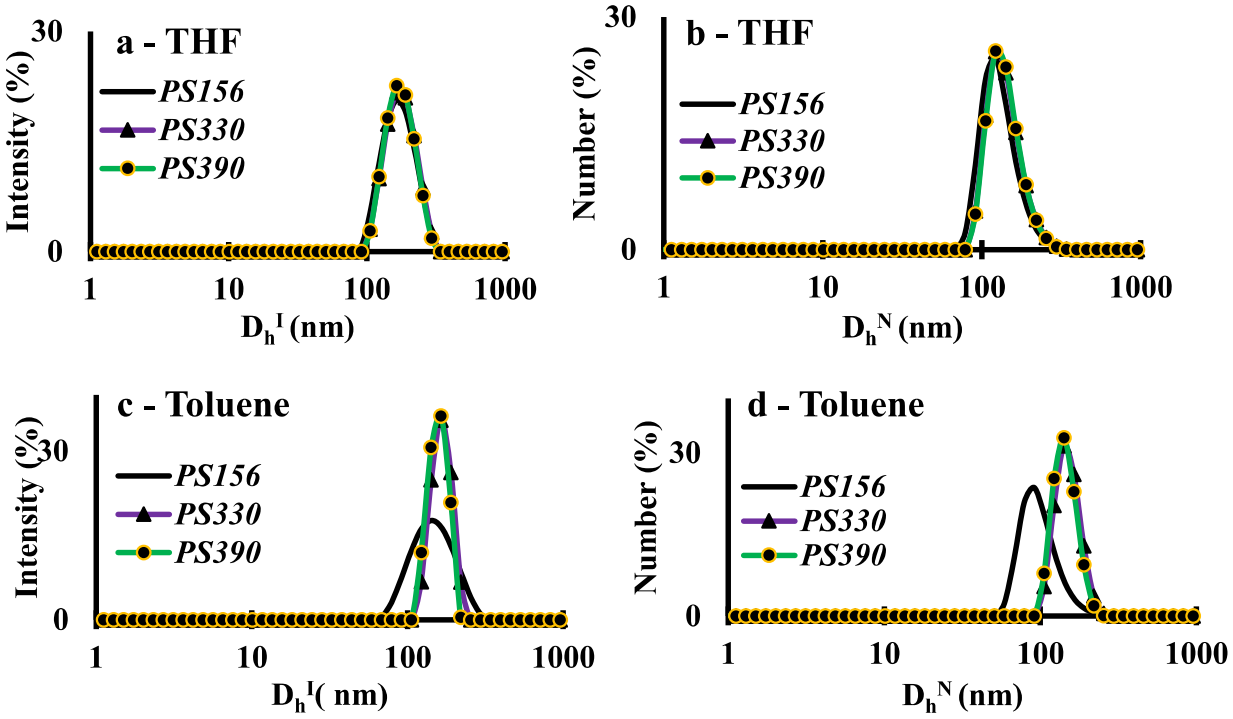

Figure 4-16. Intensity-weighted (a, c) and number-weighted (b, d) DLS size distributions for G4@PAA13-b-PS with different PS chain lengths in THF (a, b) and toluene (c, d) at 0.8 mg/mL.

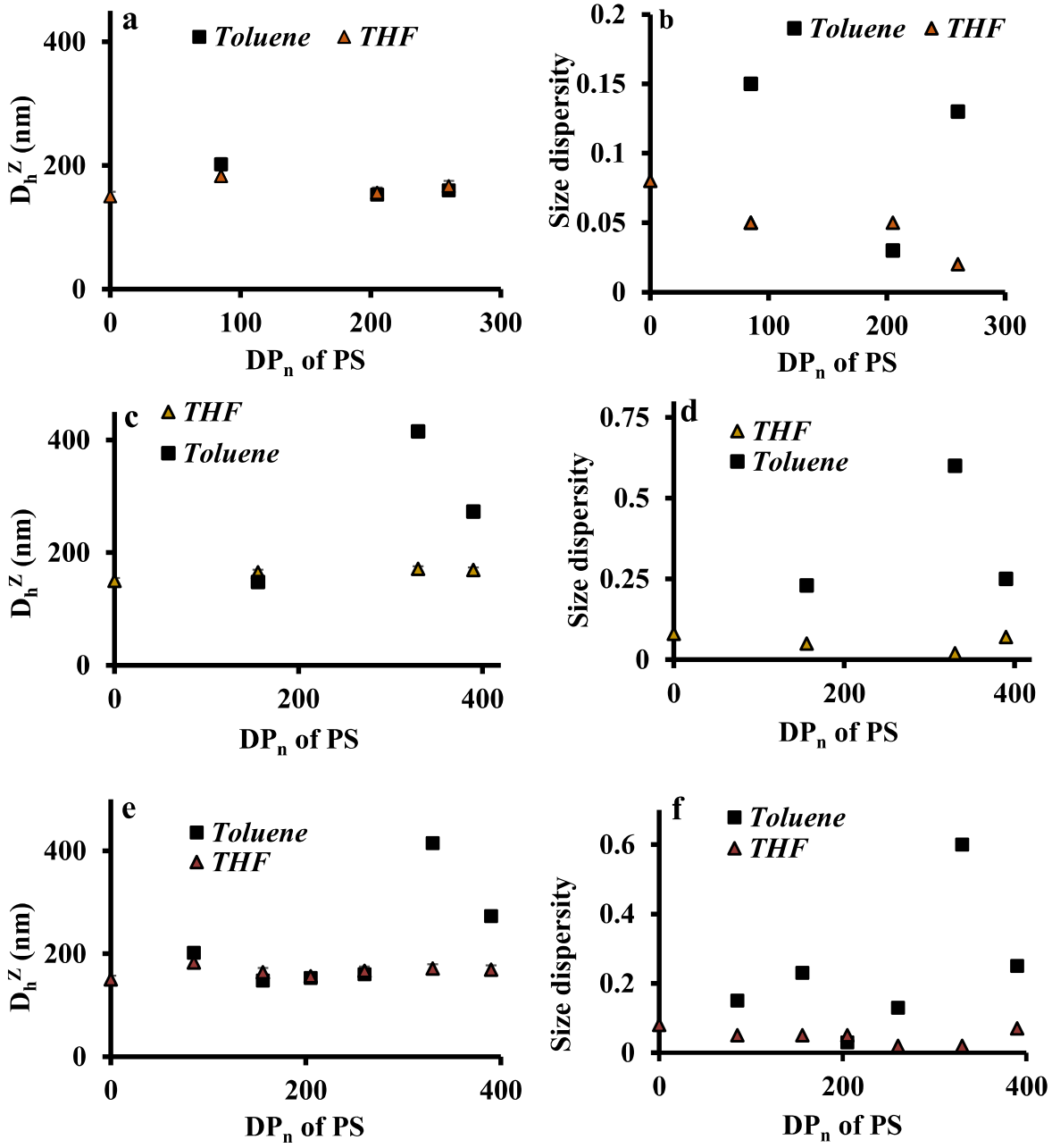

Figure 4-17. Z-average hydrodynamic diameter (a, c), and size dispersity (b, d) for G4@PAA10-b-PS (a, b) and G4@PAA13-b-PS (c, d) with different PS block lengths in toluene (▲) and in THF (■) at 0.8 mg/mL. Z-average hydrodynamic diameter (e) and size dispersity (f) for G4@PAA10-b-PS ACCs and G4@PAA13-b-PS ACCs.

In conclusion, it was shown in the DLS investigations that the size of the ACCs increased with the generation number (G2–G4) of the arborescent substrate in toluene, and a significant D_h^Z increase was

observed relatively to the substrates in most cases. The length of the PAA segments did not appear to influence the size and size dispersity of the complexes. Unfortunately the DLS results are inconclusive on their own, due to some inconsistent results which could be due either to a low level of aggregation of the ACCs, and/or to the presence of free BCP not resolved in the DLS measurements, albeit the occurrence of aggregation, in particular, could be inferred from the significant increases in size dispersity observed. Consequently, the ACCs were also investigated by TEM and AFM analysis, to gather additional information on the presence of aggregates and free BCP chains.

4.5.7 Thin film properties of the ACPSs

To provide baseline data, the arborescent P2VP copolymers were first investigated as thin (monomolecular) films by AFM and TEM to obtain information on their size and size distribution, to visualize their morphology, and to make visual comparisons among the samples. To that end, solutions of the ACPSs in THF were cast onto TEM grids and mica substrates.

For AFM imaging in the tapping mode, it can be seen from **Figure 4-18a** that the G1 copolymer has spherical PS cores protruding from the P2VP chains forming a thin and continuous layer (**Appendix B-3**, **Figure A4-3**) due to strong interactions with the mica surface.[54,55] The G1 copolymers are obviously more flexible and interpenetrable than their higher generation analogues, which makes the visualization of individual molecules difficult. The center-to-center spacing of the protruding cores for the G1 copolymer was 33 ± 3 nm, which also corresponds to the average diameter calculated for the molecules if these are assumed to be non-interpenetrating (which is unlikely to be the case in practice). The G2 copolymer (**Figure 4-18b**) yielded a better defined spherical topology, with a diameter of 57 ± 4 nm. Even though solutions of the same concentration were used for the preparation of all the samples, the density of molecules on the mica surface appeared lower in this case, but this could be due to variations in the random distribution of molecules on the mica surface during the drop casting process, and AFM images being recorded at random locations of the film. At least 20 individual particles on the

image were measured manually using the ImageJ software. In contrast to the G1 polymer, the G2 molecules do not display a clear core–shell morphology, probably due to their higher P2VP branching functionality (more rigid structure). In the AFM image a few smaller rigid particles are detected, which could be due to the presence of a minor amount of G1PS contaminant. Even though 4 cycles of precipitation fractionation in a mixture of THF/methanol (4/1 v/v) and *n*-hexane were performed, it seems that these species could not be totally removed. The G3 molecules (**Figure 4-18c**) had a diameter of 73 ± 5 nm, with likewise a round shape and no distinguishable core–shell morphology, again likely due to its high branching functionality. Finally, the G4 molecules (**d**) also had a round shape with a diameter of 95 ± 5 nm, but a close look at the height images show that their surface is not completely smooth: Fine details can be observed that appear to match a cauliflower morphology. Overall, all the ACPS molecules therefore displayed globular morphologies in AFM analysis, without clear phase separation between the PS and the P2VP phases except the G1 molecules, likely due to the relatively large size of the P2VP side chains (M_n = 27700 g/mol) and the small size of the G0PS core. The size of the molecules increased with the generation number as expected (**Table 4-4**).

Transmission electron microscopy (TEM) pictures for the G1-G4 ACPSs, obtained after casting from THF solutions and staining of the P2VP phase with iodine, are provided in **Figure 4-18**. The diameter of the ACPSs from TEM analysis (**Table 4-4)** increases with the generation number, in agreement with the AFM and DLS results. Similarly to the AFM images, the TEM pictures yield a round shape for all the ACPSs. While the resolution of the pictures is poor, many G2 copolymer molecules display a slightly brighter spot near their center, presumably corresponding to the (unstained) PS core. Such a core–shell morphology is not visible in the higher generation (G3 and G4) copolymers (insets of **Figure 4-19c** and **d**), probably because of their increased thickness relatively to the G2 molecules (3.3, 12 and 23 nm for the G2, G3 and G4 molecules, respectively, obtained from AFM section analysis).

Comparing the sizes obtained by the different methods (**Table 4-4**), as expected the D_h^Z obtained by DLS analysis is larger than the size obtained by both AFM and TEM analysis, due to swelling of the molecules by the solvent. When the sizes obtained by AFM and TEM imaging are compared, both derived from dry films, the size from TEM is larger for the G2-G4 molecules, either due to more extensive flattening on the TEM copper grids, or to partial interpenetration of the P2VP shells in the AFM samples, given the higher density of molecules on the mica surface. The G1 copolymer did not show significant size differences by the different analysis methods within error limits, however.

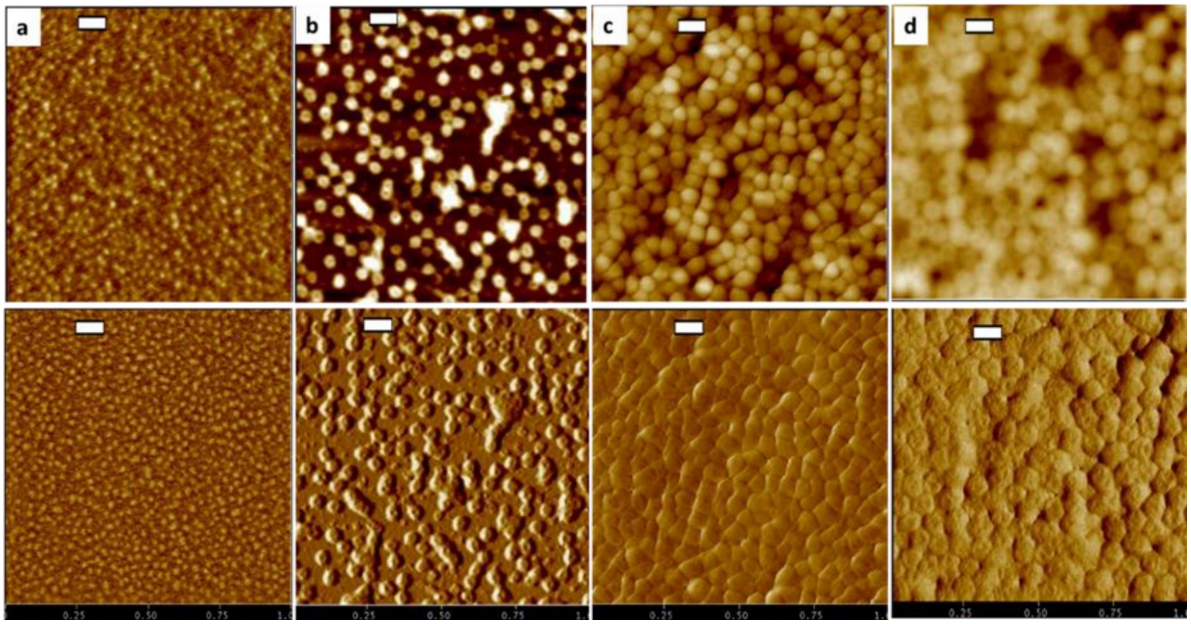

Figure 4-18. AFM height (top) and phase (bottom) images for (a) G1, (b) G2, (c) G3, and (d) G4 arborescent copolymers (scale bar = 100 nm).

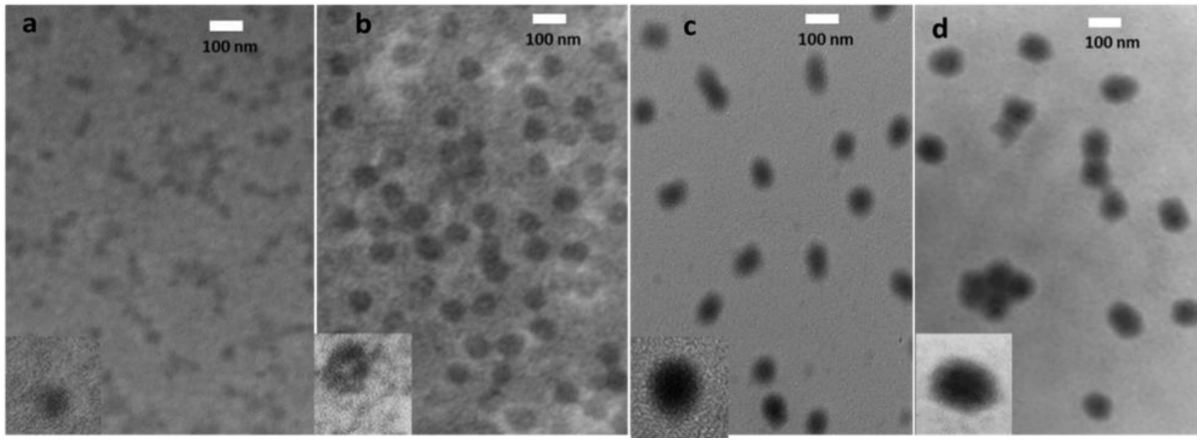

Figure 4-19. TEM images for (a) G1, (b) G2, (c) G3, and (d) G4 arborescent copolymers stained with iodine.

Table 4-4. Characterization of the ACPSs by DLS, AFM, and TEM.

	DLS			AFM [a]		TEM [a]
Sample	D_h^Z(nm)	D_h^N(nm)	Đ	D(nm)	Height (nm)	D (nm)
G1	38±6	28±1	0.08±0.02	33±5	1±0.2	28±6
G2	73±1	58±2	0.03±0.02	57±4	5.3±0.8	64±3
G3	92±1	73±2	0.07±0.01	73±5	12±2	90±6
G4	150±1	123±7	0.08±0.02	95±5	23±3	124±10

a) Obtained from at least 20 measurements using the ImageJ software.

4.5.8 Thin film imaging of the G1 ACC system

The AFM and TEM images obtained for the complex with a 1 : 1 (w/w) ratio of G1 arborescent substrate and PAA10-*b*-PS85 in toluene (transferred from THF/ethanol 90/10) are presented in **Figure 4-20**. In the AFM pictures, individual complex micelles of uniform size can be seen with a diameter (for at least 20 individual particles) of 29 ± 3 nm, slightly larger (within error limit) than the G1 arborescent copolymer substrate (27 ± 3 nm, cast from a THF solution). In contrast, TEM analysis yielded a much smaller size, 17 ± 3 nm, presumably because the PS segments forming the shell are not stained, and

therefore invisible. A lighter center, corresponding to the PS core of the molecules, is also visible in some of the particles. The investigation of the G1 ACC systems was not pursued further, as our main interest lied in the higher generation (G2-G4) systems, that were shown to display interesting phase morphologies in a previous study of molecules obtained by anionic grafting.[56]

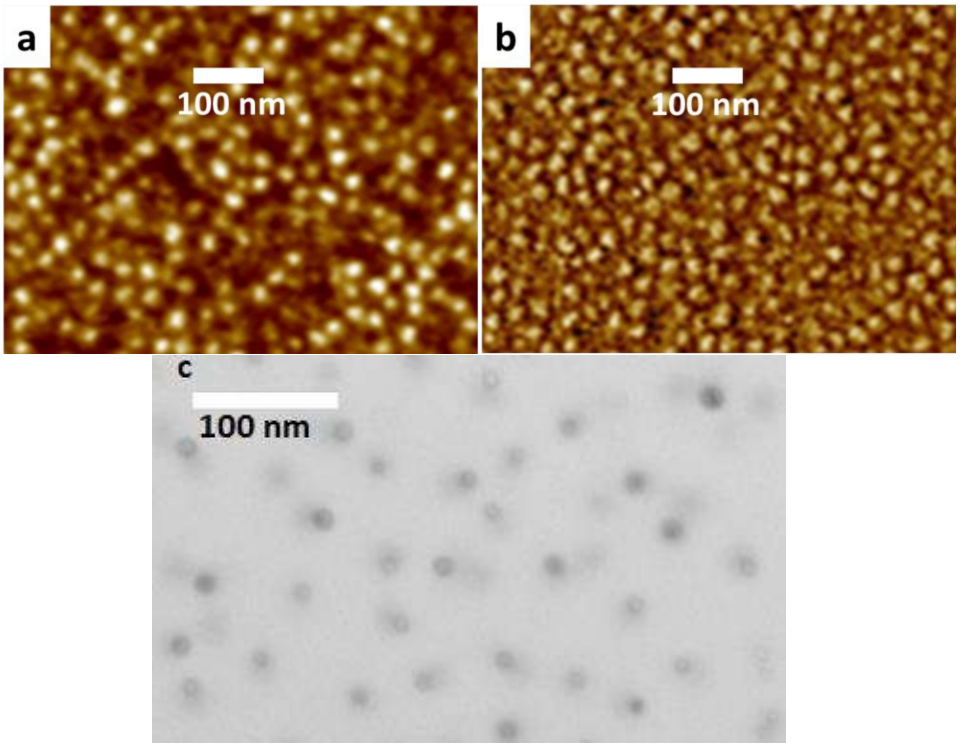

Figure 4-20. AFM height (a) and phase (b) images, and TEM image (c) for G1@PAA10-b-PS85 ACC, cast from toluene (scale bar = 100 nm).

4.5.9 Thin film imaging of the G2 ACC system

To examine the structure of the ACC and to compare the results with the DLS observations, AFM and TEM images obtained for G2@PAA13-*b*-PS390, cast from a 90:10 (v/v) toluene/ethanol mixture, are presented in **Figure 4-21.** A globular structure is evident in the AFM analysis, which is also confirmed by TEM. Their size in AFM analysis (71 ± 4 nm) is larger than the corresponding G2 substrate (57 ± 4

nm), and lower than the hydrodynamic diameter from DLS (84 ± 4 nm), as anticipated upon drying.[57] However small particle contaminants (not considered in the size analysis), circled in **Figure 4-21a**, are also visible in the phase image and possibly due to free BCP chains. As for the G1 ACC, TEM analysis provided the smallest size (64 ± 4 nm) as compared to both the AFM and DLS values. The small particle contaminant is not evident in the TEM images, which makes sense since they would not contain a P2VP component.

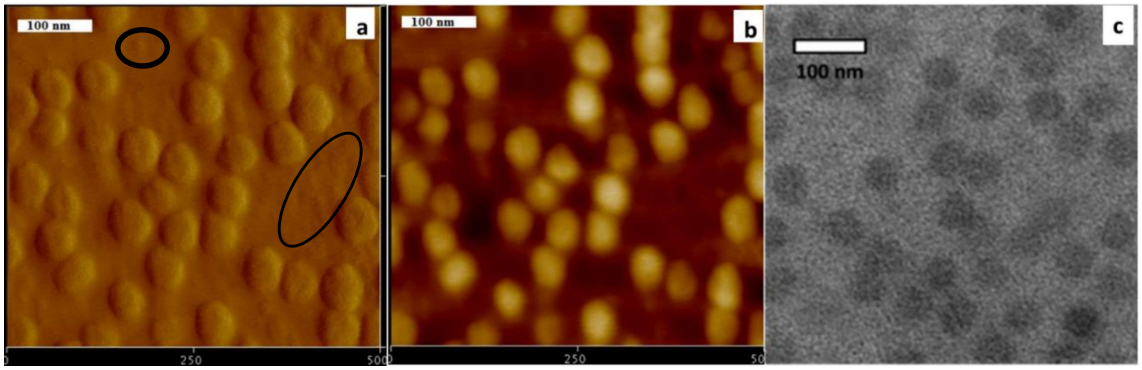

Figure 4-21. AFM phase (left) and height (middle) images, and TEM images stained with I_2 (right) for G2@PAA13-b-PS390 (1: 1), cast from toluene/ethanol (90:10) at 0.8 mg/mL.

To explore the influence of the weight ratio of G2:BCP, ACC samples of the G2@PAA10-*b*-PS205 were prepared using 1:1, 1:2, and 1:4 w/w ratios of G2:PAA10-*b*-PS205 in 90:10 (v/v) toluene/ethanol mixtures, for investigation by AFM, to obtain size and morphology information. The AFM height and phase images obtained for the corresponding ACCs are compared in **Figure 4-22**. In all cases, spherical topologies were obtained with average diameters of 62 ± 4, 64 ± 5, and 79 ± 5 nm for the 1:1, 1:2, and 1:4 mass ratios of G2:BCP, respectively. This confirms the increasing size trends observed in the DLS experiments (Section 4.5.4) for increasing amounts of BCPs, and further that the size of the ACCs obtained by self-assembly is uniform. For comparison, the D_h obtained for the 1:1, 1:2 and 1:4 ratios were 74, 85 and 93 nm, respectively. The increase in size of the complex observed with the amount of

BCP added is therefore clearly due to an increase in the corona thickness. While uniform particles are obtained in all cases, the presence of free BCP contaminant is most obvious at the 1:4 ratio (indicated by arrows in **Figure 4-22**), and as a consequence the contrast in the images is decreased. The DLS analysis of the BCP molecules, either in their free or aggregated state, apparently yielded an increase in size dispersity for the 1:4 ratio (Đ = 0.22) as compared to the 1:1 (Đ = 0.10) and 1:2 (Đ = 0.15) ratios.

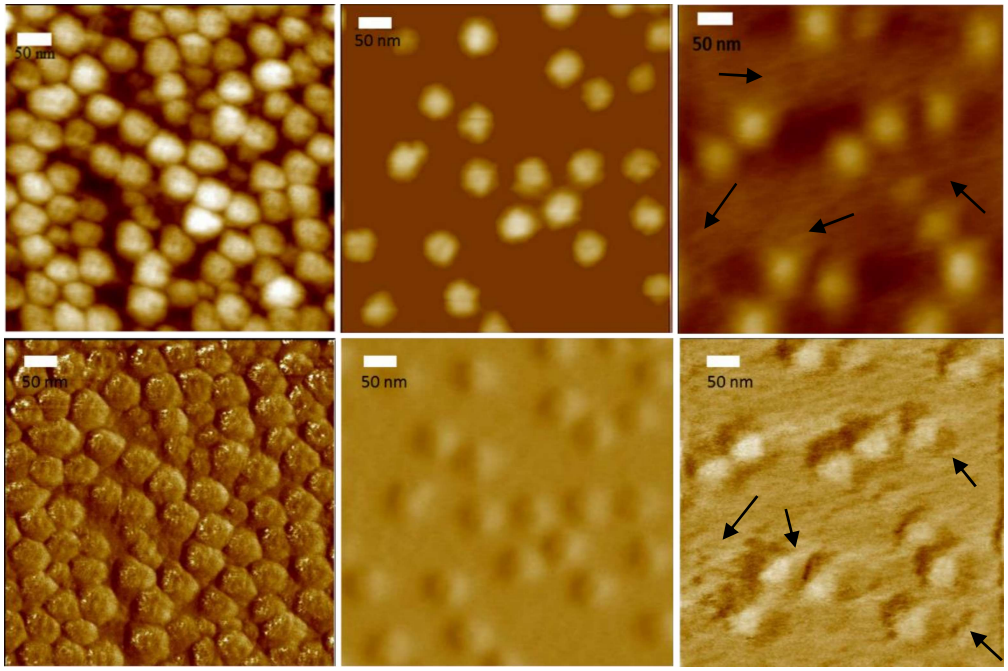

Figure 4-22. AFM height images for ACCs obtained by mixing G2@PAA10-b-PS205 at a 1:1 (left), 1:2 (middle), and 1:4 (right) G2:BCP mass ratio, prepared in 90:10 (v/v) toluene/ethanol (scale bar = 50 nm).

To assess the influence of the solvent on the stability of the ACCs, AFM pictures obtained for G2@PAA10-*b*-PS260 prepared from a 90:10 (v/v) toluene/ethanol mixture, and after transfer to pure toluene, are compared in **Figure 4-23**. The diameter of the complex obtained in the solvent mixture was 73 ± 4 nm, 8 nm larger than in pure toluene (65 ± 4 nm). This may be related to the presence of ethanol plasticizing the P2VP chains, and thus contributing to increased flattening of the particles upon

casting on the mica surface. AFM analysis also yielded smaller particle sizes than DLS: The D_h^Z in the solvent mixture and in pure toluene were 79 ± 1 and 95 ± 1 nm, respectively. Smaller particle contaminants are also visible in the AFM phase image for the sample prepared in pure toluene, which is consistent with the increased dispersity observed in DLS analysis, Đ = 0.22 ± 0.06 in pure toluene as compared to Đ = 0.13 ± 0.01 in the solvent mixture. Based on the results obtained, transfer of the ACCs to toluene after their preparation in the toluene/ethanol solvent mixture does not appear to have any influence on their stability, since the amount of linear contaminant detected in the AFM phase images appears comparable in both cases.

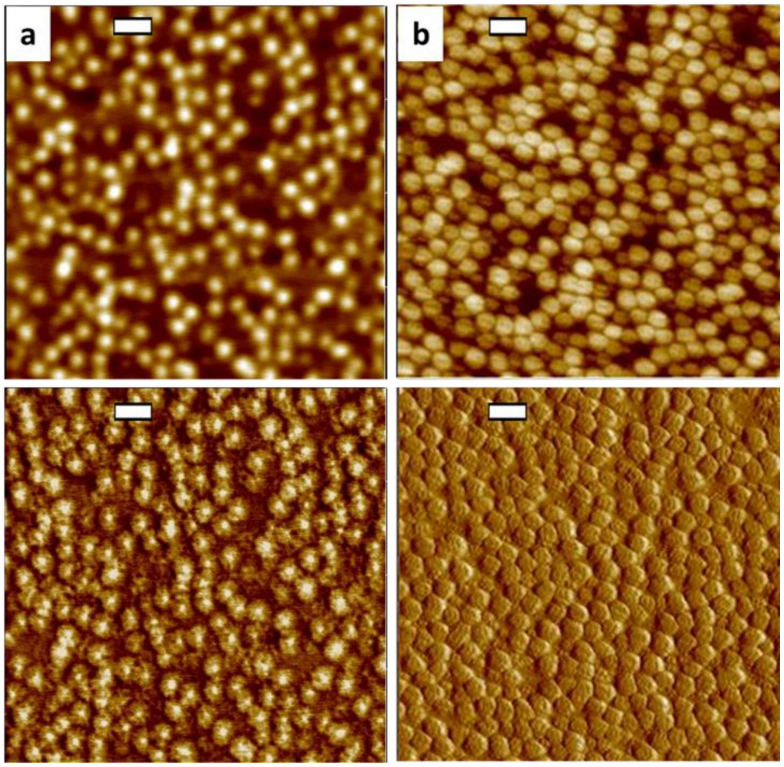

Figure 4-23. AFM height (top) and phase (bottom) images for G2@PAA10-b-PS260 in a 1:1 w/w ratio, cast from (a) toluene/ethanol (90/10 v/v), and (b) after transfer to pure toluene (scale bar = 100 nm).

The influence of the PS chain length was examined for G2 ACCs prepared from BCPs having an equal number of PAA units but different PS chain lengths, after their transfer to toluene. AFM height and phase images for the G2@PAA10-*b*-PS85, G2@PAA10-*b*-PS205, G2@PAA10-*b*-PS260, and G2@PAA10-*b*-PS305 ACCs obtained at a 1:1 ACPS:BCP mass ratio are provided in **Figure 4-24**. Increases in average diameter are observed from the substrate to the micelles in all cases, but unfortunately these increments are not statistically significant when taking into account the standard deviations on the measurements: The diameter, in dry state, for the G2 ACPS, G2@ PAA10-*b*-PS85, G2@PAA10-*b*-PS205, G2@PAA10-*b*-PS260, and G2@PAA13-*b*-PS305 complexes, was 57 ± 4, 61 ± 4, 63 ± 4, 65 ± 4, and 60 ± 5 nm, respectively. This is in contrast to the significant D_h increments observed from the substrate to the ACCs for the same samples (Section 4.5.4); in that case, the errors on the measurements were lower. A spherical topology was observed in all cases in the AFM images, with well-defined particles visible for complexes with medium-length PS chains, G2@PAA10-*b*-PS205 and G2@PAA10-*b*-PS260. The particles are not as clearly defined for the G2@ PAA10-*b*-PS85 complex, however, which may be due to interactions between the P2VP phase with the mica surface, as opposed to the presence of free BCP contaminant. The short PS chains in PAA10-*b*-PS85 may indeed not suffice to shield the particles and prevent their interactions with the mica substrate. On the other hand, the G2@PAA13-*b*-PS305 complex appears to contain more BCP contaminant, that is not clearly distinguishable but decreases the degree of definition of the particles. Considering that the BCP contaminant was not observed in the DLS analysis (Section 4.5.4), an alternate explanation for the decreased contrast of G2@PAA13-*b*-PS305 could be increased interpenetrability of the ACC particles, due to the presence of longer, more flexible PS chains forming a thicker corona layer in that system.

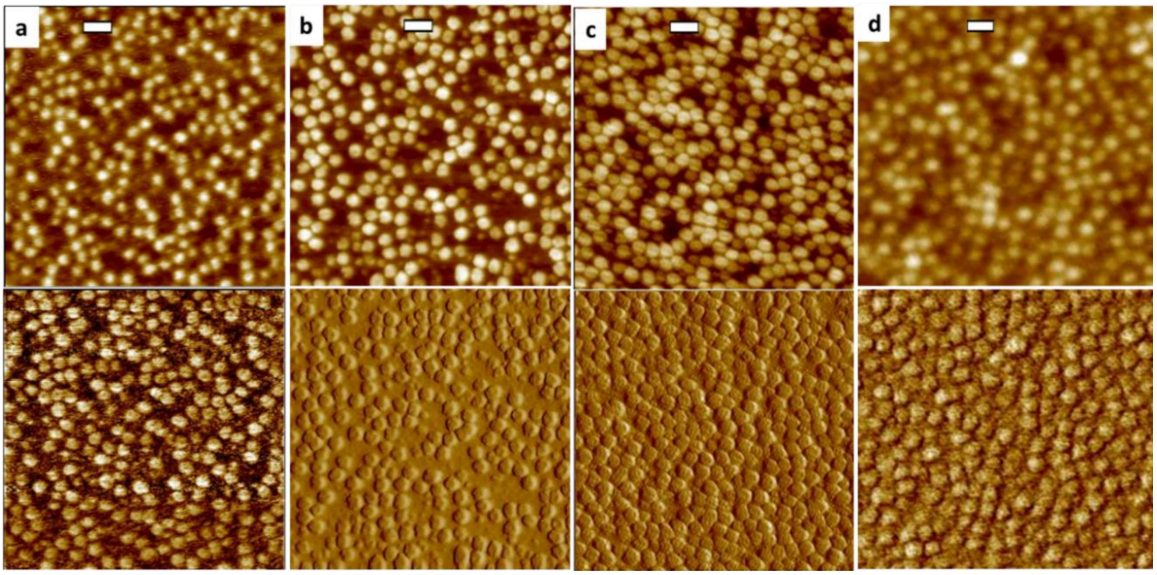

Figure 4-24. AFM height (top) and phase (bottom) images for ACCs obtained by mixing 1:1 w/w G2 with a) PAA10-b-PS85, b) PAA0-b-PS205, c) PAA10-b-PS260 and d) PAA10-b-PS305 in toluene/ethanol (90/10 v/v), followed by transfer to pure toluene (scale bar = 100 nm).

The corresponding TEM pictures for G2@PAA10-*b*-PS85, G2@PAA10-*b*-PS205, G2@PAA10-*b*-PS260, and G2@PAA10-*b*-PS305 ACC stained with iodine are provided in **Figure 4-25**. All the ACCs had spherical topologies with mean diameters of 69 ± 3, 69 ± 5, 70 ± 3, and 69 ± 4 nm for G2@PAA10-*b*-PS85, G2@PAA10-*b*-PS205, G2@PAA10-*b*-PS260, and G2@PAA10-*b*-PS305, respectively, as compared with 63 ± 5 nm obtained for TEM analysis of the G2 ACPS cast from THF. Therefore, TEM analysis did not show any significant size differences among the ACCs. This would make sense if the (unstained) stabilizing PS corona is invisible in the TEM pictures, but it also implies that the dimensions (i.e. the conformation) of the P2VP chains within the P2VP-rich ACPS did not change significantly upon complexation. While spherical particles were observed in both AFM and TEM analysis, a closer look at the TEM pictures for G2@PAA10-*b*-PS260 (inset of **Figure 4-25c**) reaveals that some particles have a lighter core surrounded by a darker ring, which could correspond either to a core–shell or a toroidal morphology. However it is clear, from the AFM imaging, that the particles are indeed spherical

rather than toroidal. This phenomenon was observed more clearly after loading this complex with $HAuCl_4$, as discussed in Chapter 5.

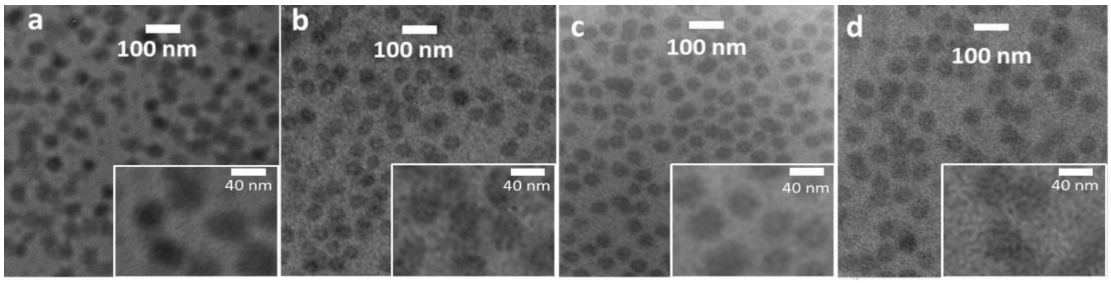

Figure 4-25. TEM pictures for (a) G2@PAA10-b-PS85, (b) G2@PAA10-b-PS205, (c) G2@PAA10-b-PS260, and (d) G2@PAA10-b-PS305 ACCs (1:1 w/w) prepared in toluene/ethanol (90/10 v/v), followed by transfer to toluene and staining with iodine (scale bar = 100 nm; inset scale bar = 40 nm).

In conclusion, AFM and TEM analysis both confirmed that the ACCs have a uniform size, consistent with the narrow size dispersity values (Đ = 0.07-0.13) obtained by DLS (**Table 4-2**).

4.5.10 Thin film imaging of the G3 ACC system

AFM images for the G3@PAA10-*b*-PS260 complex cast from THF and toluene solutions are compared in **Figure 4-26**. In THF, a non-selective solvent for the P2VP and PS phases, the particles have a spherical topology, while in toluene, a raspberry like morphology is observed. This is likely because toluene is a solvent selective for the PS phase and a non-solvent for the P2VP phase, which favors intraparticle phase separation. It is indeed well-known that intramolecular interactions are a key parameter controlling phase separation and the morphology of graft polymers.[58] Moreover, hydrogen bonding interactions are also known to affect phase morphology.[59] This seems in line with the results of the current study, as raspberry morphologies were already observed in our laboratory for similar core–shell–corona molecules obtained by anionic grafting, G2PS-*g*-(P2VP14K-*b*-PS115), however only after loading with $HAuCl_4$.[56] The formation of raspberry-like micelles was also reported for complexes formed by PS-*co*-PMAA core–shell microspheres and PS-*b*-P4VP core–shell micelles in

water.[23] It is notable that in both solvents, clean particles were obtained without visible BCP contaminant.

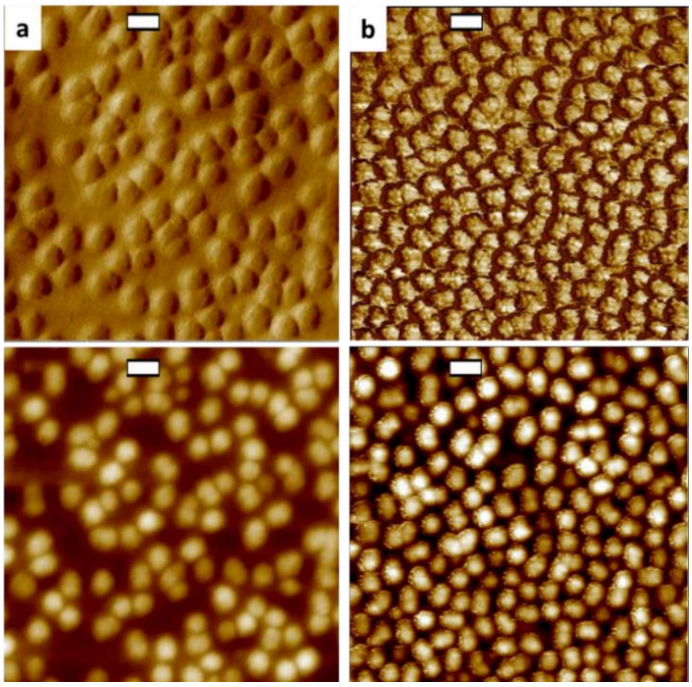

Figure 4-26. AFM phase (top) and height (bottom) images for G3@PAA10-b-PS260 ACC 1:1 w/w cast from (a) THF and (b) after solvent exchange to toluene (scale bar = 100 nm).

The influence of the PS chain length on the morphology of the G3 ACCs was examined. To this end, AFM images for G3@PAA10-*b*-PS85, G3@PAA10-*b*-PS205, G3@PAA10-*b*-PS260, and G3@PAA10-*b*-PS305 ACCs cast from toluene solutions are compared in **Figure 4-27**. Since the G3 substrate was insoluble in toluene, the ACC samples were prepared in THF and the solvent was exchanged to toluene afterwards. While a raspberry-like morphology is clearly visible for G3@PAA10-*b*-PS205 and G3@PAA10-*b*-PS260, it is barely visible for G3@PAA10-*b*-PS305, which appears closer to homogeneous spherical particles. Aggregated particles are visible in G3@PAA10-*b*-PS85, likely because the shorter PS blocks unable to effectively shield interparticle interactions. This was shown in

the DLS analysis, as a relatively larger size (118 nm) and a higher dispersity (Đ = 0.2) were obtained (**Appendix B-2**). So aggregation may have occurred in solution and increased further upon drying, but it will be shown in the Chapter 5 that aggregation was enhanced further after metal loading. The diameter obtained by AFM analysis of G3@PAA10-*b*-PS205, G3@PAA10-*b*-PS260, G3@PAA10-*b*-PS305 was 83 ± 6, 83 ± 5, and 91 ± 6 nm, respectively. These diameters are again smaller than the D_h^Z from the DLS analysis (110-119 nm) in toluene, as expected.

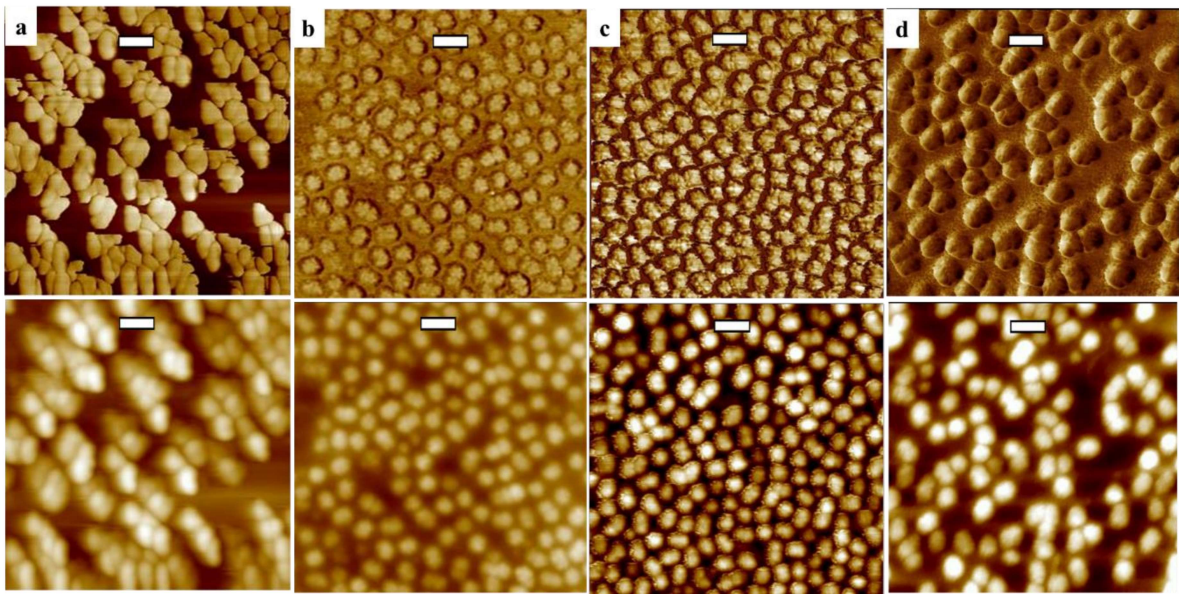

Figure 4-27. AFM phase (top) and height (bottom) images for (a) G3@PAA10-b-PS85 (b) G3@PAA10-b-PS205, (c) G3@PAA10-b-PS260, and (d) G3@PAA10-b-PS305 ACCs (1:1 w/w) prepared in THF, followed by solvent exchange to toluene (scale bar = 100 nm).

4.5.11 Thin film imaging of the G4 ACC system

The ACCs obtained by complexing the G4 copolymer substrate in THF with the BCPs in a 1:1 w/w ratio were also examined by AFM, after casting from a toluene solution. Height images obtained for the G4 substrate in THF and G4@PAA10-*b*-PS260 in toluene are provided in **Figure 4-29.** While the G4 ACPS has a spherical topology with a cauliflower-like morphology, as previously described, the

G4@PAA10-*b*-PS260 complex in toluene displays an indented sphere-like topology, with particles connected end-to-end into a necklace-type arrangement (**Figure 4-28**).

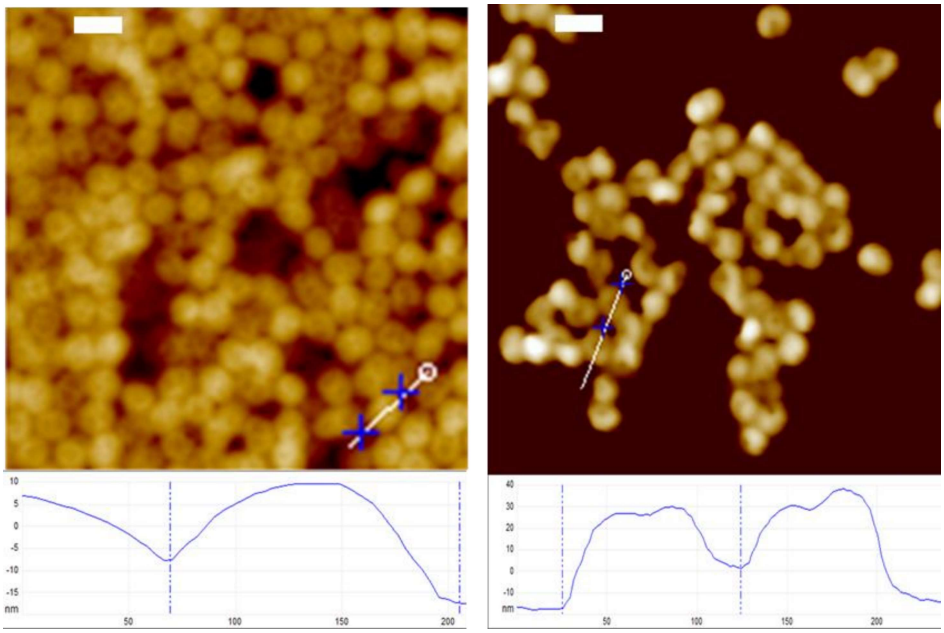

Figure 4-28. AFM height images for G4 cast from THF (left), and G4@PAA10-b-PS260 prepared in THF and transfer to toluene (right), with the corresponding height profiles (scale bar = 100 nm).

The diameter of G4@PAA10-*b*-PS260 cast from toluene, determined by AFM analysis, was 80 ± 5 nm, smaller than the corresponding G4 ACPS (95 ± 5 nm) cast from THF. The larger size of the ACPS could be due simply to adsorption of the P2VP side chains on the mica substrate, but it was also suggested that a size decrease can be triggered by the co-aggregation of hydrophobic PS blocks in a crowded environment (such as the ACC), resulting in a more condensed structure.[44] The hydrodynamic diameter measured for the ACC by DLS in toluene (160 ± 4 nm) was nevertheless larger than for the

corresponding arborescent copolymer in THF (150 ± 1 nm), which would favor the adsorption hypothesis.

On the other hand, the diameter of G4@PAA10-*b*-PS260 (80 ± 5 nm) obtained by AFM was slightly lower than the analogues G3@PAA10-*b*-PS260 (83 ± 5 nm), perhaps due to a more condensed structure for the most crowded G4 ACC. According to AFM analysis (**Figure 4-29**) G4@PAA10-*b*-PS260 also had a much smaller size than G4@PAA10-*b*-PS85 (132 ± 21 nm) and G4@PAA10-*b*-PS205 (110 ± 11 nm), despite the fact that all had an equal number of acrylic acid units (10) and were cast from toluene solutions. The larger size of G4@PAA10-*b*-PS85 was attributed to aggregation earlier, inferred from the DLS analysis due to its high D_h (200 nm) and dispersity (0.2) (**Appendix B-2**, **Table A4-5**). This can also be seen in the AFM analysis (**Figure 4-29a**), however many of the G4@PAA10-b-PS85 particles have an elongated shape which would be consistent with association of 2-3 ACCs per particle. Furthermore, an indented sphere topology is clearly visible for G4@PAA10-*b*-PS205, while G4@PAA10-*b*-PS260 combined this feature with a necklace-type arrangement. Finally, in the G4 sample, a few smaller particles are visible **(Figure 4-29)**, presumably corresponding to aggregated non-complexed block copolymers, which become more pronounced when longer BCPs are employed (discussed later).

AFM images for G4@PAA13-b-PS330 and G4@PAA13-b-PS390 are compared in **Figure 4-30**. There is no change in morphology observed as the PS block length is varied, but the toroidal topology observed for G4@PAA10-*b*-PS205 and G4@PAA10-*b*-PS260 is clearer for the G4@PAA13-*b*-PS330 and G4@PAA13-*b*-PS390 ACCs. It therefore seems that the visibility of a dimple in the ACCs adsorbed on a mica surface is enhanced for longer, more flexible PS chains. The diameters measured for G4@PAA13-*b*-PS330 and G4@PAA13-*b*-PS390 were 106 ± 7 and 115 ± 6 nm, respectively. While G4@PAA13-*b*-PS330 and G4@PAA13-*b*-PS390 were larger than G4@PAA10-*b*-PS260 (80 ± 5 nm), a second population of small particles was clearly visible in these samples (**Figure 4-30)** likely due to

the aggregation of non-complexed BCP chains in toluene, present in large numbers relatively to the ACPS due to their much lower molecular weight.

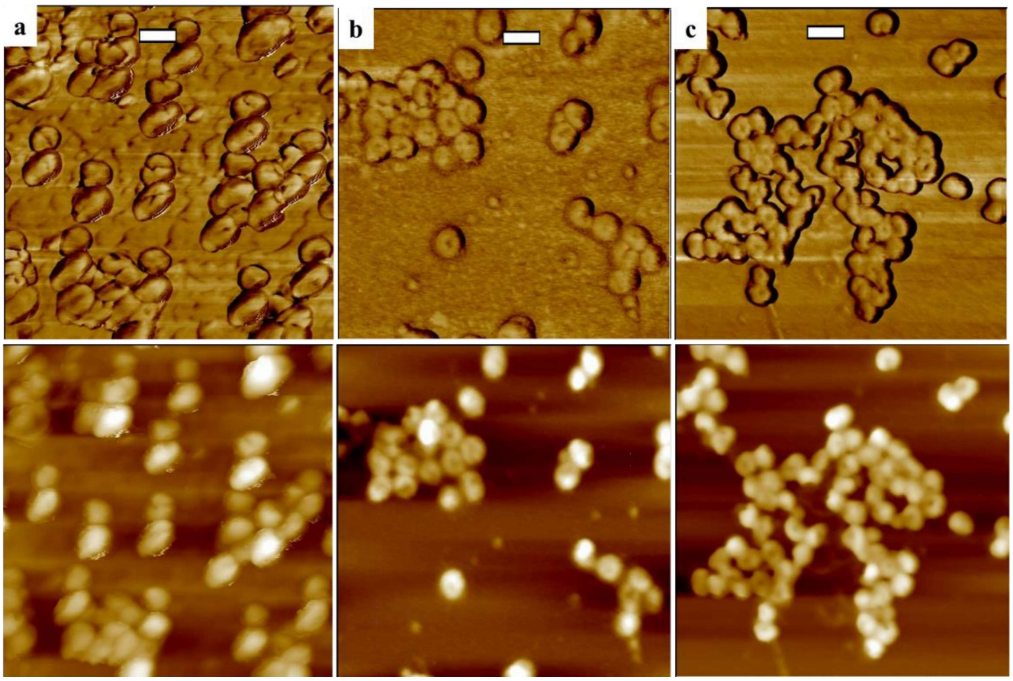

Figure 4-29. AFM phase (top) and height (bottom) images for (a) G4@PAA10-b-PS85, (b) G4@PAA10-b-PS205, and (c) G4@PAA10-b-PS260 (1:1 w/w) prepared in THF and cast from toluene after solvent exchange (scale bar = 100 nm).

The AFM observations are consistent with the DLS analysis results, in that the size dispersity was higher for most of these systems. For example, the dispersity obtained for G4@PAA13-*b*-PS330 in toluene was very high (Đ = 0.6), which is consistent with the presence of the non-complexed BCP molecules forming the smaller aggregate population in the AFM images. These BCP aggregates were not considered in the AFM size analysis, which was primarily concerned with size variations for the ACPS upon complexation with the BCP.

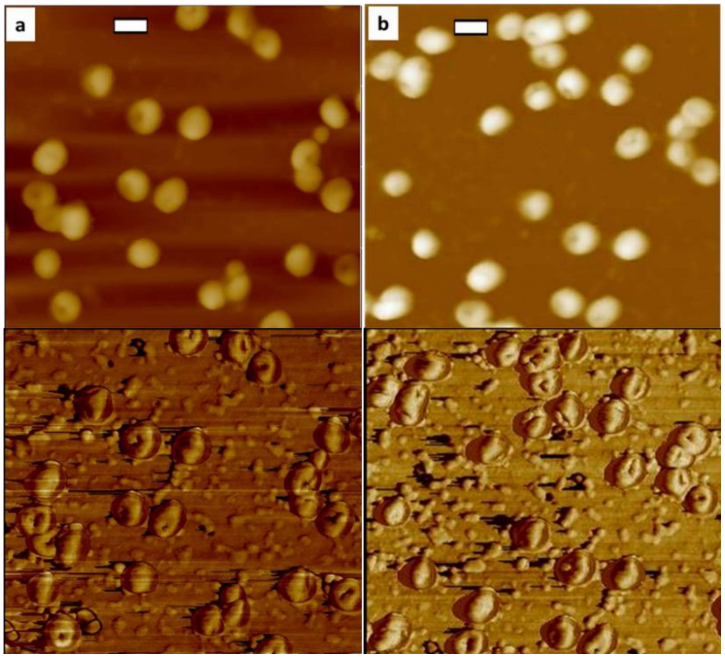

Figure 4-30. AFM height (top) and phase (bottom) images for (a) G4@PAA13-b-PS330, and (b) G4@PAA13-b-PS390 (1:1 w/w) prepared in THF and cast from toluene after solvent exchange (scale bar = 100 nm).

4.6 Conclusions

The G1–G4 arborescent copolymer substrates, with hydrodynamic diameters ranging from 37 to 150 nm depending on the generation number, had relatively low size dispersity values ($Đ \leq 0.10$) in THF, consistent with a uniform size. This was confirmed by AFM analysis, revealing that the ACPS had a spherical topology. While the topology of the G4 ACPS was likewise spherical, it also had a cauliflower-like morphology.

These ACPSs were complexed with different PAA-*b*-PS copolymers to be investigated by DLS, TEM, and AFM. The ACCs formed by the G1 copolymer had a smaller D_h^Z than the substrate in THF/ethanol mixtures. This shrinkage was attributed to the collapse of the P2VP chains in the shell upon complexation with PAA-*b*-PS, facilitated by the relatively open and flexible structure of the G1

copolymer. Even though the size was expected to increase upon adding the PS corona on the ACCs, this was apparently insufficient to compensate for extensive shrinking of the P2VP chains within the shell of the ACPS. In contrast, complexes derived from the higher generation (G2–G4) substrates generally displayed significant increases in D_h^Z, larger for BCPs with longer PS blocks. While trends in the DLS results were obscured by some inconsistencies, one single size population with a relatively low size dispersity ($Đ \leq 0.15$) was observed in most cases. Polymer-solvent interactions are known to impact the swelling of complex micelles.[60] Since toluene is a good solvent for PS, it seems reasonable that stretching of the PS chains may increase with the number of PS chains in the complex (as the BCP:ACPS weight ratio is increased), which likely contributed to micelle swelling in addition to good solvency.

AFM analysis of the complexes provided complementary information on their topology and morphology, in addition to confirming the trends in size variations obtained by DLS. Complex micelles of uniform size were observed for most samples derived from G1–G3 substrates and their structure became better defined as the substrate generation number increased, which is attributed to the increased compactness and lower interpenetratability of more highly branched substrates.[61] A spherical core–shell morphology was maintained for the G1and G2 substrates, due to their small PS core size and the large ($M_n \approx 30$ kg/mol) P2VP chains within their corona.[62] The G3 ACC systems, with shorter P2VP side chains ($M_n \approx 15$ kg/mol), displayed intramolecular phase separation with nodular nanodomains (or raspberry-like morphologies), particularly well-defined for G3@PAA10-*b*-PS205 and G3@PAA10-*b*-PS260. This phenomenon was also observed in a previous study in our laboratory for core–shell–corona copolymers obtained by anionic grafting, but only after loading with $HAuCl_4$. The complexes derived from the G4 substrate displayed an indented sphere topology, that became more visible when BCPs with a longer PS block were used. In all cases the size measured from the AFM phase images was found to increase from the substrate to the ACCs, with larger increases for longer side chains in most cases.

While the AFM images were relatively uniform in most cases, systems derived from block copolymers with shorter PS chains displayed aggregation, and elongated shapes were observed in the G2 systems with longer PS chains (**Appendix B-3**, **Figure A4-3**). A second size population, likely due to aggregation of the non-complexed block copolymer side chains in toluene, was also visible in the AFM images for the G4 systems. This observation was consistent with the DLS analysis results, in that the size dispersity of the ACCs displaying BCP aggregation in AFM was also higher in the DLS analysis, particularly for G4@PAA13-*b*-PS330 (Đ = 0.6).

Chapter 5: Arborescent Copolymer Complexes: Metal Loading and Characterization

5.1 Overview

Arborescent copolymer complexes (ACCs), obtained by the self-assembly of arborescent polystyrene-*graft*-poly(2-vinylpyridine) (PS-*g*-P2VP) copolymers of generations G2–G4 with poly(acrylic acid)-*block*-polystyrene (PAA-*b*-PS) copolymers, were investigated as templates for the preparation of metallic nanoparticles. The ACCs of all generations were loaded with $HAuCl_4$ in toluene and in solvent mixtures (toluene/ethanol, toluene/methanol, THF/methanol and chloroform). The G3 and G4 ACCs were also loaded with $Pd(OAc)_2$ in toluene. Transmission electron microscopy (TEM) analysis confirmed that the metallic compounds were successfully loaded in the ACCs, and that the metal distribution in the templates depended on the generation number, the solvent and the loading level used. Different nanomorphologies, namely spherical, raspberry-like, core–shell and toroidal (mushroom-like or nanocage), were observed for the metal-loaded ACCs due to intramolecular phase separation induced by the metal. The influence of the PS block length in the PAA-*b*-PS copolymer was also examined systematically in toluene, but the type of nanomorphology obtained appeared to be mainly governed by the generation number of the arborescent substrate. The loading level also appeared to have little influence on the morphology in the 0.25–1 equiv/2VP unit range. A comparison of dynamic light scattering (DLS), atomic force microscopy (AFM) and TEM results showed comparable trends among the samples.

5.2 Introduction

Research on metallic nanoparticles (MNPs) has gained momentum over the past decades due to their emerging applications in different areas. These materials exhibit unique physical and chemical properties, distinct from both bulk state and isolated atoms[1,2] because of their very high surface/volume ratio[3] and dispersion state.[4] The properties of MNPs strongly depend on their size, interparticle distance, and the nature of the stabilizing agent used in their preparation.[5]

Colloidal instability is a serious issue limiting the applications of nanoparticles.[6] A wide range of MNP stabilizers have been used such as amine- and thiol-functionalized surfactants, polymers functionalized with thiol,[1] amine and benzaldehyde groups,[7,8] amphiphilic block copolymers (BCPs),[9] and branched polymers,[10] including dendritic polymers.[11] Stabilization may involve complexation, electrostatic interactions, or covalent attachment through functional groups. For instance, the binding of polymers with a thiol end group to gold surfaces is well-established.[12]

Because amphiphilic BCPs can form micelles at much lower concentrations (the critical micelle concentration, CMC) than surfactants,[13,14] and their properties can be tailored by varying the chain length and the composition of each block,[15] these materials are of great interest as MNP stabilizers.[16,17] The stability of MNPs stabilized by BCPs depends on the properties of the micelles formed, and therefore on the solvent, concentration, pH, temperature, and ionic strength of the dispersions, beyond the intrinsic characteristics of the BCP molecules (molecular weight and composition of each block).[10] One significant issue encountered with block copolymer stabilizers is that the polymer chains can detach from the MNPs when the BCP concentration decreases below the CMC, which may induce aggregation of the MNPs. Star-block copolymers and other amphiphilic polymers behaving like unimolecular micelles can minimize this issue, because they have no CMC: The covalently bonded chains cannot dissociate, even at very high dilutions.[15,18] In some cases MNPs can be synthesized directly within the core of star-block copolymers, whereby the copolymers serve as templates,[15,19,20] albeit further aggregation can take place under selective solvency conditions.[18]

Dendritic polymers (dendrimers, hyperbranched, and arborescent molecules) have a highly branched structure with a large number of internal cavities that can be useful to encapsulate MNPs.[21,22] The encapsulation of metal ions can be induced by incorporating polar reactive groups like amines[11] or carboxylic acids[23] in the inner structure of dendritic polymers, or by using peripheral groups with complexing ability for the metal.[22] Metals incorporated within dendrimer structures include Pt,[24–26,

Pd,[26] Rh,[27] Ag,[26] and Au.[28] Unfortunately, the synthesis of high molecular weight (large size) dendrimers is demanding, as it requires multiple reaction cycles and purification steps. In contrast, hyperbranched polymers can be obtained with high molecular weights in facile one-pot reactions.[29] Comparable properties have been reported for gold nanoparticles prepared using either dendrimers or hyperbranched polymers as templates and stabilizers,[30,31] even though hyperbranched polymers typically have a poorly defined randomly branched structure and broader molecular weight distributions.[32]

Arborescent polymers combine features of dendrimers and hyperbranched polymers: They have a relatively well-defined structure in comparison with hyperbranched systems, and can be synthesized in fewer steps than dendrimers. Arborescent polymers were mainly synthesized by anionic grafting onto either chloromethylated[33] or acetylated[34] polystyrene substrates. The molecular weight of the building blocks and the number of grafting cycles used provided control over the characteristics of these templates such as the core size, chain flexibility, and layer thickness. Arborescent PS-*g*-P2VP copolymers were thus employed for the preparation of Pd nanoparticles.[35] More complex systems with a core–shell–corona (CSC) architecture, the arborescent polystyrene-*graft*-[poly(2-vinylpyridine)-*block*-polystyrene] copolymers, were also synthesized[36] and used as templates for the preparation of gold nanoparticles.[37] Successive generations (G0–G4) of the CSC structures were loaded with either $HAuCl_4$ or $Pd(OAc)_2$,[38] yielding different nanomorphologies within each template molecule including spherical, toroidal, raspberry-like, spherical nanocage, and cylinder-in-sphere morphologies. More recently, arborescent CSC structures (polyion complex or PIC micelles), obtained by the self-assembly of G0PS-*g*-P2VP with poly(acrylic acid)-*block*-poly(2-hydroxyethyl acrylate) (PAA-*b*-PHEA) copolymers in water,[39] were used for the preparation of Fe_3O_4 nanoparticles.[40] No systematic investigation of the nanophase separation obtained was carried out as a function of the generation number for these systems, however.

In this Chapter, arborescent copolymer complexes formed by arborescent PS-*g*-P2VP (G2–G4) substrates and PAA-*b*-PS were investigated as templates for loading metallic compounds, mainly $HAuCl_4$ (**Figure 5-1**). The size and morphology of the complexes were investigated as a function of the loading level and the solvent used by DLS, TEM, and AFM analysis. Phase separation induced by metal coordination resulted in different nanomorphologies including raspberry-like, core–shell and mushroom-like (nanocage), depending on the generation number. Loading with $Pd(OAc)_2$ was also demonstrated.

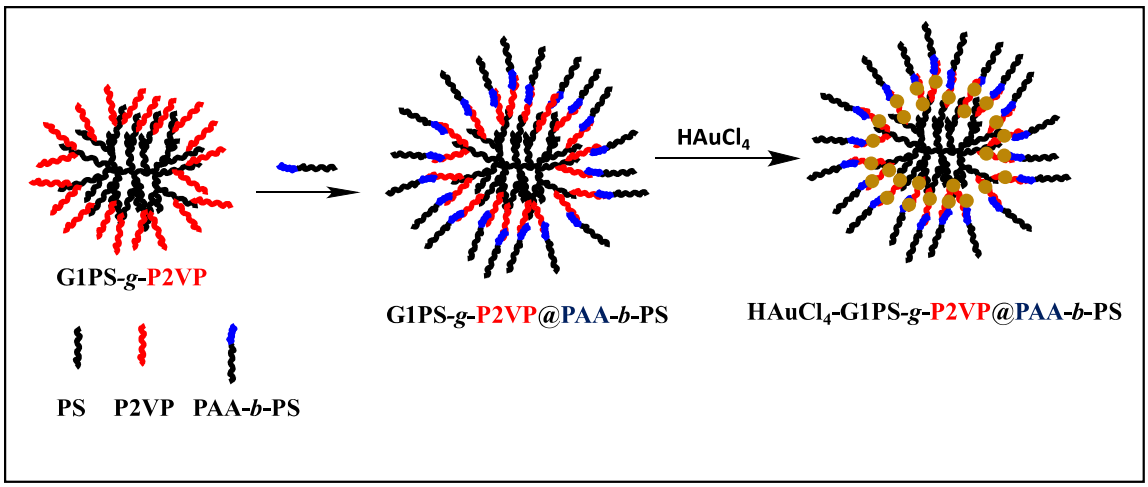

Figure 5-1. Schematic illustration of G1PS-g-P2VP@PAA-b-PS ACC formation and metal loading.

5.3 Experimental procedures

The preparation of the arborescent copolymer complexes (ACCs) used in this portion of the investigation was described in Chapter 4. The Gn@PAA-*b*-PS ACCs were obtained using a 1 : 1 (w/w) ratio of the G2–G4 substrates and the block copolymers at concentrations of 0.8 mg/mL, either in toluene, toluene/ethanol, toluene/methanol, THF/methanol, or chloroform.

5.3.1 Metal loading of the ACCs

Loading with $HAuCl_4$. Solid $HAuCl_4$ (Alfa Aesar, 99.9 %) was added with stirring to an ACC solution to achieve either 0.25, 0.5, 0.75 or 1.0 equiv of $HAuCl_4$/2VP unit. The exact amount of $HAuCl_4$ added was calculated based on the mole fraction of 2VP units in the ACC, minus the number of moles of PAA units (assuming complete complexation of the AA and 2-VP moieties). As a specific example, to load sample G1PS-*g*-P2VP30K@PAA10-*b*-PS260 with 0.5 equiv/2VP unit, 7.8 mg of $HAuCl_4$ (0.023 mmol) were added to 12.5 mL of a 0.8 mg/mL solution of the complex in toluene, prepared from 5 mg of G1PS-*g*-P2VP30K (90 %, 0.048 mmol 2VP units) and 5 mg PAA10-*b*-PS260 (2.6 %, 0.0018 mmol AA units). $HAuCl_4$ is insoluble in pure toluene or chloroform, but it dissolved within ~2 h in the ACC solution by coordination with the 2VP units. The color of the ACC solution also changed to light yellow upon metal coordination, the intensity of the color increasing with the loading level. For complexes prepared in THF/cyclohexane and toluene/methanol mixtures the color change to light yellow was instantaneous, but in all cases the metal-loaded samples were stirred for at least 24 h before analysis to ensure complete coordination.

Loading with $Pd(OAc)_2$. The ACC was dissolved in toluene at a concentration of 0.8 mg/mL. To this solution, a required amount of $Pd(OAc)_2$ (Strem Chemicals, min. 98 %) corresponding to 0.25, 0.5 or 0.75 equiv/2VP unit was added as a solid. The $Pd(OAc)_2$-loaded ACCs had a pale orange color at 0.25 equiv loading and a brown color at 0.75 equiv. The samples were allowed to stir for 24 h before analysis.

5.3.2 Dynamic light scattering (DLS)

Dynamic light scattering measurements were performed at 25 °C on a Zetasizer NanoS90 Malvern instrument equipped with a He–Ne laser light source operating at 636 nm, and a fixed angle of 90°. The $HAuCl_4$-loaded ACC solutions (0.8 mg/mL) were prepared 24 h prior to analysis. All the measurements were made using 3.5 mL glass cuvettes with a 1 cm square aperture, after filtration with 0.45 μm polytetrafluoroethylene membrane filters.

5.3.3 Atomic force microscopy (AFM)

The AFM samples were prepared through spin coating at 3000 rpm, by casting 2–3 drops of the $HAuCl_4$-loaded ACC solution with a microsyringe onto a freshly cleaved mica surface and spinning for at least 20 s. Tapping-mode measurements were performed to acquire height and phase images on a Nanoscope IIIa Multimode Digital Instruments, model MMAFM-2 system mounted on a vibration isolation table. The cantilever probes used were Vista Probes, T300 silicon with a tip radius of 8 nm, 125 μm length, 40 μm width, and 14 μm height, a spring constant of 40 $N \cdot m^{-1}$, and a resonant frequency of 300 kHz. The scan rate was typically set between 0.7 and 1 Hz, at a scan angle of 0°, acquiring 512 samples/line. To adjust the force applied on the surface, the drive amplitude was set between 25 and 50 mV and the amplitude set-point was between 0.50 and 0.85 V. The sensitivity was controlled by adjusting the integral gain from 0.1–0.5, and the proportional gain from 1–5 proportionally with the integral gain. The images were analyzed with the NanoScope Analysis software v1.40r1. To improve visualization of the features, contrast adjustments were made on some micrographs using the IrfanView (version 4.42) image viewer.

5.3.4 Transmission electron microscopy (TEM)

Thin films were prepared by casting one drop (~5 μL) of the metal-loaded ACC solution with a microsyringe onto a 300-mesh copper TEM grid coated with carbon and Formvar® (Electron Microscopy Sciences FCF300-CU) placed on a filter paper, such that excess fluid would wick through the filter paper. The grid was then transferred to a new piece of filter paper in a Petri dish and allowed to dry at least overnight at room temperature before imaging on a Philips CM10 TEM instrument operated at 60 kV. The images were recorded with an Advance Microscopy Techniques 11-megapixel digital camera and the Image Capture Software Engine (version 5.42.558). The size of the particles was measured manually for a minimum of 20 particles, to obtain reliable size

information. The IrfanView (version 4.42) image viewer was used for the size measurements, and to improve feature visualization on some of the micrographs.

5.4 Results and discussion

5.4.1 $HAuCl_4$ loading: General comments

Avoiding interparticle interactions and aggregation in the synthesis of gold nanoparticles is vital in controlling their properties.[41] Many polymeric templates have been investigated to stabilize nanoparticles, gold being the most widely studied metal due to its diverse applications. The most commonly used precursor for the preparation of gold nanoparticles is $HAuCl_4$, and pyridine moiety-containing templates can bind up to 1 equiv of $HAuCl_4$ per nitrogen atom.[42,43] The coordination of $AuCl_4^-$ ions was reported to affect their self-assembly behavior as well at the morphology of PS-*b*-P2VP copolymer micelles.[44] Loading of the arborescent PS-*g*-P2VP copolymer substrates (without addition of the BCP) was attempted in toluene but was unsuccessful due to their poor solubility in that solvent. Their loading with $HAuCl_4$ was also explored in THF at 0.8 mg/ml and appeared to be more successful (**Appendix C-1**), but these systems cannot be directly compared to the ACC systems due to the absence of a stabilizing PS corona.

In contrast, the G2–G4@PAA-*b*-PS arborescent complexes were freely soluble in toluene and other solvents (toluene with 10% ethanol, toluene with 2% methanol, THF with 25% cyclohexane, and chloroform), and were thus investigated as templates. $HAuCl_4$ is insoluble in toluene and in chloroform, but when added to the ACC solutions it gradually dissolves and the solutions turn light yellow after it coordinates with the 2VP moieties.[45] Loading of the ACCs with $HAuCl_4$ (0.25–1.0 equiv/2VP unit) was explored in most detail in toluene, and the resulting metal-coordinated particles were characterized by DLS, TEM, and AFM to obtain size, size dispersity, and morphology information.

5.4.2 $HAuCl_4$ loading in the G2 ACC System

Preliminary loading experiments used the G2@PAA13-*b*-PS305 and G2@PAA13-*b*-PS390 ACCs with 0.5 equiv of $HAuCl_4$/2VP unit in toluene/ethanol 90/10 (v/v). After adding the required amount of $HAuCl_4$ to a 20 mL vial containing the ACC solution, a light yellow color appeared within a few minutes. The samples were nonetheless stirred for 24 h prior to film casting for TEM analysis; the images obtained for the samples are provided in **Figure 5-2**. It is clear that $HAuCl_4$ was successfully loaded in the templates in both cases, as the metal can be observed as multiple small dark particles located within each ACC assembly. These dark particles should be elemental Au NPs formed upon irradiation of the $AuCl_4^-$ ion clusters by the electrons in the TEM beam.[46] Since the ACCs were prepared in a toluene/ethanol mixture, residual ethanol may also have promoted metal reduction in the TEM beam to some extent, even though the picture was recorded in the dry state. It was indeed suggested that ethanol, in the presence of an acid, can make the P2VP component swell and expand outside the core of PS-*b*-P2VP copolymer micelles,[47] perhaps exposing the gold ions to the electron beam. The average diameter of the $HAuCl_4$-loaded G2@PAA10-*b*-PS305 and G2@PAA13-*b*-PS390 ACCs determined by TEM analysis was 42 ± 4 nm and 48 ± 7 nm, respectively, while the size of the Au particles (the black dots) inside the ACCs was ~1.2 nm in both cases. The diameter of the $HAuCl_4$-loaded complex in TEM was lower than that measured without metal but after staining with iodine (69 ± 4 and 64 ± 4 nm, respectively). This could be due to strong interactions within the $HAuCl_4$-loaded P2VP phase, leading to a more spherical shape for the particles cast on the copper grid.

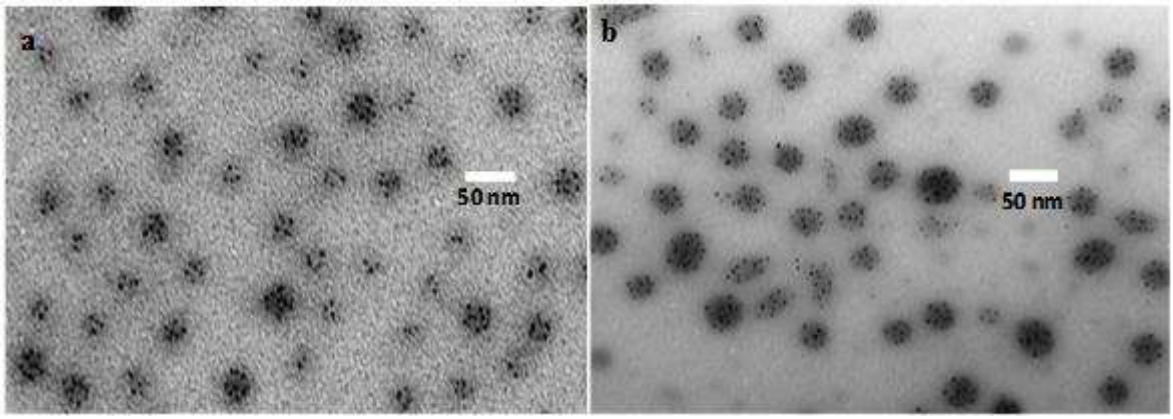

Figure 5-2. TEM images for (a) G2@PAA10-b-PS305 and (b) G2@PAA13-b-PS390 loaded with 0.5 equiv $HAuCl_4$/2VP unit in a toluene/ethanol 90/10 (v/v) mixture.

The G2@PAA13-*b*-PS390 complex was further investigated after loading with 0.5 and 1 equiv $HAuCl_4$/2VP unit in toluene. Hydrodynamic diameter distribution curves are compared in **Figure 5-3** for G2@PAA13-*b*-PS390 before and after loading with 0.5 equiv $HAuCl_4$. The z-average diameter (D_h^Z) of the G2@PAA-*b*-PS390 complex was 90 nm in toluene, increasing to 110 nm upon loading, which is a 22% increase. This could be due to swelling of the micelles upon coordination with $HAuCl_4$. TEM analysis (**Figure 5-4**) yielded number-average diameters of 96 ± 7 and 95 ± 15 nm at 0.5 and 1 equiv loadings, respectively. Therefore while the diameters were identical, the particles were more uniform (lower standard deviation) at the lower loading level. This may hint at increased aggregation at the 1 equiv loading level, due to stronger interactions between $HAuCl_4$-loaded templates.

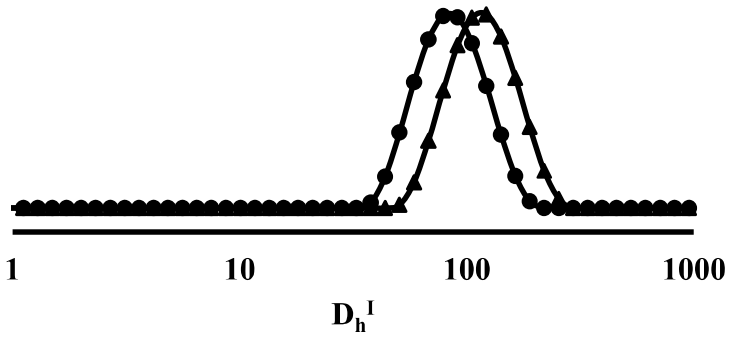

Figure 5-3. DLS intensity-weighted size distributions for G2@PAA13-b-PS390 ACC before (●) and after (▲) loading with 0.5 equiv of $HAuCl_4$/2VP unit in toluene at 0.8 mg/mL.

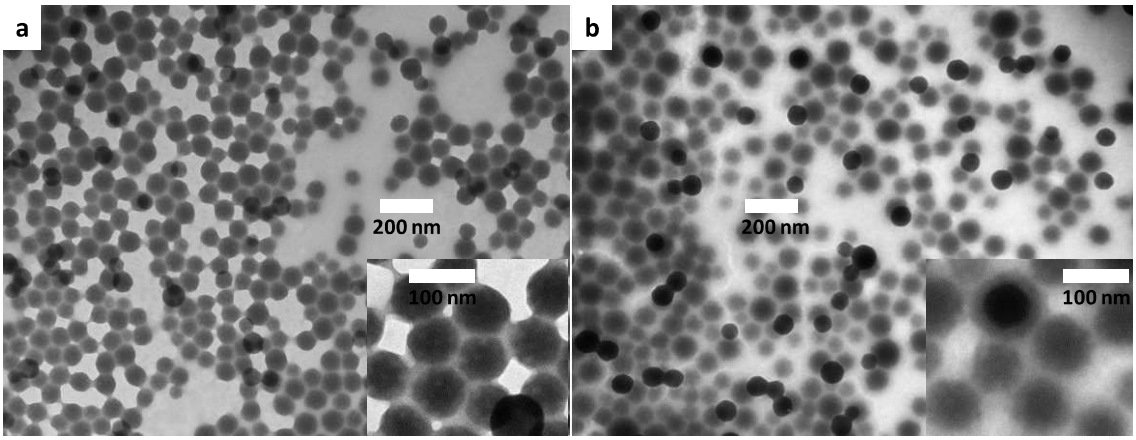

Figure 5-4. TEM images for $HAuCl_4$-loaded G2@PAA13-b-PS390 at (a) 0.5 and (b) 1 equiv/2VP unit in toluene.

To examine the influence of the PS block length on MNP formation, the G2@PAA10-*b*-PS*n* ACCs (*n* = 85, 205, 260, or 305) were loaded with 0.5 equiv of $HAuCl_4$ in toluene. The size analysis results before and after loading are summarized in **Table 5-1**, and the corresponding TEM images are provided in **Figure 5-5**. It can be seen that $HAuCl_4$ was successfully loaded in the complexes in all cases, as darker regions are present inside each ACC. For the shorter BCP sample (PAA10-*b*-PS85), however, aggregation is clearly seen after metal loading (**Figure 5-5a**). This is attributed to the shorter stabilizing

PS segments in the corona being unable to shield interparticle interactions effectively. Aggregation is also visible in the corresponding AFM image (**Figure 5-6a**), where the particles either have merged into larger aggregated particles, or are linked end-to-end to form multimolecular aggregates. On the other hand, ACCs derived from block copolymers with an intermediate PS block length (PS205 and PS260) display ring-like metal organization. This could be due to flattening of the PS chains in the corona upon transfer of the sample to the TEM copper grid. A similar metal distribution was reported for covalently grafted G1PS-*g*-P2VP-*b*-PS copolymer templates obtained by anionic grafting.[37] In that case, the ring-like nanostructures observed in TEM imaging were shown to correspond to annular phase separation in AFM measurements. While the G2 ACC also contains a G1PS core, such phase separation was not observed in AFM imaging of the ACC system (**Figure 5-6**) but rather a globular topology, irrespective of the BCP used. Since the P2VP block in both systems had a similar size (25K in G1PS-*g*-P2VP-*b*-PS vs. 30K in the G2 ACC), this suggests that phase separation is somewhat less pronounced for CSC structures prepared by self-assembly. This observation is also consistent with the assumption that the brighter region at the center of the particles in the TEM picture is due to the metal-depleted PS core. Furthermore, it should be noted that not all the G2 ACC systems display ring-like metal organization (**Figure 5-5**): While G2@PAA10-*b*-PS205 and G2@PAA10-*b*-PS260 both have clearly visible ring structures, that feature is less obvious for G2@PAA10-*b*-PS305, and G2@PAA10-*b*-PS85 even appears to contain multiple lighter (presumably PS-rich) domains within each template. The presence of multiple PS cores would also be consistent with the aggregation of multiple ACPS molecules, considering the larger (115 nm) size of the metal-loaded domains observed for the G2@PAA10-*b*-PS85 system (**Figure 5-5a**).

The size distribution of the complexes measured by DLS after metal loading was broader than before loading in toluene (**Table 5-1**). This could be related to the formation of non-uniform structures, albeit for the complex derived from the shorter block copolymer (G2@PAA10-*b*-PS85), the size dispersity

increase is more likely due to aggregation. This is also evident in the AFM images for that sample **Figure 5-6a**).

Table 5-1. Particle size characterization for G2@PAA10-b-PS ACCs before and after loading with 0.5 equiv $HAuCl_4$/2VP unit in toluene. All diameters are in nm.

Sample	DLS (ACC)		DLS ($HAuCl_4$-ACC)		TEM ($HAuCl_4$-ACC)	AFM ($HAuCl_4$-ACC)
	D_h^Z	Đ	D_h^Z	Đ	D_n	D_n
G2a	73±1	0.02	240±7	0.03	-	-
G2@PS85	90±1	0.15	218±6	0.08	115±15	120±34
G2@PS205	94±1	0.06	180±6	0.20	46±5	61±5
G2@PS260	95±1	0.22	118±2	0.24	47±4	70±7
G2@PS305	97±1	0.10	224±3	0.15	44±4	81±5

a) *The G2 substrate was measured in THF, as the substrate was not soluble in toluene below 41 ^oC.*

The diameter of the complexes measured by DLS after loading was higher than before loading (**Table 5-1**), presumably due to swelling of the micelles upon coordination with $HAuCl_4$.[46] As discussed earlier for TEM imaging, the larger D_h^Z increase observed for $HAuCl_4$-G2@PAA10-*b*-PS85 is again consistent with aggregation.

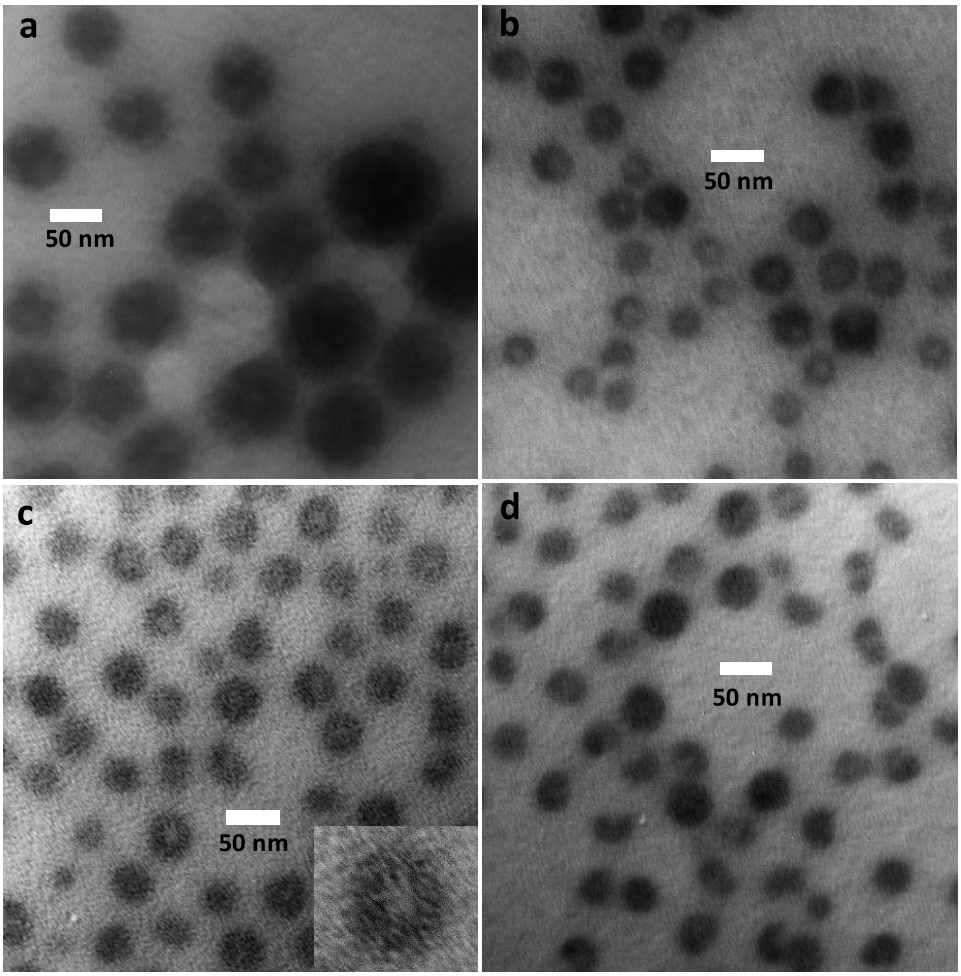

Figure 5-5. TEM imaging for (a) G2@PAA10-b-PS85, (b) G2@PAA10-b-PS205, (c) G2@PAA10-b-PS260, and (d) G2@PAA10-b-PS305 loaded with 0.5 equiv $HAuCl_4$/2VP unit in toluene.

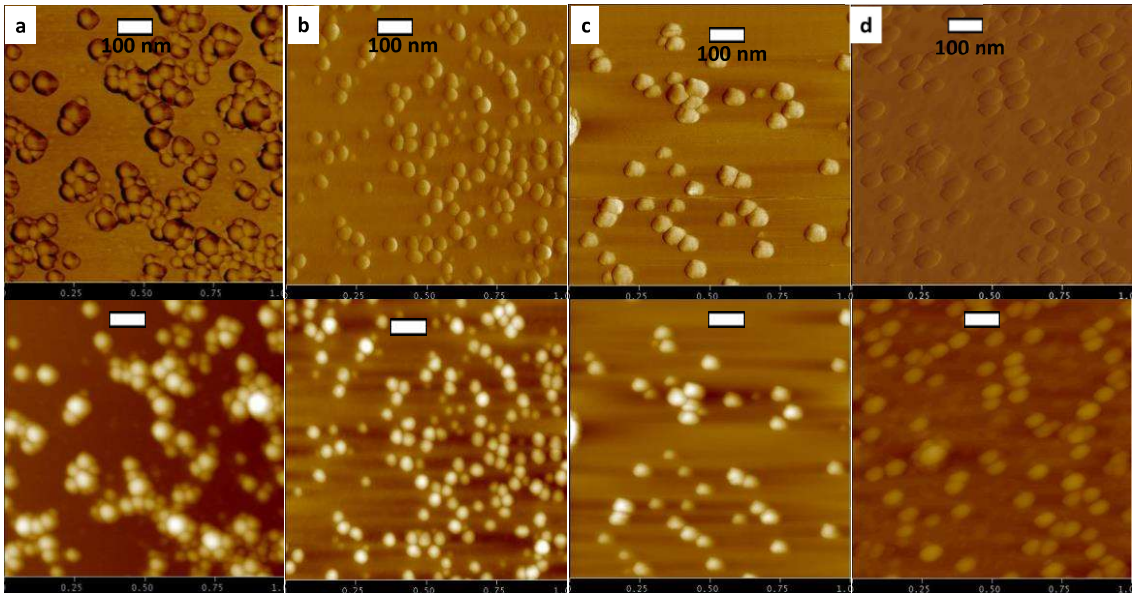

Figure 5-6. AFM phase (bottom) and height (top) images for (a) G2@PAA10-b-PS85, (b) G2@PAA10-b-PS205, (c) G2@PAA10-b-PS260, and (d) G2@PAA10-b-PS305 loaded with 0.5 equiv $HAuCl_4$/2VP unit in toluene.

To investigate the influence of the loading level on MNP formation, the number of equivalents of $AuCl_4^-$ ions coordinated with 2VP was varied. Since $HAuCl_4$ is insoluble in toluene, and metal coordination with the 2VP units leads to incompatibility of the ionic and nonionic blocks, in addition to steric effects due to the bulky anions, the solubility of the ACC templates as well as phase separation could be affected to different extents. The G2@PAA10-*b*-PS260 ACC template was thus loaded with 0.25, 0.5, 0.75 and 1.0 equiv of $HAuCl_4$/2VP unit in toluene, and the resulting metallic nanoparticles were examined by TEM (**Figure 5-7**). In all cases the metal was successfully loaded in the ACC structures, the density of the metallic domains increasing with the loading level as expected. With the exception of the 0.5 equiv loading level, displaying ring-like metal organization, the other loading levels yielded a more uniform metal distribution within the ACC structures (**Figure 5-7**). The metal distribution within the ACC templates therefore appears to depend on the loading level to some extent.

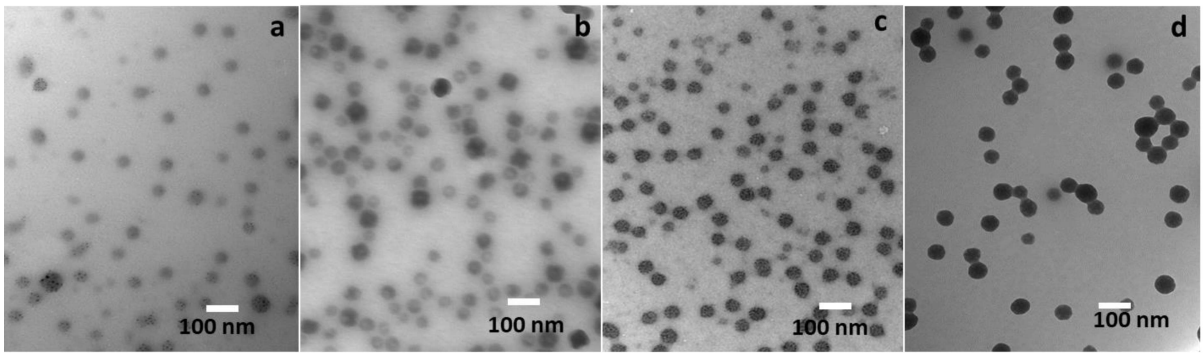

Figure 5-7. TEM images for G2@PAA10-b-PS 260 loaded with $HAuCl_4$ in toluene at (a) 0.25, (b) 0.5, (c) 0.75 and (d) 1 equiv/2VP unit.

5.4.3 $HAuCl_4$ loading in the G3 ACC System

The G3@PAA-*b*-PS ACCs were also investigated as templates for $HAuCl_4$ in toluene and other solvents. Provided in **Figure 5-8** are TEM and AFM images obtained after loading 0.5 equiv of $HAuCl_4$/2VP unit in the G3@PAA10-*b*-PS260 ACC. The dark regions observed in every particle of the TEM image confirm that loading of the complex was successful. Both the AFM and TEM images display a raspberry-like morphology after loading, which was also observed before loading but less clearly defined. Interestingly, this type of morphology was also reported in a previous investigation with covalently grafted core–shell–corona copolymers of the same generation, but only after loading.[38] The diameter of the complex determined from DLS, AFM, and TEM analysis was 171 ± 1, 107 ± 6 and 70 ± 4 nm, respectively. This corresponds to 37 % (AFM) and 59 % (TEM) size shrinkage as compared to the diameter obtained from DLS, likely due to collapse of the complex in the dry state. The size difference from AFM to TEM, corresponding to a 35 % decrease, is attributed to the fact that the PS corona should be invisible in the TEM image due to its low electron density. Moreover, different degrees of flattening of the complex on the mica and TEM grid surfaces may also have contributed to the observed size differences.

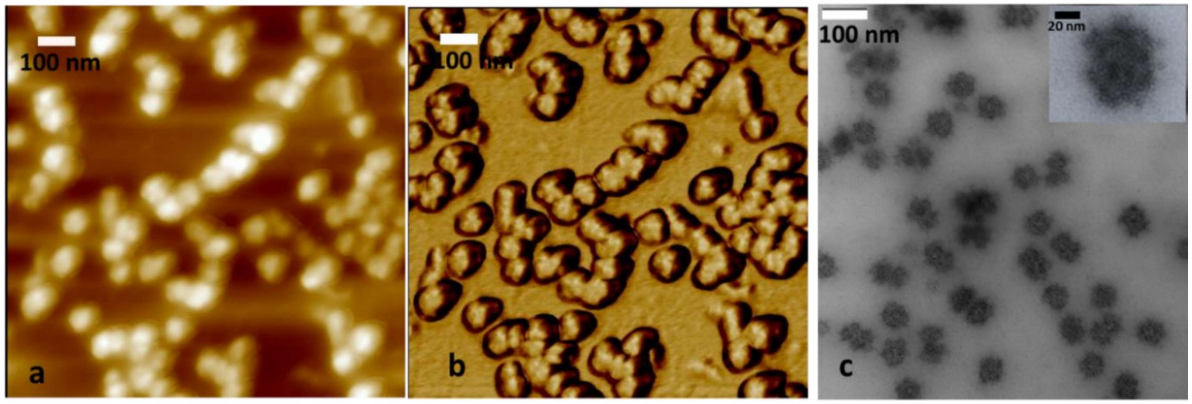

Figure 5-8. AFM height (a) and phase (b) scan images, and (c) TEM image for the G3@PAA10-b-PS260 ACC loaded with 0.5 equiv $HAuCl_4$/2VP unit in toluene.

Given the interesting raspberry-like morphology observed for the $HAuCl_4$-loaded G3@PAA10-*b*-PS260 ACC, the G3@PAA10-*b*-PS260 ACC was also prepared using a 1 : 2 mass ratio of substrate to BCP and loaded with 0.5 equiv of $HAuCl_4$/2VP unit. For comparison, the metal-loaded ACC had a D_h^Z of 154 ± 3 nm. A raspberry-like morphology was maintained in that case as well, as observed in both the TEM (73 ± 5 nm diameter) and AFM (90 ± 7 nm diameter) images of **Figure 5-9**. Moreover, the TEM images displayed enhanced light gray shadowing of the core portion of the complexes (indicated by arrows on **Figure 5-9b**). Although this result was not well-established with other samples, it thus seems that increasing the amount of PS in the stabilizing corona may enhance phase separation within the ACCs.

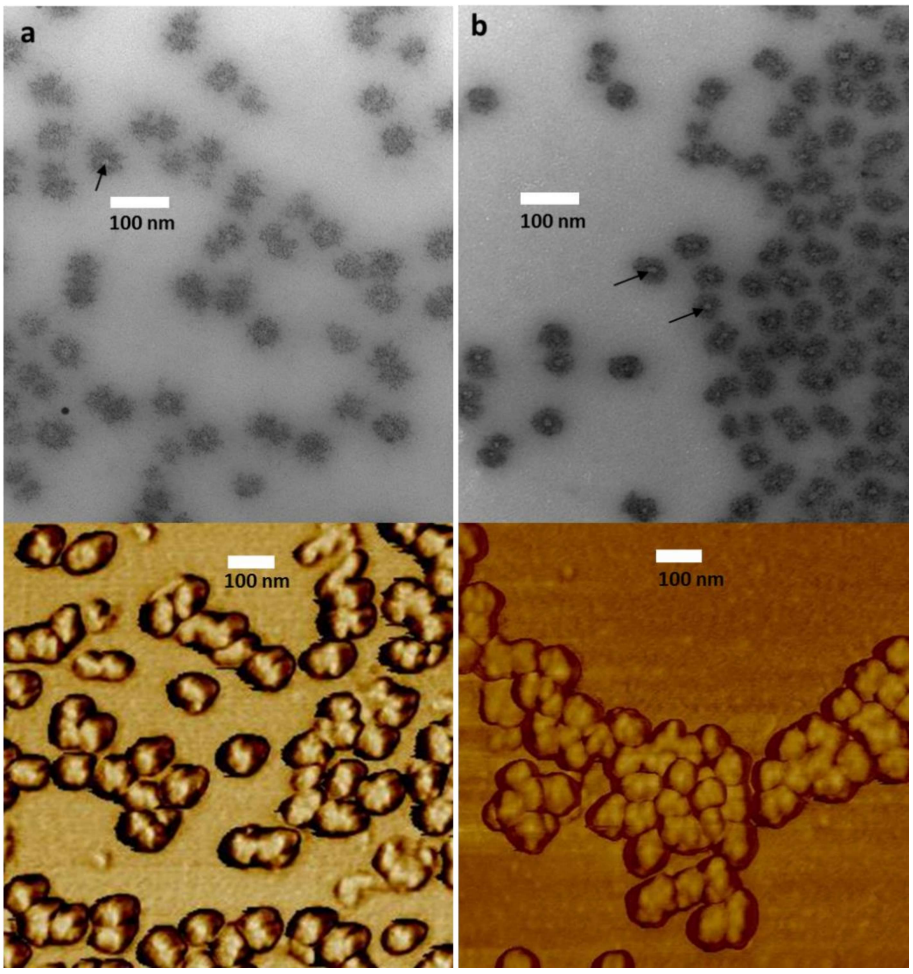

Figure 5-9. Comparison of TEM (top) and AFM phase scan (bottom) images for the G3@PAA10-b-PS260 ACC loaded with 0.5 equiv $HAuCl_4$/2VP unit, prepared using (a) 1 : 1, and (b) 1 : 2 mass ratios of G3 : PAA10-b-PS260 in toluene.

After examining the influence of the PS stabilizing corona on the morphology of the $HAuCl_4$-loaded ACC at constant length of the PS stabilizing segment, the influence of the PS block length was investigated. Provided in **Figure 5-10** are TEM images for $HAuCl_4$-loaded (0.5 equiv/2VP unit) ACCs obtained from BCPs having different PS block lengths at a G3 : BCP mass ratio of 1 : 1, and in **Figure 5-11** are the corresponding AFM images. While even the $HAuCl_4$-loaded ACC with the shortest BCP (G3@PAA10-*b*-PS85) produced a raspberry-like morphology, as confirmed by TEM and AFM

analysis (**Figure 5-10a** and **5-11a**, respectively), size analysis was impractical for this system due to extensive aggregation. This is again attributed to the thin stabilizing PS corona formed by the short (PS85) block, unable to shield efficiently interparticle interactions between the $HAuCl_4$-loaded complexes. A raspberry-like morphology was also obtained for the $HAuCl_4$-loaded G3@PAA13-*b*-PS156 ACC, as seen in both the TEM and AFM images. The TEM image (**Figure 5-10b**) is not very clear, but the AFM image (**Figure 5-11b**) does reveal minor aggregation that may likewise be due to poor stabilization provided by the still relatively short PS block (PS156). In contrast, the $HAuCl_4$-loaded G3@PAA10-*b*-PS260 sample (**Figure 5-10c**) clearly produced raspberry-like morphologies without aggregation; this demonstrates the importance of the PS block length in achieving good colloidal stability. The $HAuCl_4$-loaded G3@PAA10-*b*-PS305 ACC sample also displayed aggregation-free particles, but the raspberry-like morphology is less obvious (**Figure 5-10d**). This effect is even more obvious for the $HAuCl_4$-loaded complexes with longer BCPs, G3@PAA13-*b*-PS330 and G3@PAA13-*b*-PS390 (**Figure 5-10e** and **f**). While the raspberry-like morphology is not clearly observable in the TEM images, a closer look at the TEM images (insets of **Figure 5-11e** and **f**) still reveals the presence of nanodomains within the structures, potentially resembling a gyroid-like morphology.[48] The TEM image for the $HAuCl_4$-loaded G3@PAA13-*b*-PS390 ACC (**Figure 5-10f)** also displays a second population of smaller particles, possibly resulting from the aggregation of free BCP side chains, which are also visible in the AFM image (**Figure 5-11f**). This seems reasonable, since the long PS segment in PAA13-*b*-PS390 may make the complexation of the block copolymer with the dense G3 copolymer substrate more difficult.

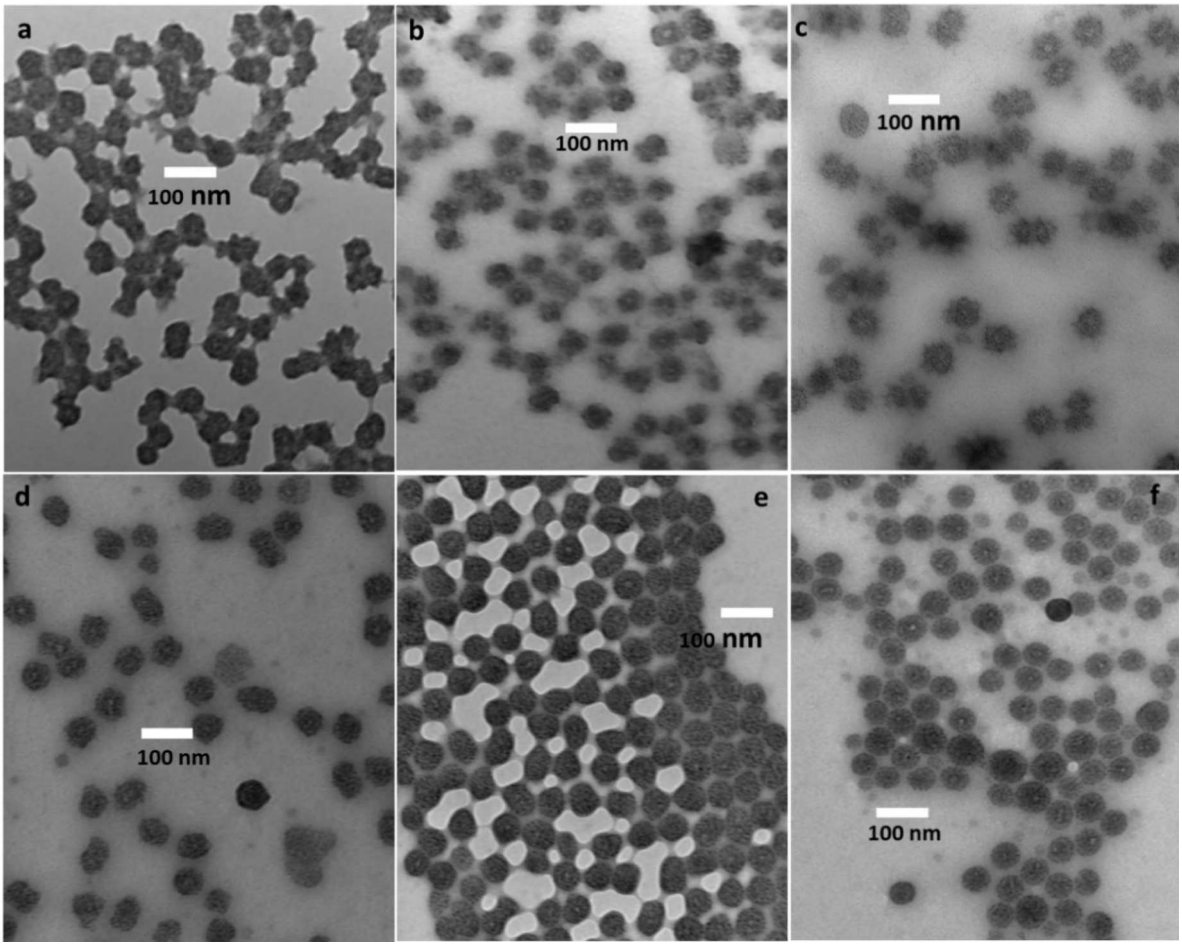

Figure 5-10. TEM images for (a) G3@PAA10-b-PS85, (b) G3@PAA13-b-PS156, (c) G3@PAA10-b-PS260, (d) G3@PAA10-b-PS305, (e) G3@PAA13-b-PS330, and (f) G3@PAA13-b-PS390 loaded with 0.5 equiv $HAuCl_4$/2VP unit in toluene.

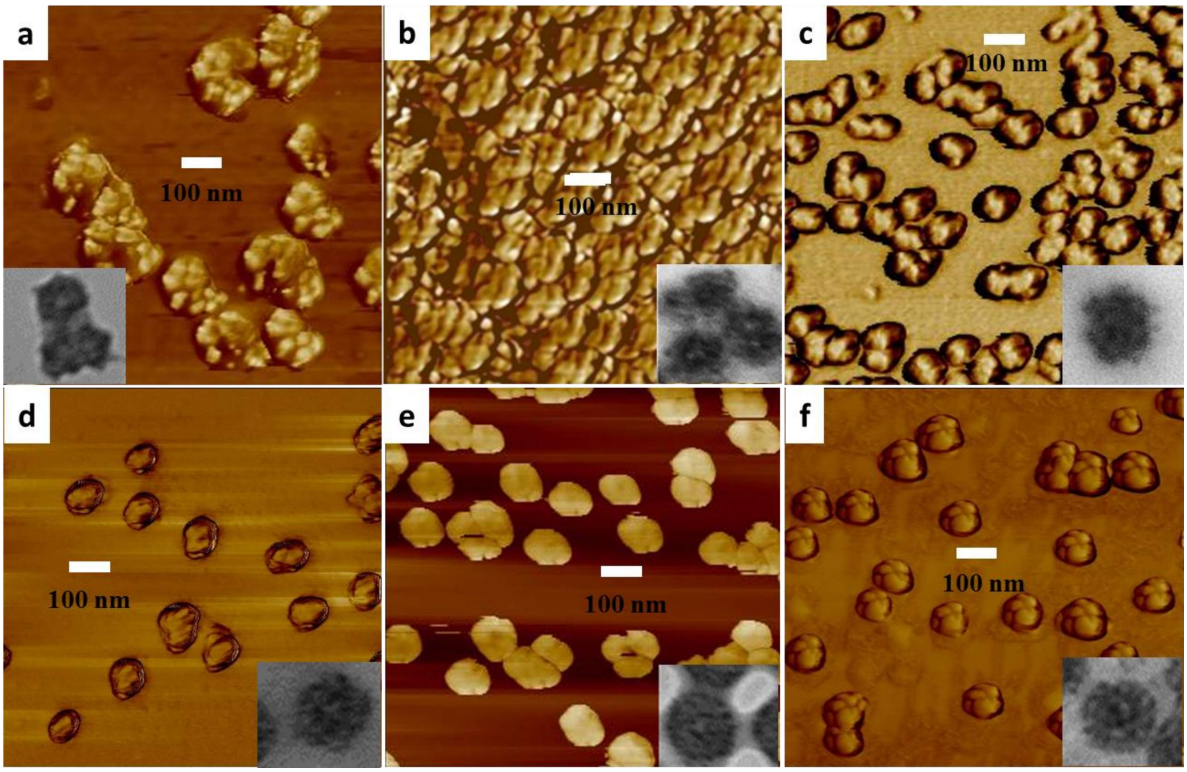

Figure 5-11. AFM phase scan images for (a) G3@PAA10-b-PS85, (b) G3@PAA13-b-PS156, (c) G3@PAA10-b-PS260, (d) G3@PAA10-b-PS305, (e) G3@PAA13-b-PS330, and (f) G3@PAA13-b-PS390 loaded with 0.5 equiv $HAuCl_4$/2VP unit in toluene. The insets are enlarged sections of the TEM images in Figure 5-10, provided for comparison.

The diameters of the $HAuCl_4$-loaded ACCs (0.5 equiv $HAuCl_4$/2VP unit) determined from TEM and AFM analyses are compared in **Table 5-2**. Also included in the table are the D_h^Z of the ACCs determined by DLS before and after loading with $HAuCl_4$. As pointed out earlier, the size obtained by TEM analysis (54–70 nm) is smaller than by AFM (101–202 nm), which is attributed to the PS corona being invisible in the TEM images. The trends among the samples are not so clear: A size increase would indeed be expected as the PS block length in the BCPs increases, but it was already mentioned that significant aggregation of the ACCs was taking place for shorter PS segments. On the other hand, the decrease in size observed for very long PS segments could be due to increased difficulty in the

complexation process. These rules seem to apply to the TEM results reported in **Table 5-2**, but the trends for the AFM and DLS results are not as clear.

Table 5-2. Particle size characterization for G3@PAA-b-PS ACCs before and after loading with 0.5 equiv of $HAuCl_4$/2VP unit in toluene.

Sample	DLS		DLS ($HAuCl_4$)		TEM ($HAuCl_4$)	AFM ($HAuCl_4$)
	D_h^Z (nm)	Đ	D_h^Z (nm)	Đ	D (nm)	D (nm)
G3 (in THF)	92±1	0.07	-	-	-	-
G3@PAA10-b-PS85	94±1	0.10	135±2	0.10	54±5	202±18
G3@PAA13-b-PS156	117±1	0.13	116±1	0.04	65±4	127±16
G3@PAA10-b-PS260	94±1	0.10	171±1	0.15	70±4	107±6
G3@PAA10-b-PS305	110±2	0.18	119±1	0.05	66±5	110±10
G3@PAA13-b-PS330	119±3	0.25	134±3	0.08	64±5	118±6
G3@PAA13-b-PS390	90±3	0.45	131±3	0.10	62±8	101±10

To study the influence of the loading level on the morphology of the ACCs, and since the G3 ACC system displayed well-defined phase separation in both AFM and TEM analysis, the G3@PAA10-*b*-PS260 ACC was loaded with different amounts of $HAuCl_4$. TEM images obtained for G3@PAA10-*b*-PS260 loaded with different amounts of $HAuCl_4$ (0.25, 0.5, 0.75, and 1 equiv of $HAuCl_4$/2VP unit) are provided in **Figure 5-12**. The darker regions observed inside each ACC sample again confirmed the successful loading of $HAuCl_4$ in all cases. Upon increasing the loading level the metal-rich domains became darker as expected, due to an increase in electron density with the amount of $HAuCl_4$ present. The $AuCl_4^-$ ions have been shown to influence the size and morphology obtained in polystyrene-*block*-poly(2-vinylpyridine) copolymer systems,[49] which was explained in terms of variations in the ionization level of the P2VP block, an increase in volume due to the coordinated metal, and increased surface energy between the ionized 2VP units and toluene.[46] Consequently, it would not

be surprising if the size and morphology of the ACC systems likewise depended on the loading level. Using TEM, the average diameter of the $HAuCl_4$-loaded ACCs was determined for at least 20 different particles. The average diameter obtained for $HAuCl_4$-loaded G3@PAA10-*b*-PS260 was 68 ± 8, 70 ± 4, 66 ± 3, and 67 ± 3 nm for 0.25, 0.5, 0.75, and 1 equiv $HAuCl_4$ loading/2VP unit, respectively. Consequently, there were no significant size variations with the loading level (within error limits) for this ACC system, at least in the dry state. This lack of trend may be related to the structural rigidity of arborescent substrates. These results also indicate that $HAuCl_4$ is efficiently constrained within the volume of the ACCs. As the loading level was increased from 0.25 to 0.75 equiv the raspberry-like morphology became more clearly visible without any obvious change in morphology, while at 1 equiv it was more difficult to observe, likely due to the increased electron density of the ACCs.

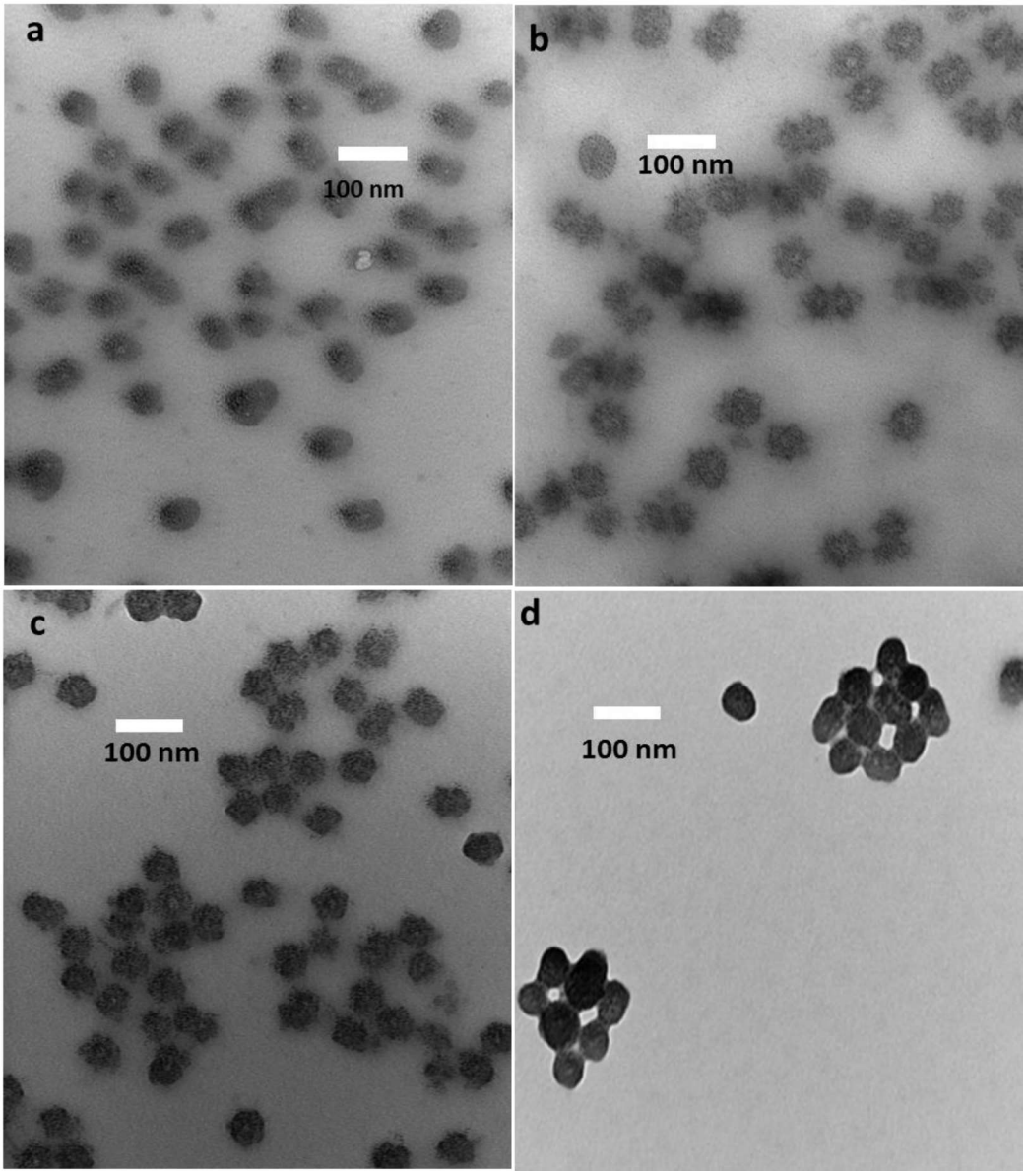

Figure 5-12. TEM images for the G3@PAA10-b-PS260 ACC loaded with (a) 0.25, (b) 0.5, (c) 0.75, and (d) 1 equiv of $HAuCl_4$/ 2VP unit in toluene.

To investigate the influence of the solvent used in the loading procedure on the morphology obtained, the G3@PAA10-*b*-PS260 complex, first prepared in THF, was transferred to either toluene with 2% methanol, THF with 25% cyclohexane, or chloroform prior to loading with 0.5 equiv of $HAuCl_4$. The

TEM images obtained for these materials, shown in **Figure 5-13**, confirm successful metal loading in all the solvents. No appreciable size differences were observed for the different solvent systems: The diameter of the $HAuCl_4$-loaded G3@PAA10-*b*-PS260 complex was 70 ± 4, 70 ± 4, 72 ± 3, and 70 ± 4 nm in toluene, toluene with 2% methanol, THF with 25% cyclohexane, and chloroform, respectively. The organization of the metal in the complexes did vary with the type of solvent used, however. As discussed earlier, a raspberry-like morphology (more clearly visible in the inset of **Figure 5-13a**) was observed in toluene. In toluene with 2% methanol a uniform metal distribution was obtained, giving a spherical topology to the ACC scaffold. This may be due to enhanced solubility of the P2VP segments in the presence of methanol. In THF with 25% cyclohexane, a higher concentration of metal was observed at the center than at the periphery of the ACCs. Since cyclohexane is a non-solvent for P2VP, protonation and coordination of the P2VP segments with $AuCl_4^-$ should only make this condition worse. Consequently, the metal-coordinated P2VP segments may rearrange towards the center of the ACCs to minimize contact with the cyclohexane component. The overall ACC morphology still looks spherical, however. In chloroform, finally, the metal distribution appears relatively uniform within the spherical ACCs, but some particles also display clearer patches (in some cases, near the core of the ACC), presumably corresponding to the PS component that is phase-separated from the metal-rich regions.

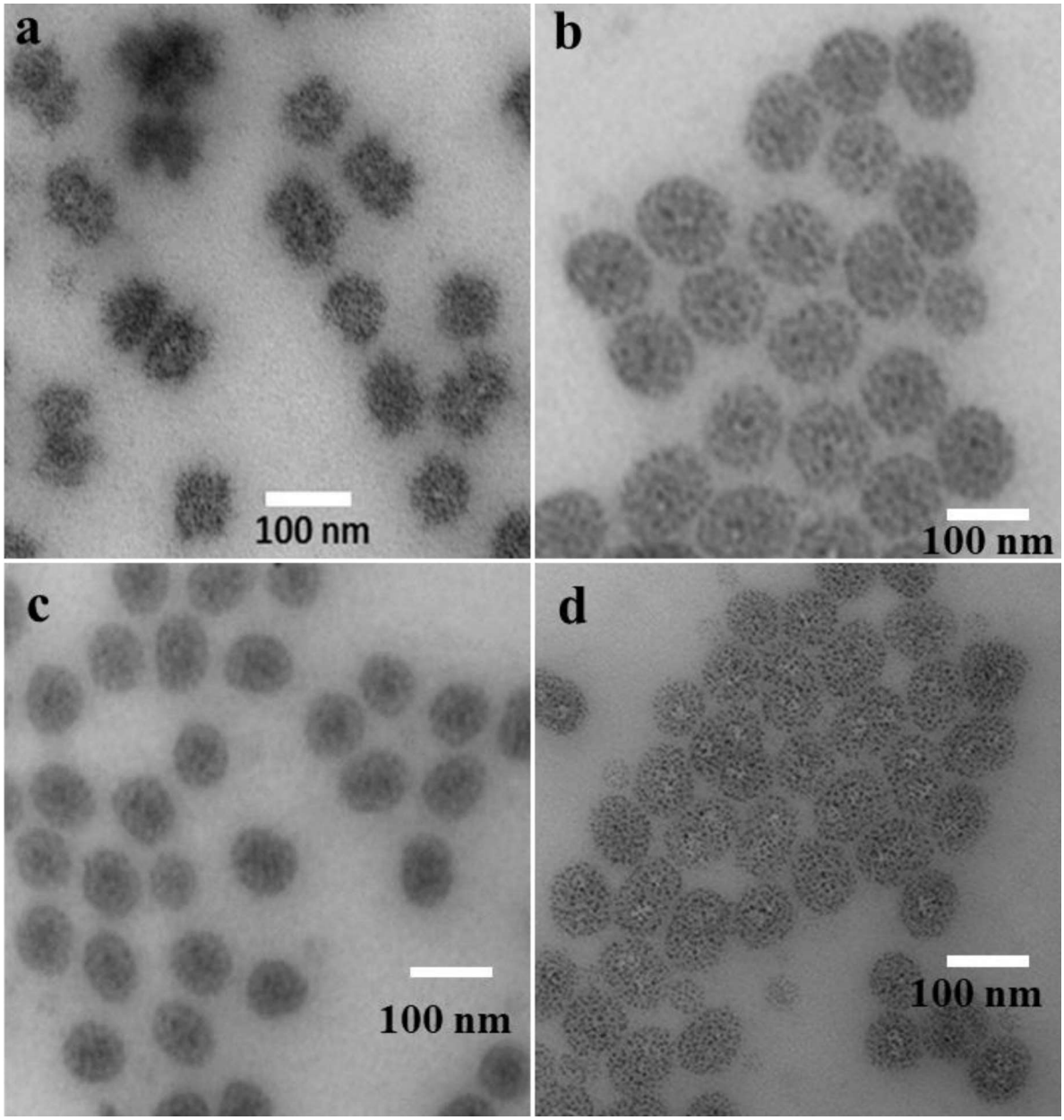

Figure 5-13. TEM images for G3@PAA10-b-PS260 loaded with 0.5 equiv $HAuCl_4$/2VP unit in (a) toluene, (b) toluene with 2% methanol, (c) THF with 25% cyclohexane, and (d) chloroform.

5.4.4 $HAuCl_4$ loading in the G4 ACC System

Metal loading in the G4@PAA10-*b*-PS complexes was investigated for the same reasons as the lower generation systems (**Sections 5.4.1** and **5.4.2**). TEM and AFM images obtained for G4@PAA10-*b*-

PS260 loaded with 0.5 equiv of $HAuCl_4$/2VP unit are provided in **Figure 5-14.** The trend in the mean diameters measured by TEM, AFM and DLS, namely 118 ± 11, 156 ± 15, and 154 ± 2 nm, respectively, can be explained as before by the fact that the PS corona is not detected in TEM imaging, while swelling of the core and corona is expected in solution.[50] The TEM image (**Figure 5-14a**) revealed phase separation between the metal-loaded domains formed by the P2VP shell, while the corona was indeed not clearly visible. A core–shell morphology is prevalent in both the TEM and AFM images, but the particles appear interconnected.

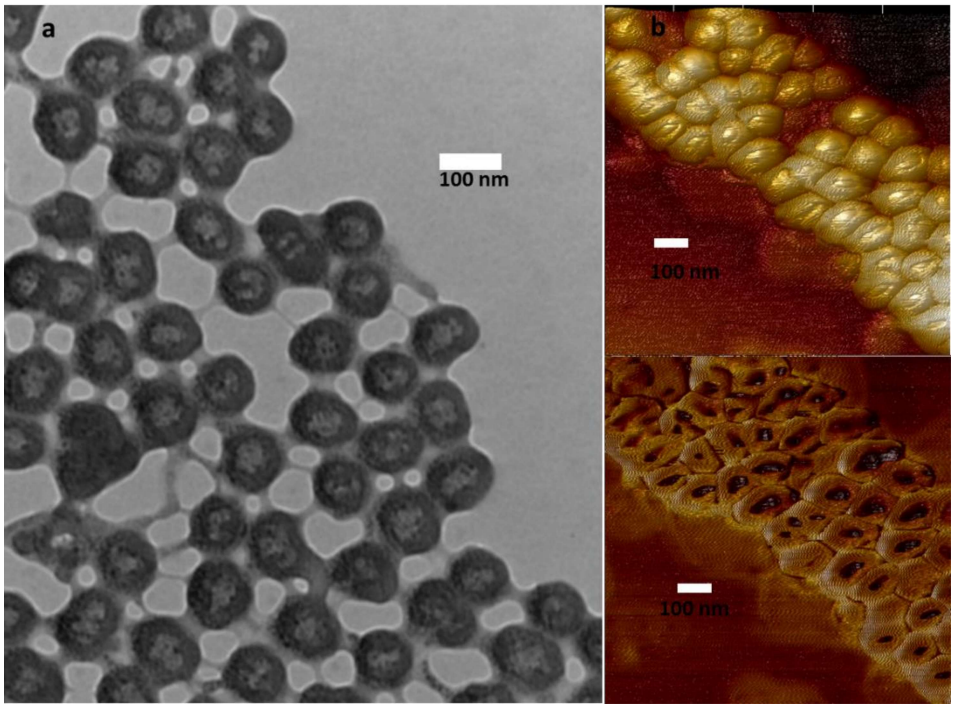

Figure 5-14. (a) TEM, and (b) AFM height scan (top) and phase scan (bottom) images for G4@PAA10-b-PS260 ACC loaded with 0.5 equiv $HAuCl_4$/2VP unit in toluene.

To better understand the phase separation process in the G4 system, complexes were prepared from the G4 substrate and PAA10-*b*-PS copolymers having different PS block lengths (in a 1 : 1 weight ratio) in THF, transferred to toluene, and loaded with 0.5 equiv of $HAuCl_4$. TEM images obtained for the

samples are compared in **Figure 5-15** for G4@PAA10-*b*-PS85, G4@PAA10-*b*-PS205, G4@PAA10-*b*-PS260, and G4@PAA10-*b*-PS305. The ACC with the shortest block copolymer, G4@PAA10-*b*-PS85, yielded a seemingly spherical $HAuCl_4$ distribution, with significant aggregation (**Figure 5-15a**) preventing clear visualization of the morphological features. This is similar to the systems previously discussed containing short BCP side chains (G2@PAA10-*b*-PS85 and G3@PAA10-*b*-PS85), which also aggregated after metal loading due to insufficient shielding of interparticle interactions. Interestingly, the extent of aggregation was much lower for G3@PAA10-*b*-PS85 and G4@PAA10-*b*-PS85 in comparison to G2@PAA10-*b*-PS85, even though interconnected individual particles were still prevalent. This suggests that the PS core also plays a role in preventing aggregation. The $HAuCl_4$-loaded G4@PAA10-*b*-PS205 and G4@PAA10-*b*-PS260 ACCs (**Figure 5-15b** and **c**) likewise revealed phase separation whereby a dark ring-like metal pattern, which should correspond to the metal-loaded P2VP inner shell, is surrounding the lighter PS core. The particles seem to be interconnected by the PS corona material, or possibly due to polyelectrolyte bridging,[51] if the PAA anchoring segment of the block copolymer simultaneously interacts with two arborescent substrate molecules. Since the G4 substrate is more rigid than the lower generation substrates, it may be more difficult for the PAA segment of the copolymers to diffuse deep into the P2VP shell of the substrate. Under these conditions the BCP may be restricted to the edge of the substrate, potentially connecting two ACC assemblies. For the same reason, the interface between the metal-poor PS core and the metal-rich P2VP shell of the ACCs appears sharper in comparison with earlier generations. Finally, the $HAuCl_4$-loaded G4@PAA10-*b*-PS305 ACC displayed a morphology distinct from the other samples in that series, closer to the raspberry-like morphology observed for the G3 complexes.

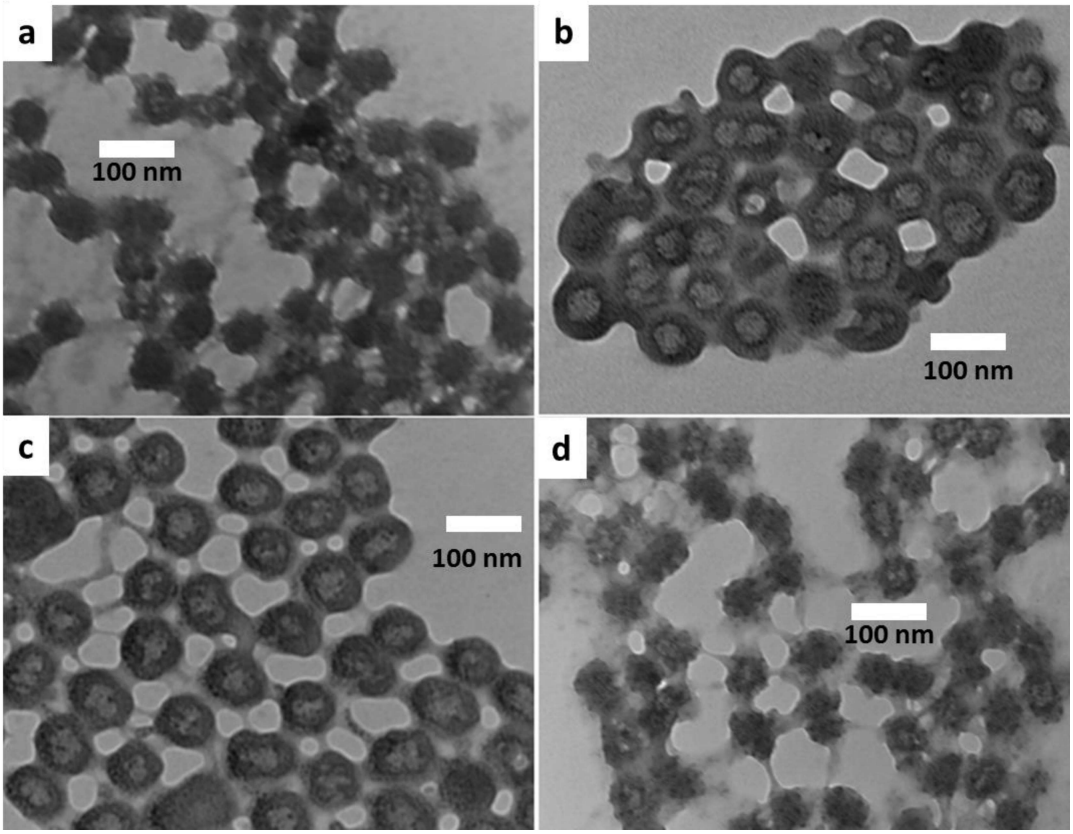

Figure 5-15. TEM images for (a) G4@PAA10-b-PS85, (b) G4@PAA10-b-PS205, (c) G4@PAA10-b-PS260, and (d) G4@PAA10-b-PS305 loaded with 0.5 equiv of $HAuCl_4$/2VP unit in toluene.

Since the metal-loaded G4 ACC systems displayed a core–shell morphology in most cases, it would be interesting to determine whether the corona could also be detected under different conditions. It has indeed be reported that under-focused TEM imaging can, in some cases, reveal more structural information than focused images due to enhanced contrast.[52] Focused and under-focused TEM images obtained for $HAuCl_4$-loaded G4@PAA10-*b*-PS260 are compared in **Figure 5-16**. It can be seen that the focused TEM image clearly highlights phase separation between the PS core (the lighter region at the center of each ACC assembly) and the metal-loaded black region, but barely reveals the PS corona layer (inset of **Figure 5-16a**). The under-focused TEM image clearly shows the PS corona layer as a

gray layer surrounding the sphere (inset of **Figure 5-16b**), however. The thickness of the corona is ~7 ± 1 nm, slightly lower than the fully extended chain length calculated for the PAA10-*b*-PS260 copolymer (8.3 nm). While nearly full extension of the block copolymer chains forming the corona appears unlikely, this result at least confirms the presence of a PS layer forming the corona of the ACC.

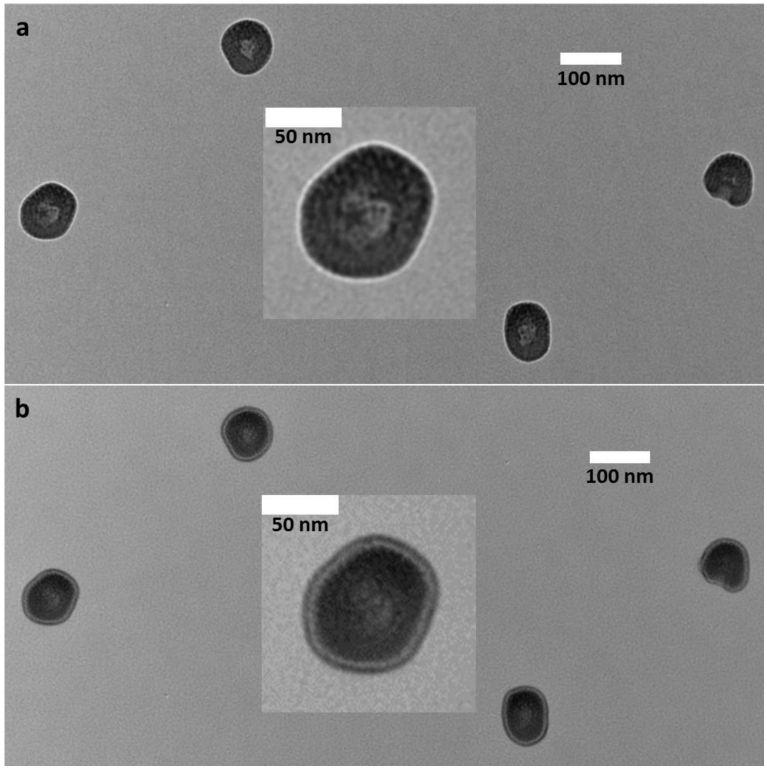

Figure 5-16. (a) Focused and (b) under-focused TEM images for G4@PAA10-b-PS260 loaded with 0.5 equiv of $HAuCl_4$/2VP unit in toluene.

The influence of the loading level was also investigated for G4@PAA10-*b*-PS260 by loading with 0.25, 0.5, 0.75 and 1 equiv of $HAuCl_4$/2VP unit; the corresponding TEM images are provided in **Figure 5-17**. At 0.25 equiv loading, a mixed morphology is visible, some of the particles showing a core–shell morphology with the metal at the periphery, but most of the particles have a spherical morphology with a uniform metal distribution. This suggests that metal uptake may not be concurrent for all the particles.

Increasing the loading level to 0.5 equiv/2VP unit transformed all the particles to a core–shell morphology, but the predominance of this morphology decreased when the loading level was further increased to 0.75 and 1 equiv. The presence of a shell and a corona is more obvious at 0.75 equiv loading in an under-focused TEM image (**Figure 5-18**). The average diameters obtained were 120 ± 15, 118 ± 11, 114 ± 8 and 114 ± 12 nm for the 0.25, 0.5, 0.75 and 1 equiv loading levels, respectively. These results are comparable to the G3 ACCs discussed previously, in that there was no significant variation in size with the loading level, probably due to the rigidity of the arborescent substrate in the dry state.

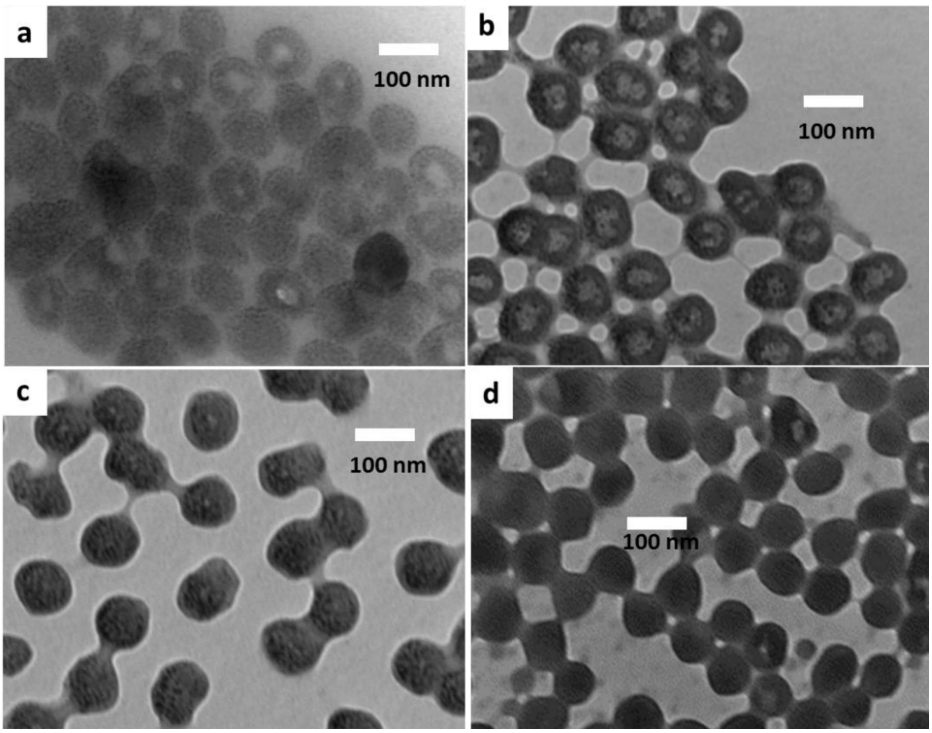

Figure 5-17. TEM images for G4@PAA10-b-PS260 loaded with $HAuCl_4$ at (a) 0.25, (b) 0.5, (c) 0.75, and (d) 1 equiv/2VP unit in toluene.

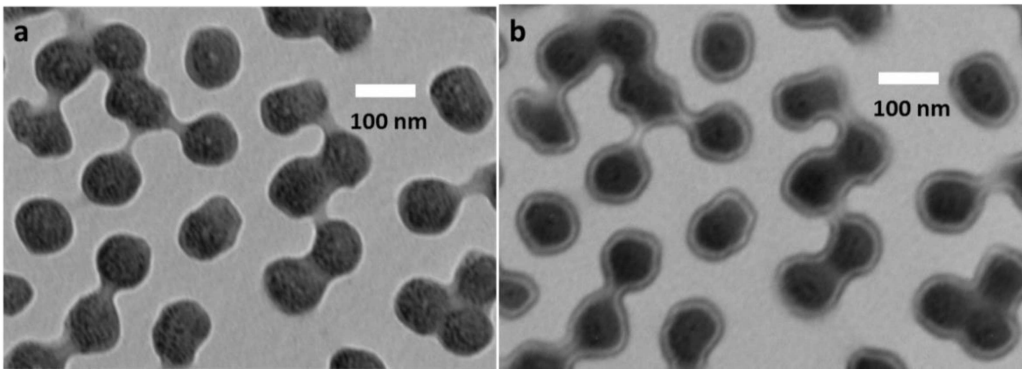

Figure 5-18. (a) Focused and (b) under-focused TEM images for G4@PAA10-b-PS260 loaded with 0.75 equiv $HAuCl_4$/2VP unit in toluene.

Since it was already determined for the G3 ACCs that the solvent composition influenced the metal distribution and the morphology of the complexes, a similar investigation was undertaken for the G4 systems. The G4@PAA10-*b*-PS260 complex was therefore prepared in THF, to be transferred to each solvent and loaded with 0.5 equiv of $HAuCl_4$/2VP unit in toluene with 2 % methanol, THF with 25 % cyclohexane, and chloroform. The TEM and AFM phase scan images obtained for samples prepared under these conditions, presented in **Figure 5-19**, show variations in metal organization. In toluene with 2% methanol, a gyroid-like metal distribution segregated by a layer of PS appears to be present in both the TEM (grey areas) and AFM images. This type of morphology was also reported for triblock copolymers of polyisoprene-*block*-polystyrene-*block*-polydimethylsiloxane.[48] In THF with 25% cyclohexane the metal was segregated closer to the center, similarly to the G3 complexes. A very thin layer, presumably corresponding to PS surrounding the metal-loaded zone, is visible in both the TEM and AFM images, with a spherical topology in both cases. In chloroform, the G4@PAA10-*b*-PS260 complex displays a distinct mushroom-like morphology where the metal is uniformly distributed within outer P2VP domains, albeit some of the particles in the TEM image also display a spherical morphology. This suggests that the distribution of PS segments within the core and the corona of the

G4 complexes is inhomogeneous in chloroform. This effect is not visible in the AFM images, however, where all the particles display a similar morphology. The minor differences observed in the TEM and AFM images may have been induced by interactions of the P2VP phase with the mica surface in the AFM samples. While the randomly distributed particles on the carbon-coated copper grid would not be expected to interact significantly with the substrate, electrostatic interactions should be much stronger between the negatively charged mica surface and the positively charged P2VP phase, which may have induced the transition from the mushroom-like morphology.[54]

Since the G3@PAA10-*b*-PS260 and G4@PAA10-*b*-PS260 complexes exhibited distinct types of phase separation, even though they had P2VP side chains of comparable dimensions, the differences observed among these samples must be related to the characteristics of the PS cores. The G3 and G4 copolymers were derived from G2PS and G3PS cores, respectively, which had different sizes (77 ± 1 and 97 ± 1 nm in THF, respectively). The G3PS substrate used to synthesize the G4 copolymer was also denser than the previous generations, which should have prevented the penetration of the P2VP phase within the PS core, resulting in the better defined core–shell morphology observed after loading (**Figure 5-16**). This is in contrast to the G2PS core serving in the synthesis of the G3 copolymer, which should be more tolerant to interpenetration of the P2VP segments within the PS core, yielding a nodular-type of arrangement of the two phases and a raspberry-like morphology after loading (**Figure 5-8b**).

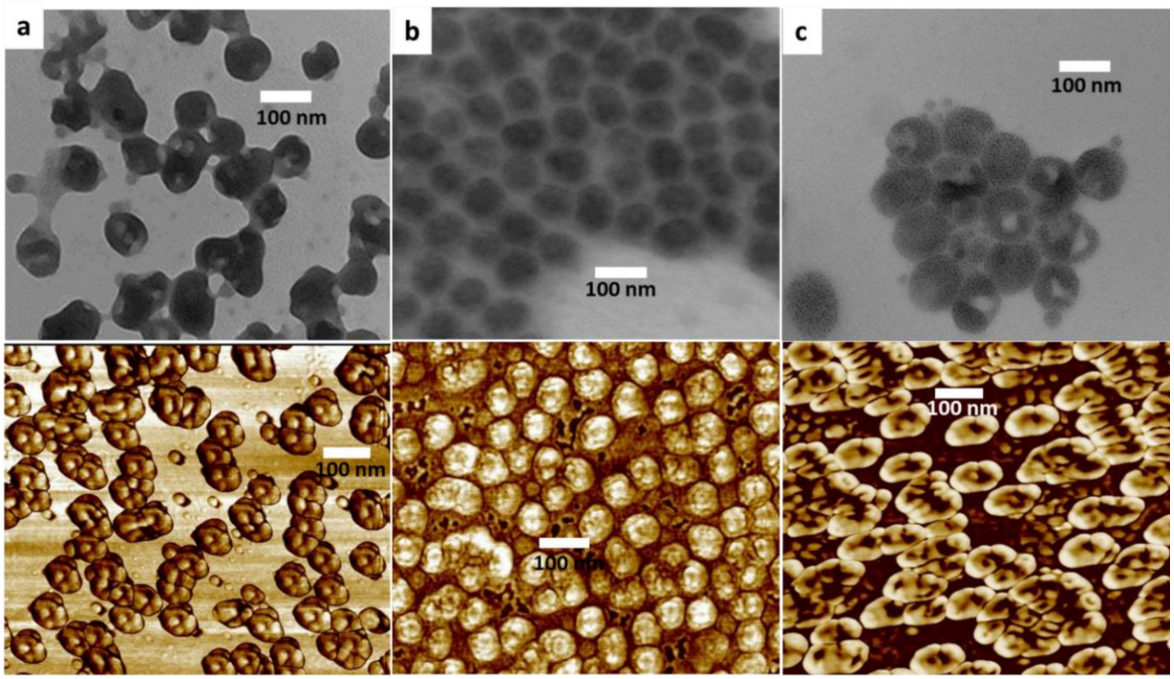

Figure 5-19. TEM (top) and AFM phase scan (bottom) images for G4@PAA10-b-PS260 loaded with 0.5 equiv $HAuCl_4$/2VP unit in (a) toluene with 2% methanol, (b) THF with 25% cyclohexane, and (c) chloroform.

5.4.5 $Pd(OAc)_2$ loading in G3@PAA-*b*-PS260 and G4@PAA-*b*-PS260 ACCs

Palladium nanoparticles have interesting applications in catalysis.[56-58] As a final investigation, it would therefore be interesting to determine whether the ACCs can also serve as templates for palladium(II) acetate, $Pd(OAc)_2$. To this end the G3@PAA-*b*-PS260 and G4@PAA-*b*-PS260 complexes, which displayed interesting phase-segregated nanomorphologies with $HAuCl_4$, were also loaded with 0.5 equiv of $Pd(OAc)_2$ in toluene. Since $Pd(OAc)_2$ is reported to coordinate with P2VP without protonating it,[57] in contrast to $HAuCl_4$, the influence of electrostatic interactions on the morphology is expected to be less significant. Consequently, the extent of phase separation may be less pronounced for the Pd-loaded systems.

Loading of G3@PAA-*b*-PS260 with 0.5 equiv of $Pd(OAc)_2$ (**Figure 5-20a**) yielded a nearly raspberry-like morphology, where ACCs with an average diameter of 69 ± 3 nm are connected in a necklace-like organization.[58] This may be due to ACC stacking, since Pd^{2+} can coordinate with pyridine rings from different ACC assemblies and therefore act as a cross-linker. Similar necklace-like organization was observed for the G4@PAA-*b*-PS260 complex at loading levels of 0.25, 0.5, and 0.75 equiv of $Pd(OAc)_2$/2VP unit (**Figure 5-20b–d**), with average diameters of ~97 ± 2, 98 ± 2 and 101 ± 4 nm, respectively. A core–shell morphology is also apparent for the $Pd(OAc)_2$-loaded systems, similar to that obtained for $HAuCl_4$, especially at the 1 equiv loading level. It therefore appears that electrostatic interactions between the metal ions and the P2VP component do not play a major role in the type of nanomorphology obtained for metal-loaded ACC systems.

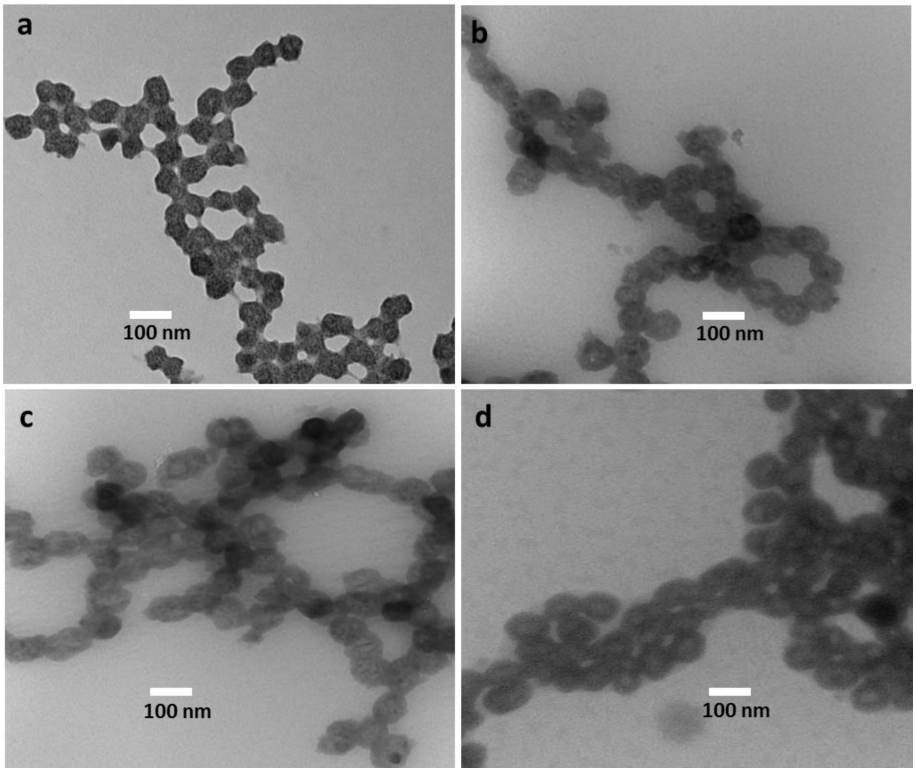

Figure 5-20. TEM images obtained after $Pd(OAc)_2$ loading in toluene: (a) G3@PAA10-b-PS260 at 0.5 equiv, and G4@PAA10-b-PS260 at (b) 0.25, (c) 0.5, and (d) 0.75 equiv/2VP unit.

5.4.6 Comparison of morphologies obtained for self-assembled and covalently grafted systems

One of the main goals of this research was to compare the nanomorphologies obtained for metal-loaded core–shell–corona (CSC) systems obtained by self-assembly with the nanostructures observed previously for covalently grafted CSC systems.[59] For a fair comparison, the behaviors of samples matched in terms of core and P2VP side chain size, loaded with the same amount of $HAuCl_4$ (0.5 equiv of $HAuCl_4$/2VP content) in the same solvent system are contrasted. Less attention was paid to the length of the PS chains forming the corona, however, since their influence was shown to be minimal beyond preventing aggregation after metal salt loading. Consequently, the G2@PA10-*b*-PS260, G3@PAA10-*b*-PS260, and G4@PAA10-*b*-PS260 ACC systems will be compared with their G1PS-*g*-(P2VP30K-*b*-PS192), G2PS-*g*-(P2VP14K-*b*-PS115), and G3PS-*g*-(P2VP14K-*b*-PS115) covalently grafted counterparts, respectively.

In toluene, both the G2@PA10-*b*-PS260 ACC and its analogous covalent CSC template, G1PS-*g*-(P2VP30K-*b*-PS192), displayed ring-like metal distribution inside the scaffolds (**Figure 5-21d** and **a**, respectively), with both templates displaying a spherical topology in spite of their different PS corona chain lengths. The G3@PAA10-*b*-PS260 ACC and its covalently grafted counterpart, G2PS-*g*-(P2VP14K-*b*-PS115), likewise revealed interamolecular phase separation, whereby a raspberry morphology was obtained in both cases (**Figure 5-21e and b**, respectively). Different morphologies were observed for G4@PAA10-*b*-PS260 ACC and the analogous G3PS-*g*-(P2VP14K-*b*-PS115) covalent template, however: A core–shell morphology was prevalent for G4@PAA10-*b*-PS260, while G3PS-*g*-(P2VP14K-*b*-PS115) had a cylinder-in-sphere morphology (**Figure 5-23c** and **f**). This might be due to the different preparation strategies since the G4@PAA10-*b*-PS260 ACC was allowed to equilibrate for 2 days in THF before it was transferred to toluene, while the anionic grafting procedure for G3PS-*g*-(P2VP14-*b*-PS115), also carried out in THF, was completed in about 30-60 min. The longer

contact time may have favored the interpenetration of the P2VP shell and the outer PS corona for sample G4@PAA10-*b*-PS260 as compared to G3PS-*g*-(P2VP14-*b*-PS115).

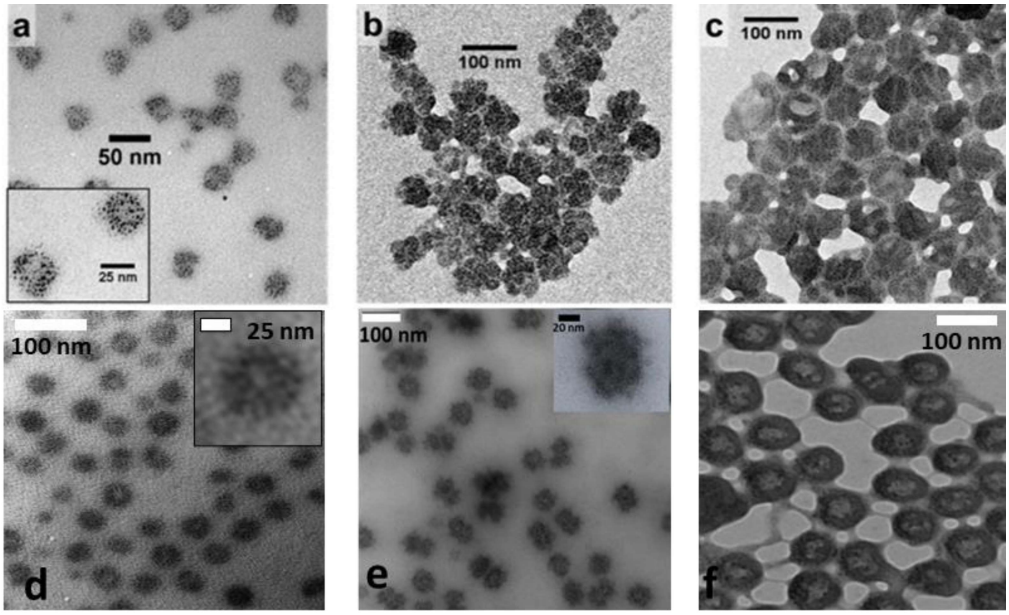

Figure 5-21. TEM images for analogous covalently bonded (top row) and ACC (bottom row) templates loaded with 0.5 equiv of $HAuCl_4$/2VP unit in toluene: (a) G1PS-g-(P2VP30K-b-PS192), (b) G2PS-g-(P2VP14K-b-PS115), (c) G3PS-g-(P2VP14K-b-PS115), (d) G2@PAA10-b-PS260, (e) G3@PAA10-b-PS260, and (f) G4@PAA10-b-PS260. The top row images are reprinted with permission from Reference 59.

In toluene with 2 % methanol both the G3@PAA10-*b*-PS260 ACC and G3PS-*g*-(P2VP14-*b*-PS115) templates, which had a raspberry morphology in toluene, displayed morphology changes. As seen in **Figure 5-22d**, the G3@PAA10-*b*-PS260 ACC had a spherical topology with uniform metal distribution, while G2PS-*g*-(P2VP14-*b*-PS115) transformed into a worm-like structure (**Figure 5-22a**). The G4@PAA10-*b*-PS260 ACC, which had a core–shell morphology in toluene, changed into a gyroid-like morphology (**Figure 5-22d**), whereas worm-in-sphere morphologies were observed in their G3PS-*g*-(P2VP14-*b*-PS115) covalent counterpart (**Figure 5-23a**).

In THF with 25% cyclohexane, the G2PS-*g*-(P2VP14K-*b*-PS115) and G3PS-*g*-(P2VP14K-*b*-PS115) graft copolymers both transformed to spherical morphologies (**Figure 5-22b** and **Figure 5-23b**, respectively). Similar observations were made for their ACC counterparts, G3@PAA10-*b*-PS260 and G4@PAA10-*b*-PS260 (**Figure 5-22e** and **Figure 5-23e**, respectively).

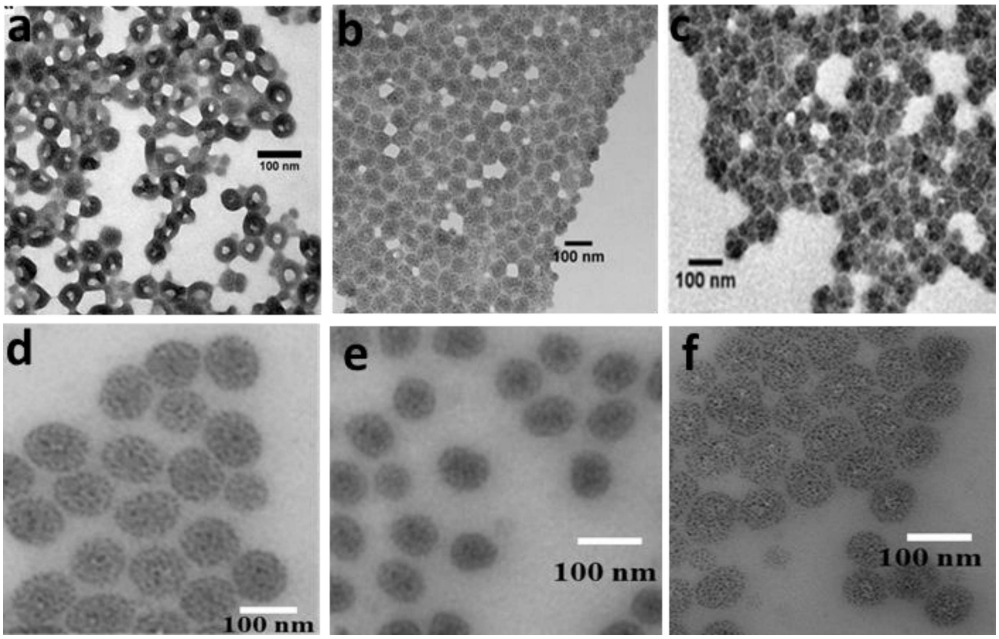

Figure 5-22. TEM images for G2PS-g-(P2VP14K-b-PS12) (top row) and for G3@PAA10-b-PS260 (bottom row) templates loaded with 0.5 equiv of $HAuCl_4$/2VP unit in toluene with 2 % methanol (a and d), in THF with 25% cyclohexane (b and e), and in chloroform (c and f). The top row images were reprinted with permission from Reference 59.

Finally in chloroform, the G3@PAA10-*b*-PS260 ACC appeared to have a spherical morphology with a relatively uniform metal distribution, while the G2PS-*g*-(P2VP14K-*b*-PS115) graft copolymer retained its raspberry nanostructure (**Figure 5-22c** and **f**, respectively). In contrast, the G4@PAA10-*b*-PS260 ACC displayed a distinct mushroom-like or nanocage morphology (**Figure 5-23f**), while its anionic graft copolymer analogue G3PS-*g*-(P2VP14K-*b*-PS115) had a somewhat different

interpenetrating worm or spherical nanocage structure (**Figure 5-23c** top). Increased solvency for P2VP in chloroform may account for the transitions observed.

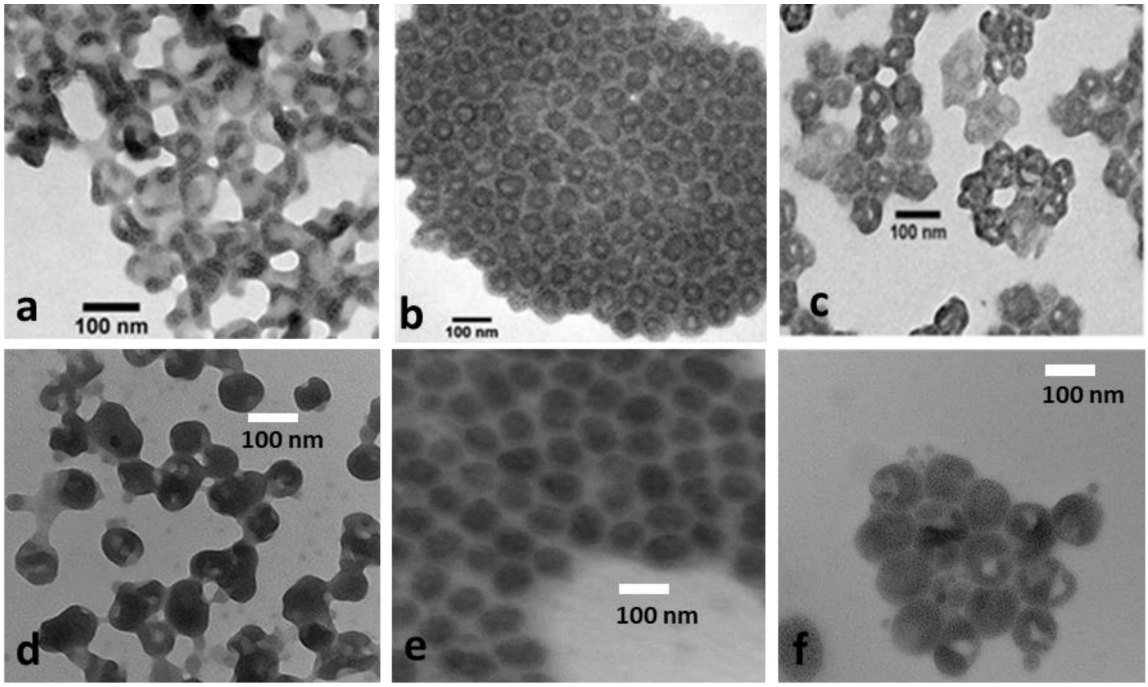

Figure 5-23. TEM images for G3PS-g-(P2VP14K-b-PS12) (top row) and for G4@PAA10-b-PS260 (bottom row) templates loaded with 0.5 equiv of $HAuCl_4$/2VP unit in toluene with 2 % methanol (a and d), in THF with 25% cyclohexane (b and e), and in chloroform (c and f). The top row images were reprinted with permission from Reference 59.

In conclusion, changes in solvency conditions transformed most of the structures observed in toluene, for both the self-assembled and covalently grafted systems. The most significant changes were observed for G3@PAA10-*b*-PS260 and its G2PS-*g*-(P2VP14K-*b*-PS115) covalent analogue, however: While these systems both yielded raspberry morphologies in toluene, the exact type of morphology observed in each system varied greatly with the solvency of the medium. These differences are likely related to the overall mobility of the P2VP and PS segments in the molecules, and therefore also the linkage

method for the PS segments making up the corona layer, but molecular modeling beyond the scope of this work would be necessary to confirm this hypothesis.

5.5 Conclusions

Arborescent core–shell–corona copolymer complexes, denoted as PS-*g*-P2VP@PAA-*b*-PS, were successfully loaded with $HAuCl_4$ at different levels (0.25–1 equiv/2VP unit). While a simple spherical morphology with uniform metal distribution was obtained for most of the G2@PAA-*b*-PS systems, the G3 and G4 complexes displayed more intricate intramolecular phase separation, with nanodomain formation within each template. These morphologies were investigated in detail by AFM and TEM imaging.

For ACC systems of all generations, the short PS block in PAA10-*b*-PS85 was unable to suppress aggregation after loading the complexes with $HAuCl_4$, while complexes derived from BCPs with longer PS segments were essentially non-aggregated.

In contrast, the G2 ACPS derived from block copolymers having PS chain segments of intermediate length (G2@PAA10-*b*-PS205 and G2@PAA10-*b*-PS260) displayed ring-like metal organization, while those with longer PS segments (>305 units) exhibited only spherical metal organization. The G3@PAA-*b*-PS complexes already appeared to exhibit nodular phase separation similar to a raspberry-like morphology within each particle even before loading with $HAuCl_4$, which was further enhanced after loading of the metal. Variations in the PS block length in the PAA-*b*-PS copolymers had little influence on the nanomorphology obtained, albeit copolymers with longer PS segments sometimes displayed a transition from raspberry-like to rather spherical, with somewhat diminished phase segregation. The G4@PAA-*b*-PS systems exhibited core–shell intramolecular phase separation in most cases, whereby a PS core surrounded by a shell of metal-coordinated P2VP was clearly observed.

Comparison of the phase separation observed in the G3@PAA-*b*-PS and G4@PAA-*b*-PS complexes, for substrates containing P2VP side chains of comparable lengths, led to the conclusion that the morphology differences observed were likely due to the characteristics of the PS cores used to synthesize the G3 and G4 copolymers. It was hypothesized that the denser G3PS substrate used to synthesize the G4 copolymer prevented the interpenetration of P2VP and PS phases in the copolymers, resulting in a better-defined core–shell morphology than for the G3 copolymer. This, in turn, should favor the formation of a better defined core–shell morphology for the metal-loaded G4@PAA-*b*-PS complexes, rather than a raspberry-like morphology.

The type of intramolecular phase separation observed in both the G3 and G4 complexes was also sensitive to the solvent used in the metal loading process. Thus when THF with 25% cyclohexane was used for both the G3 and G4 complexes, the metal was concentrated closer to the center of the complexes and intramolecular phase separation was diminished. For the G4 complex loaded in chloroform, a mushroom-like (nanocage) morphology resulted.

It is remarkable that some of the nanomorphologies observed previously for the covalently grafted CSC templates were also present in the self-assembled systems. In particular, the raspberry-like morphology was consistent between the two systems in toluene. Mixed solvents triggered intramolecular morphology changes in both cases, whereby most of the nanostructures obtained in toluene transformed into different nanostructures.

Chapter 6: Arborescent Copolymer Complex-Stabilized Gold Nanoparticles: Reduction and Characterization

6.1 Overview

Arborescent copolymer complexes (ACCs) were employed as templates for the preparation of gold nanoparticles (Au NPs). The ACCs, derived from arborescent polystyrene-*graft*-poly(2-vinylpyridine) (PS-*g*-P2VP) copolymers of generations G2–G4 and poly(acrylic acid-*block*-polystyrene) (PAA-*b*-PS) copolymers, were loaded with $HAuCl_4$ in toluene. These $HAuCl_4$-loaded ACCs were reduced with sodium borohydride, either in solution or as films, and characterized by TEM and UV-visible absorption spectroscopy. The influence of the generation number and the loading level on the size of the NPs and the long-term colloidal stability of the templates were investigated. Gold NPs with diameters ranging from 4–15 nm were obtained. The generation number of the template did not affect the size of the NPs: Comparable size particles were obtained within error limits in all cases, but the NPs obtained for higher generation (G3 and G4) systems were slightly more uniform. As compared to solution reduction, film reduction yielded somewhat larger nanoparticles for the G2 systems but had no influence for the G3 and G4 systems.

6.2 Introduction

Metallic nanoparticles (MNPs) have attracted much attention due to their unique physicochemical properties and their potential applications[1,2] in fields including separation,[3] imaging,[4,5] sensing,[5-7] medicine,[5] cancer therapy,[8] photothermal therapy,[9] optical trapping,[10] drug delivery,[11] and catalysis.[12-19] Gold nanoparticles (AuNPs) are arguably the most notable member of the MNP group[2] due to their potential applications in catalysis,[18-26] biology,[2,5] and drug release.[27] Different methodologies have been reported to synthesize MNPs.[28-42] The synthesis of metallic nanoparticles with well-defined characteristics (composition, nanomorphology, size, size uniformity) is usually necessary to achieve the desired physical properties. For the preparation of stabilized MNPs, at least two different approaches have been reported, namely the *ex situ* incorporation of pre-synthesized MNPs into polymer structures, and the *in situ* preparation of nanoparticles in the presence of polymer scaffolds.[1,2,36] The

latter approach mostly relies upon the reduction of metal salts within a polymeric structure. Over the past decades, various stabilizers have been employed to prepare Au NPs of controllable size, size distribution, and adequate stability. This includes surfactants,[38] self-assembled block copolymer micelles,[39,40] star-block copolymers,[41] and unimolecular micelle-like compounds.[18,43]

Core–shell–corona (CSC) copolymers with a dendritic architecture, namely the arborescent polystyrene-*graft*-[poly(2-vinylpyridine)-*block*-polystyrene] copolymers, were also investigated as templates for the preparation of AuNPs. These covalently bonded molecules, with an inner shell of poly(2-vinylpyridine) (P2VP) chains,[43] are much more stable than micelles obtained by the self-assembly of linear block copolymers because they have no critical micelle concentration.[44]

We now present the preparation of (reduced) Au NPs within arborescent CSC complex structures of polystyrene-*graft*-poly(2-vinylpyridine)@poly(acrylic acid)-*block*-polystyrene (PS-*g*-2VP@PAA-*b*-PS), prepared by the self-assembly of arborescent polystyrene-*graft*-poly(2-vinylpyridine) with poly(acrylic acid)-*block*-polystyrene via hydrogen bonding[45] and/or electrostatic (weak acid-weak base) interactions (**Scheme 6-1**).[46] The arborescent PS-*g*-P2VP copolymer substrates were synthesized by anionic grafting, while the PAA-*b*-PS copolymer components were synthesized by atom transfer radical polymerization (ATRP). Based upon the results obtained, ACCs appear to be promising materials as templates for the preparation of MNPs. Due to their enhanced stability, some of the problems reported for block copolymer micelles, such as the aggregation of gold nanoparticles upon dilution, can be avoided.

Different reduction methods reported in the literature used reagents in solution such as hydrazine, or sodium borohydride ($NaBH_4$), but also hydrogen peroxide in the presence of a nonionic surfactant (R–CH_2CH_2OH) acting as reducer.[47] The reduction of $AuCl_4^-$ was also achieved with hydroxyl group-containing compounds such as catechol,[25] but $NaBH_4$ is the dominant reducing agent reported in the literature and was also used in this study.

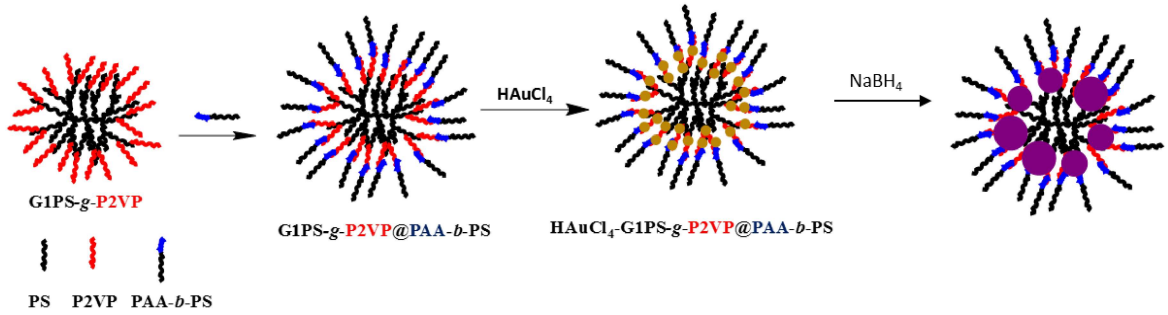

Scheme 6-1. Schematic representation of the in situ reduction of $HAuCl_4$ in ACC structures.

6.3 Experimental procedures

6.3.1 Reduction of the $HAuCl_4$-loaded ACCs

Solution reduction. The reduction of $HAuCl_4$ in solution was accomplished with a 10:1 mole ratio (relatively to $HAuCl_4$) of sodium borohydride ($NaBH_4$). For example, a solution of $NaBH_4$ (Sigma-Aldrich, 98 %) in methanol (10 mg/mL) was prepared and a calculated amount (0.45 mL, 0.12 mmol) was added under vigorous stirring to 12.5 mL of $HAuCl_4$-loaded ACC solution (0.4 mg/mL) in toluene, containing 3.9 mg of $HAuCl_4$ (0.012 mmol; 1 μmol/mL). These reaction conditions were used unless otherwise stated. The reaction yielded a deep red solution, characteristic for the transformation of Au^0 nanoparticles. The products were analyzed by TEM and UV-visible absorption spectroscopy.

Film reduction. A solution of $HAuCl_4$-loaded ACC in toluene was cast onto a TEM grid as described in Chapter 5 (Section 5.3.4). The film was allowed to dry overnight before one drop of freshly prepared $NaBH_4$ solution in methanol (10 mg/mL) was placed on the film with a microsyringe. The $NaBH_4$ solution was left on the film for 1 min and then wicked out with filter paper before gently rinsing with Milli-Q water. Residual water droplets were removed with filter paper and the film was left to dry overnight before TEM analysis.

6.3.2 Transmission electron microscopy (TEM)

TEM imaging was performed on a Philips CM10 TEM instrument operating at 60 kV. The samples were prepared and analyzed as described in Chapter 5 (Section 5.5.3.4). The ImageJ software version 1.50i was used to measure the size of the nanoparticles.

6.3.3 Atomic force microscopy (AFM)

Tapping-mode atomic force microscopy (AFM) measurements were performed on a Nanoscope IIIa Multimode Digital Instruments Model MMAFM-2 instrument mounted on a vibration isolation table. The cantilever probes used were T300 Vista Probes with a silicon tip having a radius of 8 nm, 125 μm length, 40 μm width and 14 μm height, having a spring constant of 40 $N \cdot m^{-1}$ and a resonance frequency of 300 kHz. The sample preparation method and the instrumental operating parameters used were as described in Chapter 5 (Section 5.3.3).

6.3.4 UV-visible spectrometry

UV-visible (UV-vis) spectra were recorded on a Cary 100 Bio UV-Vis spectrometer version 10 operated with the Varian Cary UV Scan software version 3.00. The absorption measurements were recorded for an $HAuCl_4$ solution, the polymer solutions before and after $HAuCl_4$ loading, and Au-polymer solutions after reduction, using a quartz cell with a 1-cm path length, in the 200–800 nm range. Baseline correction was applied for the solvent.

6.4 Results and discussion

6.4.1 Solution reduction: General comments

The synthesis of the core–shell–corona ACC structures, described in detail in Chapter 4, involved the complexation of PS-*g*-P2VP arborescent copolymer substrates (synthesized by anionic grafting) with PAA-*b*-PS block copolymers (synthesized by ATRP). The complexes were prepared in toluene/ethanol (90/10 v/v) mixtures for the G2, and in THF for the G3 and G4 systems. The solvent was exchanged to

toluene before loading with $HAuCl_4$ (0.25-1 equiv/2VP unit) and reduction with sodium borohydride ($NaBH_4$).[48] This process is illustrated in **Scheme 6-1**.

The ACC-templated Au NPs were prepared simply by adding solid $HAuCl_4$ to a stirred toluene solution of ACC, followed by reduction with $NaBH_4$. While $HAuCl_4$ is insoluble in toluene, it was gradually solubilized upon coordination with the 2VP units within a period of approximately one hour. The solution was nevertheless stirred for 24 h, to ensure complete coordination of the $HAuCl_4$ by the 2VP units. In most cases, the molar ratio of $HAuCl_4$ was maintained at 0.5 equiv/2VP unit, but to investigate the influence of the loading level on the size and stability of the Au NPs, it was varied between 0.25 and 1 equiv/2VP unit in some cases. A ten-fold ratio of $NaBH_4$ solution freshly prepared in methanol (10 mg/mL) relatively to $AuCl_4^-$ was then added to the metal-loaded ACC solution. The color of the solution turned deep red as the Au NPs formed, indicating the reduction of $AuCl_4^-$.[48]

The size and size distribution of metallic nanoparticles (MNPs) obtained by the reduction of metallic ions are controlled by the reduction kinetics.[49] When the reduction process is fast, smaller nanoparticles are produced due to concurrent nucleation. Stronger reducing agents react faster and yield smaller nanoparticles, in addition to steric restrictions due to the polymeric scaffold.[50] The reduction of the $HAuCl_4$-loaded ACCs was performed with sodium borohydride ($NaBH_4$), a fast reducing agent predominantly used in the literature. Under these conditions the mean diameter of the MNPs should be tunable by varying the loading level, the reduction protocol (film *vs.* solution), and the concentration of the solution at which the reduction is conducted.[51]

The ACCs interact with $HAuCl_4$ through the nitrogen atom of the 2VP units, which is protonated upon addition of the metallic acid. When $NaBH_4$ is added the solution becomes basic, hence the nitrogen lone pairs should interact with the elemental Au surface.[52] Despite weak Au/N interactions,

anchoring of the PS layer on the surface of the ACC structures may also play a role in controlling the reduction kinetics inside the polymeric templates.

6.4.2 Reduction of $HAuCl_4$ in the G2 ACC systems

In preliminary experiments, the G2@PA13-PS390 ACC was loaded with 0.5 equiv of $HAuCl_4$ in toluene/ethanol (90/10 v/v) mixtures (without transfer to toluene prior to metal loading) and reduced with a 10-fold ratio of $NaBH_4$. The TEM image for the sample obtained under these conditions (**Figure 6-1b**) showed small dark nanoparticles within each template, indicating the reduction of $HAuCl_4$ to Au NPs, with an average diameter of 6.2 ± 1.2 nm within the templates of 48 ± 4 nm. The distribution of Au NPs within the polymeric particles was non-uniform: Some of the complexes did not contain NPs, which suggests diffusion of the salt between the scaffolds during particle growth. The morphology of the templates also displayed a transition from spherical to toroidal upon reduction in the toluene/ethanol mixtures, as confirmed by both TEM and AFM analysis (**Figure 6-1**).

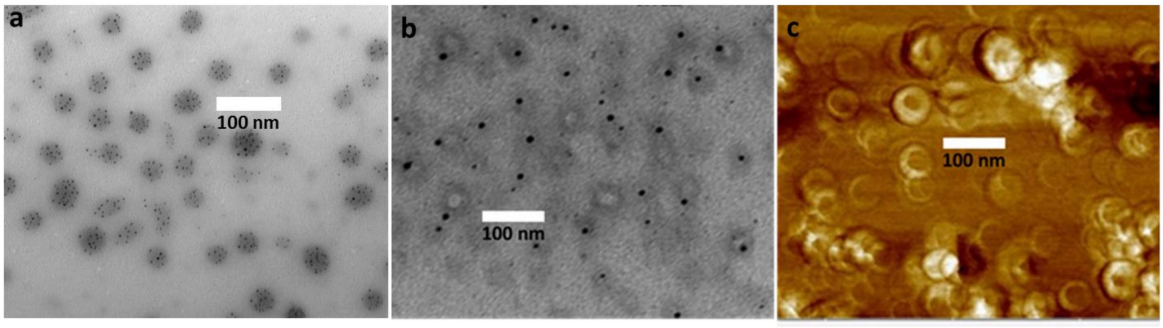

Figure 6-1. TEM images (a) before and (b) after reduction, and (c) AFM phase image after reduction of $HAuCl_4$-loaded G2@PAA13-b-PS390 in a toluene/ethanol (90/10 v/v %) mixtures (scale bar = 100 nm).

UV-visible absorption spectra were obtained for $HAuCl_4$ before and after coordination with G2@PAA13-*b*-PS390, and after reduction in toluene/ethanol mixtures (**Figure 6-2**). The templates displayed absorption maxima (λ_{max}) at 288 nm, corresponding to a $\pi \rightarrow \pi^*$ transition for the phenyl

groups in the PS chains and the pyridine groups in the P2VP chains.[53] The absorption maximum (λ_{max}) for $HAuCl_4$ shifted slightly from 319 nm (for $HAuCl_4$ in solution) to 325 nm after coordination with the 2VP units.

The Au NPs displayed a characteristic UV absorption above 500 nm arising from the surface plasmon resonance (SPR) effect, namely the coherent oscillation of free electrons due to interactions of the Au NPs with the external electromagnetic field induced by the light wave.[54,55] This plasmon oscillation is influenced by the size, shape, and the microenvironment of the Au NPs. The peak observed at 543 nm is characteristic for the SPR of Au NPs, which confirms the reduction of $HAuCl_4$ to Au^0 (**Figure 6-2**).

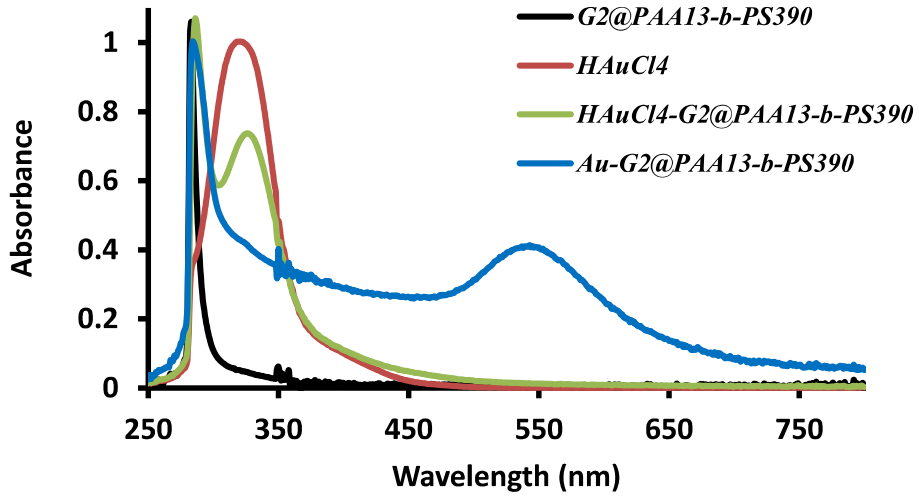

Figure 6-2. UV-vis absorption spectra for $HAuCl_4$, loaded in the G2@PAA13-b-PS390 template before and after reduction, at 0.5 equiv/2VP unit in toluene/ethanol (90/10 v/v %) mixtures.

Reduction of the gold salt was also performed for the same G2@PAA13-*b*-PS390 ACC template loaded with 0.5 equiv of $HAuCl_4$, but after solvent exchange to toluene. The size of the Au NPs obtained within the templates was 5.8 ± 1.0 nm in this case (**Figure 6-3a**), essentially identical to the size obtained using the solvent mixture (6.2 ± 1.2 nm). This shows that the size of the Au NPs did not

depend significantly on the presence of 10 % ethanol in the ACC solutions. A toroidal morphology is also clearly visible in the AFM phase image (**Figure 6-3b**).

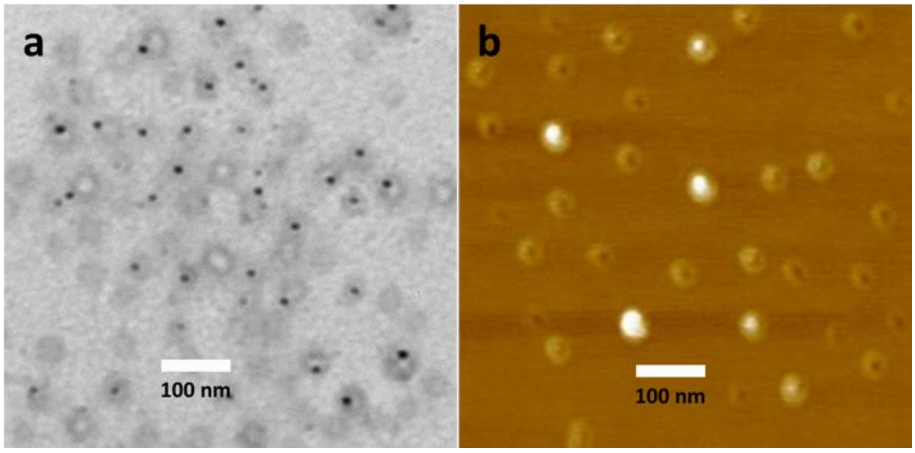

Figure 6-3. (a) TEM and (b) AFM phase images for Au-G2@PAA13-b-PS390 by reduction in toluene (scale bar = 100 nm).

A comparison of **Figures 6-1** and **6-3** also shows that, irrespective of the solvency conditions used to load $HAuCl_4$, the NPs were not distributed uniformly among the templates. Since the G2 structure is relatively open, diffusion through the scaffold may have led to the non-uniform distribution of Au NPs obtained. In both cases, a few templates did not contain Au NPs.

$HAuCl_4$-loaded ACCs in toluene containing different stabilizing PS segment lengths were also reduced with a 10-fold ratio of $NaBH_4$, and the corresponding TEM images obtained are compared in **Figure 6-4**. Sample G2@PAA10-PS85 yielded aggregated templates and larger Au NPs (19.7 ± 2.8 nm). This is attributed to short PS chains being unable to effectively shield the particles from each other. Moreover, most Au NPs are located outside the templates, likely due to the diffusion of Au seeds during the growth process. In contrast, for longer PS chains, namely G2@PAA10-*b*-PS205, G2@PAA10-*b*-PS260 and G2@PAA10-*b*-PS305, the templates did not aggregate and no particles were

formed outside the templates, indicating that the nucleation and growth processes were indeed restricted to within the ACC templates. TEM analysis also showed that the ACC templates were preserved in most cases, being visible as grey shaded areas after $NaBH_4$ reduction (**Figure 6-4**). The size of the Au NPs obtained inside the G2@PAA10-*b*-PS205, G2@PAA10-*b*-PS260, and G2@PAA10-*b*-PS305 templates was 6.1 ± 1, 6.2 ± 0.7, and 5.6 ± 1.4, respectively. This shows that the influence of the PS chain length on the size of the Au NPs was insignificant, albeit longer PS segments clearly favored the formation of NPs *within* the templates, by minimizing migration of the gold salt, and reduced NP aggregation.

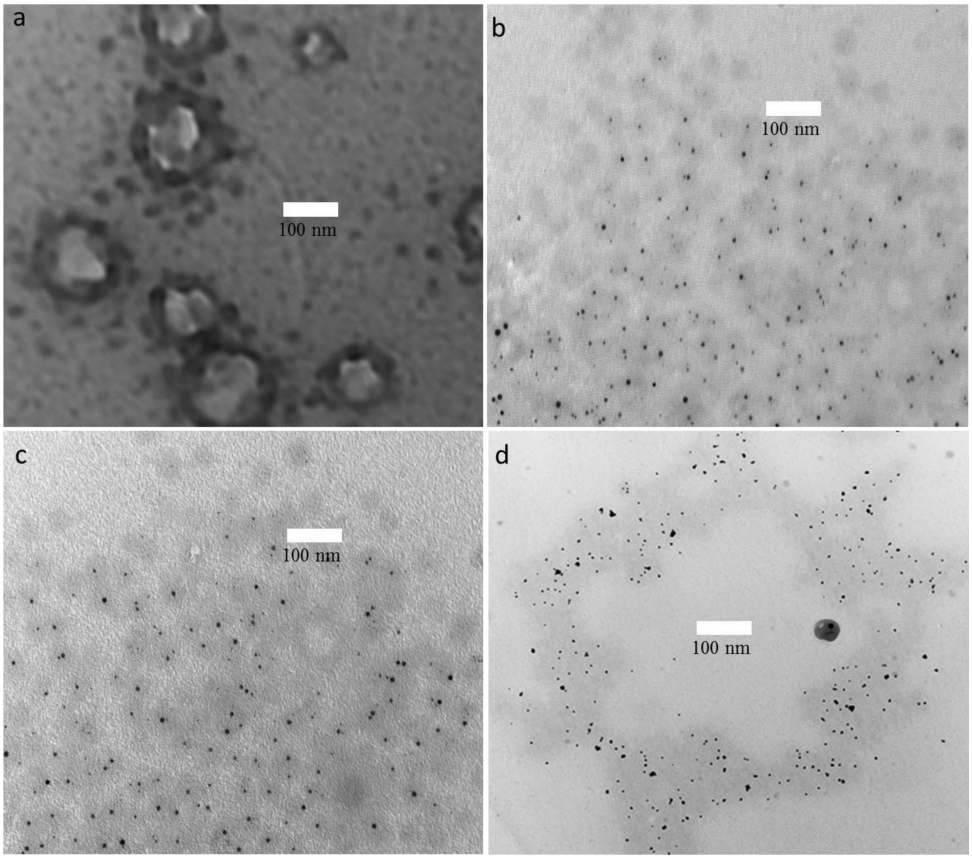

Figure 6-4. TEM images for gold nanoparticles formed by reduction with $NaBH_4$ of (a) G2@PAA10-b-PS85, (b) G2@PAA10-b-PS205, (c) G2@PAA10-b-PS260, and (d) G2@PAA10-b-PS305 (scale bar = 100 nm).

The influence of the $HAuCl_4$/2VP molar ratio on the average size and size distribution was also investigated for Au NPs templated with G2@PAA10-*b*-PS260, and the TEM images obtained are shown in **Figure 6-5**. To this end, loading levels of 0.25, 0.5 and 1 equiv of $HAuCl_4$/2VP unit were used before reduction with 10 equiv of $NaBH_4$. The average size of the Au NPs did not appear to vary significantly with the loading level, but the 1 equiv loading level yielded fewer aggregated nanoparticles that were still mostly restricted within the templates (**Figure 6-5c**). The average size of the Au NPs (excluding aggregated particles in the 1 equiv sample) was 6.2 ± 1, 6.1 ± 1 and 5.4 ± 1 nm for the 0.25, 0.5 and 1 equiv loading levels, respectively. In the latter case not only were the Au NPs slightly aggregated, but some of the templates also were also aggregated. The aggregation may be related to the evaporation of the solvent on the TEM grids.[56] This phenomenon was also observed for higher generation (G3) templates (**Figure 6-7b**), as discussed later.

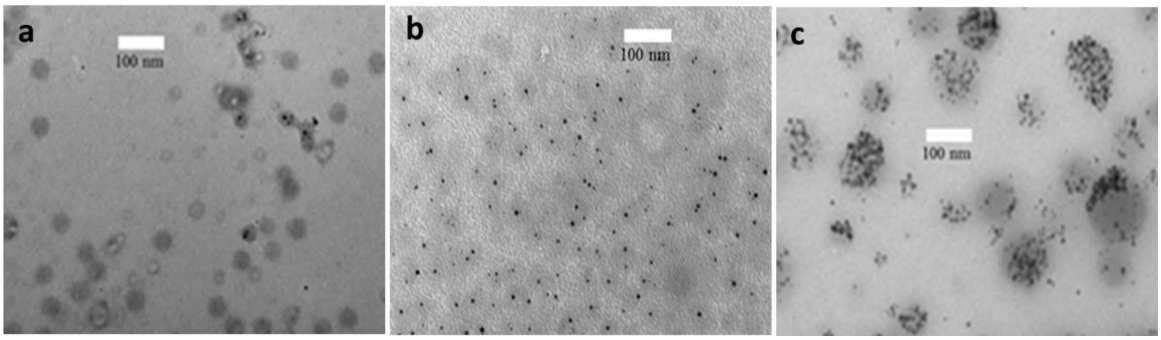

Figure 6-5. TEM images for gold nanoparticles formed by reduction of $HAuCl_4$-loaded G2@PAA10-b-PS260 with $NaBH_4$ in toluene at (a) 0.25, (b) 0.5, and (c) 1 equiv/2VP unit.

Nanoparticles of noble metals such as gold are distinct from other nanoparticles due to the surface plasmon resonance (SPR) effect, resulting from the confinement of photons to very small particles. The SPR effect leads to a strong absorbance band for Au NPs in the near-infrared region for nano-rods, or a weak band around 520 nm (depending on their size) for nano-spheres.[57] The colloidal stability of the

Au NPs prepared with the G2@PAA10-*b*-PS260 ACC (0.5 equiv loading level) was investigated by comparing their UV-vis spectra 24 h and 3 months after their synthesis (**Figure 6-6**). A small amount of precipitate was visible after 3 months, and the UV-vis absorption spectrum recorded after 24 h exhibited an SPR maximum at 531 nm, which shifted and broadened to 510-550 nm after 3 months. The broader SPR band is attributed to aggregation of the Au NPs. The increased intensity may be due to solvent evaporation leading to a slight increase in concentration of the sample.

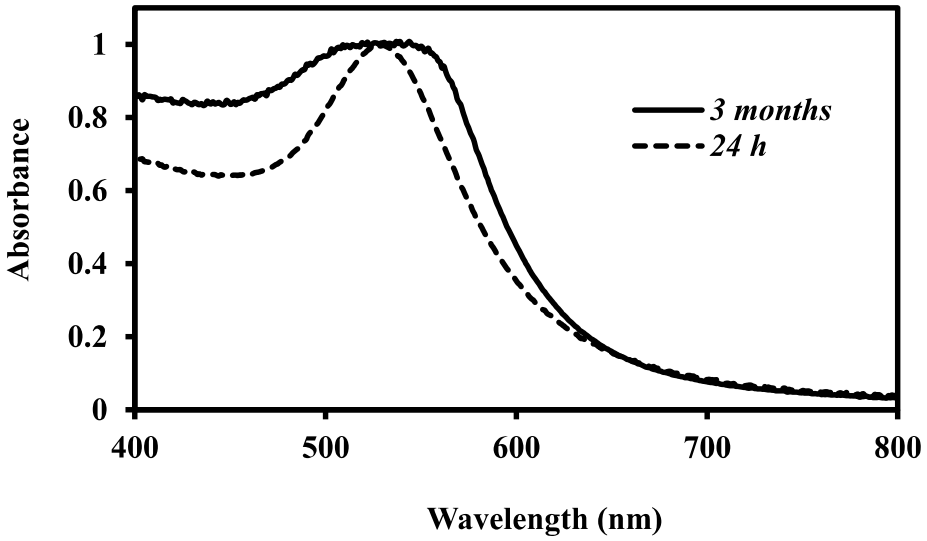

Figure 6-6. UV-vis absorption spectra for $HAuCl_4$-loaded G2@PA10-b-PS260 recorded 24 h (dotted line) and 3 months (continuous line) after reduction.

6.4.3 Reduction of $HAuCl_4$ in the G3 ACC systems

The reduction of $HAuCl_4$ loaded in the G3 ACCs was first attempted at 0.8 mg/mL concentration, but the templates tended to aggregate after reduction. The Au NPs nevertheless remained located near the surface of the templates and non-aggregated (**Figure 6-7b**). When reduction was conducted at a lower concentration (0.4 mg/mL), no template aggregation was observed and nanoparticles were still visible

within the individual templates (**Figure 6-7c**). This result seems to be in agreement with that obtained by Roescher and Möller[58] for PS-*b*-P2VP copolymer micelles. This is presumably due to decreased interparticle interactions at lower concentrations. The size of the Au NPs was unaffected by dilution, as reduction of the $HAuCl_4$-loaded (0.5 equiv/2VP content) G3@PAA10-*b*-PS260 complex yielded 4.6 ± 0.3 nm at both concentrations. UV-vis spectroscopy analysis yielded a peak at λ_{max} = 525 nm after reduction in both cases (**Figure 6-8**), characteristic for smaller spherical particles.[57] No changes in absorption characteristics nor particle size were therefore observed upon dilution.

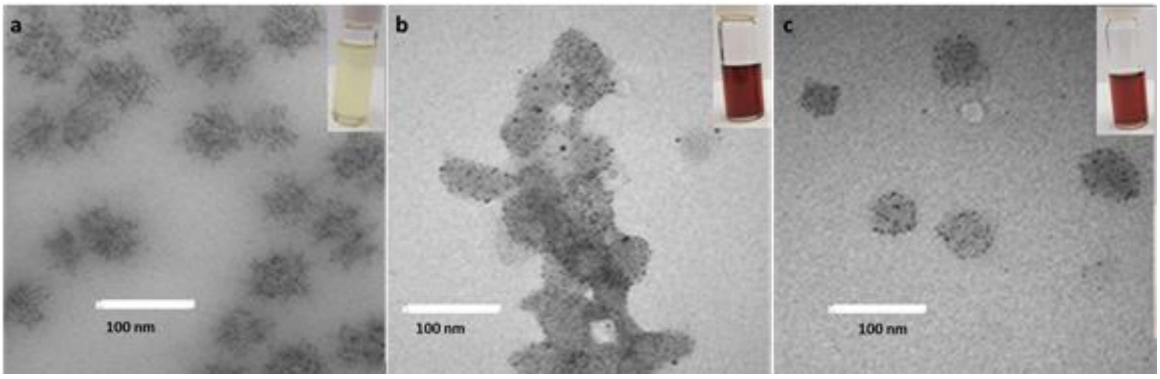

Figure 6-7. TEM images for G3@PAA10-b-PS260 complex loaded with (a) 0.5 equiv $HAuCl_4$/2VP unit in toluene, and after reduction at (b) 0.8 mg/mL and (c) 0.4 mg/mL (scale bar = 100 nm).

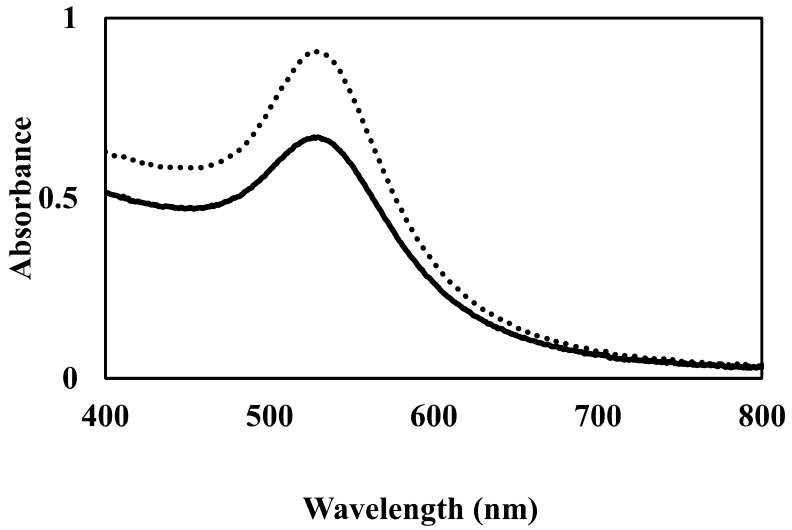

Figure 6-8. UV-Vis absorption spectra for $HAuCl_4$-G3@PAA10-b-PS260 complex with 0.5 equiv Au/2VP after reduction in toluene at 0.8 mg/mL (dotted line) and 0.4 mg/mL (solid line).

The influence of the PS chain length in the block copolymers was also assessed for the G3 ACC templates. Similarly to earlier observations for the G2@PAA10-PS85 ACC, G3@PAA10-PS85 yielded aggregated, larger and more polydisperse (18 ± 8.2 nm) Au NPs (**Figure 6-9a**). Again, the short PS chains in the corona did not effectively shield and isolate the particles from each other, leading to larger Au NPs. Interestingly, the Au NPs were mostly contained within the templates and less aggregation was observed in this case. This is in sharp contrast with the G2 systems, for which most of the Au NPs were located outside and extensive template aggregation was observed. This may be due to the different PS cores, since the G2 copolymer would have a more open structure providing less hindrance to interparticle fusion than the denser G3 copolymer.

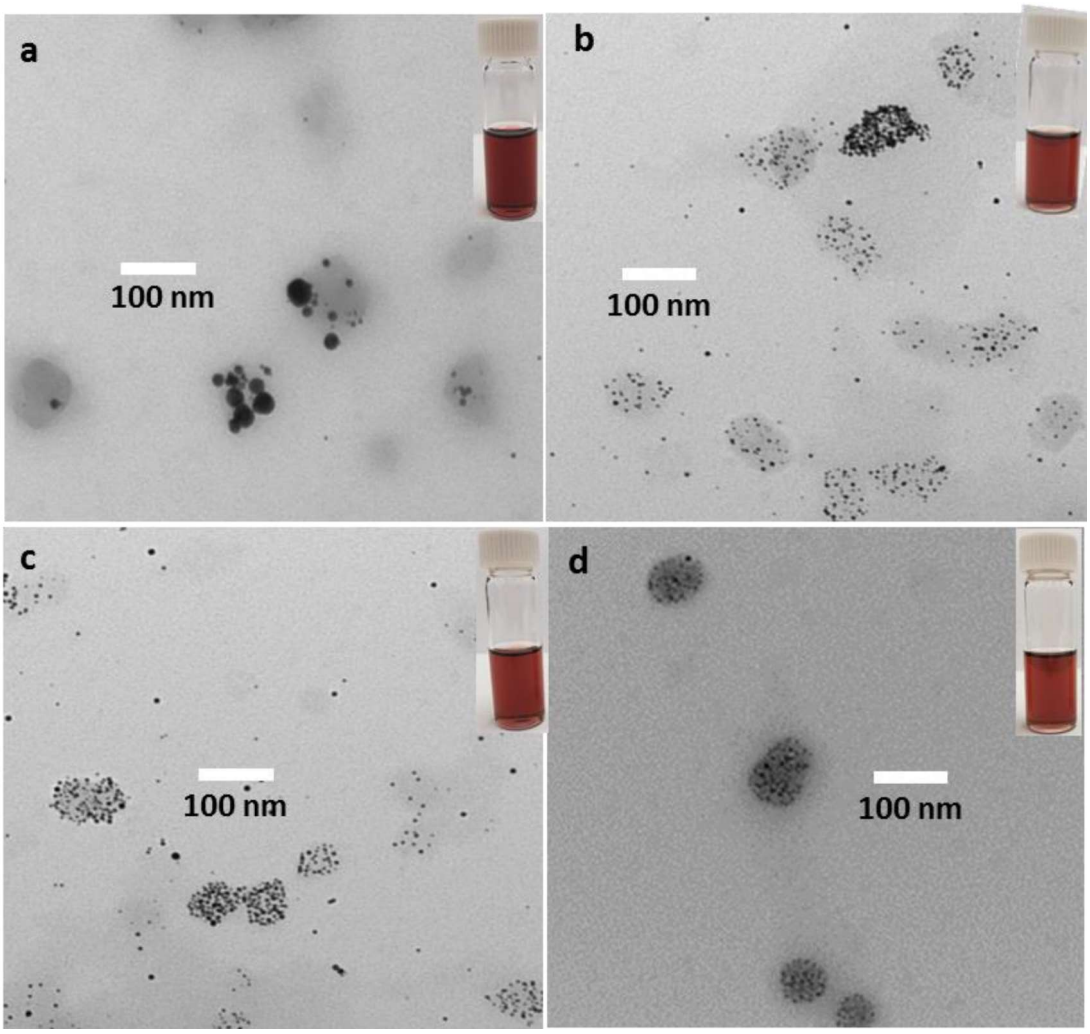

Figure 6-9. TEM images for gold nanoparticles formed by reduction with $NaBH_4$ of (a) G3@PAA10-b-PS85, (b) G3@PAA10-b-PS205, (c) G3@PAA10-b-PS260, and (d) G3@PAA10-b-PS305 (scale bar = 100 nm).

On the other hand, the G3@PAA10-*b*-PS205, G3@PAA10-*b*-PS260, and G3@PAA13-*b*-PS305 templates, with longer stabilizing PS segments, yielded neither large Au NPs nor template aggregation (**Figure 6-9b-d**). This is in agreement with the observations reported earlier for the G2 templates with longer PS segments. The size of the Au NPs obtained for G3@PAA10-*b*-PS205, G3@PAA10-*b*-PS260, and G3@PAA10-*b*-PS305 was 4.5 ± 1, 4.5 ± 1, and 4.3 ± 1 nm, respectively, which again shows that

the size of the Au NPs was not controlled by the length of the stabilizing PS segments beyond ~ 200 styrene units.

Increasing the amount of $HAuCl_4$ loaded to 1 equiv/2VP unit in G3@PAA10-*b*-PS260 did not lead to an appreciable NP size difference, but the size dispersity was slightly higher. The TEM images for Au NPs derived from G3@PAA10-*b*-PS260 at 0.5 and 1 equiv/2VP unit are compared in **Figure 6-10**. The average size at 0.5 equiv was 4.6 ± 0.3 nm, while at 1 equiv it was 5.0 ± 0.8 nm. The slight dispersity increase at 1 equiv may be related to increased inter-particle interactions at higher Au contents.

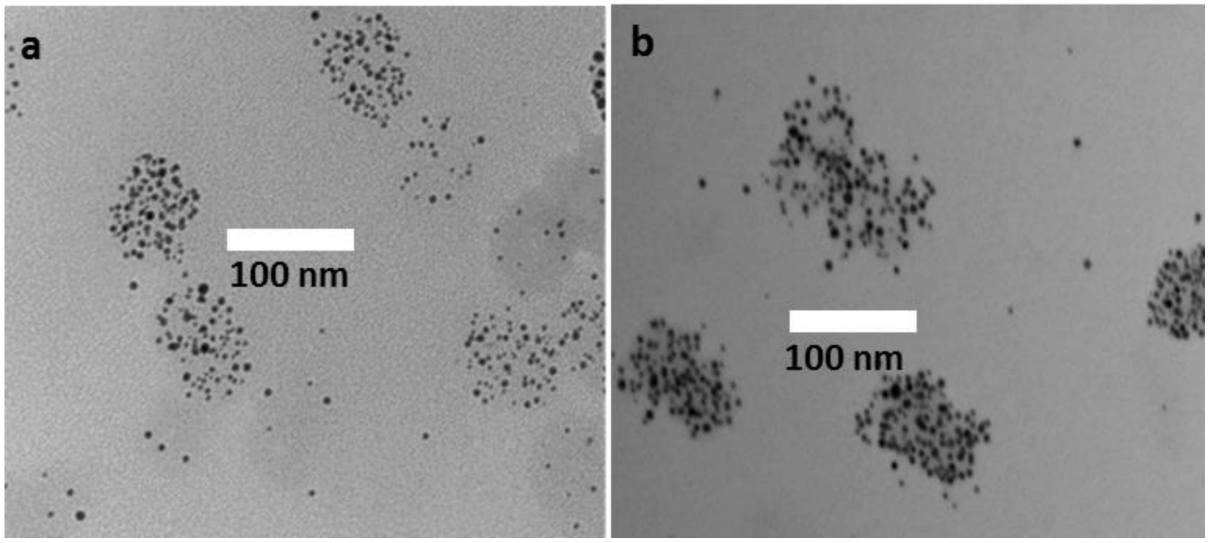

Figure 6-10. TEM images for gold nanoparticles formed by reduction of $HAuCl_4$-loaded G3@PAA10-b-PS260 by $NaBH_4$ in toluene at (a) 0.5 and (b) 1 equiv/2VP unit (scale bar = 100 nm).

In contrast to the G2 systems which exhibited a broader SPR band after 3 months, no precipitate was visible for the G3 template. The UV-vis spectra also only displayed a small λ_{max} shift from 520 to 530 nm and a slightly increased intensity (**Figure 6-11**).

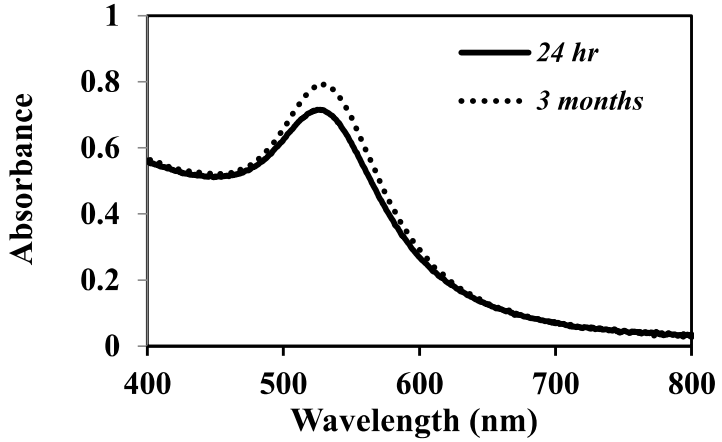

Figure 6-11. UV-vis absorption spectra for Au NPs prepared in toluene with G3@PA10-b-PS260 after 24 h (solid line) and at 3 months (dotted line).

6.4.4 Reduction of $HAuCl_4$ in the G4 ACC systems

Similarly to the G3 samples discussed in Section 6.4.3, reduction of the $HAuCl_4$-loaded G4 systems was investigated at 0.4 mg/mL. The resulting Au NPs inside each template are obvious (**Figure 6-12**), and a similar Au NP size was again obtained regardless of the PS chain length: The average size for G4@PAA10-*b*-PS85, G4@PAA10-*b*-PS205, G4@PAA10-*b*-PS260 and G4@PAA10-*b*-PS305 was 4.6 ± 0.6, 4.5 ± 0.6, 4.5 ± 0.6 and 4.8 ± 0.6 nm, respectively. No variation in size dispersity was observed either. One minor difference is that some of the Au NPs were formed outside of the template for G4@PAA10-*b*-PS85 (**Figure 6-12a**). Interestingly, increasing the loading level from 0.5 to 1 equiv for G4@PAA10-*b*-PS260 did not result in any significant size difference (4.5 ± 0.6 nm in both cases) for the resulting Au NPs (**Figure 6-13**).

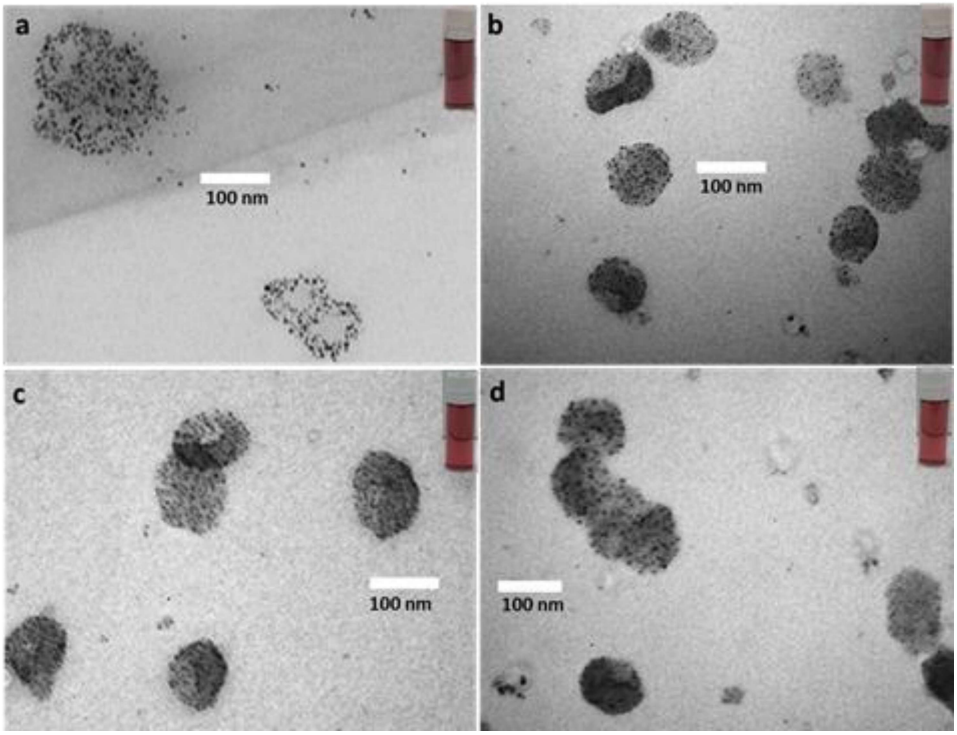

Figure 6-12. TEM images for gold nanoparticles formed by reduction at 0.4 mg/mL with $NaBH_4$: (a) G4@PAA10-b-PS85, (b) G4@PAA10-b-PS205, (c) G4@PAA10-b-PS260, and (d) G4@PAA10-b-PS305 (scale bar = 100 nm).

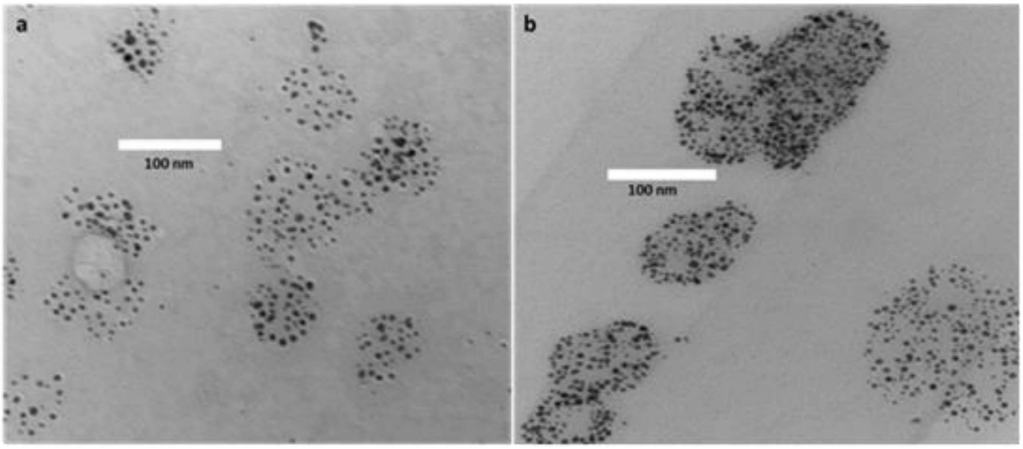

Figure 6-13. TEM images for gold nanoparticles formed by reduction of $HAuCl_4$-loaded G4@PAA10-b-PS260 with $NaBH_4$ in toluene at (a) 0.5 and (b) 1 equiv/2VP unit.

UV-vis analysis also confirmed the reduction of the gold salt for the G4 systems (**Figure 6-14**). It is noteworthy that no precipitate was observed after 3 months, and only a minimal (3 nm) shift in λ_{max}, from 524 to 527 nm, occurred over that time period (**Figure 6-14**).

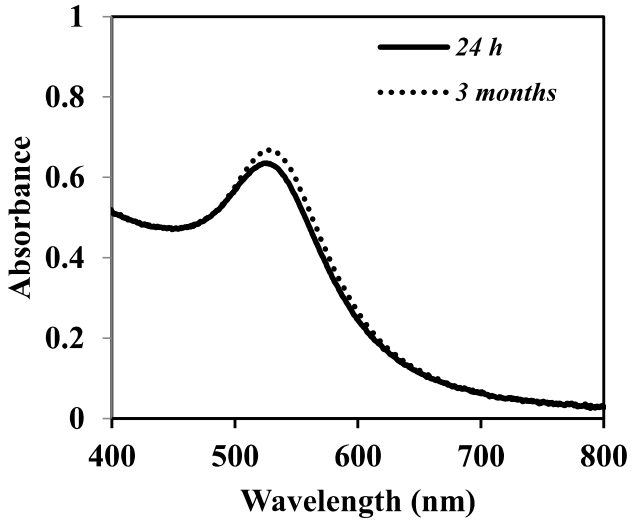

Figure 6-14. UV-vis absorption spectra for Au NPs prepared in toluene with G4@PA10-b-PS260 at 24 h (solid line) and at 3 months (dotted line).

6.4.5 Comparison between generations

A comparison of the characteristics of the Au NPs obtained for different generations of ACC templates at constant PS segment length (G2@PAA10-*b*-PS260, G3@PAA10-*b*-PS260, and G4@PAA10-*b*-PS260), at a loading level of 0.5 equiv in toluene, is provided in **Table 6-1**. No significant variations in size were observed within error limits (**Figure 6-15**): The average diameter obtained for the Au NPs within the G2, G3, and G4 ACC templates was 5.5 ± 1.0, 4.5 ± 0.6 and 4.2 ± 0.6 nm, respectively.

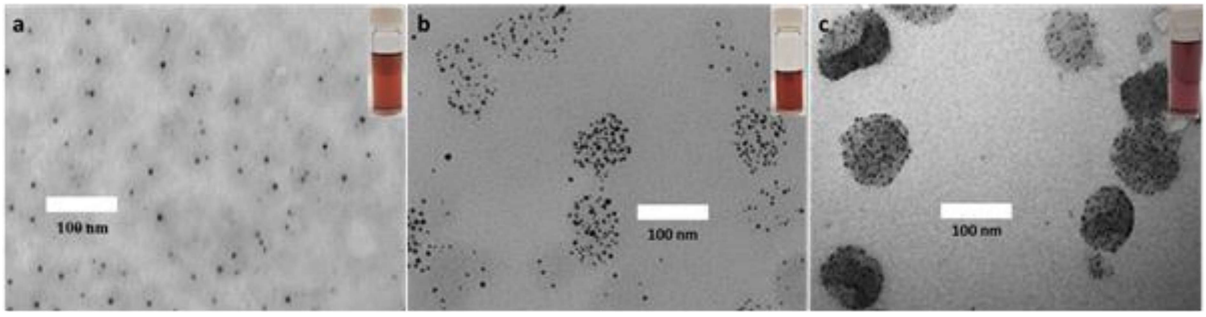

Figure 6-15. TEM images for gold nanoparticles formed by reduction with $NaBH_4$ at 0.5 equiv $HAuCl_4$/2VP unit loading in toluene: (a) Au-G2@PAA10-b-PS260, (b) Au-G3@PAA10-b-PS260, and (c) Au-G4@PAA10-b-PS260 (scale bar = 100 nm).

While the effect is not very obvious, the Au NPs formed within the higher generation (G3 and G4) ACCs were slightly more uniform than for the G2 ACC, as seen from the lower standard deviations obtained (**Table 6-1**). It is unclear whether this is due to the differences in the characteristics of the PS cores or the P2VP side chains, but it seems likely related to the higher branching functionality of the substrates leading to reduced chain mobility and steric crowding, hindering the diffusion of $AuCl_4^-$ ions during the reduction process.

The 1 equiv loading level also yielded similar trends in terms of Au NP size and uniformity among the different generations, with insignificant variations: The average particle size for the G2 ACC was 5.4 ± 1 nm, comparable within error limits to both the G3 (4.6 ± 0.3 nm) and G4 (4.5 ± 0.6 nm) systems. It is also clear that the Au NPs were more effectively constrained and less aggregated within the G3 and G4 templates templates, even at higher loading levels (**Figure 6-16**). These results demonstrate that the ACCs are effective stabilizers for the preparation of Au NPs in relatively low polarity solvents such as toluene.

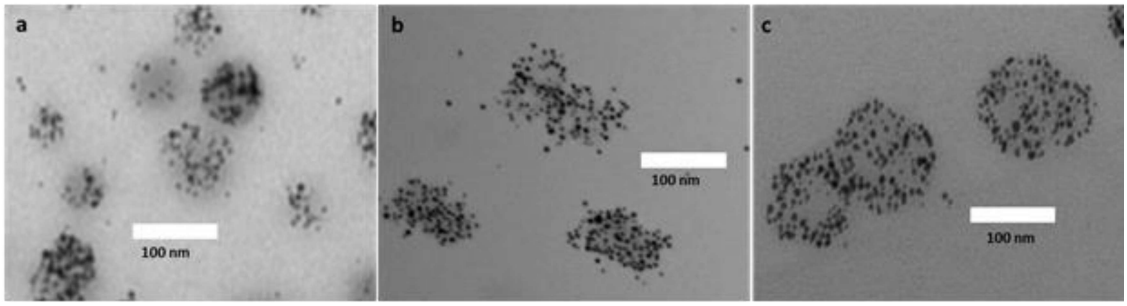

Figure 6-16. TEM images for gold nanoparticles formed by reduction with $NaBH_4$ at 1 equiv $HAuCl_4$/2VP unit in toluene: (a) G2@PAA10-b-PS260, (b) G3@PAA10-b-PS260, and (c) G4@PAA10-b-260 (scale bar = 100 nm).

Table 6-1. Characteristics of Au NPs prepared from different generations of ACCs.

Template	Time	λ_{max} (nm)	Average Size (nm)
G2@PAA10-*b*-PS260	24 h	531	5.5±1.0
G3@PAA10-*b*-PS260	24 h	525	4.6±0.3
G4@PAA10-*b*-PS260	24 h	524	4.5±0.6
G2@PAA10-*b*-PS260	3 m	546	-
G3@PAA10-*b*-PS260	3 m	530	-
G4@PAA10-*b*-PS260	3 m	527	-

The colloidal stability of the Au NPs synthesized within the ACC templates was investigated by UV-vis spectroscopy analysis (**Table 6-1**). The G3 and G4 ACCs provided Au NPs that were stable over 3 months, with minimal (3-5 nm) shift in λ_{max} as compared with the freshly prepared (24 h) particles. The G2 systems, in contrast, displayed visible precipitate formation, and the UV-vis absorption spectrum exhibited a shifted and broader SPR band (**Figure 6-6**). These trends were also consistent with the variations in aggregation level observed in the TEM analysis (**Table 6-1**).

6.4.6 Film reduction

The reduction of $HAuCl_4$ to elemental gold within films was also investigated. Reduction was performed by adding a drop of $NaBH_4$ solution (10 mg/mL in methanol) on the TEM grid on which a film of $HAuCl_4$-loaded ACC was casted from toluene. The reduction of $HAuCl_4^-$ to Au^0 was apparent as the colorless film immediately changed to dark-purple.[59] TEM images for the reduction of $HAuCl_4$-G2@PAA10-*b*-PS260 in a film and in solution are compared in **Figure 6-17**. In terms of average diameter, the Au NPs obtained in film reduction are slightly larger (9 ± 2 nm) than in solution reduction (6.2 ± 0.7 nm), albeit the error domains almost overlap. A more obvious result is that, as compared to solution reduction, film reduction was somewhat better at preserving the toroidal morphology of the G2 templates. This phenomenon was also observed for other samples in the same generation (**Appendix D-1**).

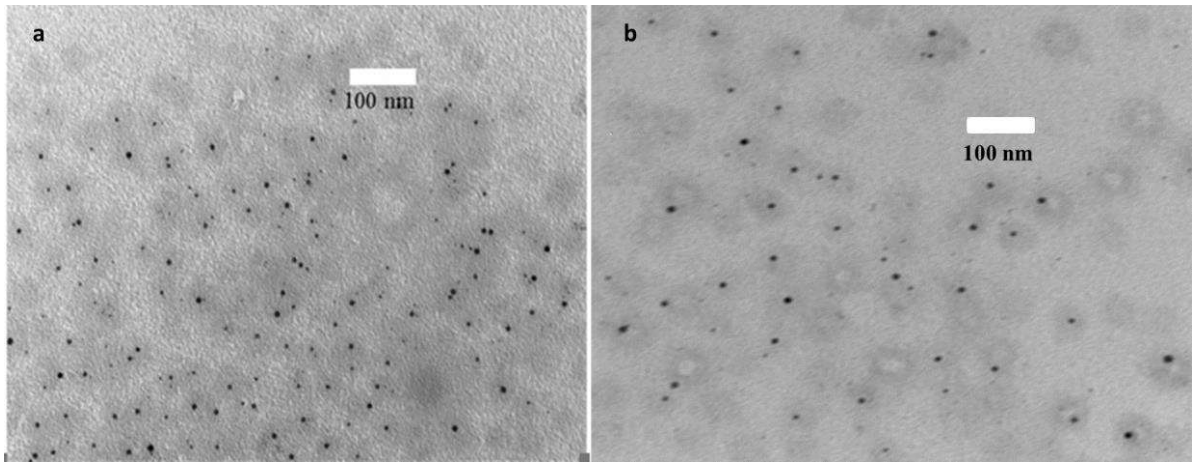

Figure 6-17. TEM images for $HAuCl_4$-G2@PAA10-b-PS260 at 0.5 equiv loading in toluene after reduction with $NaBH_4$: (a) solution and (b) film reduction.

Film reduction was also performed for the G3 and G4 templates loaded with $HAuCl_4$ in toluene. While the morphology of the reduced templates was closer to that observed before reduction as

compared with solution reduction, the distribution of nanoparticles within the polymer structures was not uniform for every template: Some of the templates had a larger number of NPs, while others had a very small number (**Figure 6-18** and **Figure 6-19**). A few NPs were also located outside the templates.

It is unclear whether film reduction of the gold-loaded G3 templates preserved the raspberry-like organization (**Figure 6-18**) observed in its non-reduced salt-loaded counterpart (**Figure 6-7a**). The G4 template more clearly exhibited ring-like organization of the Au NPs, closer to the morphology observed by TEM for the non-reduced salt-loaded precursor (**Figure 6-19**).

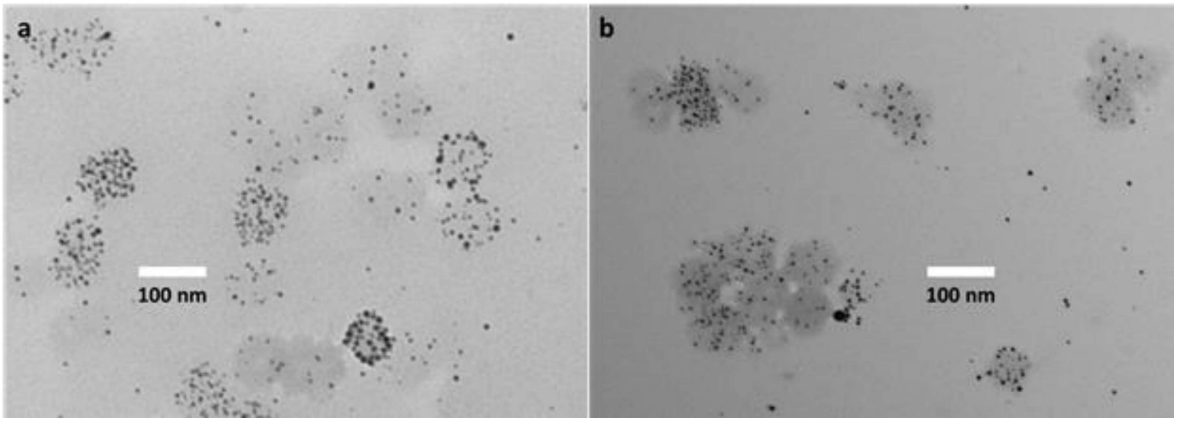

Figure 6-18. TEM images for $HAuCl_4$-loaded templates after film reduction with $NaBH_4$: (a) G3@PAA10-b-PS260 and (b) G3@PAA10-b-PS305

The size of the Au NPs obtained with the G3 and G4 ACC templates was again comparable to that for solution reduction (4.2–4.8 ± 1 nm). Overall, film reduction nevertheless led to somewhat better morphology retention than solution reduction, particularly for the G4 ACC sample.

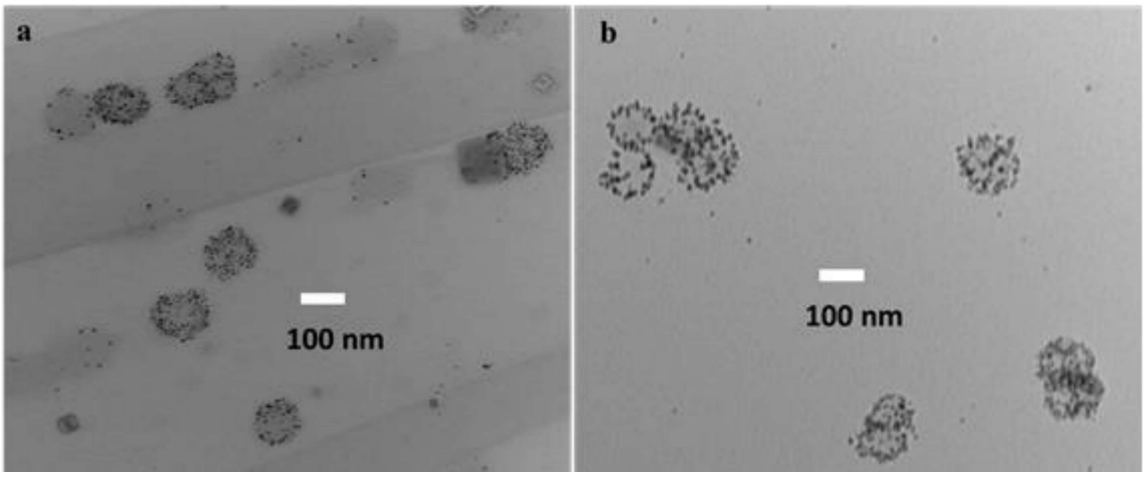

Figure 6-19. TEM images for $HAuCl_4$-loaded templates after film reduction with $NaBH_4$: (a) G4@PAA10-b-PS260, (b) G4@PAA10-b-PS305.

6.5 Conclusions

The reduction of $HAuCl_4$-loaded G2–G4 ACC templates in solution with excess sodium borohydride (10:1 $NaBH_4$:$HAuCl_4$) yielded Au NPs in a comparable size range (4 to 6.5 nm), restricted inside the templates in most cases. There PS chain length in the stabilizing block copolymers used had no significant influence on the size of the NPs formed, except for PAA10-*b*-PS85. For the G2 and G3 templates, in particular, the shortest PS chains (DP_n = 85) were unable to prevent aggregation of the templates, and many larger Au NPs were produced outside the scaffolding. This effect was somewhat less pronounced for the G4 templates. In contrast, longer PS segments (DP_n > 200) resulted in smaller and relatively more uniform gold nanoparticles, formed predominantly within the polymer template but of comparable size for all generations when the DP_n of the PS segments was > 200. The size dispersity appeared slightly larger for the G2 samples, but comparable for the G3 and G4 ACCs. Furthermore, visual and UV-visible spectroscopy analysis showed that the G3 and G4 systems were stable for at least three months, while the G2 samples yielded a small amount of precipitate and significant changes in their UV-vis spectra.

Film reduction of the gold-loaded templates with $NaBH_4$ was also performed and produced nanoparticles more clearly located within the polymer templates. As compared to Au NPs obtained by solution reduction, film reduction of the gold-loaded G2 ACC yielded slightly larger nanoparticles. Interestingly, for the higher generation (G3 and G4) ACC templates, the size of the Au NPs did not vary with the reduction method used, but film reduction led to better morphology retention than solution.

The results obtained in the current investigation clearly show that ACCs, obtained in high yield by a simple self-assembly procedure using arborescent polystyrene-*graft*-poly(2-vinylpyridine) and poly(acrylic acid)-*block*-polystyrene, have great potential as templates for the formation of metallic nanoparticles: They yield morphologies comparable to those observed for arborescent polystyrene-*graft*-poly(2-vinylpyridine)-*block*-polystyrene systems, obtained only in low yield using exclusively anionic polymerization and grafting techniques. The simplicity of the self-assembly approach developed enables the synthesis of these interesting materials on a larger (multi-gram) scale, which should facilitate the investigation of their properties in relation to applications in different areas such as sensors and catalysts.

Chapter 7: Concluding Remarks

7.1 Summary and contributions to knowledge

7.1.1 Arborescent copolymer complexes

Arborescent copolymer complexes with a core–shell–corona (CSC) architecture were prepared by self-assembly and examined as templates for the preparation of metallic nanoparticles (NPs), particularly Au NPs, in organic solvents.

The synthesis of some of the arborescent copolymer substrates used was achieved previously by Gauthier and Munam.[1] The copolymers were synthesized by grafting poly(2-vinylpyridine) side chains (~15 or 30 kg/mol) onto arborescent polystyrene substrates randomly functionalized with acetyl groups. A dynamic light scattering investigation of the arborescent copolymers revealed that, in agreement with previous studies,[2] these polymers exist as unimolecular species in solution. This was demonstrated in more detail than before, however, since while the hydrodynamic diameter of the arborescent copolymers increased with the generation number (37-150 nm in tetrahydrofuran, THF) as expected, while their size dispersity remained low ($Đ < 0.1$) with single populations in number-, volume- and intensity-weighted distributions.

Block copolymers of poly(acrylic acid) and polystyrene (PAA-*b*-PS) were successfully synthesized by ATRP and characterized by NMR, SEC, and DLS analysis. Hydrodynamic diameter analysis yielded single populations in the number distributions, but a second size population attributed to a low degree of aggregation was also detected in the intensity-weighted size distributions in most cases. Consequently, the D_h of isolated BCP chains was rather estimated from viscosity data reported for polystyrene chains having the same molecular weight as the BCP samples.

The arborescent copolymers, characterized by a hydrophobic PS core enclosed within a shell of P2VP chains, were then complexed with the PAA-*b*-PS copolymers synthesized by ATRP. This represents a new approach to the synthesis of hydrophobic CSC structures, with a composition similar to that

previously achieved by Dockendorff and Gauthier by a tedious anionic grafting procedure limited by very low grafting yields (10-30%) in most cases. The complexation reaction was investigated by dynamic light scattering, while transmission electron microscopy and atomic force microscopy served to study the arborescent copolymer complex (ACC) particles in the dry state. An increase in diameter and a single size population with a relatively narrow size distribution ($Đ < 0.18$) was evident for most ACCs by DLS analysis. The DLS data, together with the unaggregated particles of uniform size observed in AFM and TEM images, provided strong evidence of the formation of the desired complex.

An unanticipated result was obtained for the G1 ACCs upon complexation with PAA-*b*-PS in THF/ethanol mixtures: Contrary to expectations, the size (D_h^Z) of the G1 ACCs actually decreased by 3–5 nm relatively to the G1 copolymer substrate ($D_h^Z = 34 \pm 1$ nm). This effect was attributed to the collapse of the P2VP chains in the shell of the G1 copolymer substrate, presumably due to its relatively open and flexible structure. The added PS corona was apparently insufficient to compensate for shrinking of the P2VP chains within the shell of the ACPS. Shrinkage was also apparent in thin film analysis to some extent: While AFM analysis yielded a size comparable for the G1 ACPS (27 ± 3 nm for the ACC, as compared to 28 ± 6 nm for the G1 substrate), TEM analysis yielded a much smaller size (17 ± 3 for the ACC, as compared to 33 ± 5 nm for the G1 substrate), presumably because the PS segments forming the shell were not stained, and therefore invisible.

On the other hand, complexes prepared from the higher generation (G2–G4) substrates generally displayed significant increases in D_h^Z in toluene relatively to the substrates, and larger for BCPs with longer PS blocks. This is reasonable since arborescent substrates are more rigid, and toluene is a good solvent for PS, which likely contributed to micelle swelling. The length of the PAA anchoring segments did not seem to affect the size and dispersity of the complexes, however. The DLS results were not very conclusive on their own. These inconsistent results could be due to a low level of aggregation and/or the presence of free BCP chain contaminant not resolved in the DLS measurements. While the trends

in the DLS results were obscured by some discrepancies, one single size population and a relatively low size dispersity ($Đ \leq 0.15$) were still observed in most cases.

AFM analysis of the complexes provided complementary information on their topology and morphology, in addition to confirming the trends in size variations obtained by DLS. Complex micelles of uniform size were observed for most samples derived from G1–G3 substrates, and their structure became better defined as the substrate generation number increased. A spherical core–shell morphology was observed for G1 and G2 ACCs, which was attributed to their small PS core size and the large ($M_n \approx 30$ kg/mol) P2VP chains within their corona. The G3 ACC systems, with shorter P2VP side chains ($M_n \approx 15$ kg/mol), displayed intramolecular phase separation with nodular nanodomains (or raspberry-like morphologies), particularly well-defined for G3@PAA10-*b*-PS205 and G3@PAA10-*b*-PS260. Analogous morphologies were also observed in a previous study in our laboratory for core–shell–corona copolymers obtained by anionic grafting, but only after loading with $HAuCl_4$. The complexes derived from the G4 substrate displayed an indented sphere topology, which became more obvious when BCPs with a longer PS block were used. In all cases, the size determined from the AFM phase images increased from the substrate to the ACCs, with larger increases for longer side chains in most cases.

While the structures observed by AFM imaging were relatively uniform in size in most cases, the systems derived from block copolymers with shorter PS chains were clearly aggregated, and elongated shapes were also observed in the G2 systems with longer PS chains. A second (smaller) size population, likely corresponding to non-complexed block copolymer side chains that aggregated in toluene, was also visible in the AFM images for the G4 systems. This observation was consistent with the DLS analysis results, in that the size dispersity of the ACCs displaying BCP aggregation in AFM was also higher in the DLS analysis, particularly for G4@PAA13-*b*-PS330 ($Đ = 0.6$).

Overall, this method is a simple but effective way to prepare polymeric templates in high yield, as compared with the tedious anionic covalent grafting procedures using "living" block copolymers, that were marred by low grafting yields. This confirms that one of the main goals of this project, namely exploring self-assembly as an alternate approach for the synthesis of arborescent core–shell–corona (CSC) structures, was successfully attained.

7.1.2 Metal loading

Polymer templates comprising a P2VP component can coordinate with various transition metal compounds such as $HAuCl_4$. For comparison, the arborescent copolymer substrates (G1–G4), containing a P2VP shell in their structure, were loaded with 0.25 and 0.5 equiv $HAuCl_4$ per 2VP in THF. At the 0.25 equiv loading level, the solution was stable only for a few hours for lower generation (G1 and G2) copolymers, while the G3 and G4 systems remained clear for at least half a day but precipitated overnight. At the 0.5 equiv loading level, sedimentation occurred within a few minutes for the lower generations and a few hours for the higher generations. As revealed by TEM analysis, aggregation occurred in all cases regardless of the generation number, which was attributed to the absence of a PS corona shielding interactions between metal-loaded templates.

On the other hand, the ACCs loaded with $HAuCl_4$ in toluene were stable for several days to several months without precipitation. Analysis by TEM and AFM nevertheless revealed differences among the ACCs. For example, the G2@PAA10-*b*-PS85 ACC yielded aggregated metal-loaded particles after metal-coordination, as the short PS segments forming the corona were not sufficiently long to shield interparticle interactions effectively. In contrast, isolated particles with ring-like metal organization were observed for ACCs with side chains of intermediate length (PS DP_n = 205 and 260), while spherical metal organization was obtained for longer side chains (DP_n > 305).

Intramolecular phase separation was apparent after coordinating the G3@PAA-*b*-PS and G4@PAA-*b*-PS templates with $HAuCl_4$. The G3@PAA-*b*-PS complexes, that displayed nodular (raspberry-like) phase separation even before loading, had a similar but further enhanced morphology after metal loading. This morphology was also observed in a previous study[2] for the corresponding covalently grafted arborescent CSC templates, but only after metal loading. Variation in the PS block length in the PAA-*b*-PS copolymers had little influence on the nanomorphology obtained, although copolymers with longer PS segments displayed a transition to somewhat spherical, with slightly reduced phase separation. The G4@PAA-*b*-PS systems had a core–shell morphology in most cases, whereby a shell of metal-coordinated P2VP surrounding the PS core was evident.

Loading of the G3 and G4 complexes with $HAuCl_4$ was also achieved in other organic solvents including toluene with 2% methanol, THF with 25% cyclohexane, and chloroform. Intramolecular phase separation was also found to be sensitive to the solvent used in the metal loading process. The metal was thus concentrated near the center in both the G3 and G4 complexes, and intramolecular phase separation was diminished for THF with 25% cyclohexane. Loading in chloroform transformed the raspberry-like morphology obtained in toluene for the G3 system to a more spherical morphology with relatively uniform metal distribution, while the core–shell morphology observed for the G4 system in toluene changed to mushroom-like or nanocage nanostructures.

Interestingly, some of the nanomorphologies observed previously for the covalently grafted CSC templates were also identified in the self-assembled systems. This was true, in particular, for the raspberry-like morphology in toluene. Mixed solvents likewise triggered intramolecular morphology changes in both systems, whereby most of the nanostructures obtained in toluene transformed into other nanostructures.

The P2VP can also coordinate with other metals, and $Pd(OAc)_2$ was successfully loaded in the G3@PAA10-*b*-PS and G4@PAA-*b*-PS complexes. In that case, mostly pearl-necklace aggregation of the metal-loaded particles was observed.

A variety of G2-G4 ACCs, prepared by self-assembly, were proven to be effective templates for the preparation of metallic nanoparticles, by loading with $HAuCl_4$ and $Pd(OAc)_2$. This demonstrates that the other goal of the research, namely demonstrating the application of ACCs for metal loading, was attained.

7.1.3 Reduction

The reduction of $HAuCl_4$ to Au^0 in the G2–G4 ACC templates was achieved in solution with excess sodium borohydride (10:1 $NaBH_4$:$HAuCl_4$). As determined by TEM imaging and supported by UV-vis analysis, Au NPs in a comparable size range (4 to 6.5 nm) and restricted inside the templates were observed in most cases. Interestingly, the PS chain length in the block copolymer stabilizer had no significant influence on the size of the NPs formed, except for PAA10-*b*-PS85. In that case, the short PS chains ($DP_n = 85$) were not only unable to prevent aggregation of the templates, but many larger Au NPs were also produced outside the scaffolding, particularly for the G2 and G3 templates, albeit this was less evident for the G4 templates. In contrast, longer PS segments ($DP_n > 200$) resulted in smaller (4 to 6.5 nm) and relatively more uniform gold nanoparticles, formed predominantly within the templates and comparable in size for all generations. This clearly demonstrates that the ACCs are effective stabilizers for Au NPs, which was the ultimate objective of this project. Furthermore, visual sample inspection and UV-visible spectroscopy analysis showed that the G3 and G4 systems were stable for at least three months, while the G2 samples yielded a small amount of precipitate and significant changes in their UV-vis spectra.

Reduction of the gold-loaded templates with $NaBH_4$ after deposition as thin films generated nanoparticles almost exclusively located within the polymer templates. As compared to solution reduction, film reduction of the gold-loaded G2 ACC produced somewhat larger nanoparticles, but for the G3 and G4 templates the Au NP size did not vary with the reduction method used.

Overall, the results obtained in the current investigation clearly show that ACCs can be obtained in high yield by a simple self-assembly procedure using arborescent polystyrene-*graft*-poly(2-vinylpyridine) and poly(acrylic acid)-*block*-polystyrene, and have great potential as templates for the formation of metallic nanoparticles. The ACCs yielded nanomorphologies comparable to those observed for the analogous arborescent polystyrene-*graft*-poly(2-vinylpyridine)-*block*-polystyrene systems, obtained only in low yield by anionic polymerization and grafting. The simplicity, but also the versatility of the self-assembly process developed enables the preparation of these interesting materials on a larger (multi-gram) scale, which should facilitate the investigation of their properties in relation to applications in different areas such as sensors and catalysts. These accomplishments demonstrate the successful achievement of the objectives of the project.

7.1.4 Suggestions for future work

Efforts to study the stability of the ACCs by SEC resulted in one peak corresponding (on the basis of its elution volume) to the block copolymer, while the arborescent copolymer did not elute from the column. This suggests copolymer detachment from the complex upon high dilution. While the ACCs were shown to be relatively stable at higher concentrations (2–10 mg/mL), it would be important to investigate methods to stabilize the complexes at high dilution, particularly if these systems are to be explored for further applications. One strategy to achieve this could be cross-linking the shell of the complex using click chemistry. This could be done by introducing clickable groups in the ACC structure.[3] For instance, some of the carboxylic acid groups in PAA block of the PAA-*b*-PS copolymer could be modified with azido- or alkynyl-functionalized alkylamine, by activating a portion of the

residual carboxylic acid groups with a carbodiimide.[4] Alternately, after activation with a carbodiimide, the activated complex could be reacted directly with a diamine cross-linker such as 2,2'-(ethylenedioxy)bis(ethylamine). Yet another possible scenario could be using a photo cross-linker, such as coumarin derivatives of acrylic or methacrylic acid,[5,6] to introduce a short photoreactive block after the PAA block in the ATRP synthesis of the block copolymers. The cross-linking (photo-dimerization) reaction of the coumarin-containing monomer can be initiated by irradiation with UV at $\lambda \approx 310$ nm after complexation with the arborescent substrate. Another option could be the addition of benzophenone to the PAA segment of the block copolymer after complexation, followed by UV activation ($\lambda = 365$ nm) to initiate cross-linking.[7] It is indeed known that UV irradiation of the carbonyl group in benzophenone promotes the formation of radicals, which can abstract hydrogen radicals from aliphatic groups followed by radical coupling.

Molecular modeling would be beneficial to better understand the different morphologies observed after metal loading for the different generations and conditions investigated. This would further help to understand the interaction mode and the self-assembly process involved in the preparation of the ACCs.

It would also be interesting to investigate the catalytic activity of the gold nanoparticles produced in this work in some environmentally and industrially important oxidation reactions including the oxidation of carbon monoxide,[8] alkanes, and alcohols.[9] Some studies already showed that Au NPs catalysts were more stable to oxygen and displayed improved selectivity in the oxidation of alcohols as compared with Pt and Pd NPs.[9] Indeed, Au NPs also had a higher catalytic activity than Pd NPs in the oxidation of cyclohexane to cyclohexanol and cyclohexanone.[10]

Due to the fact that the Au NPs obtained in this study have a high colloidal stability and are stabilized by high molecular weight polymers, they may be advantageous over Au NPs stabilized by surfactants,

block copolymer micelles and dendrimers. Beyond a high colloidal stability, ease of recovery and regeneration may also be beneficial for these systems.

References

Chapter 1

1. Jiang, W.; Rutherford, D.; Vuong, T.; Liu, H., Nanomaterials for treating cardiovascular diseases: A review. *Bioact. Mater.* **2017**, *2* (4), 185–198.
2. Garcia-Ivars, J.; Iborra-Clar, M.-I.; Alcaina-Miranda, M.-I.; Van der Bruggen, B., Comparison between hydrophilic and hydrophobic metal nanoparticles on the phase separation phenomena during formation of asymmetric polyethersulphone membranes. *J. Membr. Sci.* **2015,** *493*, 709–722.
3. Sun, C.; Lee, J.; Zhang, M., Magnetic nanoparticles in MR imaging and drug delivery. *Adv. Drug Deliv. Rev.* **2008,** *60*, 1252–1265.
4. Yue, G.; Su, S.; Li, N.; Shuai, M.; Lai, X.; Astruc, D.; Zhao, P., Gold nanoparticles as sensors in the colorimetric and fluorescence detection of chemical warfare agents. *Coord. Chem. Rev.* **2016,** *311*, 75–84.
5. Priyadarshini, E.; Pradhan, N., Gold nanoparticles as efficient sensors in colorimetric detection of toxic metal ions: A review. *Sens. Actuators, B.* **2017,** *238*, 888–902.
6. Shivaramakrishnan, B.; Gurumurthy, B.; Balasubramanian, A., Potential biomedical applications of metallic nanobiomaterials: A review. *Int. J. Pharm. Sci. Res.*. **2017,** *8* (3), 985–1000.
7. Lin, W.; Zhang, X.; Qian, L.; Yao, N.; Pan, Y.; Zhang, L., Doxorubicin-loaded unimolecular micelle-stabilized gold nanoparticles as a theranostic nanoplatform for tumor-targeted chemotherapy and computed tomography imaging. *Biomacromolecules* **2017,** *18* (12), 3869–3880.
8. Leung, J. P.; Wu, S.; Chou, K. C.; Signorell, R., Investigation of sub-100 nm gold nanoparticles for laser-induced thermotherapy of cancer. *Nanomaterials* **2013,** *3* (1), 86–106.
9. Deng, R.; Shen, N.; Yang, Y.; Yu, H.; Xu, S.; Yang, Y.-W.; Liu, S.; Meguellati, K.; Yan, F., Targeting epigenetic pathway with gold nanoparticles for acute myeloid leukemia therapy. *Biomaterials* **2018,** *167*, 80–90.
10. Boronat, M.; Corma, A., Molecular approaches to catalysis: Naked gold nanoparticles as quasi-molecular catalysts for green processes. *J. Catal.* **2011,** *284* (2), 138–147.
11. Boronat, M.; Corma, A.; Illas, F.; Radilla, J.; Ródenas, T.; Sabater, M. J., Mechanism of selective alcohol oxidation to aldehydes on gold catalysts: Influence of surface roughness on reactivity. *J. Catal.* **2011,** *278* (1), 50–58.
12. Stratakis, M.; Garcia, H., Catalysis by supported gold nanoparticles: Beyond aerobic oxidative processes. *Chem. Rev.* **2012,** *112* (8), 4469–4506.
13. Liu, B.; Zhang, W.; Feng, H.; Yang, X., Rattle-type microspheres as a support of tiny gold nanoparticles for highly efficient catalysis. *Chem. Commun.* **2011,** *47* (42), 11727–11729.
14. Park, G.; Seo, D.; Chung, I. S.; Song, H., Poly(ethylene glycol)- and carboxylate-functionalized gold nanoparticles using polymer linkages: Single-step synthesis, high stability, and plasmonic detection of proteins. *Langmuir* **2013,** *29* (44), 13518–13526.
15. Mody, V. V.; Siwale, R.; Singh, A.; Mody, H. R., Introduction to metallic nanoparticles. *J. Pharm. Bioallied. Sci.* **2010,** *2* (4), 282–289.

16. Wang, Z.; Tan, B.; Hussain, I.; Schaeffer, N.; Wyatt, M. F.; Brust, M.; Cooper, A. I., Design of polymeric stabilizers for size-controlled synthesis of monodisperse gold nanoparticles in water. *Langmuir* **2007,** *23* (2), 885–895.
17. Nguyen, V. T. A.; De Pauw-Gillet, M.-C.; Sandre, O.; Gauthier, M., Biocompatible polyion complex micelles synthesized from arborescent polymers. *Langmuir* **2016,** *32* (50), 13482–13492.

Chapter 2

1. Katzel, J., The amazing world of nanotechnology. *Control Eng.* **2006**; *53* (7), 66–71.
2. Vaughan, A., Raman nanotechnology – The Lycurgus cup – Letter to the editor. *IEEE Electr. Insul. Mag.* **2008,** *24* (6), 4.
3. Freestone, I.; Meeks, N.; Sax, M.; Higgitt, C., The Lycurgus cup – A Roman nanotechnology. *Gold Bull.* **2007,** *40* (4), 270–277.
4. Selin, C., Expectations and the emergence of nanotechnology. *Sci. Technol. Hum. Values* **2007,** *32* (2), 196–220.
5. Toumey, C., Plenty of room, plenty of history. *Nature Nano* **2009,** *4* (12), 783–784.
6. Thakkar, K. N.; Mhatre, S. S.; Parikh, R. Y., Biological synthesis of metallic nanoparticles. *Nanomed. Nanotechnol. Biol. Med.* **2010,** *6* (2), 257–262.
7. Adams, F. C.; Barbante, C., Nanoscience, nanotechnology and spectrometry. *Spectrochim. Acta, Part B* **2013,** *86*, 3–13.
8. Cao, G., *Nanostructures and nanomaterials: Synthesis, properties and applications*. Imperial College Press: London, **2004**.
9. Zhao, Y.; Zhai, J.; Tan, S.; Wang, L.; Jiang, L.; Zhu, D., TiO_2 micro/nano-composite structured electrodes for quasi-solid-state dye-sensitized solar cells. *Nanotechnology* **2006,** *17* (9), 2090–2097.
10. Daniel, M.-C.; Astruc, D., Gold nanoparticles: Assembly, supramolecular chemistry, quantum-size-related properties, and applications toward biology, catalysis, and nanotechnology. *Chem. Rev.* **2004,** *104* (1), 293–346.
11. Rahme, K.; Nolan, M. T.; Doody, T.; McGlacken, G. P.; Morris, M. A.; O'Driscoll, C.; Holmes, J. D., Highly stable PEGylated gold nanoparticles in water: Applications in biology and catalysis. *RSC Adv.* **2013,** *3* (43), 21016–21024.
12. Kraynov, A., and Müller, T.E., Concepts for the stabilization of metal nanoparticles in ionic liquids. *In applications of ionic liquids in science and technology*. Scott Handy., *Ed.*; InTech, **2011**, pp 235–260.
13. Zhao, P.; Li, N.; Astruc, D., State of the art in gold nanoparticle synthesis. *Coord. Chem. Rev.* **2013,** *257* (3–4), 638–665.
14. Xu, Y.; Chen, L.; Wang, X.; Yao, W.; Zhang, Q., Recent advances in noble metal based composite nanocatalysts: Colloidal synthesis, properties, and catalytic applications. *Nanoscale* **2015,** *7* (24), 10559–10583.
15. Zhang, Z.; Nguyen, H. T. H.; Miller, S. A.; Ploskonka, A. M.; DeCoste, J. B.; Cohen, S. M., Polymer–metal–organic frameworks (polyMOFs) as water tolerant materials for selective carbon dioxide separations. *J. Am. Chem. Soc.* **2015,** *138*, 920−925.

16. Mirabello, V.; Calatayud, D. G.; Arrowsmith, R. L.; Ge, H.; Pascu, S. I., Metallic nanoparticles as synthetic building blocks for cancer diagnostics: From materials design to molecular imaging applications. *J. Mater. Chem. B* **2015,** *3* (28), 5657–5672.
17. Jain, P. K.; Huang, X.; El-Sayed, I. H.; El-Sayed, M. A., Noble metals on the nanoscale: Optical and photothermal properties and some applications in imaging, sensing, biology, and medicine. *Acc. Chem. Res.* **2008,** *41* (12), 1578–1586.
18. Estrada, L. C.; Roberti, M. J.; Simoncelli, S.; Levi, V.; Aramendía, P. F.; Martínez, O. E., Detection of low quantum yield fluorophores and improved imaging times using metallic nanoparticles. *J. Phys. Chem. B* **2012,** *116* (7), 2306–2313.
19. Yang, X.; Tang, Y.; Mason, S. D.; Chen, J.; Li, F., Enzyme-powered three-dimensional DNA nanomachine for DNA walking, payload release, and biosensing. *ACS Nano* **2016,** *10* (2), 2324−2330.
20. McGrath, A. J.; Chien, Y.-H.; Cheong, S.; Herman, D. A. J.; Watt, J.; Henning, A. M.; Gloag, L.; Yeh, C.-S.; Tilley, R. D., Gold over branched palladium nanostructures for photothermal cancer therapy. *ACS Nano* **2015,** *9* (12), 12283–12291.
21. Jaque, D.; Martinez Maestro, L.; del Rosal, B.; Haro-Gonzalez, P.; Benayas, A.; Plaza, J. L.; Martin Rodriguez, E.; Garcia Sole, J., Nanoparticles for photothermal therapies. *Nanoscale* **2014,** *6* (16), 9494–9530.
22. Urban, A. S.; Carretero-Palacios, S.; Lutich, A. A.; Lohmuller, T.; Feldmann, J.; Jackel, F., Optical trapping and manipulation of plasmonic nanoparticles: Fundamentals, applications, and perspectives. *Nanoscale* **2014,** *6* (9), 4458–4474.
23. Brown, S. D.; Nativo, P.; Smith, J.-A.; Stirling, D.; Edwards, P. R.; Venugopal, B.; Flint, D. J.; Plumb, J. A.; Graham, D.; Wheate, N. J., Gold nanoparticles for the improved anticancer drug delivery of the active component of oxaliplatin. *J. Am. Chem. Soc.* **2010,** *132* (13), 4678–4684.
24. Yancey, D. F.; Carino, E. V.; Crooks, R. M., Electrochemical synthesis and electrocatalytic properties of Au@Pt dendrimer-encapsulated nanoparticles. *J. Am. Chem. Soc.* **2010,** *132* (32), 10988–10989.
25. Youk, J. H.; Park, M.-K.; Locklin, J.; Advincula, R.; Yang, J.; Mays, J., Preparation of aggregation stable gold nanoparticles using star–block copolymers. *Langmuir* **2002,** *18* (7), 2455–2458.
26. Crooks, R. M.; Zhao, M., Dendrimer-encapsulated Pt nanoparticles: Synthesis, characterization and applications to catalysis. *Adv. Mater.* **1999,** *11* (3), 217–220.
27. Weires, N. A.; Baker, E. L.; Garg, N. K., Nickel-catalysed Suzuki–Miyaura coupling of amides. *Nat. Chem.* **2015,** *8*, 75-79.
28. Crooks, R. M.; Zhao, M.; Sun, L.; Chechik, V.; Yeung, L. K., Dendrimer-encapsulated metal nanoparticles: Synthesis, characterization, and applications to catalysis. *Acc. Chem. Res.* **2001,** *34* (3), 181–190.
29. Haruta, M., Catalysis of gold nanoparticles deposited on metal oxides. *CATTECH* **2002,** *6* (3), 102–115.
30. Sergeev, G. B.; Klabunde, K. J., Synthesis and stabilization of nanoparticles. *In Nanochemistry;* 2nd ed.*;* Elsevier: **2013,** pp 11–54.
31. Sardar, R.; Funston, A. M.; Mulvaney, P.; Murray, R. W., Gold nanoparticles: Past, present, and future. *Langmuir* **2009,** *25* (24), 13840–13851.

32. Turkevich, J.; Stevenson, P. C.; Hillier, J., A study of the nucleation and growth processes in the synthesis of colloidal gold. *Spec. Discuss. Faraday Soc.* **1951,** *11* (0), 55–75.
33. Janiak, C., Ionic liquids for the synthesis and stabilization of metal nanoparticles. *Z. Naturforsch., B: Chem. Sci.* **2013,** *68* (10), 1059–1089.
34. Vollmer, C.; Janiak, C., Naked metal nanoparticles from metal carbonyls in ionic liquids: Easy synthesis and stabilization. *Coord.Chem. Rev.* **2011,** *255* (17–18), 2039–2057.
35. Wilcoxon, J. P.; Williamson, R. L.; Baughman, R., Optical properties of gold colloids formed in inverse micelles. *J. Chem. Physics* **1993,** *98* (12), 9933–9950.
36. Johnson, S. R.; Evans, S. D.; Brydson, R., Influence of a terminal functionality on the physical properties of surfactant-stabilized gold nanoparticles. *Langmuir* **1998,** *14* (23), 6639–6647.
37. Selvan, T.; Spatz, J. P.; Klok, H.-A.; Möller, M., Gold–polypyrrole core–shell particles in diblock copolymer micelles. *Adv. Mater.* **1998,** *10* (2), 132–134.
38. Khullar, P.; Singh, V.; Mahal, A.; Kumar, H.; Kaur, G.; Bakshi, M. S., Block copolymer micelles as nanoreactors for self-assembled morphologies of gold nanoparticles. *J. Phys. Chem. B* **2013,** *117* (10), 3028–3039.
39. Filali, M.; Meier, M. A. R.; Schubert, U. S.; Gohy, J.-F., Star-block copolymers as templates for the preparation of stable gold nanoparticles. *Langmuir* **2005,** *21* (17), 7995–8000.
40. Ejaz, M.; Alb, A. M.; Kosakowska, K. A.; Grayson, S. M., Modular amphiphilic copolymer-grafted nanoparticles: "Nanoparticle micelle" behavior enhances utility as dispersants. *Polym. Chem.* **2015,** *6* (44), 7749–7757.
41. Dockendorff, J.; Gauthier, M.; Mourran, A.; Möller, M., Arborescent amphiphilic copolymers as templates for the preparation of gold nanoparticles. *Macromolecules* **2008,** *41* (18), 6621–6623.
42. Flores, M. V.; Voutsas, E. C.; Spiliotis, N.; Eccleston, G. M.; Bell, G.; Tassios, D. P.; Halling, P. J., Critical micelle concentrations of nonionic surfactants in organic solvents: Approximate prediction with UNIFAC. *J. Colloid Interface Sci.***2001,** *240* (1), 277–283.
43. Cui, X.; Mao, S.; Liu, M.; Yuan, H.; Du, Y., Mechanism of surfactant micelle formation. *Langmuir* **2008,** *24* (19), 10771–10775.
44. Martinek, K.; Levashov, A. V.; Klyachko, N. L.; Pantin, V. I.; Berezin, I. V., The principles of enzymes stabilization. *Biochim. Biophys. Acta, Enzymol.* **1981,** *657* (1), 277–294.
45. Dominguez, A.; Fernandez, A.; Gonzalez, N.; Iglesias, E.; Montenegro, L., Determination of critical micelle concentration of some surfactants by three techniques. *J. Chem. Educ.* **1997,** *74* (10), 1227–1231.
46. Israelachvili, J. N., *Intermolecular and surface forces*; *3 rd ed.;* Academic Press: London, **2011**, p 710.
47. Israelachvili, J. N., Thermodynamic principles of self-assembly. *In intermolecular and surface forces*; 3rd ed.*;* Academic Press*:* San Diego, **2011**, pp 503–534.
48. Chakraborty, M.; Hsiao, F.-W.; Naskar, B.; Chang, C.-H.; Panda, A. K., Surfactant-assisted synthesis and characterization of stable silver bromide nanoparticles in aqueous media. *Langmuir* **2012,** *28* (18), 7282–7290.
49. Bal, R.; Tada, M.; Iwasawa, Y., Surfactant-promoted novel reductive synthesis of supported metallic Cu nanoclusters and their catalytic performances for selective dehydrogenation of methanol. *Chem. Commun.* **2005,** (27), 3433–3435.

50. Brust, M.; Walker, M.; Bethell, D.; Schiffrin, D. J.; Whyman, R., Synthesis of thiol-derivatised gold nanoparticles in a two-phase liquid-liquid system. *J. Chem. Soc., Chem. Commun.* **1994,** (7), 801–802.
51. Yang, J.; Lee, J. Y.; Too, H.-P., Size effect in thiol and amine binding to small Pt nanoparticles. *Anal. Chim. Acta* **2006,** *571* (2), 206–210.
52. Kim, K.-S.; Demberelnyamba, N. D.; Yeon, S.-W.; Choi, S.; Cha, J.-H.; Lee, H., One-phase preparation of palladium nanoparticles using thiol-functionalized ionic liquid. *Korean J. Chem. Eng.* **2005,** *22* (5), 717–720.
53. Han, S.; Balasubramanian, R., Multidentate ionic surfactant mediated extraction and dispersion of gold nanoparticles in organic solvents. *Langmuir* **2014,** *30* (30), 9063–9070.
54. Stavens, K. B.; Pusztay, S. V.; Zou, S.; Andres, R. P.; Wei, A., Encapsulation of neutral gold nanoclusters by resorcinarenes. *Langmuir* **1999,** *15* (24), 8337–8339.
55. Perala, S. R. K.; Kumar, S., On the Mechanism of metal nanoparticle synthesis in the Brust–Schiffrin method. *Langmuir* **2013,** *29* (31), 9863–9873.
56. Uehara, A.; Booth, S. G.; Chang, S. Y.; Schroeder, S. L. M.; Imai, T.; Hashimoto, T.; Mosselmans, J. F. W.; Dryfe, R. A. W., Electrochemical insight into the Brust–Schiffrin synthesis of Au nanoparticles. *J. Am. Chem. Soc.* **2015,** *137* (48), 15135–15144.
57. Balasubramanian, R.; Kim, B.; Tripp, S. L.; Wang, X.; Lieberman, M.; Wei, A., Dispersion and stability studies of resorcinarene-encapsulated gold nanoparticles. *Langmuir* **2002,** *18* (9), 3676–3681.
58. Kim, S.; Jang, Y.; Yoon, K. Y.; Park, J., Surface engineered gold nanoparticles through highly stable metal–surfactant complexes. *J. Colloid Interface Sci.* **2016,** *464*, 110–116.
59. Tiwari, A. K.; Gangopadhyay, S.; Chang, C.-H.; Pande, S.; Saha, S. K., Study on metal nanoparticles synthesis and orientation of gemini surfactant molecules used as stabilizer. *J. Colloid Interface Sci.* **2015,** *445*, 76–83.
60. Yu; Chang, S.-S.; Lee, C.-L.; Wang, C. R. C., Gold nanorods: Electrochemical synthesis and optical properties. *J. Phys.Chem. B* **1997,** *101* (34), 6661–6664.
61. Sun, G.; Fang, H.; Cheng, C.; Lu, P.; Zhang, K.; Walker, A. V.; Taylor, J. S.; Wooley, K. L., Benzaldehyde-functionalized polymer vesicles. *ACS Nano* **2009,** *3* (3), 673–681.
62. Walker, C. H.; St. John, J. V.; Wisian-Neilson, P., Synthesis and size control of gold nanoparticles stabilized by poly(methylphenylphosphazene). *J. Am. Chem. Soc.* **2001,** *123* (16), 3846–3847.
63. Mössmer, S.; Spatz, J. P.; Möller, M.; Aberle, T.; Schmidt, J.; Burchard, W., Solution behavior of poly(styrene)-*block*-poly(2-vinylpyridine) micelles containing gold nanoparticles. *Macromolecules* **2000,** *33* (13), 4791–4798.
64. Chechik, V.; Zhao, M.; Crooks, R. M., Self-assembled inverted micelles prepared from a dendrimer template: Phase transfer of encapsulated guests. *J. Am. Chem. Soc.* **1999,** *121* (20), 4910–4911.
65. Tsunoyama, H.; Sakurai, H.; Negishi, Y.; Tsukuda, T., Size-specific catalytic activity of polymer-stabilized gold nanoclusters for aerobic alcohol oxidation in water. *J. Am. Chem. Soc.* **2005,** *127* (26), 9374–9375.

66. Tsao, S. H.; Wan, D.; Lai, Y.-S.; Chang, H.-M.; Yu, C.-C.; Lin, K.-T.; Chen, H.-L., White-light-induced collective heating of gold nanocomposite/bombyx mori silk thin films with ultrahigh broadband absorbance. *ACS Nano* ***2015,*** *9 (12), 12045–12059*.
67. Shang, L.; Qin, C.; Wang, T.; Wang, M.; Wang, L.; Dong, S., Fluorescent conjugated polymer-stabilized gold nanoparticles for sensitive and selective detection of cysteine. *J. Phys.Chem. C* **2007,** *111* (36), 13414–13417.
68. Miller, A. C.; Bershteyn, A.; Tan, W.; Hammond, P. T.; Cohen, R. E.; Irvine, D. J., Block copolymer micelles as nanocontainers for controlled release of proteins from biocompatible oil phases. *Biomacromolecules* **2009,** *10* (4), 732–741.
69. Leong, W. L.; Lee, P. S.; Lohani, A.; Lam, Y. M.; Chen, T.; Zhang, S.; Dodabalapur, A.; G. Mhaisalkar, S., Non-volatile organic memory applications enabled by in situ synthesis of gold nanoparticles in a self-assembled block copolymer. *Adv. Mater.* **2008,** *20* (12), 2325–2331.
70. Lebouille, J. G. J. L.; Vleugels, L. F. W.; Dias, A. A.; Leermakers, F. A. M.; Cohen Stuart, M. A.; Tuinier, R., Controlled block copolymer micelle formation for encapsulation of hydrophobic ingredients. *Eur. Phys. J. E* **2013,** *36* (9), 1–12.
71. Mai, Y.; Eisenberg, A., Controlled incorporation of particles into the central portion of block copolymer rods and micelles. *Macromolecules* **2011,** *44* (8), 3179–3183.
72. Lowe, A. B.; Sumerlin, B. S.; Donovan, M. S.; McCormick, C. L., Facile preparation of transition metal nanoparticles stabilized by well-defined copolymers synthesized via aqueous reversible addition-fragmentation chain transfer polymerization. *J. Am. Chem. Soc.* **2002,** *124* (39), 11562–11563.
73. Jenekhe, S. A.; Chen, X. L.,Self-assembled aggregates of rod-coil block copolymers and their solubilization and encapsulation of fullerenes. *Science* **1998,** *279* (5358), 1903–1907.
74. Zhang, W.; Shi, L.; Gao, L.; An, Y.; Wu, K., Formation of core–shell–corona micellar complexes through adsorption of double hydrophilic diblock copolymers into core–shell micelles. *Macromolecule Rapid Comm.* **2005,** *26* (16), 1341–1345.
75. Zhang, L.; Eisenberg, A., Multiple morphologies and characteristics of "crew-cut" micelle-like aggregates of polystyrene-*b*-poly(acrylic acid) diblock copolymers in aqueous solutions. *J. Am. Chem. Soc.* **1996,** *118* (13), 3168–318.
76. Li, B.; Shi, Y.; Zhu, W.; Fu, Z.; Yang, W., Synthesis of amphiphilic polystyrene-*b*-poly(acrylic acid) diblock copolymers by iodide-mediated radical polymerization. *Polym. J.* **2006,** *38* (4), 387–394.
77. Ibrahim, K.; Löfgren, B.; Seppälä, J., Synthesis of tertiary-butyl acrylate polymers and preparation of diblock copolymers using atom transfer radical polymerization. *Eur. Polym. J.* **2003,** *39* (10), 2005–2010;
78. Hua, Z.; Pitto-Barry, A.; Kang, Y.; Kirby, N.; Wilks, T. R.; O'Reilly, R. K., Micellar nanoparticles with tuneable morphologies through interactions between nucleobase-containing synthetic polymers in aqueous solution. *Polym.Chem.* ***2016,*** *7* (25), 4254–4262;
79. Greene, A. C.; Zhu, J.; Pochan, D. J.; Jia, X.; Kiick, K. L., Poly(acrylic acid-*b*-styrene) amphiphilic multiblock copolymers as building blocks for the assembly of discrete nanoparticles. *Macromolecules* **2011,** *44* (7), 1942–1951;

80. Gohy, J.-F.; Antoun, S.; Jérôme, R., pH-Dependent micellization of poly(2-vinylpyridine)-*block*-poly((dimethylamino)ethyl methacrylate) diblock copolymers. *Macromolecules* **2001,** *34* (21), 7435–7440;
81. Chan, S.-C.; Kuo, S.-W.; Lu, C.-H.; Lee, H.-F.; Chang, F.-C., Syntheses and characterizations of the multiple morphologies formed by the self-assembly of the semicrystalline P4VP-*b*-PCL diblock copolymers. *Polymer* **2007,** *48* (17), 5059–5068;
82. Minehara, H.; Pitet, L. M.; Kim, S.; Zha, R. H.; Meijer, E. W.; Hawker, C. J., Branched block copolymers for tuning of morphology and feature size in thin film nanolithography. *Macromolecules* **2016,** *49* (6), 2318–2326.
83. Yang, H.; Su, Y.; Zhu, H.; Zhu, H.; Xie, B.; Zhao, Y.; Chen, Y.; Wang, D., Synthesis of amphiphilic triblock copolymers and application for morphology control of calcium carbonate crystals. *Polymer* **2007,** *48* (15), 4344–4351.
84. Sun, L.; Liu, J.; Zhao, H., Reactive polymeric micelles with disulfide groups in the coronae. *Polym. Chem.* **2014,** *5* (22), 6584–6592.
85. Nguyen, T. B. T.; Li, S.; Deratani, A., Reverse micelles prepared from amphiphilic polylactide-*b*-poly(ethylene glycol) block copolymers for controlled release of hydrophilic drugs. *Int. J. Pharm.* **2015,** *495* (1), 154–161.
86. Davis, K. A.; Matyjaszewski, K., ABC triblock copolymers prepared using atom transfer radical polymerization techniques. *Macromolecules* **2001**, *34*, 2101–2107.
87. Sanson, N.; Bouyer, F.; Destarac, M.; In, M.; Gérardin, C., Hybrid polyion complex micelles formed from double hydrophilic block copolymers and multivalent metal Ions: Size control and nanostructure. *Langmuir* **2012,** *28* (8), 3773–3782.
88. Cohen Stuart, M. A.; Hofs, B.; Voets, I. K.; de Keizer, A., Assembly of polyelectrolyte-containing block copolymers in aqueous media. *Curr. Opin. Colloid Interface Sci.* **2005,** *10* (1–2), 30–36.
89. Gaucher, G.; Dufresne, M.-H.; Sant, V. P.; Kang, N.; Maysinger, D.; Leroux, J.-C., Block copolymer micelles: Preparation, characterization and application in drug delivery. *J. Controlled Release* **2005,** *109* (1–3), 169–188.
90. Pietsch, T.; Gindy, N.; Fahmi, A., Preparation and control of functional nano-objects: Spheres, rods and rings based on hybrid materials. *Polymer* **2008,** *49* (4), 914–921.
91. Choi, I.; Gunawidjaja, R.; Suntivich, R.; Tsitsilianis, C.; Tsukruk, V. V., Surface behavior of PSn(P2VP-*b*-PtBA)$_n$ heteroarm stars. *Macromolecules* **2010,** *43* (16), 6818–6828.
92. Yu, Y.; Zhang, L.; Eisenberg, A., Morphogenic effect of solvent on crew-cut aggregates of apmphiphilic diblock copolymers. *Macromolecules* **1998,** *31* (4), 1144–1154.
93. Chen, X.; Sun, J.-T.; Pan, C.-Y.; Hong, C.-Y., Facile synthesis of thermo-responsive Au-polymer hybrid microgels through temperature-induced co-aggregation and self-crosslinking. *Polym. Chem.* **2015,** *6* (33), 5989–5992.
94. Leiva, A.; Fuentes, I.; Bossel, E.; Urzúa, M.; Méndez, M.; Pino, M.; Radić, D.; Márquez, V.; González-Nilo, F. D., Block copolymers in the synthesis of gold nanoparticles. Two new approaches: Copolymer aggregates as reductants and stabilizers and simultaneous formation of copolymer aggregates and gold nanoparticles. *J. Polym. Sci., Part A: Polym. Chem.* **2014,** *52* (21), 3069–3079.

95. Kim, K.-S.; Choi, S.; Cha, J.-H.; Yeon, S.-H.; Lee, H., Facile one-pot synthesis of gold nanoparticles using alcohol ionic liquids. *J. Mater. Chem.* **2006,** *16* (14), 1315–1317.
96. Choi, I.; Gunawidjaja, R.; Suntivich, R.; Tsitsilianis, C.; Tsukruk, V. V., Surface behavior of PS_n(P2VP-*b*-PtBA)$_n$ heteroarm stars. *Macromolecules* **2010,** *43* (16), 6818–6828.
97. Abraham, S.; Ha, C.-S.; Batt, C. A.; Kim, I., Synthesis of stable "gold nanoparticle–polymeric micelle" conjugates: A new class of star "molecular chimera" that self-assemble into linear arrays of spherical micelles. *J. Polym. Sci., Part A: Polym. Chem.* **2007,** *45* (16), 3570–3579.
98. Cadena, L.-E. S.; Gauthier, M., Phase-segregated dendrigraft copolymer architectures. *Polymers* **2010,** *2* (4), 596–622.
99. Teertstra, S. J.; Gauthier, M., Dendrigraft polymers: Macromolecular engineering on a mesoscopic scale. *Prog. Polym. Sci.* **2004,** *29* (4), 277–327.
100. Tomalia, D. A.; Fréchet, J. M. J., Discovery of dendrimers and dendritic polymers: A brief historical perspective. *J. Polym. Sci., Part A: Polym. Chem.* **2002,** *40* (16), 2719–2728.
101. Chow, H.-F.; Mong, T. K. -K.; Nongrum, M. F.; Wan, C.-W., The synthesis and properties of novel functional dendritic molecules. *Tetrahedron* **1998,** *54* (30), 8543–8660.
102. Shi, Y.; Graff, R. W.; Cao, X.; Wang, X.; Gao, H., Chain-growth click polymerization of AB_2 monomers for the formation of hyperbranched polymers with low polydispersities in a one-pot process. *Angew. Chem. Int. Ed.* **2015,** *54* (26), 7631–7635.
103. Esumi, K.; Suzuki, A.; Yamahira, A.; Torigoe, K., Role of Poly(amidoamine) dendrimers for preparing nanoparticles of gold, platinum, and silver. *Langmuir* **2000**, *16* (6), 2604–2608.
104. Gauthier, M.; Möller, M., Uniform highly branched polymers by anionic grafting: Arborescent graft polymers. *Macromolecules* **1991**, *24* (16), 4548–4553.
105. Scott, R. W. J.; Wilson, O. M.; Crooks, R. M., Synthesis, characterization, and applications of dendrimer-encapsulated nanoparticles. *J. Phys.Chem. B* **2005**, *109* (2), 692–704.
106. Yu, T.; Wang, W.; Chen, J.; Zeng, Y.; Li, Y.; Yang, G.; Li, Y., Dendrimer-encapsulated Pt nanoparticles: An artificial enzyme for hydrogen production. *J. Phys.Chem.* **2012**, *116* (19), 10516–10521.
107. Huang, W.; Kuhn, J. N.; Tsung, C.-K.; Zhang, Y.; Habas, S. E.; Yang, P.; Somorjai, G. A., Dendrimer templated synthesis of one nanometer Rh and Pt particles supported on mesoporous silica: Catalytic activity for ethylene and pyrrole hydrogenation. *Nano Lett.* **2008**, *8* (7), 2027–2034.
108. Hermes, J. P.; Sander, F.; Peterle, T.; Urbani, R.; Pfohl, T.; Thompson, D.; Mayor, M., Gold nanoparticles stabilized by thioether dendrimers. *Chem. Eur. J.* **2011**, *17* (48), 13473–13481.
109. Zhou, T.; Wang, Y.; Dong, Y.; Chen, C.; Liu, D.; Yang, Z., Tetrahedron DNA dendrimers and their encapsulation of gold nanoparticles. *Bioorg. Med. Chem.* **2014**, *22* (16), 4391–4394.
110. Lang, H.; May, R. A.; Iversen, B. L.; Chandler, B. D., Dendrimer-encapsulated nanoparticle precursors to supported platinum catalysts. *J. Am. Chem. Soc.* **2003**, *125* (48), 14832–14836.
111. Garcia, M. E.; Baker, L. A.; Crooks, R. M., Preparation and characterization of dendrimer-gold colloid nanocomposites. *Anal. Chem.* **1999**, *71* (1), 256–258.
112. Kim, Y.-G.; Oh, S.-K.; Crooks, R. M., Preparation and characterization of 1–2 nm dendrimer-encapsulated gold nanoparticles having very narrow size distributions. *Chem. Mater.* **2004,** *16* (1), 167–172.

113. Leff, D. V.; Brandt, L.; Heath, J. R., Synthesis and characterization of hydrophobic, organically-soluble gold nanocrystals functionalized with primary amines. *Langmuir* **1996**, *12* (20), 4723–4730.
114. Guerra, J.; Rodrigo, A. C.; Merino, S.; Tejeda, J.; García-Martínez, J. C.; Sánchez-Verdú, P.; Ceña, V.; Rodríguez-López, J., PPV–PAMAM hybrid dendrimers: Self-assembly and stabilization of gold nanoparticles. *Macromolecules* **2013**, *46* (18), 7316–7324.
115. Murugan, E.; Rangasamy, R., Synthesis, characterization, and heterogeneous catalysis of polymer-supported poly(propyleneimine) dendrimer stabilized gold nanoparticle catalyst. *J. Polym. Sci., Part A: Polym. Chem.* **2010,** *48* (12), 2525–2532.
116. Pietsch, T.; Appelhans, D.; Gindy, N.; Voit, B.; Fahmi, A., Oligosaccharide-modified dendrimers for templating gold nanoparticles: Tailoring the particle size as a function of dendrimer generation and molecular structure. *Colloids Surf., A* **2009,** *341* (1–3), 93–102.
117. Spirin, M. G.; Brichkin, S. B.; Razumov, V. F., Synthesis and stabilization of gold nanoparticles in reverse micelles of aerosol OT and triton X-100. *Colloid J.* **2005,** *67* (4), 485–490.
118. Boisselier, E.; Diallo, A. K.; Salmon, L.; Ornelas, C.; Ruiz, J.; Astruc, D., Encapsulation and stabilization of gold nanoparticles with "click" polyethyleneglycol dendrimers. *J. Am. Chem. Soc.* **2010**, *132* (8), 2729–2742.
119. Li, N.; Echeverría, M.; Moya, S.; Ruiz, J.; Astruc, D., "Click" synthesis of nona-PEG-branched triazole dendrimers and stabilization of gold nanoparticles that efficiently catalyze *p*-nitrophenol reduction. *Inorg. Chem.* **2014**, *53* (13), 6954–6961.
120. D'Aléo, A.; Williams, R. M.; Osswald, F.; Edamana, P.; Hahn, U.; van Heyst, J.; Tichelaar, F. D.; Vögtle, F.; De Cola, L., Oligothia dendrimers for the formation of gold nanoparticles. *Adv. Funct. Mater.* **2004**, *14* (12), 1167–1177.
121. Graff, R. W.; Wang, X.; Gao, H., Exploring self-condensing vinyl polymerization of inimers in microemulsion to regulate the structures of hyperbranched polymers. *Macromolecules* **2015**, *48* (7), 2118–2126.
122. Pérignon, N.; Marty, J.-D.; Mingotaud, A.-F.; Dumont, M.; Rico-Lattes, I.; Mingotaud, C., Hyperbranched polymers analogous to PAMAM dendrimers for the formation and stabilization of gold nanoparticles. *Macromolecules* **2007**, *40* (9), 3034–3041.
123. Pérignon, N.; Mingotaud, A.-F.; Marty, J.-D.; Rico-Lattes, I.; Mingotaud, C., Formation and stabilization in water of metal nanoparticles by a hyperbranched polymer chemically analogous to PAMAM dendrimers. *Chem. Mater.* **2004,** *16* (24), 4856–4858.
124. Zhang, Z.; Shou, C., Synthesis of gold nanoparticles in hyperbranched polyol dispersions. *J. Appl. Polym. Sci.* **2011,** *122* (5), 2849–2854.
125. Dai, Y.; Yu, P.; Zhang, X.; Zhuo, R., Gold nanoparticles stabilized by amphiphilic hyperbranched polymers for catalytic reduction of 4-nitrophenol. *J. Catal.* **2016,** *337*, 65–71.
126. Li, H.; Zhang, L.; Jo, J. K.; Ha, C.-S.; Shchipunov, Y. A.; Kim, I., Facile synthesis of titania/hyperbranched polyglycidol nanohybrids with controllable morphologies: From solid spheres, capsules to tubes. *J. Nanopart. Res.* **2011,** *13* (5), 2117–2128.
127. Zill, A.; Rutz, A. L.; Kohman, R. E.; Alkilany, A. M.; Murphy, C. J.; Kong, H.; Zimmerman, S. C., Clickable polyglycerol hyperbranched polymers and their application to gold nanoparticles and acid-labile nanocarriers. *Chem. Commun.* **2011,** *47* (4), 1279–1281.

128. Zhai, S.; Hong, H.; Zhou, Y.; Yan, D., Synthesis of cationic hyperbranched multiarm copolymer and its application in self-reducing and stabilizing gold nanoparticles. *Sci. China Chem.* **2010,** *53* (5), 1114–1121.
129. Tomalia, D. A.; Hedstrand, D. M.; Ferritto, M. S., Comb-burst dendrimer topology: New macromolecular architecture derived from dendritic grafting. *Macromolecules* **1991,** *24* (6), 1435–1438.
130. Selb, J.; Gallot, Y., Graft copolymers: Synthesis and characterization of poly(styrene-*g*-2-vinylpyridine). *Polymer* **1979,** *20* (10), 1259–1267.
131. Selb, J.; Gallot, Y., Graft copolymers: Synthesis and characterization of poly (styrene-*g*-4 vinylpyridine). *Polymer* **1979,** *20* (10), 1273–1280.
132. Kee, R. A.; Gauthier, M., Arborescent polystyrene-*graft*-poly(2-vinylpyridine) copolymers: Synthesis and enhanced polyelectrolyte effect in solution. *Macromolecules* **2002,** *35* (17), 6526–6532.
133. Gauthier, M.; Li, J.; Dockendorff, J., Arborescent polystyrene-*graft*-poly(2-vinylpyridine) copolymers as unimolecular micelles. Synthesis from acetylated substrates. *Macromolecules* **2003,** *36* (8), 2642–2648.
134. Nguyen, V. T. A.; De Pauw-Gillet, M.-C.; Sandre, O.; Gauthier, M., Biocompatible polyion complex micelles synthesized from arborescent polymers. *Langmuir* **2016,** *32* (50), 13482–13492.
135. Nguon, O. J. Polymer-stabilized transition metal nanocatalysts: Synthesis, characterization, and applications. Ph.D. Thesis, University of Waterloo, **2015**.

Chapter 3

1. Teertstra, S. J.; Gauthier, M., Dendrigraft polymers: Macromolecular engineering on a mesoscopic scale. *Prog. Polym. Sci.* **2004,** *29* (4), 277–327.
2. Chow, H.-F.; Mong, T. K. K.; Nongrum, M. F.; Wan, C.-W., The synthesis and properties of novel functional dendritic molecules. *Tetrahedron* **1998,** *54* (30), 8543–8660.
3. Shi, Y.; Graff, R. W.; Cao, X.; Wang, X.; Gao, H., Chain-growth click polymerization of AB_2 monomers for the formation of hyperbranched polymers with low polydispersities in a one-pot process. *Angew. Chemie. Inter. Ed.* **2015,** *54* (26), 7631–7635.
4. Graff, R. W.; Wang, X.; Gao, H., Exploring self-condensing vinyl polymerization of inimers in microemulsion to regulate the structures of hyperbranched polymers. *Macromolecules* **2015,** *48* (7), 2118–2126.
5. Gauthier, M.; Möller, M., Uniform highly branched polymers by anionic grafting: Arborescent graft polymers. *Macromolecules* **1991,** *24* (16), 4548–4553.
6. Tomalia, D. A.; Hedstrand, D. M.; Ferritto, M. S., Comb-burst dendrimer topology: New macromolecular architecture derived from dendritic grafting. *Macromolecules* **1991,** *24* (6), 1435–1438.
7. Gauthier, M., Arborescent polymers and other dendrigraft polymers: A journey into structural diversity. *J. Polym. Sci., Part A: Polym. Chem.*. **2007,** *45* (17), 3803–3810.
8. Li, J.; Gauthier, M., A Novel synthetic path to arborescent graft polystyrenes. *Macromolecules* **2001,** *34* (26), 8918–8924.

9. Munam, A.; Gauthier, M., Large-scale synthesis of arborescent polystyrenes. *J. Polym. Sci., Part A: Polym. Chem.*. **2008,** *46* (17), 5742–5751.
10. Moingeon, F.; Wu, Y. R.; Cadena-Sánchez, L. E.; Gauthier, M., Synthesis of arborescent styrene homopolymers and copolymers from epoxidized substrates. *J. Polym. Sci., Part A: Polym. Chem.* **2012,** *50* (9), 1819–1826.
11. Kee, R. A.; Gauthier, M., Arborescent polystyrene-*graft*-poly(*tert*-butyl methacrylate) copolymers: Synthesis and enhanced polyelectrolyte effect in solution. *J. Polym. Sci., Part A: Polym. Chem.* **2008,** *46* (7), 2335–2346.
12. Gauthier, M.; Munam, A., Cross-linked latex particles grafted with polyisoprene as model rubber-compatible fillers. *Polymer* **2009,** *50* (25), 6032–6042.
13. Gauthier, M.; Lin, W.-Y.; Teertstra, S. J.; Tzoganakis, C., Fluorine-containing arborescent polystyrene-*graft*-polyisoprene copolymers as polymer processing additives. *Polymer* **2010,** *51* (14), 3123–3129.
14. Gauthier, M.; Li, J.; Dockendorff, J., Arborescent polystyrene-*graft*-poly(2-vinylpyridine) copolymers as unimolecular micelles. Synthesis from acetylated substrates. *Macromolecules* **2003,** *36* (8), 2642–2648.
15. Kee, R. A.; Gauthier, M., Arborescent polystyrene-*graft*-poly(2-vinylpyridine) copolymers: Synthesis and enhanced polyelectrolyte effect in solution. *Macromolecules* **2002,** *35* (17), 6526–6532.
16. Ito, S.; Senda, S.; Ishizone, T.; Hirao, A., Syntheses of exactly-defined multi-graft polymers with two or more graft chains per branch point by a new iterative methodology. *Polym. Chem.* **2016**, *7* (11), 2078–2086.
17. Selb, J.; Gallot, Y., Graft copolymers: Synthesis and characterization of poly(styrene-*g*-2-vinylpyridine). *Polymer* **1979**, *20* (10), 1259–1267.
18. Selb, J.; Gallot, Y., Graft copolymers: Synthesis and characterization of poly(styrene-*g*-4 vinylpyridine). *Polymer* **1979**, *20* (10), 1273–1280.
19. Dockendorff, J.; Gauthier, M., Synthesis of arborescent polystyrene-*g*-[poly(2-vinylpyridine)-*b*-polystyrene] core–shell–corona copolymers. *J. Polym. Sci., Part A: Polym. Chem.*. **2014,** *52* (8), 1075–1085.
20. Gauthier, M.; Munam, A., Arborescent polystyrene-*graft*-poly(2-vinylpyridine) copolymers: Solution polyelectrolyte behavior. *RSC Adv.* **2012**, *2* (7), 3100–3108.
21. Munam, A., Graft polymers: From dendrimer hybrids to latex particles. Ph.D. thesis, University of Waterloo, **2007**.
22. Davis, K. A.; Matyjaszewski, K., Atom transfer radical polymerization of *tert*-butyl acrylate and preparation of block copolymers. *Macromolecules* **2000**, *33* (11), 4039–4047.
23. Abraham, S.; Ha, C.-S.; Kim, I., Synthesis of poly(styrene-*block*-*tert*-butyl acrylate) star polymers by atom transfer radical polymerization and micellization of their hydrolyzed polymers. *J. Polym. Sci., Part A: Polym. Chem.* **2005**, *43* (24), 6367-6378.
24. Ramakrishnan, A.; Dhamodharan, R., Facile synthesis of ABC and CBABC multiblock copolymers of styrene, *tert*-butyl acrylate, and methyl methacrylate via room temperature ATRP of MMA. *Macromolecules* **2003**, *36* (4), 1039–1046.

25. Davis, K. A.; Charleux, B.; Matyjaszewski, K., Preparation of block copolymers of polystyrene and poly(*t*-butyl acrylate) of various molecular weights and architectures by atom transfer radical polymerization. *J. Polym. Sci., Part A: Polym. Chem.* **2000**, *38* (12), 2274-2283.
26. Burguière, C.; Chassenieux, C.; Charleux, B., Characterization of aqueous micellar solutions of amphiphilic block copolymers of poly(acrylic acid) and polystyrene prepared via ATRP. Toward the control of the number of particles in emulsion polymerization. *Polymer* **2003,** *44* (3), 509–518.
27. Mössmer, S.; Spatz, J. P.; Möller, M.; Aberle, T.; Schmidt, J.; Burchard, W., Solution behavior of poly(styrene)-*block*-poly(2-vinylpyridine) micelles containing gold nanoparticles. *Macromolecules* **2000,** *33* (13), 4791–4798.
28. Mendrek, B.; Trzebicka, B., Synthesis and characterization of well-defined poly(*tert*-butyl acrylate) star polymers. *Eur. Polym. J.* **2009,** *45* (7), 1979–1993.

Chapter 4

1. Kim, M.; Yeo, S. J.; Highley, C. B.; Burdick, J. A.; Yoo, P. J.; Doh, J.; Lee, D., One-step generation of multifunctional polyelectrolyte microcapsules via nanoscale interfacial complexation in emulsion (NICE). *ACS Nano* **2015**, *9* (8), 8269–8278.
2. Harada, A.; Kataoka, K., Formation of polyion complex micelles in an aqueous milieu from a pair of oppositely-charged block copolymers with poly(ethylene glycol) segments. *Macromolecules* **1995**, *28* (15), 5294–5299.
3. Kabanov, A. V.; Bronich, T. K.; Kabanov, V. A.; Yu, K.; Eisenberg, A., Soluble stoichiometric complexes from poly(N-ethyl-4-vinylpyridinium) cations and poly(ethylene oxide)-*block*-polymethacrylate anions. *Macromolecules* **1996**, *29* (21), 6797–6802.
4. Stuart, C. M. A.; Besseling, N. A. M.; Fokkink, R. G., Formation of micelles with complex coacervate cores. *Langmuir* **1998**, *14* (24), 6846–6849.
5. Gohy, J. F.; Varshney, S. K.; Antoun, S.; Jérôme, R., Water-soluble complexes formed by sodium poly(4-styrenesulfonate) and a poly(2-vinylpyridinium)-*block*-poly(ethyleneoxide) copolymer. *Macromolecules* **2000**, *33* (25), 9298–9305.
6. Pergushov, D. V.; Remizova, E. V.; Feldthusen, J.; Zezin, A. B.; Müller, A. H. E.; Kabanov, V. A., Novel water-soluble micellar interpolyelectrolyte complexes. *J. Phys. Chem. B* **2003**, *107* (32), 8093–8096.
7. Zhou, X.; Goh, S.; Lee, S.; Tan, K., XPS and FTIR studies of interactions in poly(carboxylic acid)/poly(vinylpyridine) complexes. *Polymer* **1998**, *39* (16), 3631–3640.
8. Karayianni, M.; Pispas, S. Self-assembly of amphiphilic block copolymers in selective solvents. *In fluorescence studies of polymer containing systems*; Procházka, K., Ed.; Springer, **2016,** pp 27–63.
9. Mai, Y.; Eisenberg, A., Self-assembly of block copolymers. *Chem. Soci. Rev.* **2012**, 41 (18), 5969–5985.
10. Groenewegen, W.; Lapp, A.; Egelhaaf, S. U.; van der Maarel, J. R. C., Counterion distribution in the coronal layer of polyelectrolyte diblock copolymer micelles. *Macromolecules* **2000**, *33* (11), 4080–4086.

11. Zhang, W.; Shi, L.; An, Y.; Wu, K.; Gao, L.; Liu, Z.; Ma, R.; Meng, Q.; Zhao, C.; He, B., Adsorption of Poly(4-vinyl pyridine) unimers into polystyrene-*block*-poly(acrylic acid) micelles in ethanol due to hydrogen bonding. *Macromolecules* **2004**, *37* (8), 2924–2929.
12. Adams, D. J.; Rogers, S. H.; Schuetz, P., The effect of PEO block lengths on the size and stability of complex coacervate core micelles. *J. Colloid Interface Sci.* **2008**, *322* (2), 448–456.
13. Tian, S.; Liu, G.; Wang, X.; Wu, T.; Yang, J.; Ye, X.; Zhang, G.; Hu, J.; Liu, S., pH-Regulated reversible transition between polyion complexes (PIC) and hydrogen-bonding complexes (HBC) with tunable aggregation-induced emission. *ACS Appl. Mater. Interfaces* **2016**, *8* (6), 3693–3702.
14. Ishizu, K.; Toyoda, K.; Furukawa, T.; Sogabe, A., Electrostatic interaction of anionic/nonionic polyelectrolyte prototype copolymer brushes with cationic linear polyelectrolyte. *Macromolecules* **2004**, *37* (10), 3954–3957.
15. Ding, J.; Wang, L.; Yu, H.; Huo, J.; Liu, Q.; Xiao, A., Well-controlled formation of nanofibers and double wall vesicles through the electrostatic-assisted assembly of a couple of star polyelectrolytes-complementary. *J. Phys. Chem.C* **2009**, *113* (13), 5126–5132.
16. Nguyen, V. T. A.; De Pauw-Gillet, M.-C.; Sandre, O.; Gauthier, M., Biocompatible polyion complex micelles synthesized from arborescent polymers. *Langmuir* **2016**, *32* (50), 13482–13492.
17. Inai, Y.; Kato, S. I.; Hirabayashi, T.; Yokota, K., Complexation of sequence-ordered methacrylic acid copolymers with poly(4-vinylpyridine). *J. Polym. Sci., Part A: Polym. Chem.* **1996**, *34* (12), 2341–2348.
18. Sakurai, K.; Douglas, E. P.; MacKnight, W. J., Spectroscopic study of an ionic blend made from the acid form of sulfonated polystyrene and poly[ethyl acrylate-*co*-(4-vinylpyridine)]. *Macromolecules* **1992**, *25* (18), 4506–4510.
19. Zhou, X.; Goh, S. H.; Lee, S. Y.; Tan, K. L., Interpolymer complexation between poly(vinylphosphonic acid) and poly(vinylpyridine). *Polymer* **1997**, *38* (21), 5333–5338.
20. Vyhnalkova, R.; Müller, A. H. E.; Eisenberg, A., Control of morphology and corona composition in aggregates of mixtures of PS-*b*-PAA and PS-*b*-P4VP diblock copolymers: Effects of solvent, water content, and mixture composition. *Langmuir* **2014**, *30* (44), 13152–13163.
21. Zhang, W.; Shi, L.; Miao, Z. J.; Wu, K.; An, Y., Core–shell–corona micellar complexes between poly(ethylene glycol)-*block*-poly(4-vinyl pyridine) and polystyrene-*block*-poly(acrylic acid). Macromol. *Chem. Phys.* **2005**, *206* (23), 2354–2361.
22. Zhang, W.; Shi, L.; Gao, L.; An, Y.; Wu, K., Formation of core–shell–corona micellar complexes through adsorption of double hydrophilic diblock copolymers into core–shell micelles. *Macromol. Rapid Commun*. **2005**, *26* (16), 1341–1345.
23. Jiang, X.; Wang, Y.; Zhang, W.; Zheng, P.; Shi, L., Raspberry-like aggregates containing secondary nanospheres of polystyrene-*block*-poly(4-vinylpyridine) micelles. *Macromol. Rapid Commun.* **2006**, *27* (21), 1833–1837.
24. Napper, D. H.; Netschey, A., Studies of the steric stabilization of colloidal particles. *J. Colloid Interface Sci.* ***1971***, *37* (3), 528–535.
25. Zhulina, E. B.; Borisov, O. V.; Priamitsyn, V. A., Theory of steric stabilization of colloid dispersions by grafted polymers. *J. Colloid Interface Sci.* **1990**, *137* (2), 495–511.
26. Baulin, V. A.; Trizac, E., Self-assembly of spherical interpolyelectrolyte complexes from oppositely charged polymers. *Soft Matter* **2012**, *8* (25), 6755–6766.

27. Gauthier, M.; Munam, A., Arborescent polystyrene-*graft*-poly(2-vinylpyridine) copolymers: Solution polyelectrolyte behavior. *RSC Adv*. **2012**, *2* (7), 3100–3108.
28. Gauthier, M.; Li, J.; Dockendorff, J., Arborescent polystyrene-*graft*-poly(2-vinylpyridine) copolymers as unimolecular micelles. Synthesis from acetylated substrates. *Macromolecules* **2003**, *36* (8), 2642–2648.
29. Davis, K. A.; Matyjaszewski, K., Atom transfer radical polymerization of *tert*-butyl acrylate and preparation of block copolymers. *Macromolecules* 2000, *33* (11), 4039–4047.
30. Ramakrishnan, A.; Dhamodharan, R., Facile synthesis of ABC and CBABC multiblock copolymers of styrene, *tert*-butyl acrylate, and methyl methacrylate via room temperature ATRP of MMA. *Macromolecules* 2003, *36* (4), 1039–1046.
31. Ross Hallett, F., Particle size analysis by dynamic light scattering. *Food Res. Int.* **1994**, *27* (2), 195–198.
32. Zhang, L.; Eisenberg, A., Thermodynamic vs kinetic aspects in the formation and morphological transitions of crew-cut aggregates produced by self-assembly of polystyrene-*block*-poly(acrylic acid) copolymers in dilute solution. *Macromolecules* 1999, *32* (7), 2239–2249.
33. Zhelev, N.; Barudov, S., Laser light scattering applications in biotechnology. *Biotechnol. Biotechnol. Equip.* **2005**, *19* (3), 3–8.
34. Lim, J.; Yeap, S. P.; Che, H. X.; Low, S. C., Characterization of magnetic nanoparticle by dynamic light scattering. *Nanoscale Res. Lett*. **2013**, *8* (381), 1–14.
35. Koppel, D. E., Analysis of macromolecular polydispersity in intensity correlation spectroscopy: The method of cumulants. *J. Chem. Phys.* **1972**, *57* (11), 4814–4820.
36. Yang, C.; Kizhakkedathu, J. N.; Brooks, D. E.; Jin, F.; Wu, C., Laser-light-scattering study of internal motions of polymer chains grafted on spherical latex particles. *J. Phys. Chem.B* 2004, *108* (48), 18479–18484.
37. Thomas, J. C., The determination of log normal particle size distributions by dynamic light scattering. *J. Colloid Interface Sci*. **1987**, *117* (1), 187–192;
38. Yang, S.; Vishnyakov, A.; Neimark, A. V., Self-assembly in block polyelectrolytes. *J. Chem. Phys*. **2011**, *134*, 054104–8.
39. Antony, T.; Saxena, A.; Roy, K. B.; Bohidar, H. B., Laser light scattering immunoassay: An improved data analysis by CONTIN method. *J. Biochem. Bioph. Methods* **1998**, *36* (2–3), 75–85.
40. Yeap, S.P.; Lim, J.; Ngang, H. P.; Ooi, B. S.; and Ahmad, A. L., Role of particle–particle interaction towards effective interpretation of Z-average and particle size distributions from dynamic light scattering (DLS) analysis. *J. Nanosci. Nanotechnol*. **2018**, *18*(10), 6957–6964.
41. Varennea, F.; Bottonb, J.; Merleta, C.; Hillaireaua, H.; Legranda, F.-X.; Barratta, G.; Vauthiera, C., Size of monodispersed nanomaterials evaluated by dynamic light scattering: Protocol validated for measurements of 60 and 203 nm diameter nanomaterials is now extended to 100 and 400 nm. *Inter. J. Pharm*. **2016**, *515*, 245–253.
42. Esfahani, M. R.; Stretz, H. A.; Wells, M. J. M., Abiotic reversible self-assembly of fulvic and humic acid aggregates in low electrolytic conductivity solutions by dynamic light scattering and zeta potential investigation. *Sci. Total Environ*. **2015**, *537*, 81–92.

43. Yun, S. I.; Gadd, G. E.; Lo, V.; Gauthier, M.; Munam, A., Temperature-responsive supramolecular assembly and morphology of arborescent copolymer micelles with a solvophilic core−solvophobic shell structure. *Macromolecules* **2008**, *41* (19), 7166–7172.
44. Choi, I.; Gunawidjaja, R.; Suntivich, R.; Tsitsilianis, C.; Tsukruk, V. V., Surface behavior of PS_n(P2VP-*b*-PtBA)$_n$ heteroarm stars. *Macromolecules* **2010**, *43* (16), 6818–6828.
45. Betthausen, E., Drechsler, M., Fortsch, M., Pergushov, D. V., Schacher, F. H., and Muller A.H. E., Stimuli-responsive micellar interpolyelectrolyte complexes – Control of micelle dynamics via core crosslinking. *Soft Matter* **2012**, *8* (36), 10167-10177.
46. Li, W.; Nakayama, M.; Akimoto, J.; Okano, T., Effect of block compositions of amphiphilic block copolymers on the physicochemical properties of polymeric micelles. *Polymer* **2011**, *52* (17), 3783-3790.
47. Nyrkova, I. A.; Semenov, A. N., Multimerization: Closed or open association scenario. *Eur.Phys. J. E.* **2005**, *17* (3), 327-337.
48. Huang, W.-Y.; Shen, J.-W.; Chen, X.-M., Effect of composition on phase morphology and mechanical properties of PP/PA66 in situ composites via extrusion-drawing-injection method. *J. Mater. Sci*. **2003**, *38* (3), 541-547.
49. Välimäki, S.; Khakalo, A.; Ora, A.; Johansson, L.-S.; Rojas, O. J.; Kostiainen, M. A., Effect of PEG–PDMAEMA block copolymer architecture on polyelectrolyte complex formation with heparin. *Biomacromolecules* **2016**, *17* (9), 2891–2900.
50. Mandema, W.; Zeldenrust, H., Diffusion of polystyrene in tetrahydrofuran. *Polymer* **1977**, *18* (8), 835–839.
51. Venkataswamy, K.; Jamieson, A. M.; Petschek, R. G., Static and dynamic properties of polystyrene in good solvents: Ethylbenzene and tetrahydrofuran. *Macromolecules* **1986**, *19* (1), 124–133.
52. Rusu, M.; Kuckling, D.; Möhwald, H.; Schönhoff, M., Adsorption of novel thermosensitive graft-copolymers: Core–shell particles prepared by polyelectrolyte multilayer self-assembly. *J. Colloid Interface Sci*. **2006**, *298* (1), 124–131.
53. Karl, M. K.; Ali, M. A.-S.; Michelle, M.; Vicki, L. C., The hydrodynamic size of polymer stabilized nanocrystals. *Nanotechnology* **2007**, *18* (47), 475709.
54. Roiter, Y.; Minko, S., Adsorption of polyelectrolyte versus surface charge: In situ single-molecule atomic force microscopy experiments on similarly, oppositely, and heterogeneously charged surfaces. *J. Phys. Chem. B* **2007**, *111* (29), 8597–8604.
55. Trotsenko, O.; Roiter, Y.; Minko, S., Conformational transitions of flexible hydrophobic polyelectrolytes in solutions of monovalent and multivalent salts and their mixtures. *Langmuir* **2012**, *28* (14), 6037–6044.
56. Dockendorff, J. M. Arborescent copolymers: Synthesis, properties & metallic nanoparticle templating. Ph.D. Thesis, University of Waterloo, Waterloo, ON, **2011**.
57. Gu, D.; Ladewig, K.; Klimak, M.; Haylock, D.; McLean, K. M.; O'Connor, A. J.; Qiao, G. G., Amphiphilic core cross-linked star polymers as water-soluble, biocompatible and biodegradable unimolecular carriers for hydrophobic drugs. *Polym. Chem.* **2015**, *6*, 6475–6487.
58. Zhulina, E. B.; Borisov, O. V., Structure and stabilizing properties of grafted polymer layers in a polymer medium. *J. Colloid Interface Sci.* **1991**, 144 (2), 507–520.

59. Kwak, J.; Han, S. H.; Moon, H. C.; Kim, J. K.; Koo, J.; Lee, J.-S.; Pryamitsyn, V.; Ganesan, V., Phase behavior of binary blend consisting of asymmetric polystyrene-*block*-poly(2-vinylpyridine) copolymer and asymmetric deuterated polystyrene-*block*-poly(4-hydroxystyrene) copolymer. *Macromolecules* **2015**, *48* (4), 1262–1266.
60. Yu, Y.; Zhang, L.; Eisenberg, A., Morphogenic effect of solvent on crew-cut aggregates of apmphiphilic diblock copolymers. *Macromolecules* **1998**, *31* (4), 1144–1154.
61. Dockendorff, J.; Gauthier, M.; Mourran, A.; Möller, M., Arborescent amphiphilic copolymers as templates for the preparation of gold nanoparticles. *Macromolecules* **2008**, *41* (18), 6621–6623.
62. Moffitt, M.; Khougaz, K.; Eisenberg, A., Micellization of ionic block copolymers. *Acc. Chem. Res.* **1996**, *29* (2), 95–102.
63. Rudin, A. *The elements of polymer science and engineering: An introductory text and reference for engineers and chemists*, 2nd ed.; Academic press: San Diego, **1999**.
64. Kniewskea, R.; Kulicke, W-M., Study on the molecular weight dependence of dilute solution properties of narrowly distributed polystyrene in toluene and in the unperturbed state. *Makromol. Chem.* **1983**, *184*, 2173–2186.
65. Braun, J. L.; Kadla, J. F., A relatively simple method for calculating Mark-Houwink parameters using basic definitions. J. *Appl. Polym*. Sci. **2009**, *114(5)*, 3303–3309.

Chapter 5

1. Rahme, K.; Nolan, M. T.; Doody, T.; McGlacken, G. P.; Morris, M. A.; O'Driscoll, C.; Holmes, J. D., Highly stable PEGylated gold nanoparticles in water: Applications in biology and catalysis. *RSC Adv*. **2013**, *3* (43), 21016–21024.
2. Zhao, P.; Li, N.; Astruc, D., State of the art in gold nanoparticle synthesis. *Coord. Chem. Rev.* **2013**, *257* (3–4), 638–665.
3. Thakkar, K. N.; Mhatre, S. S.; Parikh, R. Y., Biological synthesis of metallic nanoparticles. *Nanomed. Nanotechnol. Biol. Med.* **2010**, *6* (2), 257–262.
4. Kraynov, A.; Müller, E. T., Concepts for the stabilization of metal nanoparticles in ionic liquids: *In applications of ionic liquids in science and technology*; Handy, S., Ed.; IntechOpen, **2011**, pp 235–260.
5. Daniel, M.-C.; Astruc, D., Gold nanoparticles: Assembly, supramolecular chemistry, quantum-size-related properties, and applications toward biology, catalysis, and nanotechnology. *Chem. Rev*. **2004**, *104* (1), 293–346.
6. Xu, Y.; Chen, L.; Wang, X.; Yao, W.; Zhang, Q., Recent advances in noble metal based composite nanocatalysts: Colloidal synthesis, properties, and catalytic applications. *Nanoscale* **2015**, *7* (24), 10559–10583.
7. Sun, G.; Fang, H.; Cheng, C.; Lu, P.; Zhang, K.; Walker, A. V.; Taylor, J. S.; Wooley, K. L., Benzaldehyde-functionalized polymer vesicles. *ACS Nano* **2009**, *3* (3), 673–681.
8. Walker, C. H.; St. John, J. V.; Wisian-Neilson, P., Synthesis and size control of gold nanoparticles stabilized by poly(methylphenylphosphazene). *J. Am. Chem. Soc.* **2001**, *123* (16), 3846–3847.

9. Mössmer, S.; Spatz, J. P.; Möller, M.; Aberle, T.; Schmidt, J.; Burchard, W., Solution behavior of poly(styrene)-*block*-poly(2-vinylpyridine) micelles containing gold nanoparticles. *Macromolecules* 2000, 33 (13), 4791–4798.
10. Youk, J. H.; Park, M.-K.; Locklin, J.; Advincula, R.; Yang, J.; Mays, J., Preparation of aggregation stable gold nanoparticles using star-block copolymers. *Langmuir* **2002**, *18* (7), 2455–2458.
11. Chechik, V.; Zhao, M.; Crooks, R. M., Self-assembled inverted micellesprepared from a dendrimer template: Phase transfer of encapsulated guests. *J. Am. Chem. Soc*. **1999**, *121* (20), 4910–4911.
12. Lowe, A. B.; Sumerlin, B. S.; Donovan, M. S.; McCormick, C. L., Facile preparation of transition metal nanoparticles stabilized by well-defined (co)polymers synthesized via aqueous reversible addition-fragmentation chain transfer polymerization. *J. Am. Chem. Soc*. **2002**, *124* (39), 11562–11563.
13. Gaucher, G.; Dufresne, M.-H.; Sant, V. P.; Kang, N.; Maysinger, D.; Leroux, J.-C., Block copolymer micelles: Preparation, characterization and application in drug delivery. *J. Controlled Release* **2005**, 109 (1–3), 169–188.
14. Sanson, N.; Bouyer, F.; Destarac, M.; In, M.; Gérardin, C., Hybrid polyion complex micelles formed from double hydrophilic block copolymers and multivalent metal ions: Size control and nanostructure. *Langmuir* **2012**, *28* (8), 3773–3782.
15. Filali, M.; Meier, M. A. R.; Schubert, U. S.; Gohy, J.-F., Star-block copolymers as templates for the preparation of stable gold nanoparticles. *Langmuir* **2005**, *21* (17), 7995–8000.
16. Leong, W. L.; Lee, P. S.; Lohani, A.; Lam, Y. M.; Chen, T.; Zhang, S.; Dodabalapur, A.; G. Mhaisalkar, S., Non-volatile organic memory applications enabled by in situ synthesis of gold nanoparticles in a self-assembled block copolymer. *Adv. Mater*. **2008**, *20* (12), 2325–2331.
17. Mai, Y.; Eisenberg, A., Controlled incorporation of particles into the central portion of block copolymer rods and micelles. *Macromolecules* **2011**, *44* (8), 3179–3183.
18. Choi, I.; Gunawidjaja, R.; Suntivich, R.; Tsitsilianis, C.; Tsukruk, V. V., Surface behavior of PS_n(P2VP-*b*-PtBA)$_n$ heteroarm stars. *Macromolecules* **2010**, *43* (16), 6818–6828.
19. Huang, X.; Xiao, Y.; Zhang, W.; Lang, M., In situ formation of silver nanoparticles stabilized by amphiphilic star-shaped copolymer and their catalytic application. *Appl. Surface Sci.* **2012**, *258* (7), 2655–2660.
20. Abraham, S.; Ha, C.-S.; Batt, C. A.; Kim, I., Synthesis of stable "gold nanoparticle–polymeric micelle" conjugates: A new class of star "molecular chimera" that self-assemble into linear arrays of spherical micelles. *J. Polym. Sci., Part A: Polym. Chem.*. **2007**, *45* (16), 3570–3579.
21. Chow, H.-F.; Mong, T. K. K.; Nongrum, M. F.; Wan, C.-W., The synthesis and properties of novel functional dendritic molecules. *Tetrahedron* **1998**, *54* (30), 8543–8660.
22. Scott, R. W. J.; Wilson, O. M.; Crooks, R. M., Synthesis, characterization, and applications of dendrimer-encapsulated nanoparticles. *J. Phys. Chem. B* **2005**, *109* (2), 692–704.
23. Esumi, K.; Suzuki, A.; Yamahira, A.; Torigoe, K., Role of poly(amidoamine) dendrimers for preparing nanoparticles of gold, platinum, and silver. *Langmuir* **2000**, *16* (6), 2604–2608.
24. Crooks, R. M.; Zhao, M., Dendrimer-encapsulated Pt nanoparticles: Synthesis, characterization, and applications to catalysis. *Adv. Mater*. **1999**, *11* (3), 217–220.

25. Yu, T.; Wang, W.; Chen, J.; Zeng, Y.; Li, Y.; Yang, G.; Li, Y., Dendrimer-encapsulated Pt nanoparticles: An artificial enzyme for hydrogen production. *J. Phys. Chem. C* **2012**, *116* (19), 10516–10521.
26. Crooks, R. M.; Zhao, M.; Sun, L.; Chechik, V.; Yeung, L. K., Dendrimer-encapsulated metal nanoparticles: Synthesis, characterization, and applications to catalysis. *Acc. Chem. Res*. **2001**, *34* (3), 181–190.
27. Huang, W.; Kuhn, J. N.; Tsung, C.-K.; Zhang, Y.; Habas, S. E.; Yang, P.; Somorjai, G. A., Dendrimer templated synthesis of one nanometer Rh and Pt particles supported on mesoporous silica: Catalytic activity for ethylene and pyrrole hydrogenation. *Nano Lett.* **2008**, *8* (7), 2027–2034.
28. Garcia, M. E.; Baker, L. A.; Crooks, R. M., Preparation and characterization of dendrimer−gold colloid nanocomposites. *Anal. Chem.* **1999**, *71* (1), 256–258.
29. Zhai, S.; Hong, H.; Zhou, Y.; Yan, D., Synthesis of cationic hyperbranched multiarm copolymer and its application in self-reducing and stabilizing gold nanoparticles. *Sci. China Chem.* **2010**, 53 (5), 1114–1121.
30. Pérignon, N.; Marty, J.-D.; Mingotaud, A.-F.; Dumont, M.; Rico-Lattes, I.; Mingotaud, C., Hyperbranched polymers analogous to PAMAM dendrimers for the formation and stabilization of gold nanoparticles. *Macromolecules* **2007**, *40* (9), 3034–3041.
31. Lang, H.; May, R. A.; Iversen, B. L.; Chandler, B. D., Dendrimer-encapsulated nanoparticle precursors to supported platinum catalysts. *J. Am. Chem. Soc*. **2003**, *125* (48), 14832–14836.
32. Graff, R. W.; Wang, X.; Gao, H., Exploring self-condensing vinyl polymerization of inimers in microemulsion to regulate the structures of hyperbranched polymers. *Macromolecules* **2015**, *48* (7), 2118–2126.
33. Kee, R. A.; Gauthier, M., Arborescent polystyrene-*graft*-poly(2-vinylpyridine) copolymers: Synthesis and enhanced polyelectrolyte effect in solution. *Macromolecules* **2002**, *35* (17), 6526–6532.
34. Gauthier, M.; Li, J.; Dockendorff, J., Arborescent polystyrene-*graft*-poly(2-vinylpyridine) copolymers as unimolecular micelles. Synthesis from acetylated substrates. *Macromolecules* **2003**, *36* (8), 2642–2648.
35. Nguon, O.; Gauthier, M.; Karanassios, V., Determination of the loading and stability of Pd in an arborescent copolymer in ethanol by microplasma-optical emission spectrometry. *RSC Adv.* 2014, 4 (18), 8978.
36. Dockendorff, J.; Gauthier, M., Synthesis of arborescent polystyrene-*g*-[poly(2-vinylpyridine)-*b*-polystyrene] core–shell–corona copolymers. *J. Polym. Sci., Part A: Polym. Chem.* **2014**, *52* (8), 1075–1085.
37. Dockendorff, J.; Gauthier, M.; Mourran, A.; Möller, M., Arborescent amphiphilic copolymers as templates for the preparation of gold nanoparticles. *Macromolecules* **2008**, *41* (18), 6621–6623.
38. Dockendorff, J. M. Arborescent copolymers: Synthesis, properties & metallic nanoparticle templating. Ph.D. Thesis, University of Waterloo, Waterloo, ON, **2011**.
39. Nguyen, V. T. A.; De Pauw-Gillet, M.-C.; Sandre, O.; Gauthier, M., Biocompatible polyion complex micelles synthesized from arborescent polymers. *Langmuir* **2016**, *32* (50), 13482–13492.

40. Nguyen, V. T. A. Magnetic Polyion complex micelles as therapy and diagnostic agents. Ph.D. Thesis, University of Waterloo, Waterloo, ON, **2015**.
41. Abraham, S.; Ha, C.-S.; Batt, C. A.; Kim, I., Synthesis of stable "gold nanoparticle-polymeric micelle" conjugates: A new class of star "molecular chimera" that self-assemble into linear arrays of spherical micelles. *J. Polym. Sci., Part A: Polym. Chem.* **2007**, *45* (16), 3570–3579.
42. Antonietti, M.; Wenz, E.; Bronstein, L.; Seregina, M., Synthesis and characterization of noble metal colloids in block copolymer micelles. *Adv. Mater.* **1995**, *7* (12), 1000–1005.
43. Spatz, J. P.; Mössmer, S.; Hartmann, C.; Möller, M.; Herzog, T.; Krieger, M.; Boyen, H.-G.; Ziemann, P.; Kabius, B., Ordered deposition of inorganic clusters from micellar block copolymer films. *Langmuir* **2000**, *16* (2), 407–415.
44. Zhao, X.; Wang, Q.; Zhang, X.; Lee, Y.-I.; Liu, H.-G., Influence of gold species ($AuCl_4^-$ and $AuCl_2^-$) on self-assembly of PS-*b*-P2VP in solutions and morphology of composite thin films fabricated at the air/liquid interfaces. *Phys. Chem. Chem. Phys.* **2016**, *18* (3), 1945–1952.
45. Cho, Y.-H.; Yang, J.-E.; Lee, J.-S., Size control of polymeric nanoparticles from polystyrene-*b*-poly(2-vinylpyridine). *Mater. Sci. Eng., C* **2004**, *24* (1–2), 293–295.
46. Spatz, J. P.; Sheiko, S.; Möller, M., Ion-stabilized block copolymer micelles: Film formation and intermicellar interaction. *Macromolecules* **1996**, *29* (9), 3220–3226.
47. Mei, S.; Feng, X.; Jin, Z., Fabrication of polymer nanospheres based on Rayleigh instability in capillary channels. *Macromolecules* **2011**, *44* (6), 1615–1620.
48. Shefelbine, T. A.; Vigild, M. E.; Matsen, M. W.; Hajduk, D. A.; Hillmyer, M. A.; Cussler, E. L.; Bates, F. S., Core–shell gyroid morphology in a poly(isoprene-*block*-styrene-*block*-dimethylsiloxane) triblock copolymer. *J. Am. Chem. Soc.* **1999**, *121* (37), 8457–8465.
49. Lee, B.; Lo, C.-T.; Seifert, S.; Dietz Rago, N. L.; Winans, R. E.; Thiyagarajan, P., Anomalous small-angle X-ray scattering characterization of bulk block copolymer/nanoparticle composites. *Macromolecules* **2007**, *40* (12), 4235–4243.
50. Tong, Z.-Z.; Wang, R.-Y.; Huang, J.; Xu, J.-T.; Fan, Z.-Q., Regulation of the self-assembly morphology of azobenzene-bearing double hydrophobic block copolymers in aqueous solution by shifting the dynamic host–guest complexation. *Polym. Chem.* **2015**, *6* (12), 2214–2225.
51. Podgornik, R.; Ličer, M., Polyelectrolyte bridging interactions between charged macromolecules. *Curr. Opin. Colloid Interface Sci.* **2006**, *11* (5), 273–279.
52. Jambon, F.; Marchetti, L.; Sennour, M.; Jomard, F.; Chêne, J., SIMS and TEM investigation of hydrogen trapping on implantation defects in a nickel-based superalloy. *J. Nucl. Mater.* **2015**, *466*, 120–133.
53. Ulrich, S.; Seijo, M.; Stoll, S., The many facets of polyelectrolytes and oppositely charged macroions complex formation. *Curr. Opin. Colloid Interface Sci.* **2006**, *11* (5), 268–272.
54. Yagai, S.; Mahesh, S.; Kikkawa, Y.; Unoike, K.; Karatsu, T.; Kitamura, A.; Ajayaghosh, A., Toroidal nanoobjects from rosette assemblies of melamine-linked oligo(*p*-phenyleneethynylene)s and cyanurates. *Angew. Chem. Int. Ed.* **2008**, *47* (25), 4691–4694.
55. Takagi, K.; Kato, R.; Yamamoto, S.-y.; Masu, H., Amide-bridged ladder poly(*p*-phenylene): Synthesis by direct arylation and π-stacked assembly. *Polym. Chem*. **2015**, *6*, 6792–6795

56. Bortolotto, T.; Facchinetto, S. E.; Trindade, S. G.; Ossig, A.; Petzhold, C. L.; Vargas, J.; Rodrigues, O. E. D.; Giacomelli, C.; Schmidt, V., Polymer-coated palladium nanoparticle catalysts for Suzuki coupling reactions. *J. Colloid Interface Sci*. **2015**, *439*, 154–161.
57. Pathak, S.; Greci, M. T.; Kwong, R. C.; Mercado, K.; Surya Prakash, G.-K.; Olah, G.-A.; Thompson, M. E., Synthesis and applications of palladium-coated poly(vinylpyridine) nanospheres. *Chem. Mater.* **2000**, *12*, 1985–1989.
58. Jiang, X.; Wei, G.; Zhang, X.; Zhang, W.; Zheng, P.; Wen, F.; Shi, L., A strategy to facilitate reuse of palladium catalyst stabilized by block copolymer micelles. *J. Mol. Catal.* A, **2007**, *277*, 102–106.
59. Dockendorff, J.; Mourran, A.; Gumerov, R. A.; Potemkin, I. I.; Möller, M.; Gauthier, M., Metal-coordination induces phase segregation in amphipolar arborescent copolymers with a core–shell–corona architecture. *Accepted for publication in Macromolecules*.

Chapter 6

1. Xu, Y.; Chen, L.; Wang, X.; Yao, W.; Zhang, Q., Recent advances in noble metal based composite nanocatalysts: Colloidal synthesis, properties, and catalytic applications. *Nanoscale* **2015**, *7* (24), 10559–10583.
2. Daniel, M. C.; Astruc, D., Gold nanoparticles: Assembly, supramolecular chemistry, quantum-size-related properties, and applications toward biology, catalysis, and nanotechnology. *Chem. Rev.* **2004**, *104* (1), 293–346.
3. Zhang, Z.; Nguyen, H. T. H.; Miller, S. A.; Ploskonka, A. M.; DeCoste, J. B.; Cohen, S. M., Polymer–metal–organic frameworks (polyMOFs) as water tolerant materials for selective carbon dioxide separations. *J. Am. Chem. Soc*. **2015**, *183*, 920–925.
4. Mirabello, V.; Calatayud, D. G.; Arrowsmith, R. L.; Ge, H.; Pascu, S. I., Metallic nanoparticles as synthetic building blocks for cancer diagnostics: From materials design to molecular imaging applications. *J. Mater. Chem.* B **2015**, 3 (28), 5657–5672.
5. Jain, P. K.; Huang, X.; El-Sayed, I. H.; El-Sayed, M. A., Noble metals on the nanoscale: Optical and photothermal properties and some applications in imaging, sensing, biology, and medicine. *Acc. Chem. Res.* **2008**, *41* (12), 1578–1586;
6. Estrada, L. C.; Roberti, M. J.; Simoncelli, S.; Levi, V.; Aramendía, P. F.; Martínez, O. E., Detection of low quantum yield fluorophores and improved imaging times using metallic nanoparticles. *J. Phys. Chem. B* **2012**, *116* (7), 2306–2313.
7. Yang, X.; Tang, Y.; Mason, S. D.; Chen, J.; Li, F., Enzyme-powered three-dimensional DNA nanomachine for DNA walking, payload release, and biosensing. *ACS Nano* **2016**, *10* (2), 2324–2330.
8. McGrath, A. J.; Chien, Y.-H.; Cheong, S.; Herman, D. A. J.; Watt, J.; Henning, A. M.; Gloag, L.; Yeh, C.-S.; Tilley, R. D., Gold over branched palladium nanostructures for photothermal cancer therapy. *ACS Nano* **2015**, *9* (12),12283–12291.
9. Jaque, D.; Martinez Maestro, L.; del Rosal, B.; Haro-Gonzalez, P.; Benayas, A.; Plaza, J. L.; Martin Rodriguez, E.; Garcia Sole, J., Nanoparticles for photothermal therapies. *Nanoscale* **2014**, *6* (16), 9494–9530.

10. Urban, A. S.; Carretero-Palacios, S.; Lutich, A. A.; Lohmuller, T.; Feldmann, J.; Jackel, F., Optical trapping and manipulation of plasmonic nanoparticles: Fundamentals, applications, and perspectives. *Nanoscale* **2014**, *6* (9), 4458–4474.
11. Brown, S. D.; Nativo, P.; Smith, J.-A.; Stirling, D.; Edwards, P. R.; Venugopal, B.; Flint, D. J.; Plumb, J. A.; Graham, D.; Wheate, N. J., Gold nanoparticles for the improved anticancer drug delivery of the active component of oxaliplatin. *J. Am. Chem. Soc.* **2010**, *132* (13), 4678–4684.
12. Yancey, D. F.; Carino, E. V.; Crooks, R. M., Electrochemical synthesis and electrocatalytic properties of Au@Pt dendrimer-encapsulated nanoparticles. *J. Am. Chem. Soc.* **2010**, *132* (32), 10988–10989.
13. Youk, J. H.; Park, M.-K.; Locklin, J.; Advincula, R.; Yang, J.; Mays, J., Preparation of aggregation stable gold nanoparticles using star–block copolymers. *Langmuir* **2002**, *18* (7), 2455–2458;
14. Lam, E.; Hrapovic, S.; Majid, E.; Chong, J. H.; and Luong. J. H. T., Catalysis using gold nanoparticles decorated on nanocrystalline cellulose. *Nanoscale*, **2012**, 4, 997–1002.
15. Crooks, R. M.; Zhao, M., Dendrimer-encapsulated Pt nanoparticles: Synthesis, characterization, and applications to catalysis. *Adv. Mater.* **1999**, *11* (3), 217–220.
16. Weires, N. A.; Baker, E. L.; Garg, N. K., Nickel-catalysed Suzuki–Miyaura coupling of amides. *Nat. Chem.* **2015**, *8*, 75–79.
17. Tada, M.; Bal, R.; Namba, S.; Iwasawa, Y., Surfactant-promoted novel synthesis of supported metallic Cu nanoparticles active for selective dehydrogenation of methanol. *Appl. Catal., A* **2006**, *307* (1), 78–84.
18. Crooks, R. M.; Zhao, M.; Sun, L.; Chechik, V.; Yeung, L. K., Dendrimer-encapsulated metal nanoparticles: Synthesis, characterization, and applications to catalysis. *Acc. Chem. Res.* **2001**, *34* (3), 181–190.
19. Haruta, M., Catalysis of gold nanoparticles deposited on metal oxides. *CATTECH **2002***, 6 (3), 102–115.
20. Zhang, R.; Lyu, G.; Chen, C.; Lin, T.; Liu, J.; Liu, P. N.; Lin, N., Two-dimensional superlattices of Bi nanoclusters formed on a Au(111) surface using porous supramolecular templates. *ACS Nano* **2015**, *9* (8) 8547–8553.
21. Zhang, L.; Xie, Z.; Gong, J., Shape-controlled synthesis of Au-Pd bimetallic nanocrystals for catalytic applications. *Chem. Soc. Rev*. **2016**, *45* (14), 3916–3934.
22. Rahme, K.; Nolan, M. T.; Doody, T.; McGlacken, G. P.; Morris, M. A.; O'Driscoll, C.; Holmes, J. D., Highly stable PEGylated gold nanoparticles in water: Applications in biology and catalysis. *RSC Adv*. **2013**, *3* (43), 21016–21024.
23. Knight, D. A.; Nita, R.; Moore, M.; Zabetakis, D.; Khandelwal, M.; Martin, B. D.; Fontana, J.; Goldberg, E.; Funk, A. R.; Chang, E. L.; Trammell, S. A., Surface plasmon resonance promotion of homogeneous catalysis using a gold nanoparticle platform. *J. Nanopart. Res*. **2014**, *16* (6), 2400.
24. Murugan, E.; Rangasamy, R., Synthesis, characterization, and heterogeneous catalysis of polymer-supported poly(propyleneimine) dendrimer stabilized gold nanoparticle catalyst. J. *J. Polym. Sci., Part A: Polym. Chem.* **2010**, *48* (12), 2525–2532.
25. Marcelo, G.; López-González, M.; Mendicuti, F.; Tarazona, M. P.; Valiente, M., Poly(N-isopropylacrylamide)/gold hybrid hydrogels prepared by catechol redox chemistry. Characterization and smart tunable catalytic activity. *Macromolecules* **2014**, *47* (17), 6028–6036.

26. Li, Y.; Fan, X.; Qi, J.; Ji, J.; Wang, S.; Zhang, G.; Zhang, F., Gold nanoparticles–graphene hybrids as active catalysts for Suzuki reaction. *Mater. Res. Bull.* **2010**, *45* (10), 1413-1418.
27. Wang, X.; Cai, X.; Hu, J.; Shao, N.; Wang, F.; Zhang, Q.; Xiao, J.; Cheng, Y., Glutathione-triggered "off–on" release of anticancer drugs from dendrimer-encapsulated gold nanoparticles. *J. Am. Chem. Soc*. **2013**, *135* (26), 9805–9810.
28. Zhan, Z.; Xu, R.; Mi, Y.; Zhao, H.; Lei, Y., Highly controllable surface plasmon resonance property by heights of ordered nanoparticle arrays fabricated via a nonlithographic route. *ACS Nano* **2015**, *9* (4), 4583-4590.
29. Yu; Chang, S.-S.; Lee, C.-L.; Wang, C. R. C., Gold Nanorods: Electrochemical synthesis and optical properties. *J. Phys. Chem. B* **1997**, *101* (34), 6661–6664.
30. Wilcoxon, J. P.; Williamson, R. L.; Baughman, R., Optical properties of gold colloids formed in inverse micelles. *J. Chem. Phys*. **1993**, *98* (12), 9933–9950.
31. Wang, J.; Chen, S.; Cui, K.; Li, D.; Chen, D., Approach and coalescence of gold nanoparticles driven by surface thermodynamic fluctuations and atomic interaction forces. *ACS Nano* **2016**, *10* (2), 2893–2902.
32. Caldera Villalobos, M.; Martins Alho, M.; García Serrano, J.; Álvarez Romero, G. A.; Herrera González, A. M., Colloidal synthesis of Au nanoparticles using polyelectrolytes with 1,3,4-thiadiazole as reducing agents. *J. Appl. Polym. Sci*. **2019**, 136, 47790.
33. Stavens, K. B.; Pusztay, S. V.; Zou, S.; Andres, R. P.; Wei, A., Encapsulation of neutral gold nanoclusters by resorcinarenes. *Langmuir* **1999**, *15* (24), 8337–8339.
34. Chung, Y.-H.; Ha, M. G.; Na, Y.; Park, H.-Y.; Kim, H.-J.; Henkensmeier, D.; Yoo, S. J.; Kim, J. Y.; Lee, S. Y.; Lee, S. W.; Park, H. S.; Kim, Y.-T.; Jang, J. H., Polyethylenimine-assisted synthesis of Au nanoparticles for efficient syngas production. *Electroanalysis* **2019**, *31*, 1401–1408.
35. Sathiyanarayanan, G.; Vignesh, V.; Saibaba, G.; Vinothkanna, A.; Dineshkumar, K.; Viswanathan, M. B.; Selvin, J., Synthesis of carbohydrate polymer encrusted gold nanoparticles using bacterial exopolysaccharide: A novel and greener approach. *RSC Adv.* **2014**, *4* (43), 22817–22827.
36. Zhao, P.; Li, N.; Astruc, D., State of the art in gold nanoparticle synthesis. *Coord. Chem. Rev.* **2013**, *257* (3–4), 638–665.
37. Sayo, K.; Deki, S.; Hayashi, S., A novel method of preparing nano-sized gold and palladium particles dispersed in composites that uses the thermal relaxation technique. *Eur. Phys. J. D* **1999**, *9* (1), 429–432.
38. Johnson, S. R.; Evans, S. D.; Brydson, R., Influence of a terminal functionality on the physical properties of surfactant-stabilized gold nanoparticles. *Langmuir* **1998**, *14* (23), 6639–6647.
39. Selvan, T.; Spatz, J. P.; Klok, H.-A.; Möller, M., Gold–polypyrrole core–shell particles in diblock copolymer micelles. *Adv. Mater*. **1998**, *10* (2), 132–134.
40. Khullar, P.; Singh, V.; Mahal, A.; Kumar, H.; Kaur, G.; Bakshi, M. S., Block copolymer micelles as nanoreactors for self-assembled morphologies of gold nanoparticles. *J. Phys. Chem. B* **2013**, *117* (10), 3028–3039.
41. Filali, M.; Meier, M. A. R.; Schubert, U. S.; Gohy, J.-F., Star-block copolymers as templates for the preparation of stable gold nanoparticles. *Langmuir* **2005**, *21* (17), 7995–8000.

42. Lawrence, M.; Testen, A.; Koklic, T.; Smithies, O., A simple method for the size controlled synthesis of stable oligomeric clusters of gold nanoparticles under ambient conditions. *J. Visualized Exp*. **2016,** 108, 53388.
43. Dockendorff, J.; Gauthier, M.; Mourran, A.; Möller, M., Arborescent amphiphilic copolymers as templates for the preparation of gold nanoparticles. *Macromolecules* **2008**, *41* (18), 6621–6623.
44. Gauthier, M.; Li, J.; Dockendorff, J., Arborescent polystyrene-*graft*-poly(2-vinylpyridine) copolymers as unimolecular micelles. Synthesis from acetylated substrates. *Macromolecules* **2003**, *36* (8), 2642–2648.
45. Zhang, W.; Shi, L.; Gao, L.; An, Y.; Wu, K., Formation of core–shell–corona micellar complexes through adsorption of double hydrophilic diblock copolymers into core–shell micelles. *Macromol. Rapid Commun.* **2005**, *26* (16), 1341–1345.
46. Zhou, X.; Goh, S.; Lee, S.; Tan, K., XPS and FTIR studies of interactions in poly(carboxylic acid)/poly(vinylpyridine) complexes. *Polymer* **1998**, *39* (16), 3631–3640.
47. Li, Q.; Lu, B.; Zhang, L.; Lu, C., Synthesis and stability evaluation of size-controlled gold nanoparticles via nonionic fluorosurfactant-assisted hydrogen peroxide reduction. *J. Mater. Chem.* **2012**, *22* (27), 13564–13570.
48. Alsawafta, M.; Badilescu, S.; Vo-Van, T.; Packirisamy, M., The effect of hydrogen nanobubbles on the morphology of gold–gelatin bionanocomposite films and their optical properties. *Nanotechnology* **2012**, *23* (6), 065305.
49. Smithies, O.; Lawrence, M.; Testen, A.; Horne, L.-P.; Wilder, J.; Altenburg, M.; Bleasdale, B.; Maeda, N.; Koklic, T., Stable oligomeric clusters of gold nanoparticles: preparation, size distribution, derivatization, and physical and biological properties. *Langmuir* **2014**, *30* (44), 13394–13404.
50. Antonietti, M.; Wenz, E.; Bronstein, L.; Seregina, M., Synthesis and characterization of noble metal colloids in block copolymer micelles. *Adv. Mater*. **1995**, *7* (12), 1000–1005.
51. Hostetler, M. J.; Wingate, J. E.; Zhong, C.-J.; Harris, J. E.; Vachet, R. W.; Clark, M. R.; Londono, J. D.; Green, S. J.; Stokes, J. J.; Wignall, G. D.; Glish, G. L.; Porter, M. D.; Evans, N. D.; Murray, R. W., Alkanethiolate gold cluster molecules with core diameters from 1.5 to 5.2 nm: Core and monolayer properties as a function of core size. *Langmuir* **1998**, *14* (1), 17–30.
52. Esumi, K.; Suzuki, A.; Yamahira, A.; Torigoe, K., Role of poly(amidoamine) dendrimers for preparing nanoparticles of gold, platinum, and silver. *Langmuir* **2000**, *16* (6), 2604–2608.
53. Goldmann, C.; Lazzari, R.; Paquez, X.; Boissière, C.; Ribot, F.; Sanchez, C.; Chanéac, C.; Portehault, D., Charge transfer at hybrid interfaces: Plasmonics of aromatic thiol-capped gold nanoparticles. *ACS Nano* **2015**, *9* (7), 7572–7582.
54. Pons, T.; Medintz, I.-L.; Sapsford, K.-E.; Higashiya, S.; Grimes, A.-F.; English, D.-S Mattoussi, H., On the quenching of semiconductor quantum dot photoluminescence by proximal gold nanoparticles. *Nano Lett*. **2007**, *7* (10), 3157–3164.
55. Tiwari, A. K.; Gangopadhyay, S.; Chang, C.-H.; Pande, S.; Saha, S. K., Study on metal nanoparticles synthesis and orientation of gemini surfactant molecules used as stabilizer. *J. Colloid Interface Sci*. **2015**, *445*, 76–83.

56. Abraham, S.; Ha, C.-S.; Batt, C. A.; Kim, I., Synthesis of stable "gold nanoparticle-polymeric micelle" conjugates: A new class of star "molecular chimera" that self-assemble into linear arrays of spherical micelles. *J. Polym. Sci., Part A: Polym. Chem.* **2007**, *45* (16), 3570–3579.
57. Huang, X.; El-Sayed, M. A., Gold nanoparticles: Optical properties and implementations in cancer diagnosis and photothermal therapy. *J. Adv. Res.* **2010**, *1* (1), 13–28.
58. Roescher, G. A.; Möller, M., Extraction of aqueous gold sols with styrene/2-vinylpyridine block copolymers in toluene. *Adv. Mater*. **1995**, *7* (2), 151–154.
59. Wong, K. H.; Davis, T. P.; Barner-Kowollik, C.; Stenzel, M. H., Gold-loaded organic/inorganic nanocomposite honeycomb membranes. *Aust. J. Chem.* **2006**, *59* (8), 539–543.

Chapter 7

1. Gauthier, M.; Munam, A., Arborescent polystyrene-*graft*-poly(2-vinylpyridine) copolymers: Solution polyelectrolyte behavior. *RSC Adv*. **2012**, *2* (7), 3100–3108.
2. Dockendorff, J. M., Arborescent copolymers: Synthesis, properties & metallic nanoparticle templating. Ph.D. Thesis, University of Waterloo, **2011**.
3. Lin, L. B.; Yu, Q. Y.; Gu, Z. Q.; Jiang, X. Z.; Zhu, M. F., Reduction-degradable shell cross-linked micelle with pH-responsive cores prepared via click chemistry. *Mater. Sci. Forum* **2016**, *848*, 527–531.
4. O'Reilly, R. K.; Joralemon, M. J.; Wooley, K. L.; Hawker, C. J., Functionalization of micelles and shell cross-linked nanoparticles using click chemistry. *Chem. Mater*. **2005**, *17* (24), 5976–5988.
5. Jiang, J.; Qi, B.; Lepage, M.; Zhao, Y., Polymer micelles stabilization on demand through reversible photo-cross-linking. *Macromolecules* **2007**, *40* (4), 790–792.
6. Zhang, X.; Wang, Y.; Li, G.; Liu, Z.; Zhongwen, Liu, Z.; Jiang J., Amphiphilic imbalance and stabilization of block copolymer micelles on-demand through combinational photo-cleavage and photo-crosslinking. *Macromol. Rapid Commun*. **2017**, *38* (1600543), 1–7.
7. Orelma, H.; Vuoriluoto, M.; Johansson, L.-S.; Campbell, J. M.; Filpponen, I.; Biesalski, M.; Rojas, O. J., Preparation of photoreactive nanocellulosic materials via benzophenone grafting. *RSC Adv*. **2016**, *6* (88), 85100–85106.
8. Bond, G. C.; Thompson, D. T., Gold-catalyzed oxidation of carbon monoxide. *Gold Bull.* **2000**, *33*(2), 1–50.
9. Carabineiro, S. A. C., Supported gold nanoparticles as catalysts for the oxidation of alcohols and alkanes. *Front. Chem.* **2019**, *7* (702), 1–32.
10. Mayani, V. J.; Mayani, S. V.; Kim, S. W., Palladium, gold, and gold-palladium nanoparticle-supported carbon materials for cyclohexane oxidation. *Chem. Eng. Commun.* **2016**, *203* (4), 539–547.

Appendix A

Appendix A-1. Anionic grafting scheme for the synthesis of arborescent polystyrene

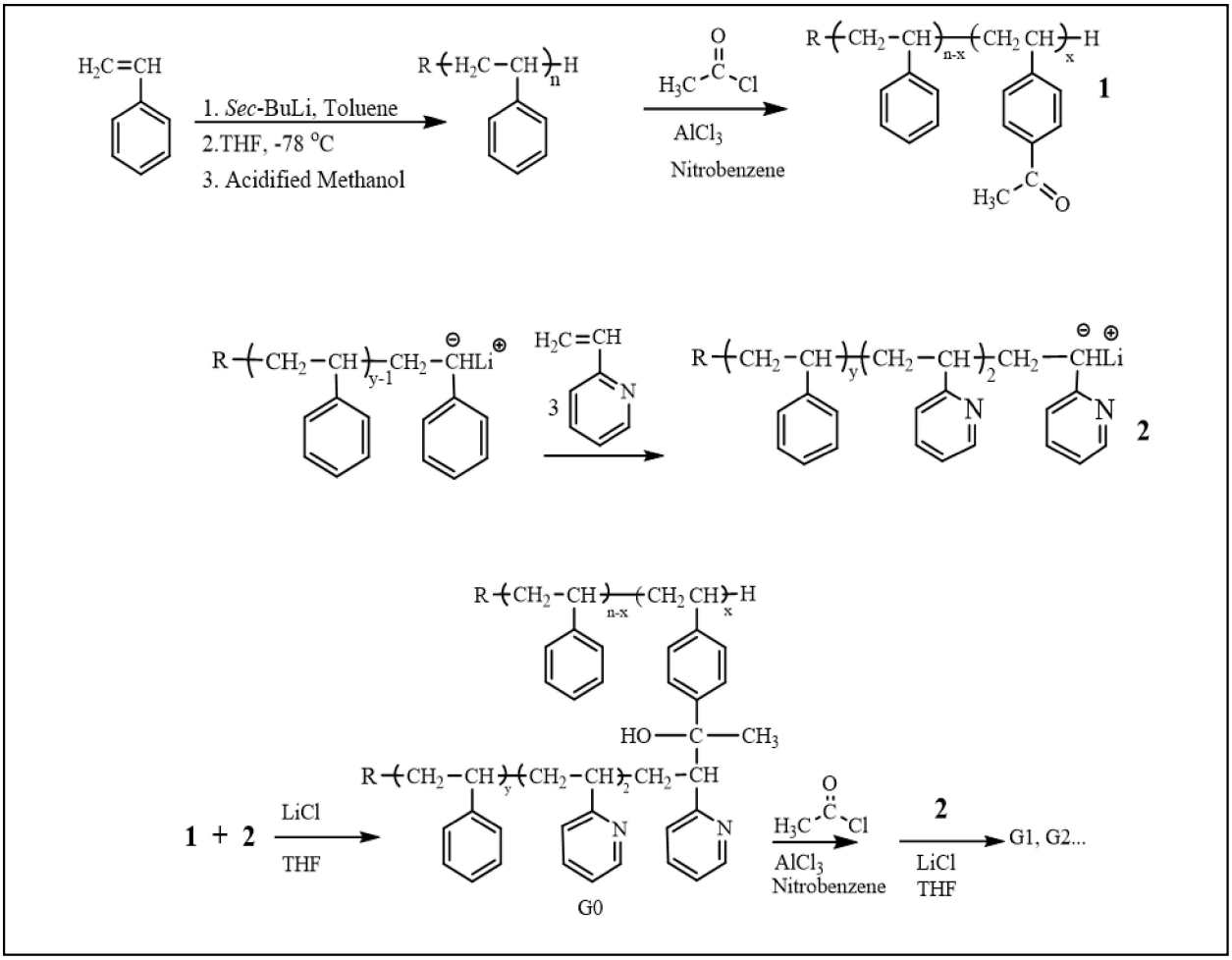

Appendix A-2. Determination of the acetylation level of polystyrene and the 2VP content in an arborescent copolymer by ^{1}H NMR analysis

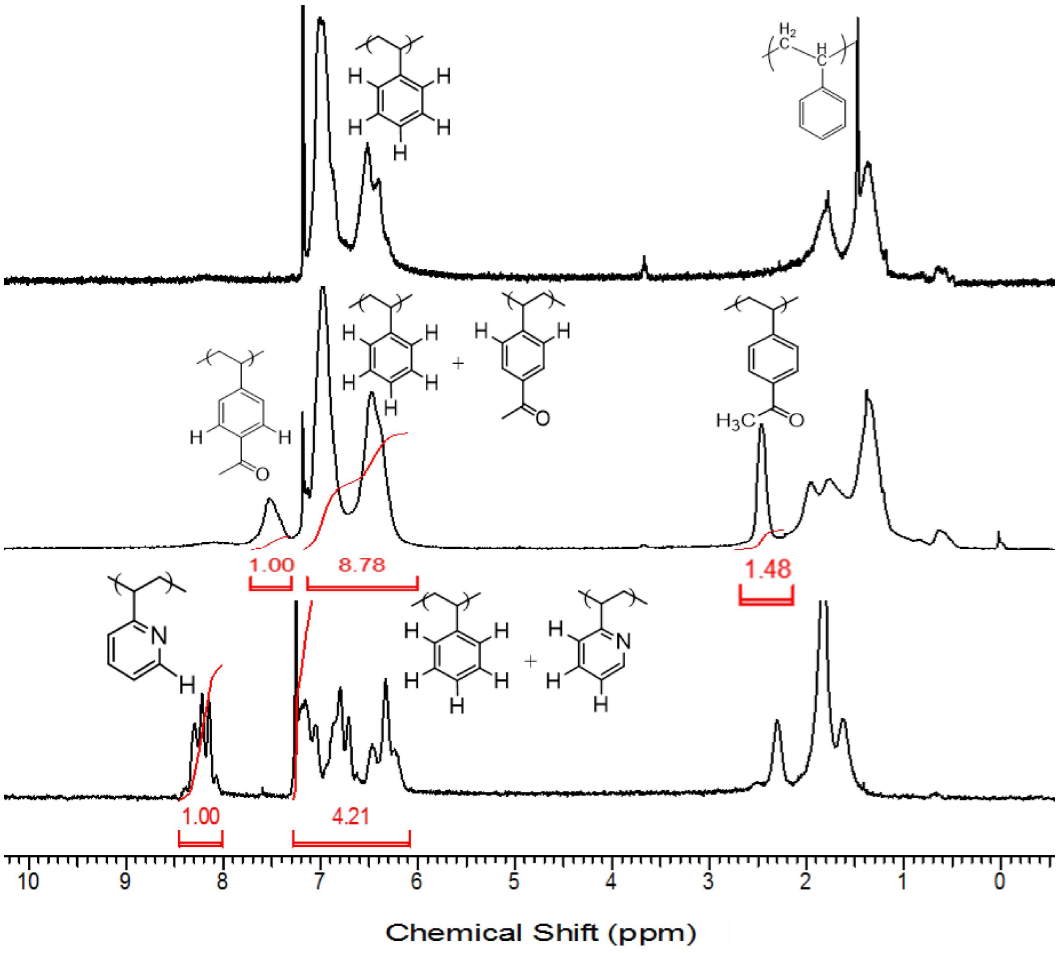

2 × Aromatic = 1.00 or 3 × Acetyl = 1.48 => Acetyl groups = 0.5
(2 × Aromatic) + (5 × Styrene) = 8.78 => Styrene = 1.56
Acetylation mol% = Acetyl/(Acetyl + Styrene)
Acetylation mol% = 0.5/(1.56 + 0.5) = 0.243
Acetylation level = 24.3 mol%

2VP = 1.00
(3 × 2VP) + (5 × Sty) = 4.21
Sty = 0.242
mol% 2VP = 2VP/(2VP + Sty) = 0.805 (80.5%)

Appendix A-3. Characterization of the arborescent substrates

The grafting yield (G_y) was determined by SEC analysis using the DRI detector, from the peak areas for the graft polymer and the side chains, as

$$G_y = 100 \times \text{graft polymer peak area} / (\text{graft polymer} + \text{side chains}) \text{ peak areas}$$

The coupling efficiency was calculated from $C_e = f_n / F_n$, where f_n is the measured number-average branching functionality of the product, and F_n is the number-average number of coupling sites available on the substrate.

The experimentally determined branching functionality $f_n = [M_n(G) - M_n(G\text{-}1)] / M_n(\text{side chains})$, where $M_n(G)$ is the number-average molecular weight of the graft polymer of generation G, and $M_n(G-1)$ is number-average molecular weight of the preceding generation.

The number of grafting sites of the substrate is $F_n = (M_n / M_{n(avg)})\ F$, where $M_{n(avg)}$ is the average molecular weight per structural units for the acetylated and unreacted styrene units, expressed as $M_{n(avg)} = F\ M_{fm} + (1\text{-}F)\ M_m$, where M_m and M_{fm} represent the molecular weight of a styrene unit and an acetylated styrene unit, respectively.

Appendix A-4. ^{13}C NMR spectra for a PtBA-*b*-PS copolymer

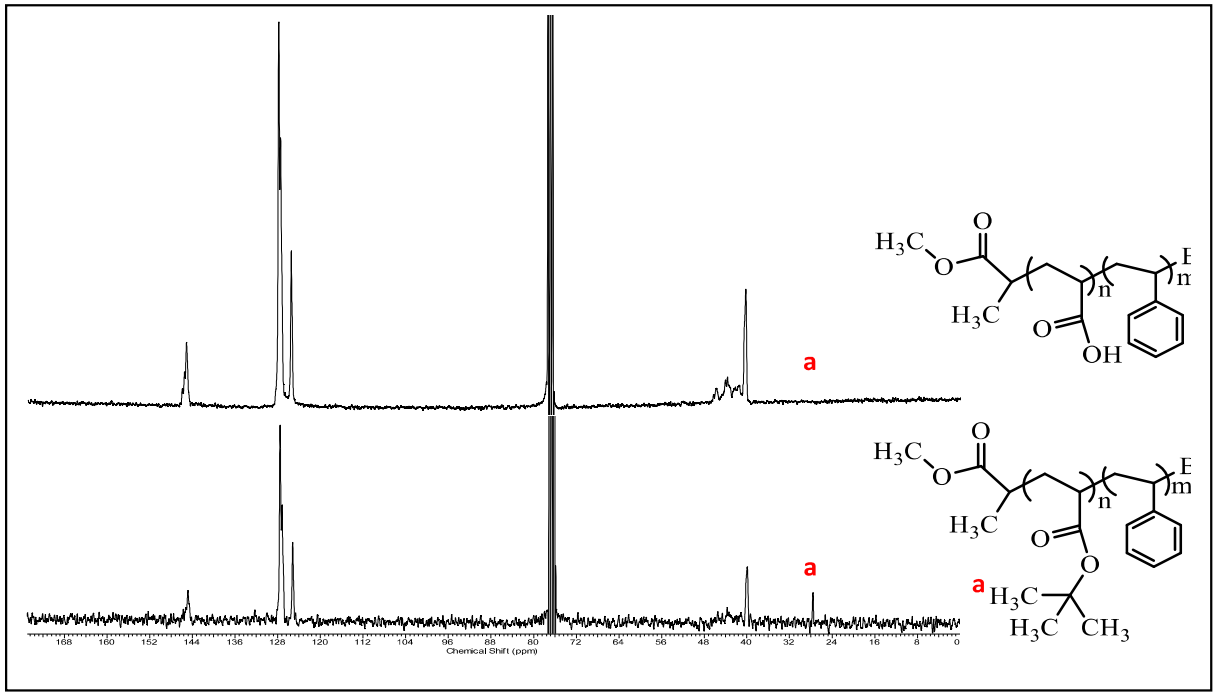

^{13}C NMR spectra for PAA-b-PS (top) and PtBA-b-PS (bottom) in chloroform-d, with X_n = 10 for the PtBA/PAA block and X_n = 85 for the PS block. It clearly confirms the complete hydrolysis of the tBA units at δ 27.7 ppm, indicated as (a).

Appendix B

Appendix B-1. Solution properties of PAA-b-PS

Table A4-1. Characterization of the BCP samples by NMR and SEC before deprotection.[a]

Sample	1H NMR	SEC	
	Mn (g/mol)	**Mn (g/mol)**	**PDI**
P*t*BA10-*b*-PS85	1.0×10^4	1.9×10^4	1.05
P*t*BA 10-*b*-PS205	2.3×10^4	2.9×10^4	1.13
P*t*BA 10-*b*-PS260	2.8×10^4	3.0×10^4	1.20
P*t*BA 10-*b*-PS305	3.3×10^4	3.5×10^4	1.14
P*t*BA 13-*b*-PS156	1.8×10^4	2.0×10^4	1.13
P*t*BA 13-*b*-PS330	3.5×10^4	2.8×10^4	1.26
P*t*BA 13-*b*-PS390	4.2×10^4	4.0×10^4	1.17
P*t*BA 17-*b*-PS195	2.3×10^4	2.7×10^4	1.24
P*t*BA 17-*b*-PS250	2.8×10^4	3.3×10^4	1.13
P*t*BA 17-*b*-PS395	4.3×10^4	5.8×10^4	1.08

a) The results reported here were obtained before deprotection because the PAA block interacted with the SEC column; the M_n values obtained by ^1H NMR analysis before deprotection are provided for comparison.

The (deprotected) PAA-*b*-PS copolymers yielded clear solutions in organic solvents such as THF, THF/ethanol (100/0-80/20 v/v) and toluene/ethanol (100/0-80/20 v/v) mixtures at concentrations of 10 mg/mL. While the characterization of these block copolymers by DLS was attempted, the hydrodynamic diameters obtained were deemed to be unreliable because a second size population was detected in the intensity-weighted size distributions in most cases.

As an example, a comparison of the number-, intensity- and volume-weighted size distributions for PAA10-*b*-PS205 is provided in **Figure A4-1.** These inconsistencies are likely due to a low aggregation level, since the size derived from the signal intensity is strongly biased towards larger particles (the scattered intensity is proportional to the sixth power of the particle size).[31] The variation in the hydrodynamic diameter with the BCP block length was also found to be inconsistent, without any clear trend, and broad size distributions ($Đ \geq 0.2$) were obtained. Consequently, the theoretical D_h of the BCP samples was rather estimated from viscosity data published for polystyrene homopolymers.

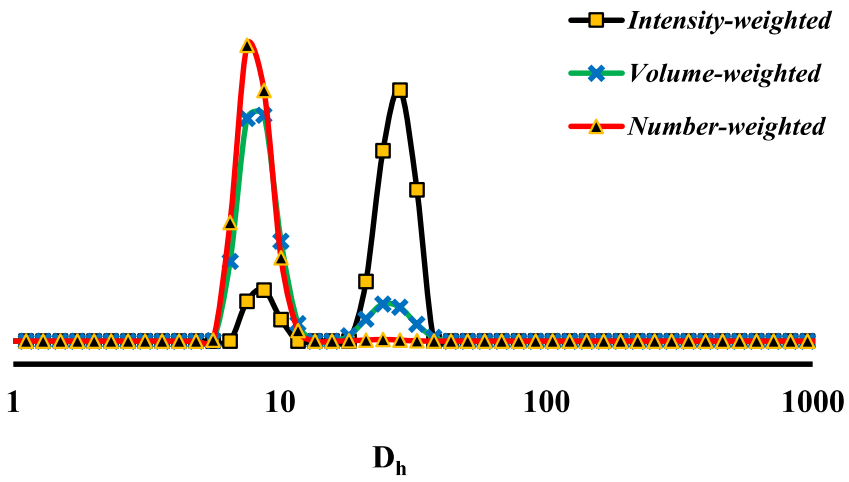

Figure A4-1. Comparison of number-, intensity- and volume-weighted size distributions for PAA10-b-PS205 at 5.0 mg/mL in a THF/ethanol (90/10 v/v) mixture at 25 °C.

The intrinsic viscosity [η] is related to the viscosity-average molecular weight of a polymer (M_v) through the Mark–Houwink–Sakurada (MHS) equation,

$[\eta] = KM_v^{\alpha}$

where K and α are the MHS parameters which depend on the polymer composition, the solvent and the temperature. The exponent α = 0.5 for theta solvents, and 0.7–0.8 for good solvents.[63] The intrinsic viscosity is related to the hydrodynamic volume (V_h) through the equation

$$[\eta] = 2.5\ N_A\ V_h / M_v$$

where N_A is Avogadro's number, and the hydrodynamic volume is related to the hydrodynamic radius through

$$V_h = (4/3)\ \pi\ R_h^3$$

By combining the above equations, the hydrodynamic radius can be related to the M_v of the polymer, but since the weight-average molecular weight (M_w) is usually close to M_v, particularly for polymers with narrow molecular weight distributions (such as the ones used in this investigation), it follows that[63]

$$R_h = 5.4\times10^{-9}\ [KM_w^{\alpha+1}]^{1/3}$$

To the best of our knowledge there are no reports of MHS parameters for PtBA-*b*-PS copolymers, but since the copolymers are mostly composed of polystyrene, MHS parameters reported for polystyrene in the same molecular weight range as the PtBA-*b*-PS copolymers were used to calculate their approximate R_h. No MHS values could be found for polystyrene in THF/ethanol or toluene/ethanol mixtures at 25°C, so the R_h values were calculated using MSH parameters reported for polystyrene in pure THF and toluene at room temperature.

The R_h values for polystyrene samples having a M_w identical with the block copolymers are provided in **Table A4-2**. The MHS parameters used for THF were K= 1.10×10^{-2} cm^3/g and α = 0.72, valid at 25 °C in a molecular weight range from 1000 to 1×10^6 g/mol.[64] For polystyrene in toluene, the MHS parameters K = 1.05×10^{-2} cm^3/g and α = 0.73, valid at 25 °C in a molecular

weight range from 5000 to 4×10^5 g/mol were used.[65] The R_h values in toluene and THF are very close as expected, since both are good solvents for polystyrene.

Table A4-2. Hydrodynamic radii for polystyrene samples with the same molecular weights as the PtBA-b-PS samples, in pure THF and toluene, at 25 °C.

Sample	**M_w(abs) (g/mol)**	**D_h[a], (THF) nm**	**D_h[b] (Toluene) nm**
P*t*BA10-*b*-PS85	2.0×10^4	7	7.2
P*t*BA10-*b*-PS205	3.3×10^4	9.4	9.6
P*t*BA10-*b*-PS260	3.6×10^4	9.8	10
P*t*BA10-*b*-PS305	4.0×10^4	10.4	10.7
P*t*BA13-*b*-PS156	2.3×10^4	7.6	7.8
P*t*BA13-*b*-PS330	3.5×10^4	9.6	9.8
P*t*BA13-*b*-PS390	4.7×10^4	11.4	11.7
P*t*BA17-*b*-PS195	3.3×10^4	9.4	9.6
P*t*BA17-*b*-PS250	3.7×10^4	10	10.2
P*t*BA17-*b*-PS395	6.2×10^4	13.6	13.7

a) $K= 1.10\times10^{-2}$ cm^3/g, $\alpha = 0.72$ in THF at 25 °C; b) $K = 1.05\times10^{-2}$ cm^3/g, $\alpha = 0.73$ at 25 °C in toluene.

Appendix B-2. Characterization of G2, G3 and G4 ACC systems by DLS

Table A4-3. Diameter and dispersity of G2 ACCs in toluene/ethanol (90/10 v/v) mixtures (all diameters are in nm).

Sample	D_h^Z	D_h^V	D_h^N	Đ
G2	60±1	54±1	48±1	0.02±0.004
G2@PAA10-*b*-PS85	77±1	68±1	57±1	0.07±0.006
G2@PAA10-*b*-PS 205	74±1	67±1	56±2	0.10±0.01
G2@PAA10-*b*-PS 260	79±1	69±1	55±1	0.13±0.007
G2@PAA10-*b*-PS 305	81±1	72±1	58±1	0.11±0.003
G2@PAA13-*b*-PS 156	73±1	65±1	53±1	0.01±0.006
G2@PAA13-*b*-PS 330	91±2	80±3	69±2	0.17±0.04
G2@PAA13-*b*-PS 392	84±1	73±1	58±2	0.11±0.02
G2@PAA17-*b*-PS 195	81±1	71±1	58±1	0.07±0.01
G2@PAA17-*b*-PS 250	78±1	69±1	57±1	0.09±0.007
G2@PAA17-*b*-PS 395	84±2	74±5	65±3	0.18±0.09

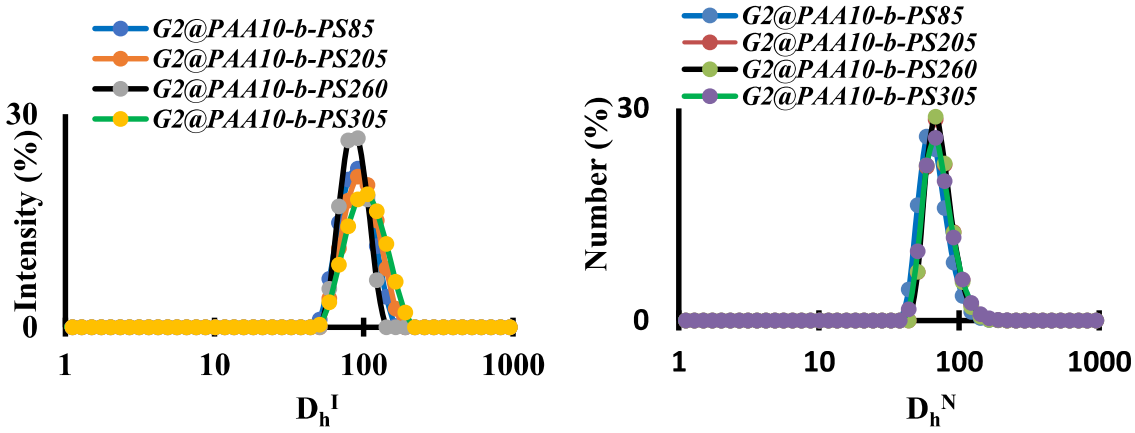

Figure A4-2. DLS intensity- (left) and number-weighted (right) size distributions for the G2@PAA10-b-PSx ACCs with different PS chain lengths x in toluene at 0.8 mg/mL.

Table A4-4. Diameter and dispersity of G3 ACCs (all diameters are in nm).

Sample name	THF			Toluene		
	D_h^Z	D_h^N	Đ	D_h^Z	D_h^N	Đ
G3	92±1	74±2	0.07±0.01	-	-	-
G3@PAA10-*b*-PS85	94±4	72±2	0.3±0.10	118±2	78±3	0.21±0.01
G3@ PAA10-*b*-PS205	94±1	65±2	0.15±0.05	89±1	65±3	0.15±0.05
G3@ PAA10-*b*-PS260	94±1	71±2	0.12±0.04	114±4	94±6	0.08±0.06
G3@ PAA10-*b*-PS305	92±8	58±5	0.4±0.12	115±1	85±3	0.08±0.02
G3@ PAA13-*b*-PS156	99±1	77±3	0.05±0.01	117±1	87±1	0.13±0.01
G3@ PAA13-*b*-PS330	95±1	78±1	0.03±0.01	119±3	85±3	0.25±0.08
G3@ PAA13-*b*-PS390	93±2	72±2	0.10±0.04	89±4	56±5	0.36±0.07

Table A4-5. Diameter and dispersity of G4 ACCs (all diameters are in nm).

Sample name		THF			Toluene		
		D_h^Z	D_h^N	Đ	D_h^Z	D_h^N	Đ
G4		150±1	123±7	0.08±0.02	-	-	-
G4@	PAA10-*b*-	183±1	151±5	0.05±0.01	200±8	198±8	0.20±0.09
G4@	PAA10-*b*-	156±4	129±3	0.05±0.02	144±4	118±2	0.05±0.02
G4@	PAA10-*b*-	168±1	143±2	0.02±0.01	160±4	124±2	0.13±0.06
G4@	PAA13-*b*-	165±2	135±3	0.05±0.01	148±1	103±3	0.23±0.02
G4@	PAA13-*b*-	171±1	141±3	0.02±0.02	415±12	141±4	0.60±0.05
G4@	PAA13-*b*-	169±2	142±1	0.07±0.01	273±4	95±108	0.25±0.02

Appendix B-3. AFM pictures for molecular films of the ACPSs and G2 ACCs.

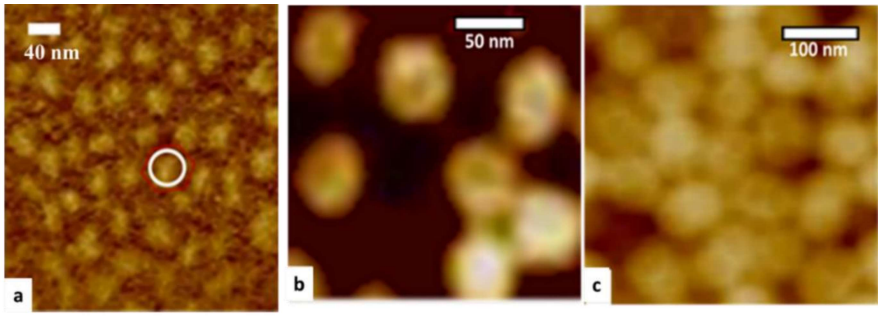

Figure A4-3. Zoomed-in AFM height images for (a) G1, (b) G2 and (c) G4 ACPSs.

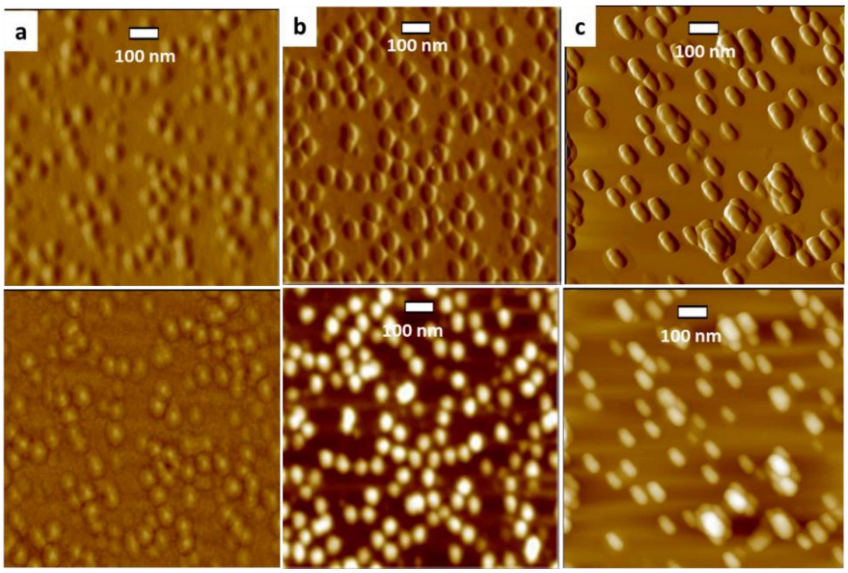

Figure A4-4. AFM phase (top) and height (bottom) images for (a) G2@PAA13-b-PS330, (b) G2@PAA13-b-PS390, and (c) G2@PAA17-b-PS395 cast from toluene at 0.8 mg/mL (scale bar = 100 nm).

The AFM images for G2@PAA13-*b*-PS330, G2@PAA13-*b*-PS390, and G2@PAA17-*b*-PS395 in toluene display a slightly elongated particle shape in toluene (**Figure A4-4**), with

average diameters of 71 ± 4, 74 ± 5, and 76 ± 5 nm, respectively. These are smaller than the sizes derived from DLS measurements.

Appendix C

Appendix C-1. Metal loading in arborescent copolymer substrates (ACPSs)

Loading of the ACPSs was limited to lower levels, namely either 0.25 or 0.5 equiv/2VP unit, because higher loadings led to immediate precipitation when stirring was stopped. The colloidal stability of the metal-loaded copolymers also depended on their loading level and aging. Thus at 0.25 equiv of $HAuCl_4$/2VP unit, the faint yellow solutions became cloudy within a few hours in the absence of stirring. Precipitation was observed for the G1 (G0-*g*-P2VP30K) and G2 (G1-*g*-P2VP30K) copolymers, while the G3 (G2-*g*-P2VP13K) and G4 (G3-*g*-P2VP15K) copolymer solutions remained clear for at least half a day but precipitated overnight. At a loading level of 0.5 equiv/2VP unit, sedimentation occurred within a few minutes when stirring was discontinued for the lower generations, and after a few hours for the higher generations. The TEM images obtained for ACPSs loaded with 0.25 equiv of $HAuCl_4$ in THF are provided in **Figure A5-1**. It is clear that aggregation occurred in all cases, regardless of the generation number; this is attributed to the absence of a PS corona shielding the interactions between metal-loaded templates. The aggregation level varied among the different generations, however: For metal-loaded G1 (G0-*g*-P2VP30K) and G2 (G1-*g*-P2VP30K) copolymers only aggregated particles were observed, while some free particles were present for the metal-loaded G3 (G2-*g*-P2VP13K) and G4 (G3-*g*-P2VP15K) copolymers. In the case of the G3 copolymer, smaller metallic particles were visible outside of the arborescent structures. This could be due to a small amount of copolymer degradation occurring during reduction of the gold salt particles by the TEM beam, since the particles were observed to move and coalesce while the pictures were being recorded.

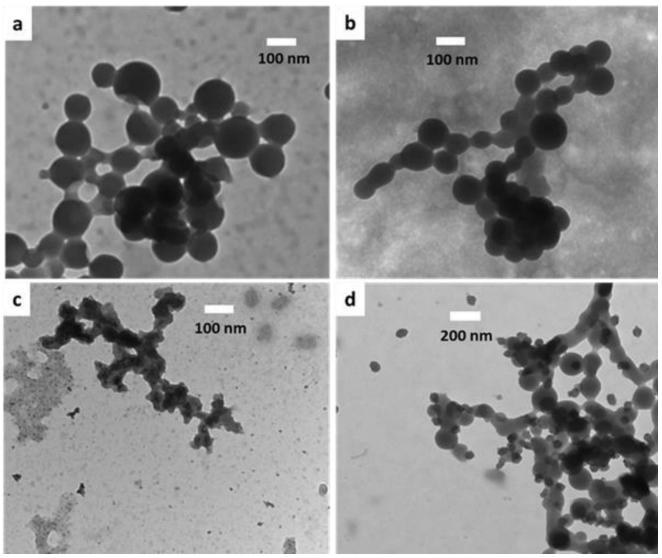

Figure A5-1. TEM images for ACPSs loaded with 0.25 equiv $HAuCl_4$/2VP unit in THF: (a) G0-g-P2VP30K, (b) G1-g-P2VP30K, (c) G2-g-P2VP13K, and (d) G3-g-P2VP15K.

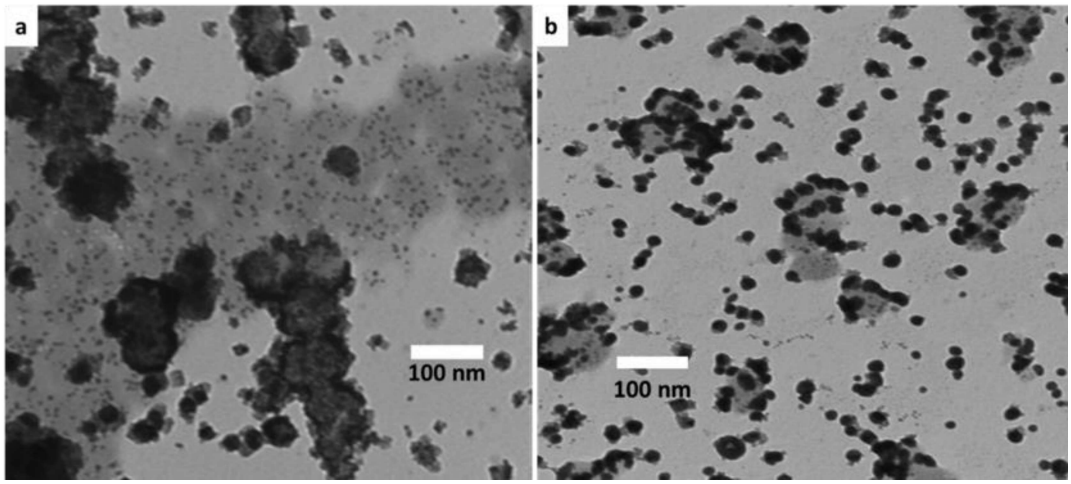

Figure A5-2. TEM images for $HAuCl_4$-loaded G2PS-g-P2VP13K copolymers: (a) solution loading in THF, and (b) film loading.

The solution and film loading procedures were compared by TEM analysis for the G3 (G2-*g*-P2VP13K) copolymer (**Figure A5-2**). Solution loading was achieved at 0.5 equiv/2VP unit, while for film loading one drop of a 10 mg/mL THF solution of $HAuCl_4$ was added to a TEM grid on which a

0.8 mg/mL solution of the G3 copolymer solution in THF had been deposited. As the TEM images suggest, film loading produced larger metallic particles outside of the copolymer scaffold, but the metal-loaded copolymers were less aggregated as compared to solution loading. This is obviously the result of decreased mobility, as the film was cast on the grid before loading. In contrast, solution loading yielded more aggregated particles with most of the metal loaded inside the copolymer molecules, and only a few metallic particles outside the templates.

Appendix D

Appendix D-1. Comparison of solution versus film reduction

Solution reduction was examined for samples containing 17 acrylic acid anchoring units in the block copolymer forming the complex, namely G2@PAA17-*b*-PS195, G2@PAA17-*b*-PS250 and G2@PAA17-*b*-PS395, loaded with 0.5 equiv of $HAuCl_4$/2VP unit in toluene. The TEM images obtained (**Figure A0-1**) showed that solution reduction resulted in the formation of 8-10 nm nanoparticles within the templates. The diameter of the NPs obtained for G2@PAA17-*b*-PS195, G2@PAA17-*b*-PS250 and G2@PAA17-*b*-PS395 was 10 ± 3, 8 ± 2 and 8 ± 2 nm, respectively.

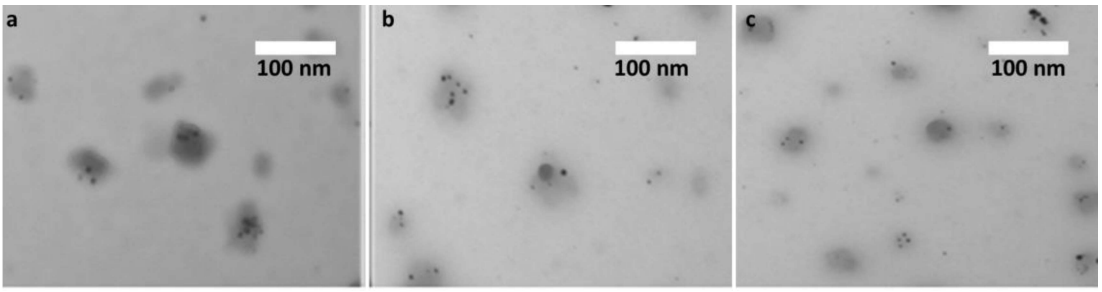

Figure A6- 1. TEM images for $HAuCl_4$-loaded templates in toluene reduced in solution with $NaBH_4$: (a) G2@PAA17-b-PS195, (b) G2@PAA17-b-PS250, and (c) G2@PAA17-b-PS395.

Film reduction of these samples yielded slightly different results (**Figure A6-2**). Particles with a diameter of 10.3 ± 2.9 nm were obtained for G2@PAA17-*b*-PS195, and many were located outside the templates. In the other cases, Au NPs were produced only inside the templates, with average diameters of 7.1 ± 1.7 and 6.0 ± 1.4 nm for G2@PAA17-PS250 and G2@PAA17-PS395, respectively. While the results suggest that the BCP chain length does not have a very significant influence on the size of the Au NPs formed, given the broad size distributions obtained, the BCPs with longer PS segments

definitely isolate the Au-rich domains of the templates more effectively from each other, thus minimizing migration of the gold salt during reduction.

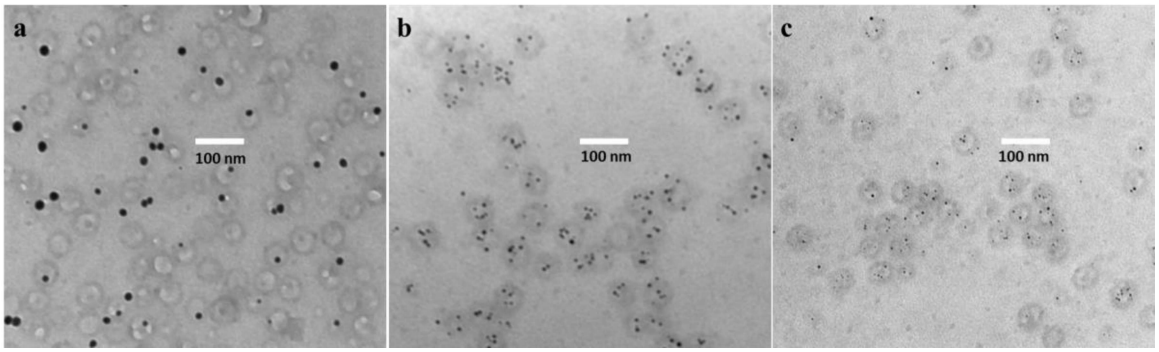

Figure A6- 2. TEM images for $HAuCl_4$-loaded templates in toluene reduced in films with $NaBH_4$: (a) G2@PAA17-b-PS195, (b) G2@PAA17-b-PS250, and (c) G2@PAA17-b-PS395.